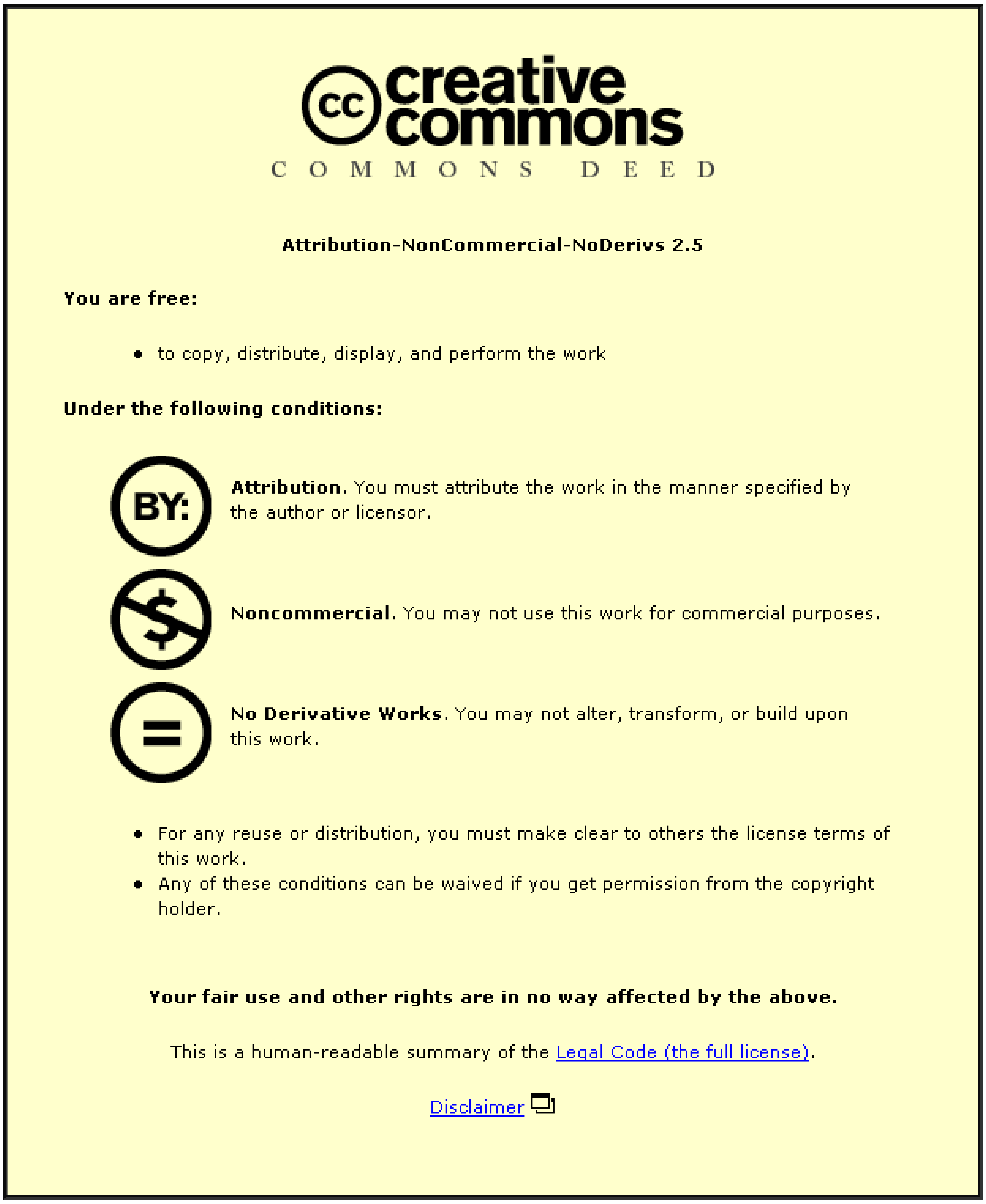

Computer Modelling of Night-time Natural Ventilation

Liam Harrington
Department of Civil and Building Engineering
Loughborough University

A Doctoral Thesis submitted in partial fulfilment of the requirements for the award of Doctor of Philosophy of Loughborough University

15th November 2001

Abstract

Wind-induced ventilation has the potential to reduce cooling energy use in buildings. One method this can be achieved is by the use of night-time ventilation to cool down the structure of a building, resulting in lower air and radiant temperatures during the day. To design effective naturally ventilated buildings, evaluation tools are needed that are able to assess the performance of a building. The primary goal of this work was to develop such a tool, that is suitable for use in annual building energy simulation. The model presented, is intermediate in complexity between a CFD numerical model and current single air node models, having seven nodes.

The thesis describes how numerical and experimental data have been used to develop the structure and define the parameters of the simplified nodal model. Numerical calculations of the flow and temperature fields have been made with a coupled flow and radiant exchange CFD code. Numerically derived velocity dependent convective heat transfer coefficients are compared with experimental measurements made in room ventilated by cross-flow means, and with empirical correlations cited by other studies. Bulk convection between the air nodes of the simplified nodal model has been derived from a numerical study of contaminant dispersal. The performance of the model is demonstrated by making comparisons with the predictions of a single air node model.

Acknowledgements

I would like to thank my supervisors Mr Henk Versteeg and Dr Philip Haves for their guidance and enthusiasm. I gratefully acknowledge the financial support of E.A.Technology and the UK Building Research Establishment for making this work possible.

I would like to thank my colleagues in the Department of Civil and Building Engineering for all their help during my time there. Finally, I am indebted to my family for providing support and encouragement throughout all my student years.

Contents

1 **Introduction** 1

1.1 Background 1

1.2 Scope 2

1.3 Overview of the Thesis 4

2 **Development of a Zonal Model of Night-time Cross-flow Ventilation** 5

2.1 Objectives 5

2.2 Background 6

2.2.1 Previous research 6

2.2.2 Implications of Previous Research on Study 7

2.2.3 Thermal Analysis Codes 8

2.2.4 Building Air Flow Modelling 9

2.2.5 LIGHTS 9

2.3 Modelling Method 11

2.3.1 Bulk Convection in the Zonal Model 13

2.3.2 The Zonal Model Proposed 15

2.4 Conclusions 18

3 **CFD Models of Night-time Cross-flow Ventilation** 20

3.1 Objectives 20

3.2 A Description of Computational Fluid Dynamics 21

3.2.1 The Reynolds Averaged Navier-Stokes Equations 21

3.2.2 Turbulence Closure Model 22
3.2.3 The Energy Equation 23
3.2.4 Radiative Heat Transfer 24
3.2.5 Solution Procedure 26
3.2.6 Wall Boundaries 32
3.2.7 Flow Boundaries 34
3.3 Background 35
3.3.1 Previous Research 36
3.3.2 Implications of Previous Work 38
3.4 Modelling Method 40
3.4.1 Geometry 41
3.4.2 Boundary Conditions 41
3.4.3 Computational Grid 43
3.4.4 Physical Properties 45
3.4.5 Buoyancy Induced Instability 45
3.4.6 The steady state parametric study 46
3.4.7 Transient CFD model 47
3.5 Results and Discussion 49
3.5.1 Pressure Difference Between Room Openings 50
3.5.2 Velocity Field and Flow Detachment 54
3.5.3 Convective Heat Transfer Coefficients 65
3.5.4 Mass Flows 74
3.5.5 Effect of y^+ Values 76
3.6 Conclusions 78

4 Experimental Procedure 81

4.1 Objectives 81
4.2 Background 82
4.2.1 Convective Heat Transfer 82
4.2.2 Full-Scale Investigations 83
4.2.3 Wind Tunnel Tests 83

4.2.4 Implications of Previous Work 85
4.3 Experimental Method 86
4.3.1 Experimental Room 86
4.3.2 Preliminary Experiment 89
4.3.3 Experimental Equipment 90
4.3.4 The Experiment Proper 95
4.4 Results 95
4.4.1 Wind data 95
4.4.2 Room Air Speed and Air Temperatures 97
4.4.3 Detachment Point 105
4.4.4 Room Temperatures 108
4.4.5 Heat Flux 111
4.4.6 Heat Transfer Coefficients 111
4.5 Conclusions 120

5 CFD Analysis of the Experimental Room 123

5.1 Objectives 123
5.2 Modelling Method 123
5.2.1 Geometry and grid 123
5.2.2 Boundary conditions 125
5.3 Results 126
5.3.1 Grid Dependence 126
5.3.2 Flow Field 127
5.3.3 Detachment Point 137
5.3.4 Temperature Field 139
5.3.5 Air Speed 141
5.4 Conclusions 147
5.4.1 Findings 147
5.4.2 Further Work 149

6 Using the Zonal Model 150

6.1 Objectives 150

6.2 Method 150

6.2.1 Comparison between the zonal model and a 'fully mixed' model . . 150

6.2.2 Zonal Model Parameters 152

6.2.3 The Fully Mixed Model 154

6.3 Results 157

6.3.1 Comparison between the zonal model and a 'fully mixed' model . . 157

6.3.2 Zonal model sensitivity study 160

6.4 Conclusions 162

7 Conclusions 164

7.1 Outlook 164

7.2 Scope 165

7.3 Major Findings 166

7.4 Importance and Limitations of this Study 171

7.5 Directions for Further Work 173

A LIGHTS Zone definition example 175

B Zonal Model Equations 184

B.1 Calculating the Zonal Model Parameters 184

B.2 Heat Balance Equations 187

B.3 Mass Balance Equations 188

C Instrument Calibration 190

C.1 Anenometer Calibration 190

C.2 Thermocouple Calibration 190

C.2.1 Water Bath Calibration 190

C.2.2 In-situ Calibration of the Surface Thermocouples 191

C.3 Heat Flux Meter Calibration 193

C.4 Uncertainty in convective heat flux coefficient, h_c 193

C.5 Summary of Measurement Errors 194

List of Figures

2.1 The path of the main flow stream as predicted by CFD for an inlet velocity of 0.25 ms^{-1} and three different temperature differences between the inlet air and the ceiling: 0 K (top); 6 K (middle); and 12 K (bottom). 12

2.2 The control volumes of a zonal model superimposed on a diagram of the flow stream through a room (before mass flows have been derived). 13

2.3 The control volumes of a zonal model superimposed on a schematic diagram of the flow stream through a room (after mass flows have been derived). 14

2.4 Zonal model for nighttime cross-flow ventilation. 15

2.5 Zonal model when the main flow stream remains attached to the ceiling. . 16

2.6 Zonal model when the main flow stream does not attach to the ceiling. . . 17

2.7 Zonal model when the main flow stream detaches in zone 3. 17

3.1 A notional one-dimensional control volume with constant node spacing. . 27

3.2 A schematic diagram of the CFD model of cross flow ventilation. 41

3.3 The main computational grid used for the parametric study (6000 cells). . 44

3.4 Pressure difference between the inlet and outlet openings versus inlet velocity for a 0 K temperature difference between inlet air and ceiling surface. 51

3.5 k versus the temperature difference between the inlet air and the ceiling surface. 53

3.6 Vector plots for an inlet velocity of 0.25 ms^{-1} with the main flow stream path superimposed. The temperature differences between the inflow air and the ceiling are: 0 K (top); 2 K(second); 4 K(third); 6 K(fourth); 8 K(fifth); 10 K(bottom). 55

3.7 Vector plots for an inlet velocity of 0.5 ms^{-1} with the main flow stream path superimposed. The temperature differences between the inflow air and the ceiling are: 0 K (top); 4 K(second); 8 K(third); 10 K(fourth); 12 K(fifth); 15 K(bottom). . . . 56

3.8 Vector plots for an inlet velocity of 0.75 ms^{-1} with the main flow stream path superimposed. The temperature differences between the inflow air and the ceiling are: 0 K (top); 4 K(second); 8 K(third); 15 K(bottom). . . . 57

3.9 Vector plots for an inlet velocity of 1.0 ms^{-1} with the main flow stream path superimposed. The temperature differences between the inflow air and the ceiling are: 0 K (top); 4 K(second); 8 K(third); 15 K(bottom). . . . 58

3.10 Vector plots for an inlet velocity of 2.0 ms^{-1} with the main flow stream path superimposed. The temperature differences between the inflow air and the ceiling are: 0 K (top); 4 K(second); 8 K(third); 15 K(bottom). . . . 59

3.11 A main flow stream path that detaches from the ceiling. . . . 60

3.12 Cumulative horizontal mass flow along sections A, B and C. Mass flow is plotted in dimensionless form, i.e. $\frac{\dot{m}}{\dot{m}_{in}}$. . . . 61

3.13 Distance from inflow boundary that detachment occurs plotted against Archimedes number. . . . 62

3.14 A first order fit of Archimedes number versus detachment distance from inlet. . . . 64

3.15 The convective heat flux predicted at the room surfaces (y-axis in Wm^{-2}) versus the temperature difference (x-axis in K) between the inflow air and the ceiling for a particular inlet velocity: 2 ms^{-1} (top left); 1.5 ms^{-1} (top right); 1 ms^{-1} (second left); 0.75 ms^{-1} (second right); 0.5 ms^{-1} (third left); 0.25 ms^{-1} (third right); 0.1 ms^{-1} (bottom right). . . . 66

3.16 The predicted convective heat transfer coefficients at the room surfaces (y-axis in $\mathrm{Wm}^{-2}\mathrm{K}^{-1}$) versus the temperature difference between the inflow air and the ceiling (x-axis in K) for a particular inlet velocity: 2 ms^{-1} (top left); 1.5 ms^{-1} (top right); 1 ms^{-1} (second left); 0.75 ms^{-1} (second right); 0.5 ms^{-1} (third left); 0.25 ms^{-1} (third right); 0.1 ms^{-1} (bottom right). . . 68

3.17 The convective heat transfer coefficients taken from the numerical results for the zonal model. . . . 70

3.18 The ceiling convective heat transfer coefficient empirical relationships compared with data from the literature. . . . 72

3.19 The floor and wall convective heat transfer coefficient empirical relationships compared with data from the literature. . . . 74

3.20 Dimensionless mass flows ($\dot{m}_{l,n}/\dot{m}_{in}$) from the recirculating region into the main flow stream: temperature difference of 0 K (top); inlet velocity of 2 ms^{-1} (middle); inlet velocity of 1 ms^{-1} (bottom). 75

3.21 Predicted heat transfer coefficient for ceiling node C1 in cases with y^+ values above and below 30. 78

4.1 Outside view of David Collett residence. Experimental room is in the middle of photo with ultrasonic anemometer protruding from window. . . 87

4.2 A plan of the bedroom in David Collett 87

4.3 Inside view of the experimental room towards the door. 88

4.4 Elevation of the bedroom 88

4.5 View inside the experimental room and the hopper. 89

4.6 The positioning of the anemometer stands 91

4.7 The vertical positioning of the anemometer in the room 92

4.8 The vertical positioning of the anemometer in the doorway 92

4.9 The thermocouples/heat flux meters on the ceiling 94

4.10 Local site weather station wind data. 96

4.11 Hourly averaged wind speed outside the experimental room. 96

4.12 Air velocity from the ultrasonic anemometer positioned outside the experimental room. 98

4.13 Air speed in the hopper opening. 99

4.14 The air speed in the hopper opening averaged over hourly intervals. 99

4.15 Air temperature in the hopper. 100

4.16 Air speed at heat flux meter sites A and B, and in the hopper. 100

4.17 Air speed profile at sensor site B. 101

4.18 Air speed ratio at heat flux meter site A. 103

4.19 Air speed ratio at heat flux meter site B. 103

4.20 Air speed ratio at heat flux meter site A. 104

4.21 Air speed ratio at heat flux meter site B. 104

4.22 Archimedes number versus time during experiment. 106

4.23 Archimedes number versus air speed ratio at heat flux meter site A. . . . 106

4.24 Archimedes number versus air speed ratio at heat flux meter site B. 107

4.25 North wall thermocouple placement. 108

4.26 North wall temperature. 109

4.27 Ceiling temperature, radiant temperature, and the air temperature at heat flux meter site A. 110

4.28 Ceiling temperature, radiant temperature, and the air temperature at heat flux meter site B. 110

4.29 Ceiling heat flux at flux meter site A. 112

4.30 Ceiling heat flux at flux meter site B. 112

4.31 Convective heat transfer coefficient versus local air speed at heat flux meter site A plotted along with the estimated uncertainty. 113

4.32 Convective heat transfer coefficient versus local air speed at heat flux meter site B plotted along with the estimated uncertainty. 114

4.33 Convective heat transfer coefficient versus local air speed compared with correlations (see Chapter 3). 115

4.34 Convective heat transfer coefficient versus local air speed compared with correlations when data at instances where the difference between the ceiling temperature and the local air temperature is less than 0.75 K are ignored. 116

4.35 Convective heat transfer coefficient versus local air speed compared with correlations from the literature and the CFD simulations in Chapter 3. . . 118

4.36 Convective heat transfer coefficient versus hopper air speed compared with correlations from the literature and the CFD simulations in Chapter 3. . . 119

5.1 3D CFD model geometry of the experimental room. 124

5.2 Initial coarse grid used for the simulations, 63347 cells. 124

5.3 The fine grid used for the simulations, 506776 cells. 125

5.4 Vector plot along y plane near the middle of the room from an isothermal simulation of the 3 a.m. period. 127

5.5 Vector plot along x plane from an isothermal simulation of the 3 a.m. period. 128

5.6 Vector plot along z plane 0.1 m above the floor from an isothermal simulation of the 3 a.m. period. 128

5.7 Stream lines from the inflow boundary from an isothermal simulation of the 3 a.m. period. 129

5.8 Stream lines along the north wall boundary from an isothermal simulation of the 3 a.m. period. 130

5.9 Stream lines from the top of the south wall boundary from an isothermal simulation of the 3 a.m. period. 130

5.10 Stream lines from the bottom of the south wall boundary from an isothermal simulation of the 3 a.m. period. 131

5.11 Stream lines released near the floor boundary from an isothermal simulation of the 3 a.m. period. 131

5.12 Vector plot along y plane near the middle of the room from a thermal and buoyancy simulation of the 3 a.m. period. 132

5.13 Vector plot along x plane from a thermal and buoyancy simulation of the 3 a.m. period. 132

5.14 Stream lines from the inflow boundary from a thermal and buoyancy simulation of the 3 a.m. period. 133

5.15 Stream lines from the top of the south wall boundary from a thermal and buoyancy simulation of the 3 a.m. period. 134

5.16 Stream lines from the bottom of the south wall boundary from a thermal and buoyancy simulation of the 3 a.m. period. 134

5.17 Vector plot close to the floor from a thermal and buoyancy simulation of the 3 a.m. period. 135

5.18 Stream lines from the inflow boundary from a thermal and buoyancy simulation of the 12 a.m. period. 135

5.19 Stream lines along the north wall boundary from a thermal and buoyancy simulation of the 12 a.m. period. 136

5.20 Stream lines from the bottom of the south wall boundary from a thermal and buoyancy simulation of the 12 a.m. period. 136

5.21 Vectors on a z-plane 0.1 m above the floor from a thermal and buoyancy simulation of the 12 a.m. period. 137

5.22 Stream lines along the south and east wall boundaries from a thermal and buoyancy simulation of the 12 a.m. period. 138

5.23 Temperature contour plot, 12 a.m. period. 139

5.24 Temperature contour plot, 3 a.m. period. 140

5.25 Comparison between CFD and experimental temperatures at 12 a.m. . . . 140

5.26 Comparison between CFD and experimental temperatures at 3 a.m. 141

5.27 Dantec stand locations. 142

5.28 Average air speed at three vertical locations during the 3 a.m. period. Comparison between the experimental data and the numerical results from the isothermal simulations. Stand A nearest the window (top), Stand B (middle), and Stand C furthest from window (bottom). 143

5.29 Average air speed at three vertical locations during the 3 a.m. period. Comparison between the experimental data and the numerical results from the isothermal, and the thermal simulations. 144

5.30 Average air speed at three vertical locations during the 12 a.m. period. Comparison between the experimental data and the numerical results from the isothermal simulations. 145

5.31 Average air speed at three vertical locations during the 12 a.m. period. Comparison between the experimental data and the numerical results from the isothermal, and the thermal simulations. 146

6.1 The zonal model network diagram. 151

6.2 Fully mixed model. 155

6.3 Comparison of ceiling temperature prediction using the zonal model and the fully mixed model with an inlet velocity of 1.5 m/s and wall/ceiling thermal mass ratio of 0.2. 155

6.4 Temperature at the 5 ceiling nodes in the zonal model with an inlet velocity of 1.5 m/s and wall/ceiling thermal mass ratio of 0.2. 156

6.5 Comparison of wall and floor temperature prediction using the zonal model and the fully mixed model with an inlet velocity of 1.5 m/s and wall/ceiling thermal mass ratio of 0.2. 156

6.6 Comparison of ceiling temperature prediction using the zonal model and the fully mixed model with an inlet velocity of 0.1 m/s and wall/ceiling thermal mass ratio of 0.2. 157

6.7 Temperature at the 5 ceiling nodes in the zonal model with an inlet velocity of 0.1 m/s and wall/ceiling thermal mass ratio of 0.2. 158

6.8 Comparison of wall and floor temperature prediction using the zonal model and the fully mixed model with an inlet velocity of 0.1 m/s and wall/ceiling thermal mass ratio of 0.2. 158

6.9 Comparison of temperature drop of the ceiling between the beginning and end of the 12 hour simulation using the zonal model and the fully mixed model for a range of wall/ceiling thermal mass ratios. 159

6.10 Comparison of ceiling temperature prediction using the zonal model with an inlet velocity of 1.5 m/s and different convective heat transfer coefficients. 161

B.1 Zonal model for nighttime cross-flow ventilation. 185

List of Tables

3.1 Constants used in the k–ε Turbulence Model 23

3.2 Physical properties of the fluid modelled. 45

3.3 Cases modelled in the parametric study to investigate the effect of inlet velocity and the temperature difference between the inflow air and the ceiling. 46

3.4 The pressure difference coefficients for a variety of temperature differences. 52

3.5 Detachment position related to Archimedes number (first order fit). 64

3.6 Convective heat transfer coefficient empirical relationships for the flow regimes given in Table 3.5. 70

3.7 Correlations for convective heat transfer coefficient, h_c ($\mathrm{Wm^{-2}K^{-1}}$), (Spitler, Perdersen, and Fisher 1991). 72

3.8 Dimensionless mass flow rates for flow regimes (1–5) given in Table 3.5. . 76

4.1 Correlation between hourly averaged air speed at various locations and the weather data. 101

4.2 Correlation between hourly averaged air speed at various locations and the ultrasonic anemometer. 102

4.3 Correlation between hourly averaged air speed at various locations and the hopper air speed. 102

4.4 Correlation data for the hourly averaged hopper air speed. 105

4.5 The uncertainty in the different experimental equipment. 113

4.6 Coefficients to Equation 4.9 when h_c is fitted with respect to local air speed or hopper air speed. 117

5.1 Boundary conditions used in the CFD simulations. 126

6.1 Zonal model simulation cases. 151

6.2 Heat extracted from the ceiling over a twelve hour simulation period. . . . 160

C.1 Difference between the hand held thermocouple and the logged surface mounted thermocouples readings. 192

C.2 The errors for the different experimental measurements. 194

Nomenclature

Roman Letters

A_{C1}, A_{C2}, A_{C3}, A_{C4}, A_{C5}	area of zonal model ceiling nodes $C1$, $C2$, $C3$, $C4$ and $C5$ respectively $[m^2]$.
A_{east}	area of zonal model east wall node *east* $[m^2]$.
A_{flr}	area of zonal model floor node *flr* $[m^2]$.
A_{in}	area of inflow opening $[m^2]$.
A_{west}	area of zonal model west wall node *west* $[m^2]$.
Ar	Archimedes number.
a_P, a_E, a_W, a_N, a_S	coefficients of discretised equation.
$\bar{c}_{e,n}$	mean contaminant concentration along the east boundary of MFS zone n.
$\bar{c}_l$	mean contaminant concentration of the lower recirculating region.
$\bar{c}_n$	mean contaminant concentration of MFS zone n.
$\bar{c}_u$	mean contaminant concentration of the upper recirculating region.
$\bar{c}_{w,n}$	mean contaminant concentration along the west boundary of MFS zone n.
$C_{\varepsilon 1}$, $C_{\varepsilon 2}$	turbulence model constant in the ε equation.
C_μ	model constant in the definition of turbulent viscosity.
C_d	discharge coefficient.
C_p	pressure coefficient.
$C_{p,i}$	average pressure coefficient for the upwind opening area.

$C_{p,o}$	average pressure coefficient for the downwind opening area.
c_p	specific heat $[J\,kg^{-1}K^{-1}]$.
E	constant in the log-law wall function.
G	turbulent energy production due to the buoyancy forces $[kg\,m^{-1}s^{-3}]$.
g	gravitational acceleration $[m\,s^{-2}]$.
g_i	gravitational acceleration vector $[m\,s^{-2}]$.
H	total enthalpy $[J\,kg^{-1}]$.
h	static enthalpy $[J\,kg^{-1}]$.
h_c	convective heat transfer coefficient $[W\,m^{-2}\,K^{-1}]$.
h_{C1}, h_{C2}, h_{C3}, h_{C4}, h_{C5}	convective heat transfer coefficient of zonal model ceiling nodes $C1$, $C2$, $C3$, $C4$ and $C5$ respectively $[W\,m^{-2}\,K^{-1}]$.
h_{east}	convective heat transfer coefficient of zonal model east wall node *east* $[W\,m^{-2}\,K^{-1}]$.
h_{flr}	convective heat transfer coefficient of zonal model floor node *flr* $[W\,m^{-2}\,K^{-1}]$.
h_{west}	convective heat transfer coefficient of zonal model west wall node *west* $[W\,m^{-2}\,K^{-1}]$.
I	radiation intensity $[W\,m^{-2}sr^{-1}]$.
J	local radiosity $[W\,m^{-2}sr^{-1}]$.
K_a	gas absorption coefficient.
K_s	gas scattering coefficient.
k	turbulent kinetic energy $[m^2s^{-2}]$.
L	turbulent length scale $[m]$.
$\dot{m}_{in}$	mass flow through room inflow opening $[kg\,s^{-1}]$.
$\dot{m}_{l,n}$	mass flow from the lower recirculating region to MFS zone n (also the mass flow from the MFS zone n to the lower recirculating region) $[kg\,s^{-1}]$.
$\dot{m}_{u,n}$	mass flow from the upper recirculating region to MFS zone n (also the mass flow from the MFS zone n to the upper recirculating region) $[kg\,s^{-1}]$.
$m_{l,n}$	dimensionless mass flow between the lower recirculating region and MFS zone n ($m_{l,n} = \dot{m}_{l,n}/\dot{m}_{in}$).

$m_{u,n}$	dimensionless mass flow between the upper recirculating region and MFS zone n ($m_{u,n} = \dot{m}_{u,n}/\dot{m}_{in}$).
p, P	pressure $[Pa]$.
P_k	turbulent energy production due to the strain term $[kg\, m^{-1} s^{-3}]$.
Pe	Peclet number.
ΔP_{io}	pressure difference between inflow and outflow openings $[Pa]$.
q_c	heat flux due to convection $[W\, m^{-2}]$.
q_r	heat flux due to radiation $[W\, m^{-2}]$.
q_t	total heat flux due to convection and radiation $[W\, m^{-2}]$.
S_ϕ	general source term in transport equations.
t	time $[s]$.
T	temperature $[K]$.
T_a	air temperature $[K]$.
T_{C1}, T_{C2}, T_{C3}, T_{C4}, T_{C5}	temperature of zonal model ceiling nodes $C1$, $C2$, $C3$, $C4$ and $C5$ respectively $[K]$.
T_{ma}, T_{mb}, T_{mc}, T_{md}, T_{me}	temperature of zonal model MFS nodes ma, mb, me, me and me respectively $[K]$.
T_{east}	temperature of zonal model east wall node $east$ $[K]$.
T_{flr}	temperature of zonal model floor node flr $[K]$.
T_{in}	inflow air temperature $[K]$.
T_{rl}, T_{ru}	temperature of zonal model recirculating region node rl and ru respectively $[K]$.
T_s	surface temperature $[K]$.
T_{west}	temperature of zonal model west wall node $west$ $[K]$.
ΔT_{ci}	temperature difference between ceiling surface and air at the inflow opening $[K]$.
u^+	non-dimensional distance parallel to the wall.
u', v', w'	fluctuating components of velocities $[m\, s^{-1}]$.
U, V, W	mean velocities $[m\, s^{-1}]$.

$\dot{v}$	volumetric flow rate $[m^3\,s^{-1}]$.
$\dot{v}_{in}$	volumetric flow rate through inflow opening $[m^3\,s^{-1}]$.
$\dot{v}_{l,n}$	volumetric flow rate from lower recirculating region to MFS zone n $[m^3\,s^{-1}]$.
$\dot{v}_{u,n}$	volumetric flow rate from upper recirculating region to MFS zone n $[m^3\,s^{-1}]$.
v_{in}	air velocity at inflow opening $[m\,s^{-1}]$.
V_l	volume of lower recirculating region $[m^3]$.
V_n	volume of MFS zone n $[m^3]$.
V_u	volume of upper recirculating region $[m^3]$.
x_i	Cartesian coordinates.
y^+	non-dimensional distance normal to the wall.
y_l	y position of the lower boundary of the MFS $[m]$.
y_u	y position of the upper boundary of the MFS $[m]$.
$y_{ceiling}$	y position of the ceiling, m.

Greek Letters

Γ	diffusive transport coefficient.
Ω	solid angle $[sr]$.
β	volumetric expansion factor$[K^{-1}]$.
ϵ	emissivity.
ε	rate of turbulent kinetic energy dissipation $[m^2 s^{-3}]$.
λ	thermal conductivity $[W\,m^{-1}\,K^{-1}]$.
μ	molecular viscosity $[kg\,m^{-1}\,s^{-1}]$.
μ_t	turbulent viscosity $[kg\,m^{-1}\,s^{-1}]$.
ν	kinematic viscosity $[m^2 s^{-1}]$.
ρ	density $[kg\,m^{-3}]$.
σ	Prandtl number.
σ_ε	Prandtl number governing diffusion of turbulent energy dissipation rate.

σ_k	Prandtl number governing diffusion of turbulent kinetic energy.
σ_T	turbulent Prandtl number.
σ	Stefan-Boltzmann constant [5.6696E-8 $W\,m^{-2}K^{-4}$].
τ_{ij}	viscous stress tensor [$N\,m^{-2}$].
ϕ	scalar variable.

CHAPTER 1

Introduction

1.1 Background

Since the advent of air conditioning, members of the engineering community have resisted considering natural ventilation as a cooling strategy citing:

- Reliable methods to predict the efficacy of natural ventilation do not exist;
- Compared to air conditioning, wind-induced natural ventilation is intrinsically unreliable.

Pollution, exhaustion of natural resources, global warming, ozone depletion, political instability in oil producing areas of the world have all contributed to place natural ventilation as a real alternative to air conditioning. Moreover, implementing a natural ventilation scheme can mean savings on mechanical cooling equipment which can cost up to 10 % of the cost of a building.

Wind-driven natural ventilation can affect building cooling energy loads and human comfort through three mechanisms:

1. During the night, air flow through the building can cool down its structure. This results in lower air and, importantly, radiant temperatures during the day.
2. During the day, air flows can offset solar and internal heat gains.
3. Indoor air motion can cool building occupants directly by increasing convective and evaporative heat loss from the body.

The simulation of annual energy usage in buildings, is treated by a number of energy analysis programs, e.g. (EDS 1992; BLAST 1986; BESG 1982; FACET 1991). Whilst the building heat transfer processes may be modelled in different ways within such programs they generally have the common feature that the thermal conditions within each room or zone are modelled on the basis of the air being fully mixed. It is this drawback principally, that needs to be overcome to enable systems like natural ventilation to be modelled realistically.

Building flows can be modelled with more complexity using Computation Fluid Dynamics (CFD). The use of CFD in building design increases as commercial codes improve and computation speed increases, although, at this time CFD is typically only used for novel designs by large building practitioners. CFD simulations are normally run in their steady state form on a space (i.e., atria) of particular interest. Although CFD packages have been linked to thermal codes (IES 1999b) they cannot realistically be used for a yearly building simulation.

1.2 Scope

The overall objective of the work described here has been to develop a suitable thermal model that incorporates the relevant features of natural ventilation, to address the complaint that, "Reliable methods to predict natural ventilation do not exist". In developing the model the aim has been to develop a tool that is:

1. Capable of assessing the performance of natural ventilation with a level of accuracy comparable to that expected for the prediction of the performance of other cooling strategies such as air conditioning.
2. Accessible to the designer when these important decisions have to be made. This is an important requirement because many of the decisions affecting the future performance of naturally ventilated buildings are taken in the early stages of the design process.

Fulfilling the first objective is difficult due to the number of variables that affect the performance of a naturally ventilated building that are not present in other cooling strategies. The performance of natural ventilation is more strongly coupled to a large number of parameters than other cooling strategies:

- Exterior geometry of the building;
- Site of building;
- Orientation of the building with respect to prevailing wind direction;
- Fenestration design, placement, size and detailing;

- Wind speed and direction;
- Outside air temperature;
- Thermal mass of the building;
- Interior geometry;
- Interior obstructions.

It is inherently difficult to design a modelling or experimental procedure that can study these parameters parametrically. In fact the objective of this study was not to study these parameters as other studies have done before but to concentrate effort in areas where previous studies have ignored. A number of investigations (Ernest 1991; Sobin 1983; Givoni 1969; Chand, Sharma, and Bhargava 1977; Chandra 1983) have used wind tunnel experiments to examine many of these parameters. The isothermal nature of wind-tunnel tests has not allowed the following important parameters to be assessed:

- The effect of buoyancy induced forces on flow path;
- The effect of flow path on the local heat transfer coefficients;
- A detailed look at the velocity field.

Therefore this study concentrates on non-isothermal cases where new information can be found to improve current natural ventilation modelling.

The second aim, "To produce a tool that can be used in the design process", was tackled by implementing the model within an existing thermal analysis code, LIGHTS (Sowell 1989). Although LIGHTS is not routinely used by practitioners it has been interfaced within HVACSIM+ (Clark 1985). The model could easily be added to other modular codes such as TRNSYS (Klein, Beckmann, and Duffie 1976) and IES which are used more often within the building industry. Although the tool must have sufficient detail to enable heat transfer and comfort conditions to be predicted with reasonable accuracy, it must retain sufficient computational speed to be practical for annual energy simulation. The model presented here is, accordingly, of intermediate complexity between that of a single air node model ('fully mixed' model), and that of a CFD model. The model is of the type that has been called a 'zonal model' or 'nodal model'. In this type of model the room heat transfer paths are described by a network of nodes, at which heat balances are calculated, that are interconnected by conductances representing bulk air movement or convective heat transfer paths.

In order to develop a model of this type it is necessary to have convective heat transfer data and a method to determine mass flows between zonal model nodes. This data can come from either numerical calculations or experiments. In the study presented here, numerical studies of the flow and heat transfer in rooms with cross-flow ventilation have been made. In view of the importance of the radiant coupling in rooms with natural ventilation, a coupled flow (CFX 1997b) and radiation solver has been used (CFX 1997a). Experimental measurements were taken in a naturally ventilated room to support the findings of the numerical calculations.

The structure of the nodal model has been developed through a number of stages. The air flow network has been developed by reference to both numerically predicted and experimentally observed air flow paths. Numerical techniques have been employed to find values for the bulk air flow (capacity rate) parameters of the zonal model. The convection coefficient parameters of the model have also been found numerically, and by reference to established correlations.

The zonal model was then run, using the parameters obtained by the numerical and experimental work, under a number of conditions and the results compared to those from a fully mixed model (one room air node) that would be typically used in building simulation today.

1.3 Overview of the Thesis

This document is divided into a number of chapters:

- Chapter 2 describes the zonal model development environment and proposes a zonal model for night-time cross-flow ventilation;
- Chapter 3 describes the CFD study used to determine values for the zonal model parameters;
- Chapter 4 presents an experiment undertaken in a room ventilated by means of night-time cross-flow to examine flow regime and ceiling convective heat transfer coefficients;
- Chapter 5 describes the use of CFD to model the experimental room;
- Chapter 6 completes the zonal model proposed using the parameters derived from the CFD and experimental work and uses it in a number of simulations;
- Chapter 7 gives the conclusions made from the work reported and presents ideas for further work.

CHAPTER 2

Development of a Zonal Model of Night-time Cross-flow Ventilation

2.1 Objectives

The objective of the work described in this document has been to develop a thermal model of rooms ventilated by wind driven cross-flow means. The model proposed is of the type commonly known as a 'zonal' or 'nodal' model. The procedure divides the room into large control volumes or zones (with a node representing each). Typically the nodes of such models are identified with room surfaces, room air or equipment that impacts on the thermal performance of the system. The nodes are 'connected up' to form a network in which each connection represents a heat flow path between the zones in question:

- Surface-to-surface node connections represent the radiative heat transfer paths;
- Surface-to-air node connections represent heat flow paths of convection from room walls into the room air;
- Air-to-air node connections represent heat transport due to bulk air movement inside the room.

The development of the model structure and the derivation of the parameter values are two separate but interacting processes, numerical calculations and experiments have informed the structure of the model. The numerical and experimental data is then revisited to determine model parameter values. The zonal model can then be run which may change the choice of model structure which means parameters have to be re-evaluated from the data.

This chapter summarises the existing literature in this area before discussing the environment used for the zonal model development. A zonal model for cross-flow ventilation is then proposed and the parameters highlighted. The following chapters then use CFD and experimental data to derive values for those parameters.

2.2 Background

2.2.1 Previous research

Zonal Models

Various types of 'zonal models' have been developed for rooms with convective heat emitters. Allard and Inard (1992) have reviewed the development of such models. Lebrun (Lebrun 1970; Lebrun and Ngendakumana 1987) was amongst the first to identify that there was a systematic difference in heat transfer between results predicted by isothermal models of such systems (i.e. with a single air node) and experimental results. Lebrun suggested splitting the room into zones connected by mass conductances to model convection from one part of the room to another. A number of authors have developed this idea, notably Howarth (1983) who used a two zone model, and Inard and Buty (1991) who have used a five zone model and a twelve zone dynamic model of rooms with radiator type heat emitters.

Such models are semi-empirical in that they rely on empirically derived constants in their formulation. It is also true to say that simplified models such as these can only be expected to represent each physical situation when there is a clearly defined air flow pattern, such as the circulation driven by the plume from a radiator. The performance of the heating models discussed by Allard and Inard has recently been compared favourably with the results of CFD simulations in the context of IEA annex 20. Dalicieux and Bouia (1993) have recently developed a more general model for heating applications by introducing pressure as a state variable and solving the energy and mass balance equations for the order of twenty cells representing the room. Similar approaches have been used to model the macroscopic movement of air within large spaces such as atria (Togari, Arai, and Miura 1993; Arai, Togari, and Miura 1994).

A further class of models can be identified as 'grey box models', such as those developed by De Moor and Berckmans (1994) for predictive control purposes. In this modelling technique a combination of features described by physical law relationships and mathematical 'black box' methods like neural networks are used. Such models are developed by fitting or training the model using empirical or CFD data. Similarly, a 'black box' modelling method can be conceived, where there is no reliance on prescribed physical law relationships but the model is trained on experimental or simulation data alone.

Empirical Correlations

The direct measurement of interior air flows in scale models placed in boundary layer wind tunnels has been shown to be a useful technique for the prediction of indoor air motion (Aynsley 1982; Poreh, Cermak, and Peterka 1982).

Ernest (1991) used scale model testing to develop a tool for the evaluation of the performance of naturally ventilated buildings. The effects of a large set of building parameters on natural ventilation performance are presented: orientation, floor plan, obstructions, window design etc. Correlations were developed relating indoor air velocity distributions to surface wind pressure data. Other correlations were developed to account for the effects of additional building parameters including window size, location and interior partitions. These correlations may be adequate for specifying a building's performance in terms of occupant comfort during day time ventilation. The thermal performance is less adequately treated by this method as the effect of buoyancy forces on flow path is not considered.

External surface pressure coefficients (C_p) measured on sealed models can be used to estimate velocities at inlets (Aynsley 1982). The method makes use of discharge coefficients (C_d) to account for the characteristics of the inflow and outflow openings. However, this method is limited to buildings with low wall porosities (under 20%).

2.2.2 Implications of Previous Research on Study

There are associated limits to the current prediction methods:

- Full-scale measurements, obviously, come too late to be useful in the design process;
- Complex numerical simulations and direct wind tunnel investigations are for all practical purposes unaccessible to designers;
- The consequence of the effect of buoyancy forces cannot easily be treated in wind tunnel studies;
- The use of CFD for accurate results of buoyancy driven flows in buildings require a detailed knowledge of CFD. A large cost related to time and effort of a CFD practitioner is incurred;

When the effect of buoyancy forces on flow path are considered it is in terms of convective flows from radiators. Cross-flow ventilation flows can be affected by buoyancy forces. No previous work addresses this problem directly.

The work here concentrates on non-isothermal cases where flow regime, and more significantly, whether or not flow remains attached to the ceiling, effects the thermal performance of the system. The zonal model can be linked to other studies that investigate the effect of building parameters (geometry, and wind incident angle etc.) on inlet/outlet pressure difference (Ernest 1991).

2.2.3 Thermal Analysis Codes

Simulation has made significant progress towards establishing itself as a routine part of the building and building services design process. This is part due to the fact that a large number of software programs have been developed to model the thermal processes within buildings, many of which are reliable and easy to use. Gough (1999) presents a review of the software available for analysing the thermal performance of buildings including IDA (Sahlin and Bring 1991), TRNSYS (Klein, Beckmann, and Duffie 1976), HVACSIM+ (Clark 1985), CLIM 2000 (Gautier and Rongere 1991), SPARK (SRG 1997), APACHE-sim (FACET 1991), Tas (EDS 1992), ESP-r (IES 1999a), and DOE-2 (BESG 1982). Modular Simulation Environments such as TRNSYS, HVACSIM+, and IDA, separate the model description from the solver side into modules. Sahlin (1996) has compiled an annotated list of software tools and development environments.

The important physical processes modelled by these programs are:

- Heat transfer by conduction, convection and long-wave radiation;
- Transmission, reflection and absorption of solar radiation;
- Heat and moisture transport associated with air infiltration, ventilation and interzonal flow;
- Sensible and latent room gains.

Outputs from the model include:

- Room air temperatures, surface temperatures;
- Various measures of thermal comfort;
- Room humidities;
- Room loads (heating, cooling, humidification, dehumidification).

Dynamic modelling is required in the representation of heat transfer in the building mass via conduction. One-dimensional heat transfer is normally assumed. The time-step used is normally determined by the resolution of the weather data and is most typically 1 hour.

2.2.4 Building Air Flow Modelling

Software is available for simulating the flow of air into and through buildings induced by wind, thermal buoyancy and mechanical ventilation. Programs specialising in this field include COMIS (Pelletret and Keilholz 1997), CONTAM (Walton and Emmerich 1994; Walton 1997), and BREEZE (BRE 1992). Other programs such as ESP, APACHE-sim and Tas also provide facilities for this type of simulation, either integrated with the thermal analysis or handled via links to separate modules. Tas concentrates on natural ventilation modelling, omitting infiltration through cracks. TRNSYS has a link with COMIS.

A common approach is to model the building as a network of zones connected to each other and to the exterior by a set of apertures through which air is allowed to flow. The apertures can represent large openings such as windows or small ones such as cracks. Each aperture is assigned a pressure/flow relationship that describes how the flow through it varies with the applied pressure difference. Bi-directional flow may be driven by buoyancy effects. Pressure differences in the system are set up by wind, buoyancy and mechanical ventilation, and the simulation task consists of solving the resulting network flow problem.

Solving such a problem requires linearisation of the equations and an iterative process. Convergence is assisted by the use of under-relaxation. The most common approach when a combined air and thermal solution is required is to solve the thermal problem separately from the air problem and to iterate between the two.

The zonal model approach to the analysis of convective air movement within a single room (Wurtz, Nataf, and Winkelmann 1999) is used for example in the simulation of displacement ventilation (Hensen and Hamelinck 1995).

2.2.5 LIGHTS

A generalised nodal thermal modelling program LIGHTS, developed by Sowell (1989) has been used to develop the zonal model for night-time cross-flow ventilation. LIGHTS was originally developed for the detailed study of the thermal and luminous aspects of building lighting systems and can model the non-linear behaviour of lighting elements—although these features are not used in the present context. The program is capable of modelling thermal systems in either dynamic or steady state conditions. Nodes can be connected in a very general way, with a combination of fluid flow, thermal mass, and convection being either defined or calculated at each node. Radiation between nodes is dealt with in two wave bands in an exact manner on the basis of view factors input by the user (Sowell and O'Brien 1972). Fluid flows in the LIGHTS program are represented as one-way conductances and always have to be pre-defined.

The basic formulation used in the program is, in vector-matrix form:

$$Q^O - U^C T - A \sum_j V_j . J_j^o = MT' \tag{2.1}$$

where:

Q^0	represents the vector of source powers at each node;
$U^C T$	represents conductive/convective transport away from each of these nodes;
T	is the vector of nodal temperatures that must satisfy this equation;
A	is a diagonal matrix of surface areas;
V_j	are special transfer matrices describing interreflections and transmissions within the enclosure;
J^o	is a matrix of source radiation terms at each node and in each wave band;
M	is a diagonal matrix of heat capacitances; and
T'	is the derivative vector of temperature.

The summation term represents net radiative transport away from each node in both short and long-wave bands. The notation J_j^o means that the jth column is involved in the matrix multiplication. The equation is non-linear due to temperature dependence of Q^o, U and J^o. In steady state the MT' term is equal to zero.

To facilitate solution, the vector of nodes and Equation 2.1 can be partitioned into nodes with finite thermal mass and those declared to be massless

$$\begin{bmatrix} O & O \\ O & M_d \end{bmatrix} \begin{bmatrix} T_s' \\ T_d' \end{bmatrix} = \begin{bmatrix} Q_s^o \\ Q_d^o \end{bmatrix} - \begin{bmatrix} U_{11}^c & U_{12}^c \\ U_{21}^c & U_{22}^c \end{bmatrix} \begin{bmatrix} T_s \\ T_d \end{bmatrix} - \begin{bmatrix} A_{11} & O \\ O & A_{22} \end{bmatrix} \sum_j \begin{bmatrix} V_{11} & V_{12} \\ V_{21} & V_{22} \end{bmatrix} \begin{bmatrix} J_s^o \\ J_d^o \end{bmatrix} . \tag{2.2}$$

Matrix algebra then leads to an equation with the temperature vector representing only the algebraic modes, and a specially defined Q^o term, Q_d^o which represents the effect of net heat transfer from the dynamic nodes

$$M_d T' = Q_d^o - U_{21}^c T_s - U_{22}^c T_d - A_{22} \sum_j (V_{21} J_s^o + V_{22} J_d^o) . \tag{2.3}$$

The result of the partitioning is a set of algebraic equations and a set of differential equations that are coupled through the temperature vector.

The solution scheme is then straightforward. Using the initial conditions at the dynamic nodes, the Q_d^o term is evaluated, and the algebraic set is solved with Newton-Raphson iteration. The differential set is then solved after the next time step, using a variable time step, predictor-corrector method. The corrector step requires invocation of the algebraic solver, since the temperature of the algebraic nodes must be updated as the dynamic node temperatures adjust to their new values. The process is then repeated throughout the period of interest

In the implementation, zone geometric, thermal, and radiative properties are accepted from an input file, an annotated example of which is given in Appendix A. The input files definition of which nodes are to be held at constant temperature, and which are to be held at a specified net heat transfer rate. User defined output include temperature, net heat flux, and radiative and convective heat transfer at each node.

LIGHTS has been adapted for use with HVACSIM+ (Sowell 1991) and could also be easily implemented within other modular thermal simulation environments.

Section 2.3 explains the zonal model developed in this research, which has been implemented within LIGHTS.

2.3 Modelling Method

The thermal modelling program LIGHTS was used for this research because it allows the zonal model to be implemented as a text file that includes the network of thermal connections etc., see Appendix A. LIGHTS did not need any extra coding for it to solve the zonal model developed.

From early CFD simulations and engineering knowledge it was decided that the zonal model must incorporate the thermal consequences of whether or not the main flow stream remained in contact with the ceiling. The room dimensions used in the CFD modelling were 3 m high by 12 m wide and therefore the zonal model developed might be applied to office sized spaces where cross flow ventilation might be used as a cooling technique. Three distinct cases were observed in the preliminary CFD work. Figure 2.1 shows vector plots of air velocity from three CFD simulations where the inlet velocity was $0.25\,\mathrm{ms}^{-1}$ and the temperature difference between the inlet air and the ceiling was altered from 0 K to 6 K to 12 K. The main flow stream between the inlet and outlet is superimposed on the vector plot in black.

1. When the inlet velocity is high, or the temperature difference between the inlet air and the room surfaces is low, the main flow stream remains attached to the ceiling throughout its path through the room (Figure 2.1 top). In this case there is one recirculating region in the lower portion of the room.

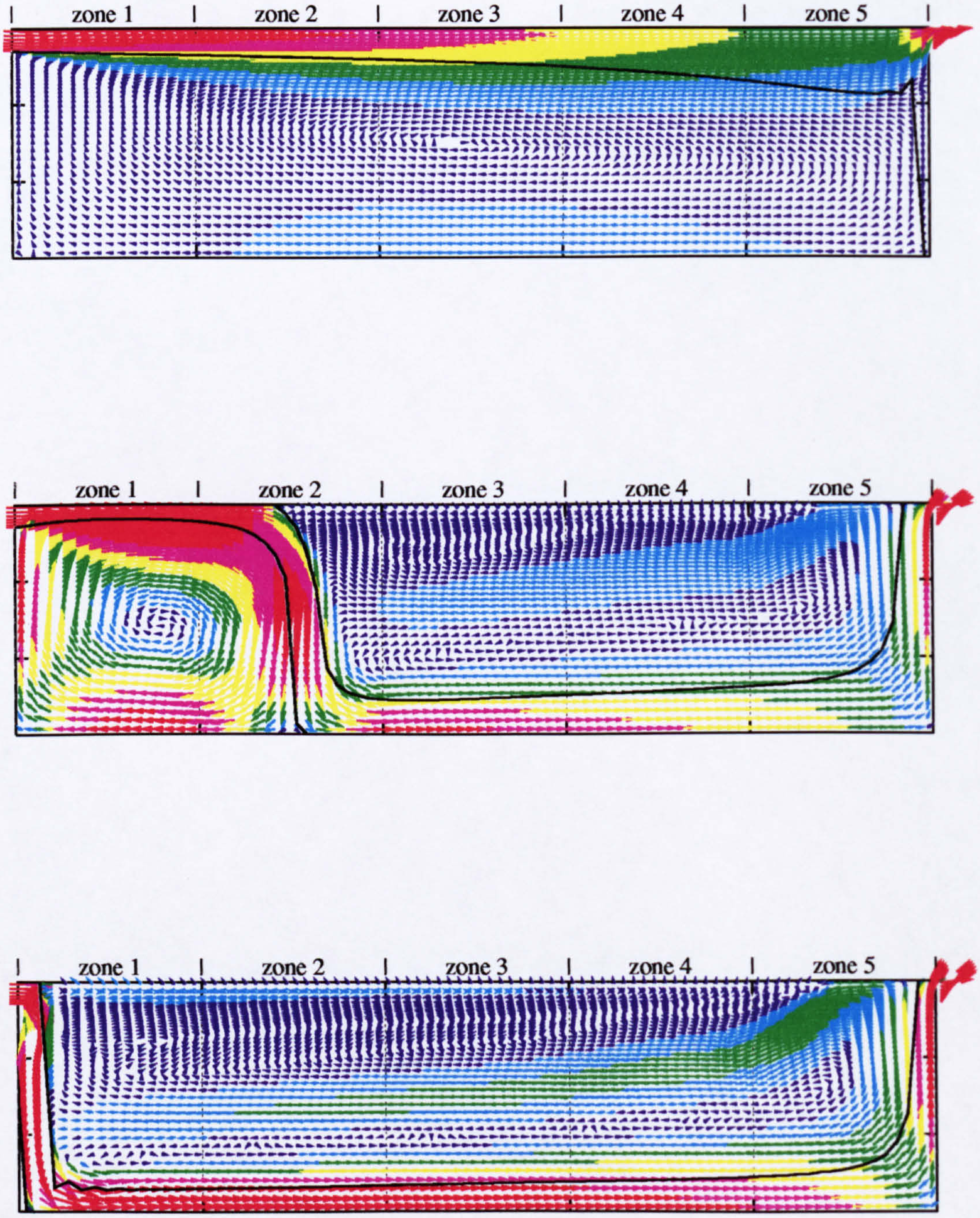

Figure 2.1: The path of the main flow stream as predicted by CFD for an inlet velocity of 0.25 ms^{-1} and three different temperature differences between the inlet air and the ceiling: 0 K (top); 6 K (middle); and 12 K (bottom).

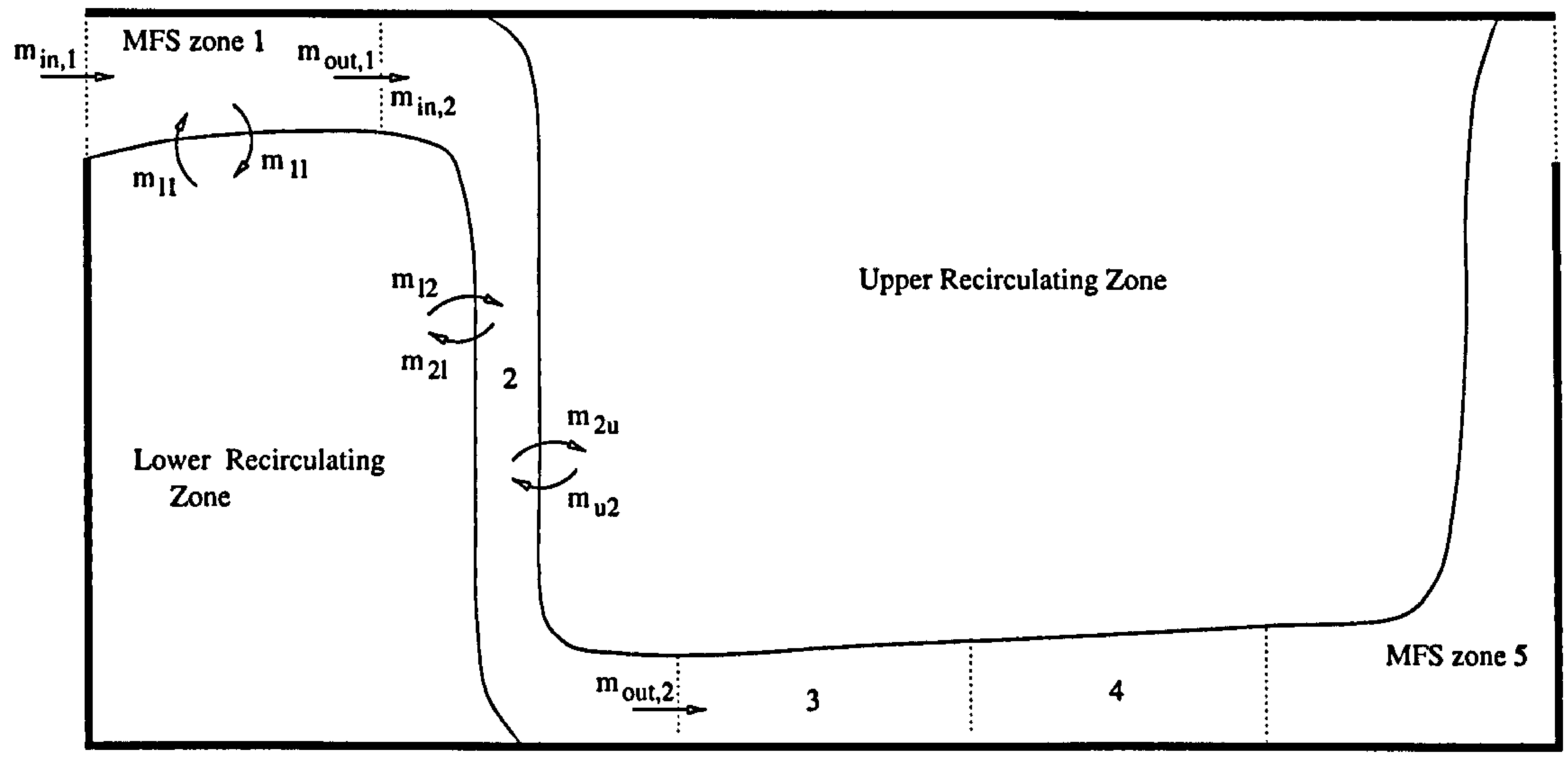

Figure 2.2: The control volumes of a zonal model superimposed on a diagram of the flow stream through a room (before mass flows have been derived).

2. When the inlet velocity is low, and the temperature difference between the inlet air and the room surfaces is appreciable, the main flow stream does not attach to the ceiling but descends to the floor upon entry through the inlet (Figure 2.1 bottom). Here the recirculating region is in the upper portion of the room.

3. Between these two extremes the main flow stream can detach some way along the ceiling before descending to the floor (Figure 2.1 middle). Here two recirculating regions exist: one below the main flow stream near the inlet; and one above the main flow stream near to the outlet.

2.3.1 Bulk Convection in the Zonal Model

The zonal model proposed models the thermal consequence of a number of regions of bulk air convection: the main flow stream (MFS) which flows between the inlet and outlet openings; and one or two recirculating regions. The exchange of air between the recirculating region or regions and the MFS is also modelled.

Mass Flow Between the MFS and the Recirculating Regions

Figure 2.2 shows the volumes of air that the zonal model represents when the flow detaches from the ceiling. The model proposed, which is discussed further in this chapter, consists of 5 zones representing the main flow stream, a zone for the upper recirculating region, and a zone for the lower recirculating region. Each zone represents a fixed volume of room air which depends on the path of the main flow stream which in turn depends on the driving forces of the flow (the pressure difference between the room openings and

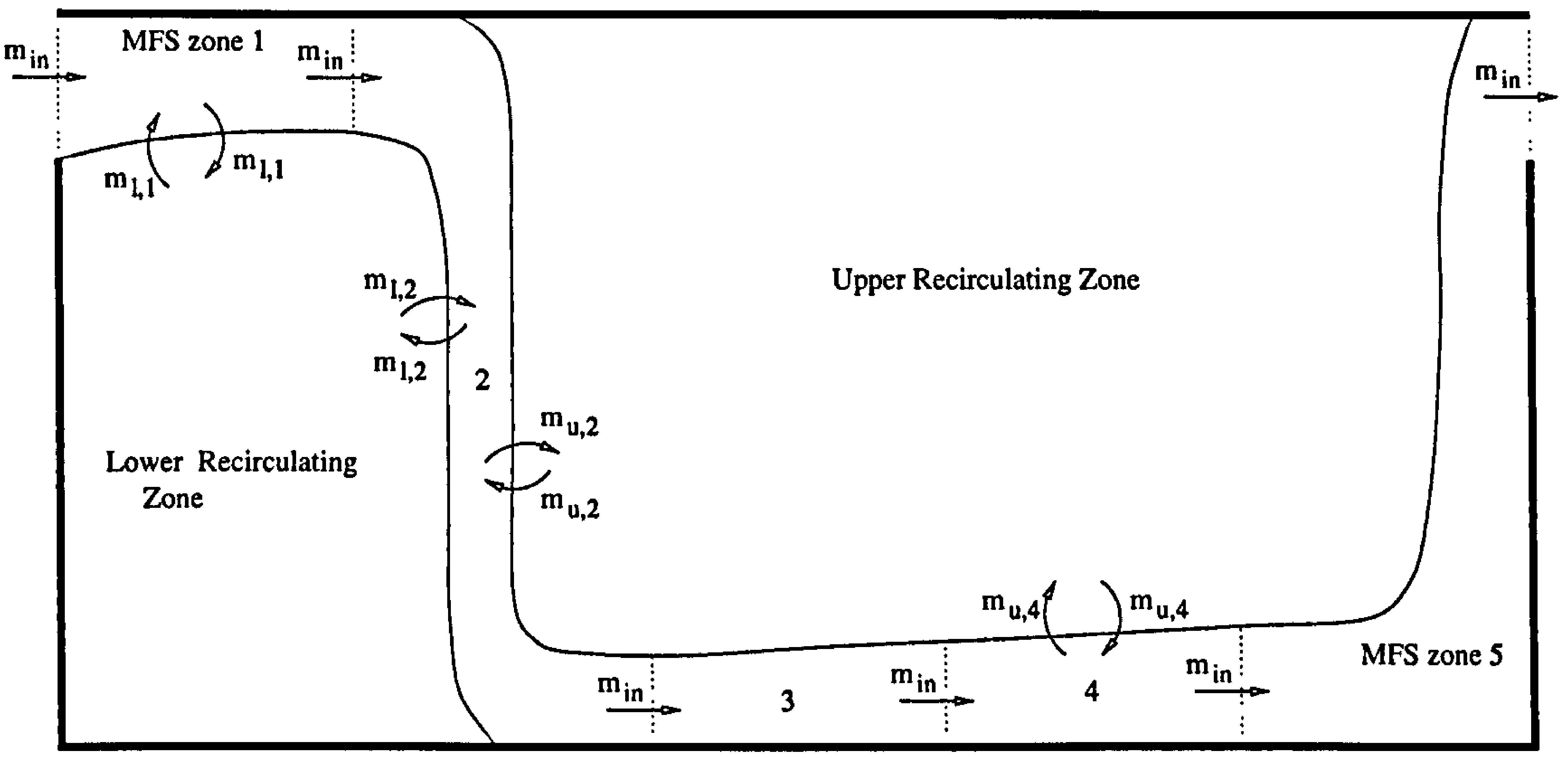

Figure 2.3: The control volumes of a zonal model superimposed on a schematic diagram of the flow stream through a room (after mass flows have been derived).

the buoyancy forces generated by room air at differing temperatures). The net mass flow from the recirculating regions into each of the MFS zones must equal zero for mass conservation to be satisfied, see Figure 2.3. This can be shown by examining the mass flux of air in and out of each zone. Consider main flow stream zone 1 in Figure 2.2. For mass conservation to be satisfied mass flow into a zone must equal the mass flow out,

$$0 = (\dot{m}_{in,1} + \dot{m}_{l1}) - (\dot{m}_{out,1} + \dot{m}_{1l}). \tag{2.4}$$

The main flow stream is defined as having the same horizontal flow throughout its length,

$$\dot{m}_{in,1} = \dot{m}_{out,1} = \dot{m}_{in}, \tag{2.5}$$

and therefore

$$\dot{m}_{l1} = \dot{m}_{1l}. \tag{2.6}$$

A similar treatment of mass flow into the lower recirculating zone yields

$$0 = (\dot{m}_{1l} + \dot{m}_{21}) - (\dot{m}_{l1} + \dot{m}_{l2}). \tag{2.7}$$

Substituting Equation 2.6 into Equation 2.7 gives

$$\dot{m}_{l2} = \dot{m}_{2l}, \tag{2.8}$$

and conservation of mass in MFS zone 2 means

$$\dot{m}_{u2} = \dot{m}_{2u}. \tag{2.9}$$

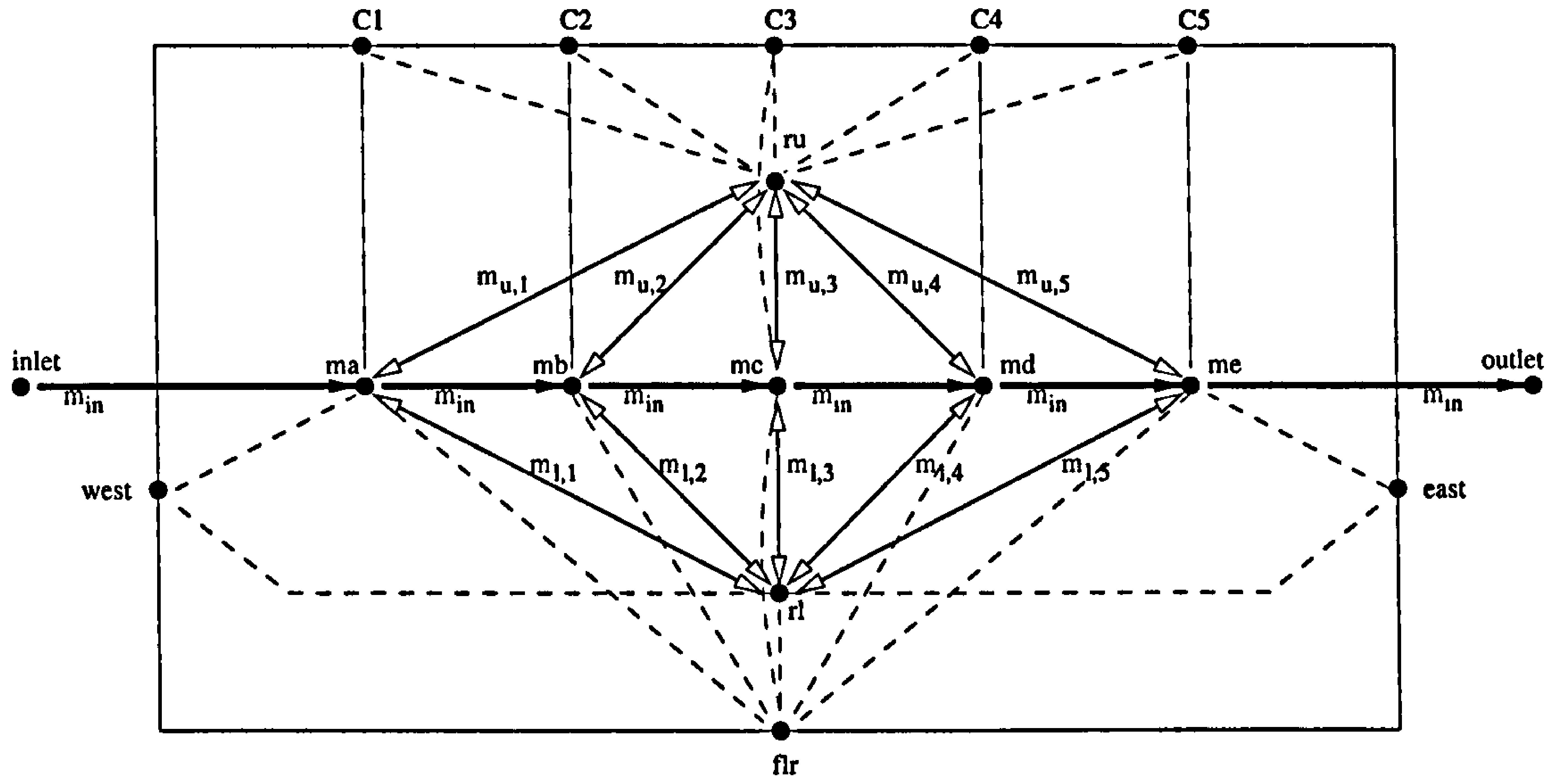

Figure 2.4: Zonal model for nighttime cross-flow ventilation.

Forthwith, $\dot{m}_{l,n}$ will be used to refer to the mass flow from the lower recirculating region into the MFS zone n as well as the mass flow from the MFS zone n into the lower recirculating region. Similarly, $\dot{m}_{u,n}$ will be used to refer to the mass flow from the upper recirculating region into the MFS zone n as well as the mass flow from the MFS zone n into the upper recirculating region, see Figure 2.3.

2.3.2 The Zonal Model Proposed

Figure 2.4 shows the zonal model proposed to represent night-time cross-flow ventilation. There are ten surface nodes which comprise of five ceiling nodes, (*C1, C2, C3, C4, C5*), four wall nodes, (*west, east, north,* and *south*), and a node for the floor, (*flr*). The network diagram in Figure 2.4 does not show the *north* and *south* wall nodes for clarity. There are nine air nodes, two of these are outside of the room modelled, (*inlet* and *outlet*), five specify the main flow stream from the inlet opening to the outlet opening, (*ma, mb, mc, md* and *me*), while the remaining two specify the two possible recirculating regions, (*rl* and *ru*).

Five nodes were used for the ceiling zones while one node was used for each of the walls and floor because it was assumed that a building with high level openings and a night-time cooling strategy would have most of the thermal mass at the ceiling.

In Figure 2.4 bulk convective air flows, i.e. flow between air nodes, are represented by solid lines with an arrow showing direction of flow. Solid lines finishing in two white arrow heads actually represent two flows of equal capacity, one in each direction. For example, the connection between *ma* and *rl*, $\dot{m}_{l,1}$, actually consists of two flows *ma* to *rl*, $\dot{m}_{1,l}$, and *rl* to *ma*, $\dot{m}_{l,1}$. Representing the connections between the main flow stream nodes and the nodes of the recirculating regions in this way simplifies the diagram. As

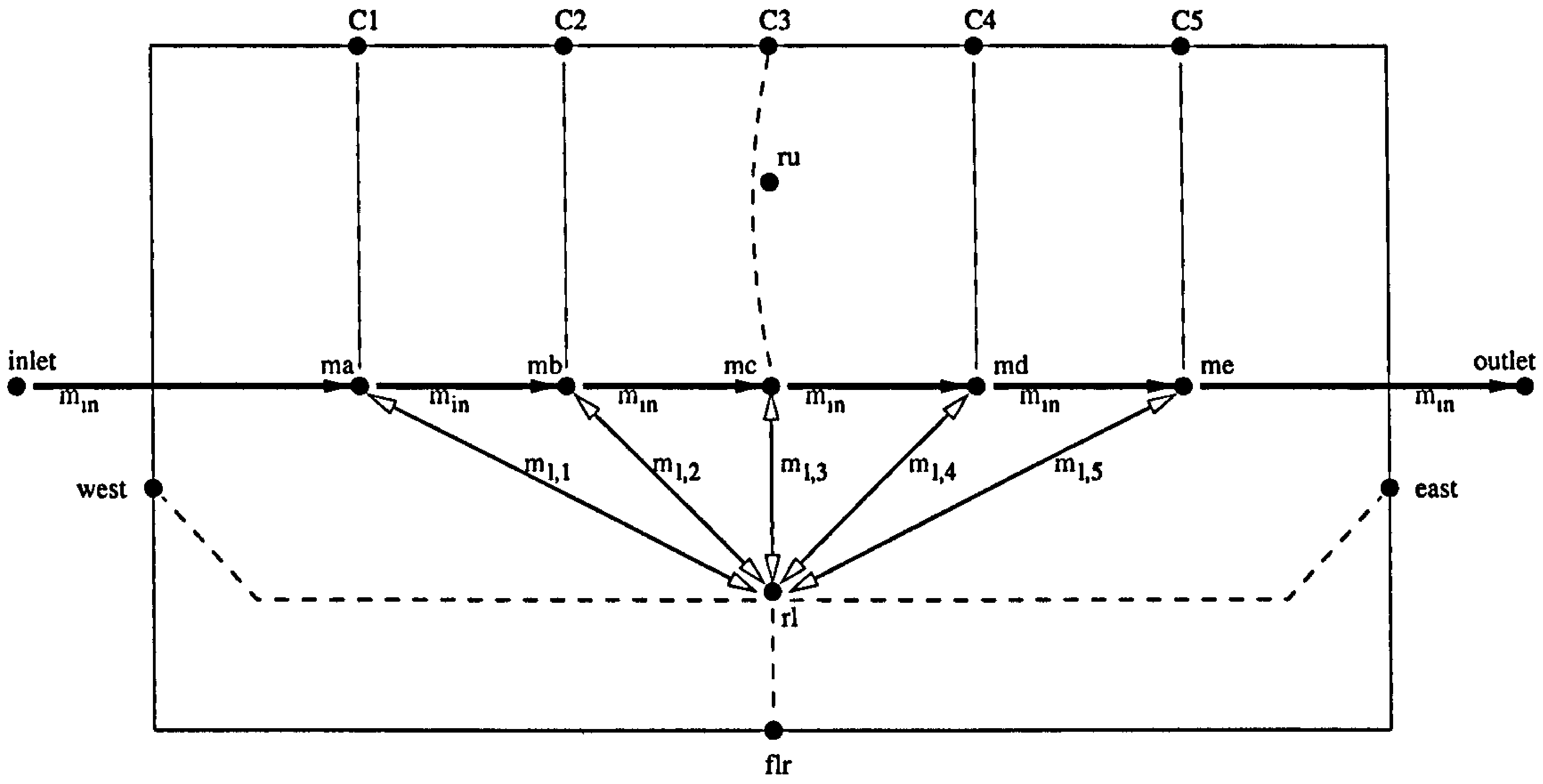

Figure 2.5: Zonal model when the main flow stream remains attached to the ceiling.

the main flow stream is defined as having the same horizontal mass flow throughout its length, the flow between air nodes in the MFS is equal to $\dot{m}_{in}$.

Convective flows between air nodes and surface nodes are represented by dashed lines in Figure 2.4. There are also radiative heat flows between surface nodes that can 'see' each other that will depend on the view factors in question. Radiative heat flow connections are not shown in Figure 2.4 for the sake of clarity. It is assumed that no radiative heat transfer takes place between the room surfaces and the air as this effect is small for office sized spaces with low humidity.

Handling Flow Detachment

The different types of connections in the zonal model can be switched on and off depending on the boundary conditions of a simulation and where the flow is expected to detach. The criteria used to determine where the flow detaches is the Archimedes number of the flow, see Section 3.5.2.

Figure 2.5 shows the heat flow connections used when the main flow stream remains attached to the ceiling throughout its path through the room. In this case there is no upper recirculating region and therefore no connections to the upper recirculating node. There is air to surface convection between the main flow stream and the ceiling. There is bulk air convection between the main flow stream nodes and the lower recirculating node. The *west, east, north, south,* and *flr* surface nodes are convectively coupled to the lower recirculating node but not the nodes of the main flow stream.

Figure 2.6 shows the heat flow connections used when the main flow stream does not attach to the ceiling but descends to the floor on entry. In this case the main flow stream

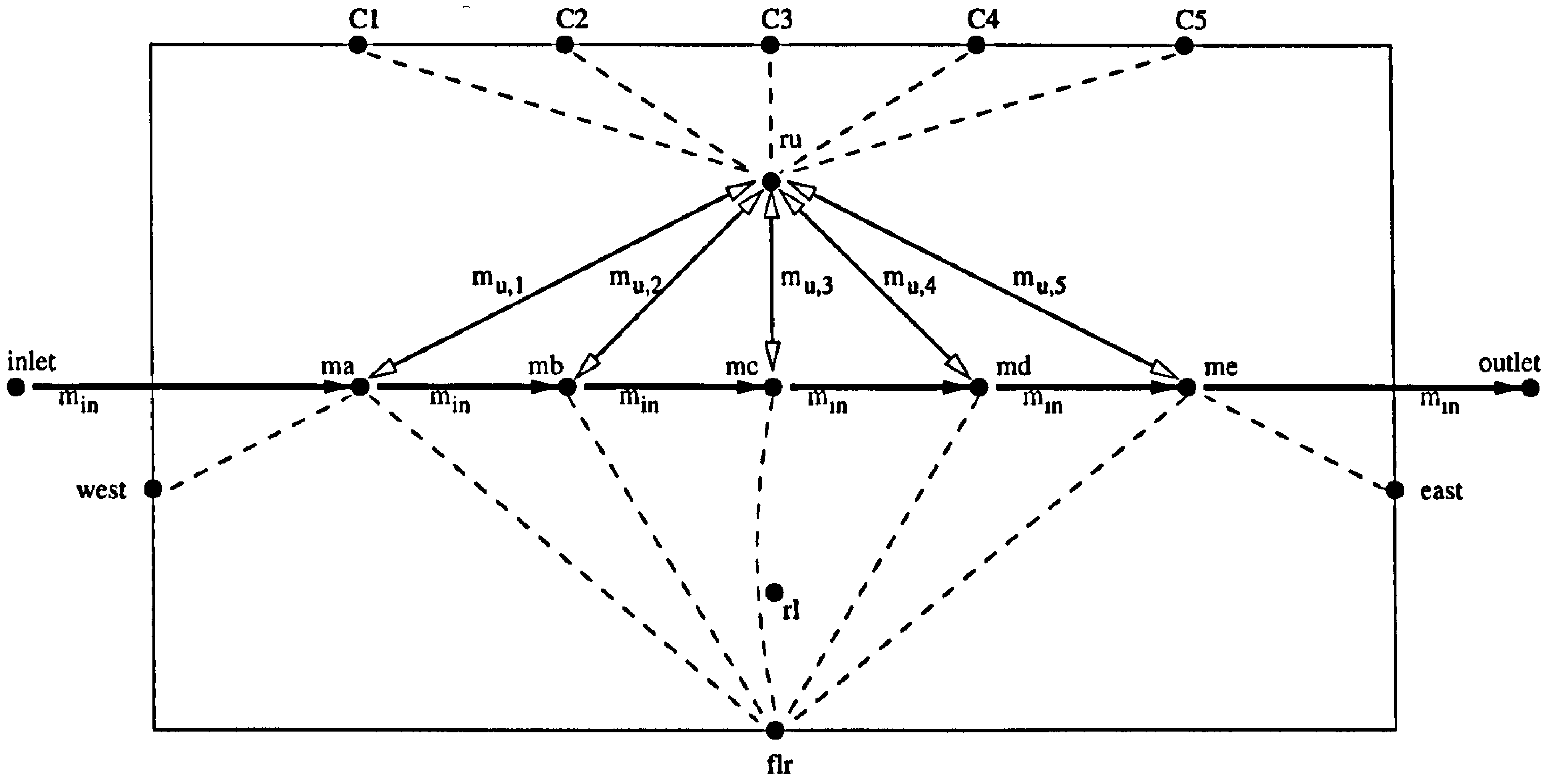

Figure 2.6: Zonal model when the main flow stream does not attach to the ceiling.

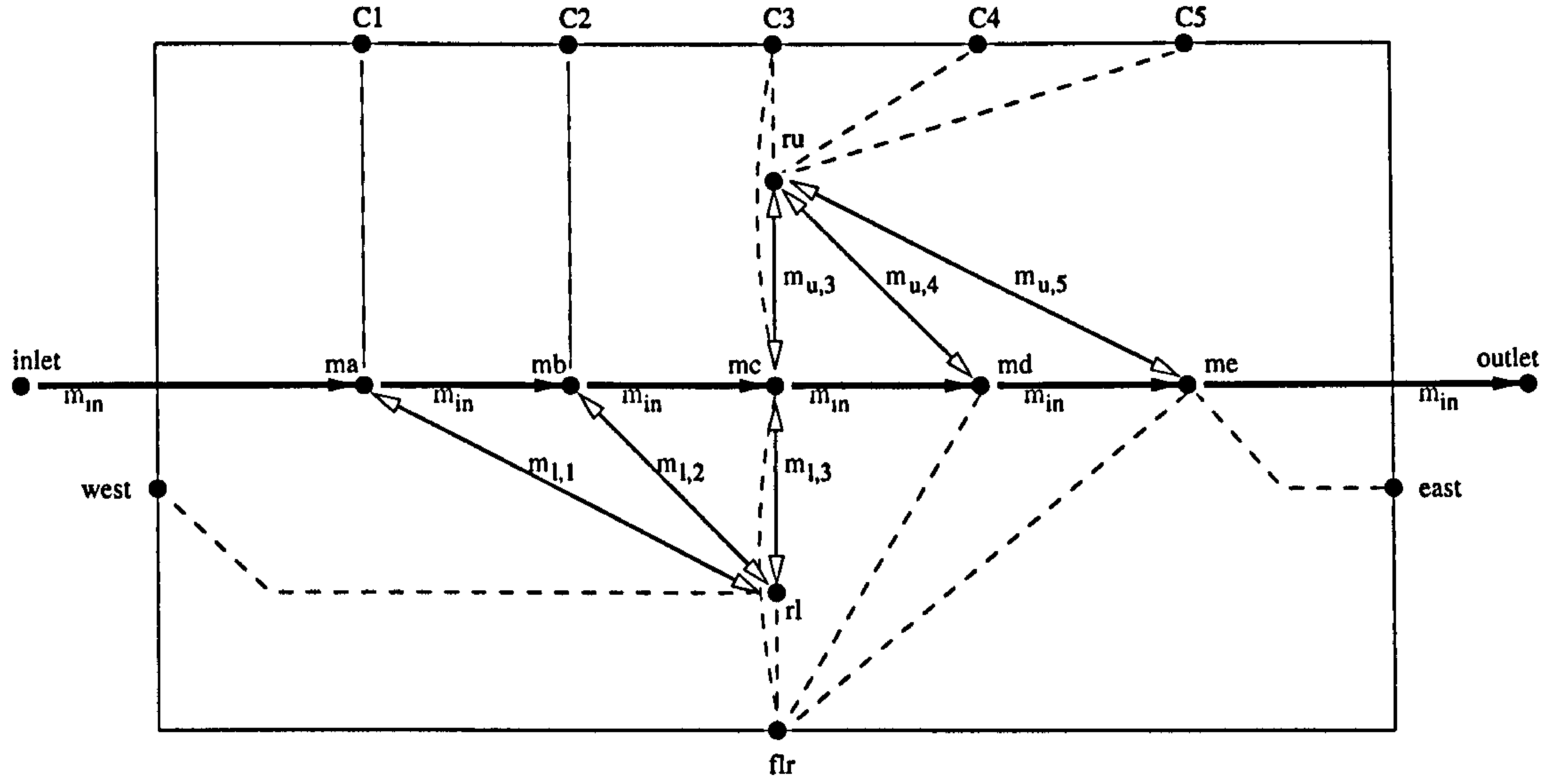

Figure 2.7: Zonal model when the main flow stream detaches in zone 3.

is convectively coupled to the *east, west,* and *flr* nodes rather than the ceiling nodes. The ceiling nodes are convectively coupled to the upper recirculating node, *ru*, and there is entrainment between *ru* and the main flow stream nodes. There is no lower recirculating region so *rl* is left unconnected. The *north,* and *south* nodes are connected to the upper recirculating region.

Figure 2.7 shows the heat flow connections used when the main flow stream detaches in the third main flow stream zone. In this case there are two recirculating regions. For surface nodes *C1*, *C2* and west, and air nodes *ma* and *mb*, the heat flow connections remain the same as the case where the main flow stream remains attached to the ceiling.

After detachment the main flow stream is convectively coupled to the floor and there is entrainment from the main flow stream into the upper recirculating region. In the main flow stream zone in which detachment occurs, (represented by air node *mc*), the main flow stream is attached to the ceiling for part of the zone and to the floor for the rest. The heat transfer connections take this into account, for example, there is a connection representing entrainment into the upper recirculating region as well as a connection representing entrainment into the lower recirculating region. The *north,* and *south* nodes are connected to the upper and lower recirculating regions.

2.4 Conclusions

A zonal model has been proposed that models three heat transfer processes important in naturally ventilated systems:

1. The radiation between room surfaces;
2. Convective heat transfer between surface and air nodes;
3. Bulk convection between air nodes.

The room air is split into 7 zones, 5 nodes which described the main flow stream through the room and two nodes for the two recirculating regions possible. The first recirculating zone is bounded by the MFS above it and the floor below it and the second is bounded by the ceiling above it and the MFS below it. Splitting the room this way allows the consequence of whether the MFS remains attached to the ceiling or travels along the floor. 5 MFS zones allow for multiple detachment points along the ceiling surface and along with the 5 ceiling nodes allows for different convective heat transfer coefficients to be used before and after flow detachment. The initial assumption that the thermal mass in the room is concentrated in the ceiling means the model uses 5 nodes for the ceiling and one node is used for each of the other room surfaces.

In order to implement the model, data is needed to supply the parameter values:

- 24 convective heat transfer parameters;
- 26 bulk air convection capacity rates;
- 10 surface emissivity values, the selection of which is relatively straight forward, a value of 0.05 was used in the long wave radiation range.

The remaining part of this document describes how CFD and experimental techniques have been employed to determine these parameters. Chapter 6 completes the zonal model proposed using the parameters derived from the CFD and experimental work and uses it in a number of simulations. Appendix B gives the equations that LIGHTS calculates in a more general form that may be used to implement the zonal model in another thermal modelling program.

CHAPTER 3

CFD Models of Night-time Cross-flow Ventilation

3.1 Objectives

In order to derive a simplified model of the thermal processes involved in a night-time cross-flow ventilated system, data is required to inform the details of the model. In this study, data has been obtained in two ways: via experimental readings taken in a naturally ventilated room; and via a numerical study of cross-flow ventilation. This chapter describes the main numerical study undertaken.

Methods of calculating room air flow and heat transfer based on computational fluid dynamics have certain advantages over experimental techniques:

- Boundary conditions and room geometry can be easily altered allowing a variety of parametric studies to be undertaken;
- Velocity, temperature and pressure fields are generated in greater detail than is practical to obtain experimentally;
- Flow visualisation techniques, included in the post-processing modules of many CFD packages, may help to increase understanding of room air flow.

The aims of making numerical calculations of cross-flow ventilation were threefold:

- To generate data that can be used to formulate the structure of the zonal model, i.e. the number and positions of nodes and connections;
- To generate data that can be used to determine the values of the parameters of the zonal model, i.e. the bulk air flows and convective heat transfer coefficients;

- To determine empirical relationships that relate a particular parameter (mass flow or convective heat transfer coefficient) to the zonal model boundary conditions of pressure difference between room openings and temperature difference between inlet air and ceiling surface.

To this end, a commercial CFD package with a multi-block flow solver (CFX 1997b) and coupled radiant exchange model (CFX 1997a) has been used.

3.2 A Description of Computational Fluid Dynamics

This section gives a brief summary of aspects of computational fluid dynamics important in the understanding of the modelling issues and decisions taken in this work. A more detailed examination of the field of computational fluid dynamics is given in many books (Versteeg and Malalasekera 1995).

3.2.1 The Reynolds Averaged Navier-Stokes Equations

The fundamental equations governing fluid flow are the continuity equation and the momentum transport equations, which together are known as the Navier-Stokes equations. In this section we follow the descrition given in CFX (1997b). The formulation of the Navier-Stokes equations solved in the method used here involves a number of simplifications and modelling assumptions that are commonly made in dealing with problems such as room air flows. Firstly the Navier-Stokes equations are formulated in their Reynolds Averaged form by separating the velocity components into mean (noted by upper case variables) and fluctuating parts (noted by lowercase variables) and time averaging the equations. The time averaging treatment of the momentum equations results in additional terms involving the fluctuating velocity components $\rho\overline{u_i u_j}$—the Reynolds stresses. These Reynolds stresses need to be determined by the use of a turbulence model of some form (discussed in Section 3.2.2). The Reynolds Averaged Navier Stokes (RANS) equations can be stated in Cartesian tensor notation as

$$\frac{\partial \rho}{\partial t} + \frac{\partial \rho U_i}{\partial x_i} = 0 \tag{3.1}$$

$$\begin{aligned}\frac{\partial \rho U_i}{\partial t} + \frac{\partial \rho U_i U_j}{\partial x_j} &= -\frac{\partial P}{\partial x_i} + \frac{\partial}{\partial x_j}\mu\left(\frac{\partial U_i}{\partial x_j} + \frac{\partial U_j}{\partial x_i}\right) \\ &\quad + \rho g_i - \frac{\partial}{\partial x_j}\left(\rho\overline{u_i u_j}\right) + S_i.\end{aligned} \tag{3.2}$$

It is also assumed that the flow can be treated as incompressible. This simplification means that the first term of the continuity equation is eliminated and that ρ in most of the terms of the momentum equation can be replaced by a constant reference density ρ_0

determined by a constitutive relation at a reference temperature T_0. For buoyancy effects to be modelled the body force term ρg_i needs a slightly different treatment. Firstly, ρg_i is written as $\rho_0 g_i + (\rho - \rho_0)g_i$ and the $\rho_0 g_i$ term is absorbed into the pressure gradient term. Density changes are then related to temperature difference by use of the thermal expansion coefficient β, so that the body force term becomes $\rho_0\beta(T-T_0)g_i$ (the Bousinesq assumption).

The model of turbulence used in this work is based on the eddy viscosity hypothesis. The eddy viscosity hypothesis makes an analogy between molecular viscous stresses and turbulent shear stresses by introducing the idea of turbulent viscosity, μ_t, so that the Reynolds stresses are proportional to the mean rates of strain,

$$-\rho\overline{u_i u_j} = \mu_t(\frac{\partial U_i}{\partial x_j} + \frac{\partial U_j}{\partial x_i}) - \frac{2}{3}\rho_0\delta_{ij}k. \tag{3.3}$$

Closure of the Reynolds Averaged Navier-Stokes equations using an eddy viscosity turbulence model then becomes a question of modelling and solving further equations for the turbulent viscosity. When the Bousinesq assumption and an eddy viscosity turbulence model are employed the RANS equations can then be expressed as

$$\frac{\partial U_i}{\partial t} + \frac{\partial U_i U_j}{\partial x_j} = -\frac{1}{\rho_0}\frac{\partial P'}{\partial x_i} + \frac{\partial}{\partial x_j}\nu_{\text{eff}}\left(\frac{\partial U_i}{\partial x_j} + \frac{\partial U_j}{\partial x_i}\right) + \beta(T - T_0)g_i + S_i \tag{3.4}$$

with an effective viscosity ν_{eff} defined by $\nu_{\text{eff}} = \nu_t + \nu$ and the pressure modified so that

$$P' = P + \frac{2}{3}\rho_0 k - \rho_0 g_i x_i. \tag{3.5}$$

3.2.2 Turbulence Closure Model

In this work, the high-Reynolds-number k-ε turbulence closure model is used (CFX 1997b). The k-ε model is the most widely used and validated turbulence model for building flows and is used in a wide range of engineering problems. It is based on the two equation eddy viscosity model of Launder and Spalding (1974). In eddy viscosity models such as this the basic hypothesis is that turbulent viscosity is proportional to a turbulence velocity scale, V_c, multiplied by a length scale (representative of the larger eddy sizes), L_c, such that $\mu_t = \rho V_c L_c$. In the k-ε model used here the velocity scale is the square root of the turbulent kinetic energy k (where $k = \frac{1}{2}\overline{u_i u_i}$) and the length scale is defined as $L_c = k^{\frac{3}{2}}/\varepsilon$, where ε is the rate of dissipation of k. A modelling constant C_μ is also introduced such that

$$\mu_t = \rho C_\mu \frac{k^2}{\varepsilon}. \tag{3.6}$$

Constant	C_μ	$C_{\varepsilon 1}$	$C_{\varepsilon 2}$	σ_k	σ_ε
Value	0.09	1.44	1.92	1.0	1.217

Table 3.1: Constants used in the k–ε Turbulence Model

The modelled k equation, after introducing a modelling constant σ_k, is then of the form

$$\frac{\partial \rho k}{\partial t} + \frac{\partial U_j k}{\partial x_j} - \frac{\partial}{\partial x_j}\left((\mu + \frac{\mu_t}{\sigma_k})\frac{\partial k}{\partial x_j}\right) = P_k + G - \rho\varepsilon, \tag{3.7}$$

where P_k is the production due to strain term given by

$$P_k = \mu_{\text{eff}}\left(\frac{\partial U_i}{\partial x_j} + \frac{\partial U_j}{\partial x_i}\right)\frac{\partial U_i}{\partial x_j}, \tag{3.8}$$

and G is the production due to buoyancy forces given by

$$G = \frac{\mu_{\text{eff}}}{\sigma_T}\beta g_i \frac{\partial T}{\partial x_i}. \tag{3.9}$$

The generation rate of ε is assumed to be proportional to P_k, the generation rate of k. The destruction rate of ε is assumed to be proportional to the rate of destruction of k, which is just ε. The resulting modelled epsilon equation is

$$\frac{\partial \rho\varepsilon}{\partial t} + \frac{\partial \rho U_j \varepsilon}{\partial x_j} - \frac{\partial}{\partial x_j}\left((\mu + \frac{\mu_t}{\sigma_\varepsilon})\frac{\partial \varepsilon}{\partial x_j}\right) = C_{\varepsilon 1}\frac{\varepsilon}{k}P_k - C_{\varepsilon 2}\rho\frac{\varepsilon^2}{k}, \tag{3.10}$$

The constants C_μ, $C_{\varepsilon 1}$ and $C_{\varepsilon 2}$ are found from empirical observations and here have the values given in Table 3.1.

3.2.3 The Energy Equation

The energy equation in its most general form is usually expressed in terms of total specific enthalpy[1] H ($H = h + \frac{1}{2}U^2$). Here, however, the energy equation is formulated in terms of static (thermodynamic) enthalpy h, as the flow is being treated as low Mach Number (hence incompressible), and the kinetic energy term $\frac{1}{2}U^2$ in the total enthalpy can be assumed to be relatively insignificant. Similarly the pressure work and kinetic heating terms of the general equation are ignored. The energy equation given these simplifications, and subjected to a similar time averaging treatment to the RANS equations, can be expressed in terms of static enthalpy as

$$\frac{\partial \rho h}{\partial t} + \frac{\partial \rho U_j h}{\partial x_j} - \frac{\partial}{\partial x_j}\left(\frac{\lambda}{C_p}\frac{\partial h}{\partial x_j} + \rho\overline{u_j h}\right) = S_e, \tag{3.11}$$

---

[1] H is used to denote total specifc enthalpy (J/kg) rather than total system enthalpy (J) as in thermodynamics texts.

where λ is the thermal conductivity, $-\rho\overline{u_j h}$ are the turbulent enthalpy fluxes which arise from the time averaging of the non-linear convection term in a similar manner to the Reynolds stresses of the RANS equations, and S_e is a source term which might be used to include such phenomena as radiant heating of the air.

The energy equation must be closed by using a calorific equation of state defining the relationship between static enthalpy and temperature and pressure, $h = h(T, p)$. For air in building services applications the static enthalpy is a function of temperature only: $h = C_p T$.

With a two equation eddy viscosity model, such as that used here, the turbulent heat fluxes are modelled using the eddy diffusivity hypothesis (analogous to the treatment of the turbulent momentum fluxes) so that

$$-\rho\overline{u_j h} = \frac{\mu_t}{\sigma_H}\frac{\partial h}{\partial x_j}, \tag{3.12}$$

where μ_t is calculated with the turbulence model and σ_H is C_p multiplied by σ_T the turbulent Prandtl number.

Given the use of the k–ε turbulence model and the modelling of the turbulent enthalpy flux as defined in Equation 3.12 the modelled Reynolds averaged energy equation becomes

$$\rho\frac{\partial h}{\partial t} + \rho\frac{\partial U_j h}{\partial x_j} - \frac{\partial}{\partial x_j}\left(\frac{\lambda}{C_p} + \frac{\mu_t}{\sigma_H}\right)\frac{\partial h}{\partial x_j} = S_e. \tag{3.13}$$

3.2.4 Radiative Heat Transfer

The radiant coupling between wall, ceiling and floor surfaces is an important process of heat exchange within naturally ventilated rooms. CFD simulations in this work use a general radiation calculation procedure coupled to the flow calculation. The radiation calculation procedure used is known as the 'discrete transfer' method (Shah 1979). The discrete transfer method was originally developed for the treatment of radiation in combustion calculations and can be applied to complex geometries as well as treating absorption and scattering effects (Lockwood and Shah 1980). The discrete transfer method has also been applied to the calculation of room radiant heat transfer (Malalasekera and James 1993). The method determines the radiative fluxes by tracking rays of light, projected from the surface node, through a set of zones that form the computational domain. The radiation calculation was called every 5 outer iterations of the flow solver to ensure the convergence of the enthalpy equation.

The fundamental equation for the transfer of thermal radiation can be expressed as

$$\frac{dI}{ds} = -(K_a + K_s)I + K_a\frac{E_g}{\pi} + \frac{K_s}{4\pi}\int_{4\pi} P(\Omega, \Omega')I(\Omega')\,d\Omega' \tag{3.14}$$

where I is the radiant intensity in the direction Ω, s is the distance in that direction and

E_g is the black body emissive power of the gas (σT_g^4). K_a and K_s are the gas absorption and scattering coefficients and $P(\Omega, \Omega')$ is the probability that incident radiation in the direction Ω' will be scattered into the increment of solid angle $\delta\Omega$ about Ω.

This equation can be expressed more concisely as

$$\frac{dI}{ds^*} = I\frac{E^*}{\pi} \tag{3.15}$$

where an extinction coefficient ($K_e = K_a + K_s$) is defined so that distance is expressed as optical depth ($ds^* \equiv K_e ds$) and E^* is a modified emissive power given by

$$E^* = \frac{1}{K_e}\left(K_a E + \frac{K_s}{4}\int_{4\pi} P(\Omega, \Omega')I(\Omega')\,d\Omega'\right). \tag{3.16}$$

To discretise Equation 3.16 the flow domain is divided by a series of planes crossing each other to form a number of zones (which are arranged to be the union of a number of flow cells in a coupled flow-radiation calculation) and divide each surface into a number of panels. A number of uniformly distributed rays are traced back from reference points on each surface panel (at which the ray is imagined to have arrived), along a straight path passing through a number of intermediate zones, until another surface is encountered. Equation 3.16 is discretised by integrating along the ray to yield the recurrence relation:

$$I_{n+1} = I_n e^{-\delta s^*} + \frac{E^*}{\pi}(1 - e^{-\delta s^*}) \tag{3.17}$$

where n and $n+1$ indicate positions where the ray enters and leaves each zone.

The recurrence relationship is applied as follows. An initial estimate of the intensity leaving the source surface panel is made from the current temperature field using the relation:

$$I^n = \frac{\epsilon_s \sigma T_w^4}{\pi}. \tag{3.18}$$

The intensity at each point along the ray path and at the surface panel is then found by applying the recurrence relation. Surface heat fluxes are then arrived at by integrating the effect of all the rays arriving at each panel such that the irradiation G is obtained from:

$$G = \sum_{j=1}^{nj} I_j(\Omega_j . n)\delta\Omega \tag{3.19}$$

where I_j is the calculated intensity in the discretised angle $\delta\Omega$ and n is a unit vector normal to the surface. For a 'grey' wall the local radiosity J is given by:

$$J = (1 - \epsilon_s)G + \epsilon_s \sigma T_s^4 \tag{3.20}$$

where ϵ_s is the surface emissivity.

Where the method is used apart from any flow calculation to calculate radiant fluxes the calculated radiosity J is used to find a new value for the intensity leaving the surface (from the relation $I = J/\pi$). This is then used as the new initial intensity when reapplying the recurrence relation. This procedure is repeated until the change in the G from one iteration to the next falls below a certain tolerance. At the end of the procedure the net flux on each surface panel can be found from $q_s = G - J$.

In a combined flow-radiation calculation, the coupling is achieved by passing heat flux information from the flow solver to the radiation solver and temperature information in the reverse direction (or vice versa). The information from one solver is then used to form the boundary conditions for the next calculation in the other.

3.2.5 Solution Procedure

Solution of the governing flow and heat transfer equations by numerical means requires firstly, discretisation of the differential equations, linearisation of the resulting algebraic equations and application of the boundary conditions before final application of algebraic solver algorithms to the large sets of simultaneous algebraic equations. The solution methodology can be thought of consisting of a number of sub-processes or algorithms which together constitute a method of producing a solution to the coupled non-linear partial differential equations. Many of these sub-processes are algorithms that have been extensively tested and reported upon in the literature and for this reason are described and discussed only briefly in this section. There are many sources available if a more complete treatment is required (Versteeg and Malalasekera 1995).

Discretisation of the Equations

Numerical solution of the governing partial differential equations results in values of the fundamental variables of these equations being found at discrete points in a geometric mesh of the flow field. There are several approaches to discretising the equations (e.g. Finite Difference or Finite Element methods). The method used here is known as the 'Finite Volume' method. The finite volume formulation is to be preferred over other methods on the basis that the consistency and conservation properties of the original differential equations are guaranteed to be preserved in the discrete analogue (Patankar 1980). In the finite volume formulation the partial differential equations are firstly integrated over a finite control volume. The resulting algebraic equations then describe the transport of fluxes of the fundamental quantities.

The governing equations can be expressed as a generalised convection-diffusion equation such as

$$\frac{\partial \rho\phi}{\partial t} + \frac{\partial \rho U_j \phi}{\partial x_j} - \frac{\partial}{\partial x_j}\left(\Gamma \frac{\partial \phi}{\partial x_j}\right) = S_\phi, \tag{3.21}$$

where Γ is the appropriate diffusion coefficient and S_ϕ the source term with appropriate dimensions.

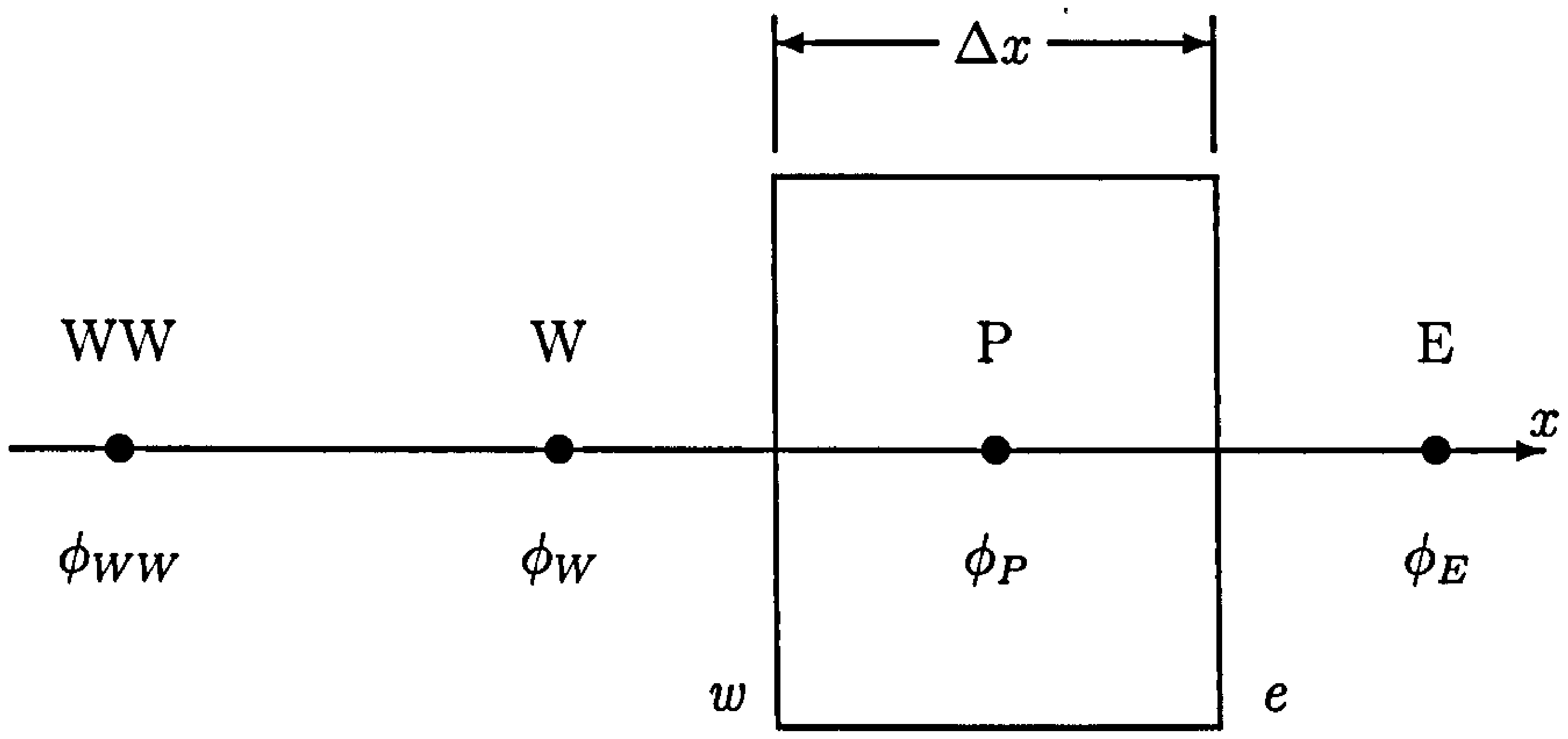

Figure 3.1: A notional one-dimensional control volume with constant node spacing.

The finite volume formulation can be illustrated by reference to a one dimensional example. The first step in discretising this type of equation by the finite volume method is to integrate it over the cell volume. Equation 3.21 in its one dimensional form and integrated in this way becomes

$$\int \frac{\partial \rho \phi}{\partial t} dx + \int \frac{\partial \rho U_j \phi}{\partial x} dx - \int \frac{\partial}{\partial x} \left(\Gamma \frac{\partial \phi}{\partial x} \right) dx = \int S_\phi \, dx. \tag{3.22}$$

A notional one-dimensional control volume is shown in Figure 3.1 over which the above integrated equation is to be evaluated to find the value of ϕ at point P. (Constant cell spacing is shown but the extension to variable spacing is straight forward.) First it should be noted that a number of assumptions are made in forming the algebraic equations (Patankar 1980):

- ϕ is constant over the face of the cell;
- The source term S_ϕ is constant over the control volume, at a value determined at the cell centroid P;
- The diffusion coefficient Γ varies linearly between grid nodes if it is dependent on ϕ.

Firstly, the source term of Equation 3.21 is normally arranged to allow for a dependency on the variable and linearised so that:

$$\int S_\phi \, dx = B\phi_P + C, \tag{3.23}$$

where the dimensions of B and C are suitably modified from that of B^* and C^*. Taking the diffusion term of Equation 3.22 next, this becomes

$$\int_w^e \frac{\partial}{\partial x}\left(\Gamma\frac{\partial\phi}{\partial x}\right) dx = \left[(\Gamma\frac{\partial\phi}{\partial x})_w - (\Gamma\frac{\partial\phi}{\partial x})_e\right], \tag{3.24}$$

and the convection term becomes

$$\int_w^e \frac{\partial\rho U_j\phi}{\partial x} dx = \left[(\rho U\phi)_w - (\rho U\phi)_e\right]. \tag{3.25}$$

From the integration of the convection and diffusion terms it is apparent that it is necessary to find an algebraic expression for the values of ϕ (and its gradients) at the cell faces involving only values at other cell centres. These expressions or interpolating polynomials are defined by a differencing scheme.

The Differencing Schemes

The hybrid differencing scheme used here is the default scheme in the CFD package used for the study (CFX 1997b). The hybrid differencing scheme was also used in the studies of Cook and Lomas (1998) and Rees (1998).

Hybrid Differencing Scheme (HDS) The hybrid differencing scheme was proposed by Spalding (1972) and is an attempt to combine the best features of the central (CDS) and upwind (UDS) schemes (CFX 1997b). It can be shown that when the central differencing scheme is used to discretise both convection and diffusion terms the limit on numerical stability of the resulting set of algebraic equations is determined by a cell Peclet number of 2. The cell Peclet number Pe_c is a non-dimensional number and is defined as the ratio of convection to diffusion so that in this example

$$Pe_c = \frac{\rho U \Delta x}{\Gamma}. \tag{3.26}$$

The hybrid scheme is designed such that where $Pe_c < 2$ the CDS is applied, and where $Pe_c \geq 2$ the UDS is applied. In this case of the west face in Figure 3.1 then

$$\begin{aligned} \phi_w &= \tfrac{1}{2}(\phi_W + \phi_P) && \text{for } \mathrm{Pe_c} < 2, \\ \phi_w &= \phi_W && \text{for } \mathrm{Pe_c} \geq 2, \mathrm{U_w} > 0, \\ \phi_w &= \phi_P && \text{for } \mathrm{Pe_c} \geq 2, \mathrm{U_w} < 0. \end{aligned} \tag{3.27}$$

This arrangement has the advantage that where convection dominates the flow numerical stability is promoted (although there is a risk of false diffusion errors) and where diffusion dominates (across streams and in areas of low flow) second order accuracy is retained.

Assembly of the Algebraic Equations

Returning to the example one-dimensional Equation 3.24, the diffusion term in the equation can be evaluated by using a central difference approximation for the gradients of ϕ at the faces of the cell so that

$$\int_w^e \frac{\partial}{\partial x}\left(\Gamma \frac{\partial \phi}{\partial x}\right) dx \approx \left[(\Gamma_w \frac{(\phi_P - \phi_W)}{\Delta x}) - (\Gamma_e \frac{(\phi_E - \phi_P)}{\Delta x})\right], \qquad (3.28)$$

where Γ may be linearly interpolated so that $\Gamma_w = (\Gamma_W + \Gamma_P)/2$ and $\Gamma_e = (\Gamma_P + \Gamma_E)/2$. The convection term can be evaluated using the Upwind scheme so that,

$$[(\rho U \phi)_w - (\rho U \phi)_e] \approx [(\rho U)\phi_W - (\rho U)\phi_P], \qquad (3.29)$$

assuming that $U > 0$ at each face.

It is now possible, after expressing the discretised equation in terms of values of ϕ at neighbouring cells, to gather together terms using a series of coefficients a_{nb} associated with the neighbouring cells so that the whole equation is

$$\begin{aligned} \frac{\partial}{\partial t}(\rho\phi\Delta x) &= a_E(\phi_E - \phi_P) + a_W(\phi_W - \phi_P) + B_P\phi_P + C_P \\ &= \sum_{nb} a_{nb}(\phi_{nb} - \phi_P) + B_P\phi_P + C_P, \end{aligned} \qquad (3.30)$$

where $\sum_{nb}$ implies summation over the neighbouring cells. In a three dimensional case this would simply include terms for the other six neighbouring cells.

To accommodate the temporal term an implicit backward differencing approach is used here, so that where the superscript n indicates the current time step,

$$\frac{\rho\Delta x}{\Delta t}(\phi^n - \phi^{n-1}) = \left[\sum_{nb} a_{nb}(\phi_{nb} - \phi_P) + B_P\phi_P + C_P\right]^n. \qquad (3.31)$$

This can be re-written as an expression for ϕ at the current time step by absorbing the ϕ_P^{n-1} term into the source term,

$$(A_P - S_P)\phi_P = \sum_{nb} a_{nb}\phi_{nb} + S_U, \qquad (3.32)$$

where,

$$\begin{aligned} A_P &= \sum_{nb} a_{nb}, \\ S_P &= B_P - \frac{\rho\Delta x}{\Delta t}, \\ S_U &= C_P + \frac{\rho\Delta x}{\Delta t}\phi^{n-1}. \end{aligned}$$

The discretised equations for each cell form a large set of algebraic equations that can be expressed in matrix form as,

$$[A]\,[\phi] = [B]\,, \tag{3.33}$$

where $[A]$ is the coefficient matrix (and is generally dependent on ϕ), $[\phi]$ is the vector of unknowns, and $[B]$ is the vector of source terms.

The sets of equations to be solved in this case are formulated in terms of the fundamental variables U, V, W, h, P, k and ε. Each of these equations are coupled together and made non-linear by velocity appearing in the coefficients of the convection terms. In the case of the k and ε equations these are also made non-linear by μ_t appearing in the coefficients, and the nature of the source terms. In order to deal with these non-linearities in the solution procedure an iterative approach is used where the algebraic equations are successively re-linearised. At each iteration step, values from the previous iteration are used to re-calculate the equation coefficients before re-applying a linear algebraic equation solver algorithm.

The coefficient matrices $[A]$ are narrowly banded and amenable to the application of a number of linear equation solver algorithms. These linear equation solver algorithms typically require a number of iterations to solve the algebraic equations (to a given tolerance). Thus the solution procedure consists of (at each time step in a transient solution) an outer iteration loop where the equation sets are linearised and coefficient matrices reformed, and a series of inner iteration loops where each of the equation sets is solved, in sequence, by the application of a linear algebraic solver algorithm.

The algebraic solver algorithms used here are the Line Relaxation algorithm (applied to the k and ε equations), the STONE algorithm (applied to the momentum and energy equations) and the ICCG Preconditioned Conjugate Gradients method (applied to the pressure correction equation) (CFX 1997b).

The Pressure Correction Algorithm

For an incompressible flow calculation an equation for pressure is found by substituting a form of the momentum equation into the continuity equation giving an equation for a pressure correction δP. This equation is discretised and solved in a similar manner to the other equations. The velocities are then calculated in a two step process. The procedure used here is known as SIMPLEC (Van Doormaal and Raithby 1984) which is a refinement of the SIMPLE[2] algorithm (Patankar and Spalding 1972).

In this type of pressure correction procedure the velocity field is first calculated with the existing pressure field P^n to give a first estimate of the velocity U^* which will not satisfy the continuity requirement. The aim is to find a pressure correction δP such

---

[2] Semi-Implicit-Method-for-Pressure-Linked-Equations. The additional C of the SIMPLEC acronym stands for 'Consistent'.

that $P^{n+1} = P^n + \alpha_P \delta P$ and a corresponding velocity correction δU such that the new velocity field given by $U^{n+1} = U^* + \delta U$ satisfies continuity. An equation for the velocity correction can be found by subtracting the momentum equation for U^* from the momentum equation for U^{n+1}. In discretised form this would give for the U velocity correction,

$$\left(\frac{\Delta x \Delta y \Delta z}{\Delta t} + a^U_{nb}\right) \delta U_P = -\sum_{nb} a^U_{nb} \delta U_{nb} - \Delta y \Delta z (\delta P_e - \delta P_w), \tag{3.34}$$

and similarly for the δV and δW velocity corrections. In the SIMPLE algorithm the $\sum a^U_{nb} \delta U_{nb}$ term is simply dropped to find an explicit form of velocity correction equation. In the SIMPLEC algorithm a more accurate approximation to Equation 3.34 is sought by subtracting $\sum_{nb} a^U_{nb} \delta U_P$ from both sides and dropping the $\sum_{nb} a^U_{nb}(\delta U_{nb} - \delta U_P)$ term from the right-hand side to give,

$$\delta U_P = dip(\delta P_w - \delta P_e) \tag{3.35}$$

where

$$dip = E \Delta y \Delta z / [(1 + E) a^U_P - E \sum a^U_{nb}] \tag{3.36}$$

and

$$E = \Delta t \, a^U_{nb} / \Delta x \Delta y \Delta z. \tag{3.37}$$

Substitution of $U^{n+1} = U^* + \delta U$ etc. into the continuity equation gives the pressure correction equation, a Poisson equation for δP, which in tensor notation is:

$$\frac{\partial}{\partial x_i}\left(\frac{\partial \delta P}{\partial x_i}\right) = \frac{1}{\Delta t}\left(\frac{\partial U_i^*}{\partial x_i}\right). \tag{3.38}$$

The pressure correction procedure can therefore be summarised as:

1. Solve momentum equations to find the approximate velocity field U^* etc. using current pressure field P^n;
2. Solve pressure correction Equation 3.38 to find δP;
3. Use δP to make velocity corrections using Equation 3.37;
4. Update the pressure field using $P^{n+1} = P^n + \alpha_P \delta P$, where α_P is a relaxation factor.

A smaller relaxation factor α_P is required when correcting the pressure field when using the SIMPLE algorithm compared to the SIMPLEC algorithm due to the less accurate form of the velocity correction equation. Van Doormaal and Raithby (1984) showed that although more work per iteration was involved in the SIMPLEC algorithm, less iterations were required and there was an overall saving in computational effort. Here the SIMPLEC algorithm has been used exclusively and α_P has been set at 1.0.

3.2.6 Wall Boundaries

To establish boundary conditions for the momentum and energy equations at wall boundaries it is necessary to know the velocity and temperature gradients in the boundary cells. Velocity and temperature vary rapidly at wall boundaries and to resolve accurately the gradients near walls would be computationally expensive. Wall functions are empirical non-dimensionalised functions that can be used to define the relationships between a variable (e.g. U_P or T_P) at some distance from the wall and its flux at the wall (τ_w or Q_w). Wall functions are used then to define the wall boundary conditions with the first cell centroid placed some significant distance from the wall.

Bakhmeteff (1936) found a logarithmic law defining the velocity profile in forced convection wall boundary layers of the form

$$u^+ = \frac{u}{u_\tau} = C_1 log(y^+) + C_2, \tag{3.39}$$

where u^+ is the non-dimensional velocity parallel to the wall and y^+ is the non-dimensional distance normal to the wall surface given by

$$y^+ = \frac{y u_\tau}{\nu}, \tag{3.40}$$

and u_τ is the friction velocity given by,

$$u_\tau = \sqrt{\frac{\tau_w}{\rho}}. \tag{3.41}$$

The log law is found to be valid in the range $30 < y^+ < 300$. In the viscous sublayer ($y^+ < 11.6$) the velocity profile is linear (between these limits the profile is less well defined).

A more generalised form of wall function can be found by normalising the turbulent kinetic energy on the basis that in a boundary layer the shear stress is related to k by $\tau^2 = C_\mu \rho^2 k^2$. This is the form of wall function used by Launder and Spalding (1974) and is the default model in this work. A new quantity τ_k is defined such that:

$$\tau_k = \rho C_\mu^{1/2} k. \tag{3.42}$$

This can then be used to define u^+ and y^+,

$$u^+ = -\frac{(\rho \tau_k)^{1/2}}{\tau} U, \tag{3.43}$$

$$y^+ = \frac{(\rho \tau_k)^{1/2}}{\mu} y. \tag{3.44}$$

The velocity wall function is then given by

$$u^+ = \begin{cases} y^+ & \text{for } y^+ < 11.6, \\ \frac{1}{\kappa} log(Ey^+) & \text{for } y^+ \geq 11.6 \end{cases} \tag{3.45}$$

where E is a constant dependent on the roughness of the surface (9.0 for a smooth surface).

Using this form of non-dimensionalisation means that k can be calculated in the normal way in the cells adjacent the wall (except that the velocity gradients in the P_K term are calculated according to the wall function) and Equation 3.42 used to find the shear stress. The turbulent dissipation ε can be found from k (on the basis that the production of k is in equilibrium with its dissipation) using the relation:

$$\varepsilon = \frac{C_\mu^{3/4} k^{1/2}}{\kappa y}. \tag{3.46}$$

The treatment of enthalpy (and other scalars) is handled in an analogous way to the velocity wall function so that:

$$\phi^+ = \begin{cases} Pr_\phi y^+ & \text{for } y^+ < 11.6, \\ \frac{\sigma_\phi}{\kappa} log(E_\phi y^+) & \text{for } y^+ \geq 11.6, \end{cases} \tag{3.47}$$

where Pr is the Prandtl number μ/Γ_ϕ. ϕ^+ is defined in a similar way to u^+

$$\phi^+ = \frac{(\rho \tau_k)^{1/2}}{J_\phi}(\phi_w - \phi), \tag{3.48}$$

where ϕ_w is the value at the wall and J_ϕ is the flux of ϕ at the wall $\left(\frac{\partial \phi}{\partial n}\right)_w$.

The commonly adopted formula of Jayatilleke (1969) is used here. The variation is defined by

$$E_\phi = Eexp\left[9.0\kappa((\frac{Pr}{\sigma_\phi})^{0.75} - 1)(1 + 0.28exp(-0.007(\frac{Pr}{\sigma_\phi}))\right] \tag{3.49}$$

where E is the constant velocity 'log law' wall function.

There are two types of thermal boundary condition involving the calculation of radiation at the walls. The energy balance at a wall element can be expressed in general terms as:

$$\lambda_c \frac{\partial T}{\partial n} + \lambda_a \frac{\partial T}{\partial n} + q_s = 0, \tag{3.50}$$

where the first term represents conduction through the wall, the second term represents convection, and the third is the net radiant flux. The first boundary condition of concern is an adiabatic wall condition, in which case the first term becomes zero and the convective flux must be in balance with the radiant flux. The second condition is one of conjugate heat transfer, where the radiant flux must balance both the conductive and convective fluxes. An energy balance at each surface can be assured by passing temperature and heat flux information in opposite directions between the flow and radiation codes and as the solution progresses towards convergence the heat fluxes calculated by one code will become consistent with the temperatures calculated by the other. The question remains as to which code calculates the surface temperatures and which calculates the surface fluxes.

The most obvious form of boundary condition treatment is for temperatures to be passed from the flow solver to the radiation solver. In this case the temperatures would then be used in Equation 3.18 to find the next estimate of the intensity. Where conduction and convection wall fluxes dominate this procedure can be used successfully. However, where the radiant flux is more dominant instability can arise due to the radiant flux being sensitive to the fourth power of temperature and the other fluxes being sensitive to simple temperature difference (not important in rooms with small temperature differences), but could certainly arise in combustion calculations, for which the method was devised. In these cases it is necessary to pass heat fluxes from the flow solver to the radiation solver. In this case, if q_s^n is the required flux passed from the flow solver, the next estimate of intensity can be found using the previous estimate of G thus,

$$I^n = \frac{J}{\pi} = \frac{1}{\pi}(G^{n-1} - q_s^n). \tag{3.51}$$

After the recurrence relationship has been applied, G^n can be calculated using Equation 3.19. The temperature to be passed back to the flow solver can then be calculated as follows,

$$J = G - q_s \tag{3.52}$$

and substituting for J using equation 3.20,

$$(1-\epsilon)G^n + \epsilon E = G^n - q_s^n \tag{3.53}$$

$$\epsilon\sigma T^4 = \epsilon G^n - q_s^n \tag{3.54}$$

so that after applying some under-relaxation

$$T^{n+1} = \alpha\left(\frac{1}{\epsilon\sigma}(\epsilon G^n - q_s^n)\right)^{\frac{1}{4}} + (1-\alpha)T^n. \tag{3.55}$$

3.2.7 Flow Boundaries

INLET Boundary

An *INLET* boundary can be used to model an inflow or outflow boundary when the velocity profile is known (CFX 1997b). In an incompressible flow, the primary variables need to be specified using Dirichlet boundary conditions (set at a constant value) at inlets. There are certain variables that do not need setting:

- Enthalpy, which is computed from the inlet temperature;
- Viscosity, which is computed at the inlet as a function of the flow field;
- Pressure (as long as the flow is incompressible), which is extrapolated from downstream.

MASS FLOW Boundary

A *MASS FLOW* boundary can be used to model an inflow or outflow boundary when the total mass flow is known but the detailed velocity profile is not (CFX 1997b). Neumann boundary conditions (constant gradient) are imposed on all variables. A zero gradient is specified for T, k and ε. When using a pressure correction procedure, it is important that there is global mass continuity in order that the pressure correction equation is well posed. This requires that the velocity gradient is modified from a zero gradient condition to a constant normal gradient in order to ensure global mass continuity. The velocity gradients at the outlet cells are modified as follows:

- Apply a nominal zero gradient boundary condition $\frac{\partial U_i}{\partial n} = 0$;
- Calculate the discrepancy between the actual mass flow and the total inlet flow;
- Add an increment to U_i in the direction of the outward facing unit normal to give the correct outflow.

This is equivalent to applying the boundary condition

$$\frac{\partial U_i}{\partial n} = \lambda n_i \tag{3.56}$$

where the constant λ is chosen to give the correct outward mass flow rate. Applying Neumann boundary conditions at the outlet in this way implies that the flow is fully developed approaching the outlet.

3.3 Background

Although CFD methods are clearly very powerful, care must be taken in applying them to naturally ventilated spaces. Despite the everyday nature of wind driven room flows, calculation of flow fields that can have a number of recirculating regions and that may be driven by pressure, momentum and buoyancy forces possess a considerable challenge for both the practitioner and code developers. McGuirk and Whittle (1991) outline some of the issues involved in the numerical modelling of room air flows including:

- The low velocities and Reynolds number associated with room air flows and their effect on the choice of turbulence closure model and mesh structure;
- The accurate prediction of room surface convective heat transfer rates;
- The lack of experimental data and benchmarks to validate the numerical predictions, particularly the heat transfer from horizontal surfaces (the ceiling and floor) into the room air;
- The difficulty in achieving a converged solution when modelling buoyancy driven flows.

3.3.1 Previous Research

Interest in using computational fluid dynamics to model room air flow and heat transfer has grown steadily since the 1980's (Awbi and Gan 1991; Alamdari 1991). Use of these techniques in studying room flows has, however, lagged behind application to other areas (e.g. aerospace). Codes using either finite element (Baker 1983), or the more commonly used finite volume method (Patankar 1980), have now been specifically developed with room air flow applications in mind (IES 1999b). Such codes are generally able to deal with prediction of the turbulent, non-isothermal, buoyant air flows found in naturally ventilated rooms, and are able to model complex geometries. The general development of these numerical methods and their application to room air flows is described by Jones and Whittle (1992). There is a large body of literature concerned with the modelling of fluid flows, turbulence and numerical methods in general. The aim of the literature review given here, however, has been to focus on that literature that is of particular relevance to cross-flow ventilation.

CFD Studies of Cross-Ventilation

Tsutsumi, Katayama, Hayashi, and He (1992) present a CFD study of flow in and around a single-unit house. The house is represented by a cube with square openings in two of the wall surfaces. The computational domain models the exterior environment as well as the room flow. In a further paper, Tsutsumi et al. (1995) extend the room model by modelling an internal partition with a door like opening which allows flow through the building. The partition opening is placed on and off-centre with respect to the window openings. Also the effect of the partition position is examined with a number of distances between the windward opening and the partition modelled.

Iwamoto, Ishii, Katayama, and Tsutsumi (1992) present a study of cross-flow in a four-story building. As with Tsutsumi et al. the exterior environment is modelled as well as the room flow. The flow field around the multi-story building can be seen to dramatically effect the flow through each of the four floors. The exterior flow field near to the opening on the fourth floor has a large vertical component of velocity which is transmitted through the windward opening where the flow impinges on the ceiling. At the openings on the first two floors the dynamic pressure of the wind has mostly been converted to static pressure because of the large obstruction that the building presents to the wind. The flow through these lower floors is horizontal. The predicted flow rate decreases towards the top floor.

These studies show that it is feasible to conduct isothermal CFD calculations covering internal and external flow which investigate parameters such as building geometry and internal partitions. They also show that internal flow is strongly effected by building geometry and that it is hard to look at room flow alone. Studies on building geometry etc., are comprehensibly tackled by many wind tunnel investigations (Ernest 1991).

Other Natural Ventilation Studies

Gan and Awbi (1994) (also (Awbi and Gan 1991)) used a CFD program to model a naturally ventilated room. The problem included radiant and convective heat transfer as well as buoyancy. The inlet velocity was calculated from the air change rate measured experimentally. The room modelled was not designed for cross-flow ventilation though. The outflow boundary was assumed to be a small gap between the bottom of a door and the floor.

There are more studies of room air flow that, although not wind induced, are applicable to the work pursued here. Cook and Lomas (1998) use CFD to model natural ventilation driven exclusively by buoyancy forces. The problem modelled was based on the work of Linden et al. (1990) who examine the fluid mechanics of buoyancy driven natural ventilation mathematically.

There are a number a CFD studies of air flow in atria (Chikamoto et al. 1992; Ozeki et al. 1992; Schild et al. 1995; Alamdari et al. 1991; Kato et al. 1995). All studies model the effects of buoyancy but ignore the effect of wind on ventilation.

Heat Transfer at Wall Surfaces

The standard k–ε model is only suitable for high-Reynolds-number flows. Near wall surfaces the local Reynolds number is very low, and therefore the model is not valid. It is conventional to use 'wall functions' to describe the velocity and temperature gradients between the wall surface and the first nodes of the computational mesh. The wall functions in general have been developed from empirical studies of forced convection boundary layers. Standard k–ε turbulence models generally use a logarithmic function to describe the velocity profile in the turbulent part of the boundary layer. A number of studies have raised questions on the ability of wall functions to accurately predict the convective heat transfer at wall surfaces (Yuan 1995; Chen and Jiang 1992; Yuan et al. 1993). According to Yuan et al. the difficulty in accurately predicting wall heat transfer with wall functions arises from the fact that the velocity profiles in the boundary layer, and just outside the boundary layer, are somewhat different in the case of natural, as opposed to forced convection. Yuan et al. have developed a set of alternative wall functions for the case of natural convection from vertical surfaces which have given some promising results.

3.3.2 Implications of Previous Work

The use of CFD in numerical investigations of room air flow is common in the literature. Most of this research concentrates on mechanical ventilation. When natural ventilation is considered then the driving forces tend to be either wind or buoyancy, but rarely both. The literature on cross-ventilation concentrates on air flow prediction in simple geometries and tends to ignore heat transfer, buoyancy and radiation, of particular importance in night-time cross-flow situations examined in this work. Thus, it was concluded that this research should concentrate on the air flow in non-isothermal cases where there is little data.

It is clear from other research (Jones 1995) that CFD simulations of buoyancy driven flows often require the use of a transient simulation or false time-stepping (Rees 1998; Cook and Lomas 1998) to achieve a converged solution—thus computation time is great. For this reason, methods were sought to keep the number of cells, and therefore computation time required, to a minimum:

- The use of two-dimensional simulations instead of three-dimensional simulations;
- Decoupling the internal environment from the external environment, and choosing to model the internal environment alone.

Now we examine the implications of these two modelling decisions in turn. The choice to model a problem using a two-dimensional simulation is common (Cook and Lomas 1998; Iwamoto et al. 1992). Sometimes this decision is questionable; Iwamoto et al. choose to model the flow through and around a four story building using a two-dimensional simulation. This implies that the width of the building is great and the air flows over the building rather than around the side which is clearly far from the case in typical multistory buildings which limits the applicability of the study. A two-dimensional slice of room air flow (as used in this study and shown in Figure 3.2) means that a number of assumptions have been made including:

- The open window area is constant over the whole of the building facade;
- The end walls parallel to the flow direction through the room have little effect of the flow;

- The effect of wind direction cannot be examined;
- It does not allow the investigation of the effect of internal geometry such as partitions and office furniture.

In fact the huge number of factors that effect room air flow make it impossible to study them all parametrically. Although, our requirement to produce a generalised zonal model mean these limitations are not important.

The choice to decouple the internal environment from the external environment, modelling the internal environment only, means that many parameters cannot be examined, for example:

- Building geometry;
- Wind direction;
- External environment.

These factors, along with many others, are comprehensibly covered by the work of many wind tunnel studies (Ernest 1991). However, wind tunnel studies ignore the thermal environment further supporting the decision to concentrate on the room air flow effected by buoyancy forces. This being the case, the zonal model must rely on the many studies examining pressure fields around buildings to link the CFD boundary conditions to the weather data set used.

The overall external pressure field around the building may be affected by the presence of openings in the structure. This means that pressure data taken around sealed models may differ significantly to pressure levels when there are openings to the air flow. However, studies that have addressed this issue have shown that the use of pressures measured on sealed models lead to errors of less than 10 % for predicted flow rates (Aynsley 1988). This means that the zonal model can be coupled to the research of others on pressure distributions around buildings, even though the CFD predictions are driven by the total pressure at the inflow boundary rather than the static pressure as measured by sealed model testing. Results will be sufficiently accurate as long as wall porosities remain below 25 %. The design implications of a limitation on porosity are not that great as most buildings are within this limit.

A number of studies have raised questions on the ability of wall functions to predict heat transfer at wall surfaces (Yuan 1995; Chen and Jiang 1992; Yuan et al. 1993). Even so, it was decided that the standard high-Reynolds k-ε model with wall functions would be used for this study as it is the most widely used and validated model. Converged solutions are also easier to obtain with the standard model than the low-Reynolds k-ε model.

In summary it was concluded that:

- CFD simulations were needed where room air flow is effected by buoyancy forces as well as window opening pressure differences.
- Computation time required will be reduced by:
  - The use of two-dimensional simulations;
  - Modelling the internal environment only.
- The zonal model can use the large number of studies of external pressure distributions (i.e., those obtained on sealed wind tunnel models) to link results from the CFD simulations with the weather data sets used.
- The CFD simulations will use the standard high-Reynolds k-ε turbulence model with wall functions.

3.4 Modelling Method

The approach to the numerical modelling has been to:

- Identify a simple room geometry that may be used in night-time cross-flow ventilation. It can be seen from buildings such as the Powergen building in Coventry that high level openings can be used to promote night-time air flow next to a thermally massive ceiling slab. A two-dimensional slice through such a room was modelled due to the time needed to solve flow driven by buoyancy. The geometry used is discussed in Section 3.4.1.
- A steady state parametric study was performed to see how air flow and heat transport are affected by the boundary conditions of a simulation, see Section 3.4.6. The boundary conditions of particular interest are those used as zonal model inputs, the pressure difference between room openings, and the temperature difference between the inflow air and the ceiling. Zonal model parameters determined from the steady state study were as follows:
  - Convective heat transfer at surfaces corresponding to a zonal model surface node;
  - Flow regime in terms of a detachment position along the ceiling surface.
- A transient parametric study was performed to examine the bulk air flow capacity rates between nodes of the simplified model, see Section 3.4.7.

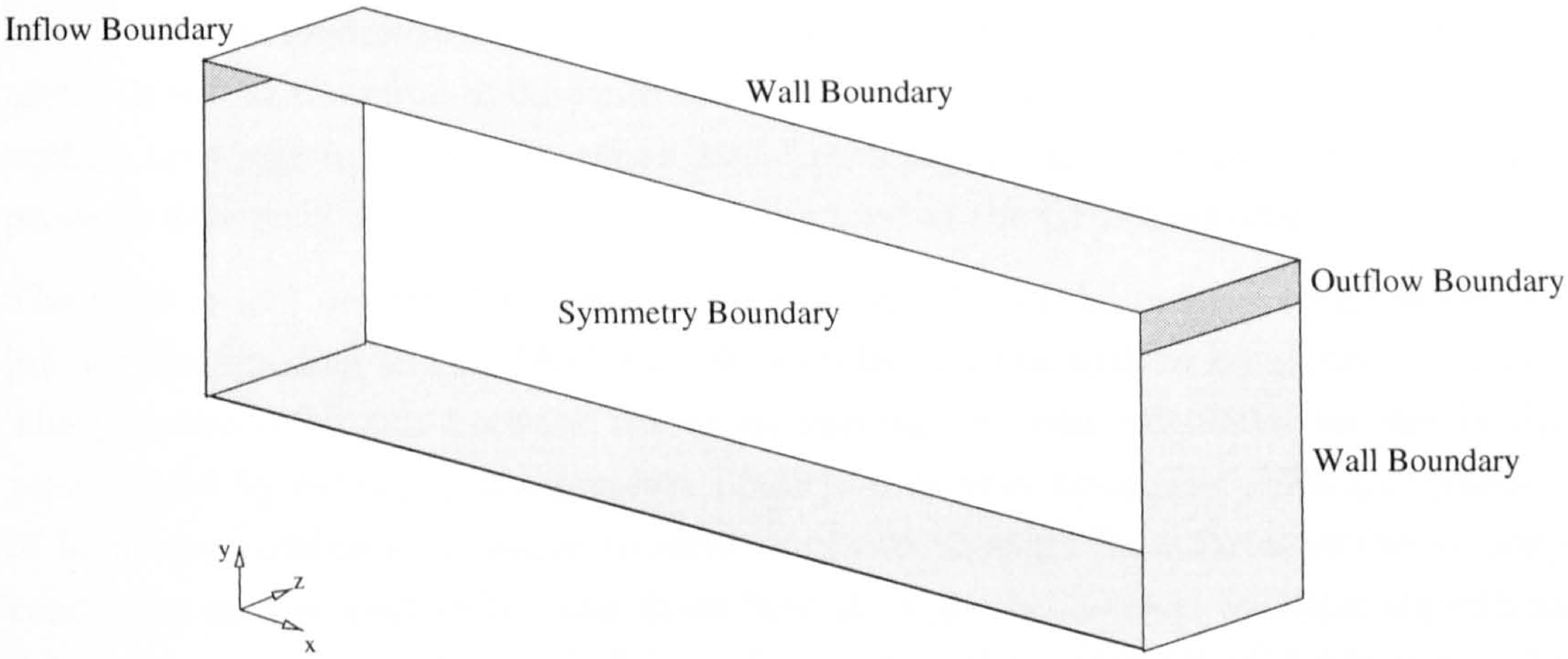

Figure 3.2: A schematic diagram of the CFD model of cross flow ventilation.

3.4.1 Geometry

The CFD model used in this study is a two-dimensional section through a room designed with night-time cross-flow ventilation in mind with a high level opening along the whole of the room facade. The geometry used in the study was a room 12 m wide and 3 m high with inflow and outflow openings of 0.3 m in height. Figure 3.2 shows a schematic diagram of the CFD model used in the parametric study. Even though the study uses a two-dimensional simulation, in the CFD software used (CFX 1997b) two-dimensional problems are treated the same as three-dimensional but with only one cell depth in the third (z) direction. Hence, the geometry shown in Figure 3.2 is a representation of the geometry as specified in the pre-processing stage of the CFD modelling where the mesh is created. In the figure, different boundary types are distinguished by the darkness of the shading used. The flow boundaries are depicted using the darkest shading while the wall boundaries have a lighter shading. In a two dimensional simulation, a symmetry boundary is set by the software on the cell faces on the z plane (the symmetry boundaries are unshaded in Figure 3.2).

3.4.2 Boundary Conditions

It is the boundary conditions that determine the nature of the solution to the velocity and temperature field. The treatment of boundary conditions in the parametric study is addressed below.

Flow Boundaries Used in Study

Pressure boundaries seem readily applicable to naturally ventilated buildings as there is a lot of data from the literature on pressure distributions across the external wall surfaces of buildings. The pressure difference across room openings is also a boundary condition used in air flow models to calculate flow through a building (Feustel and Rayner-Hooson 1992). It would therefore make sense to use pressure boundaries at both the inflow and outflow openings in order that zonal model parameters can be related directly to the pressure difference between the room opening used in the CFD simulation.

The CFD model described in this chapter uses an *INLET* boundary condition for the inflow room opening and a *MASS FLOW* boundary for the outflow boundary condition. The pressure difference between the room openings is then calculated for use in the zonal model by averaging the pressure prediction at each boundary. This combination of boundary conditions is easier to solve than two pressure boundaries as the velocity conditions at the inlet define the mass flow through the domain and the algorithms enforce the condition of mass balance. Even when the intermediate fields inside the calculation domain are poorly converged, the calculations are strongly driven in the direction of the correct mass flow as specified at the inlet boundary. Pressure boundary conditions, on the other hand, leave the mass flow rate floating because, in a converged solution, the mass flow rate will bring any fluid kinetic energy rise and frictional energy losses in balance with the work done by the pressure forces. The friction depends on the velocity field so the mass flow rate through the domain is usually incorrect until the entire simulation has converged. Although the code will still enforce a mass balance, the mass flux through the inflow boundary will change as the calculation proceeds. This tends to result in the solution taking longer to converge.

It is difficult to specify values for the turbulence quantities. In most rooms turbulent intensity, i, could be expected to be in the range 0.01–0.3 (Rees 1998). The flow is not, in fact, sensitive to the value of turbulence intensity at the inlet and was set at 0.05 in the work reported. The turbulent kinetic energy, k_{in}, can be obtained using the relationship,

$$k_{in} = 1.5(iu_{in}) \tag{3.57}$$

where u_{in} is the mean inlet velocity. A value of ε at the inlet was then estimated from:

$$\varepsilon_{in} = \frac{k_{in}^{3/2}}{0.3D} \tag{3.58}$$

where D is the hydraulic diameter of the inlet:

$$D = 4\frac{A}{P} \tag{3.59}$$

where A is the area of the inflow opening, and P is the perimeter of the inlet.

Room Surfaces

The parametric study uses a wall boundary with a prescribed temperature which is constant along its length for the ceiling. The floor and wall surfaces are modelled as adiabatic, their temperatures are calculated by the code and depend on the radiative flux from other surfaces and the convective flux into the air. The reason for choosing to set the ceiling temperature, while leaving the other surface temperatures to 'float', was the assumption that in the night-time naturally ventilated buildings of interest in this study it is the temperature of the thermally massive ceiling that dominates the performance of the system and not the other surfaces, which are assumed to have a smaller thermal mass.

The ceiling, floor and wall surfaces are modelled using the no-slip condition where the components of velocity are set to zero at the wall boundary. Variables such as velocity and temperature vary rapidly at wall boundaries. Resolving the gradients of variables near walls would require extremely fine grids in these regions which is prohibitive with respect to computing time. For this reason, a logarithmic wall function is employed here to allow coarser grids near wall surfaces. Wall functions are used to define the wall boundary conditions with the first cell centroid placed some significant distance from the wall, see Section 3.2.6.

Radiative Heat Transfer

It is possible to specify how the transmission medium interacts with the radiation by specifying an absorption coefficient and a scattering coefficient. These coefficients are low for atmospheric air (assuming low humidity), and can be ignored for rooms of office size; they were set to zero for all simulations in the work reported. To complete the specification of a radiation calculation, it is also necessary to specify the emissivity of walls and flow boundaries, and the specular roughness of walls. To reduce computational time the emissivity of both the walls and the flow boundaries was set to 1. This meant that all the radiation falling on a surface was absorbed and the radiation calculation did not need to track reflected photons. This also meant that specular roughness was unimportant, it was set to zero. A more realistic value for the emissivity of the wall surfaces would be 0.95. The error in setting emissivity to a value of 1 is small, and was checked by a simulation with a wall emissivity of 0.95 and a wall roughness of 0.5.

3.4.3 Computational Grid

A number of grids were used for the parametric study. At higher air velocities it was possible to use finer meshing near the wall boundaries while keeping the y^+ values greater than 30. In all grids used, the meshing near to the flow boundaries was finer than that used in the lower portion of the room. The mesh was also finer near the vertical wall surfaces in comparison to the middle of the room. Figure 3.3 shows the computation grid used for most of the cases in the parametric study (6000 cells), a coarser grid (5400 cells) was used for low inlet velocity cases ($\leq 0.25\,\mathrm{ms}^{-1}$). At inlet velocities below $0.25\,\mathrm{ms}^{-1}$ it

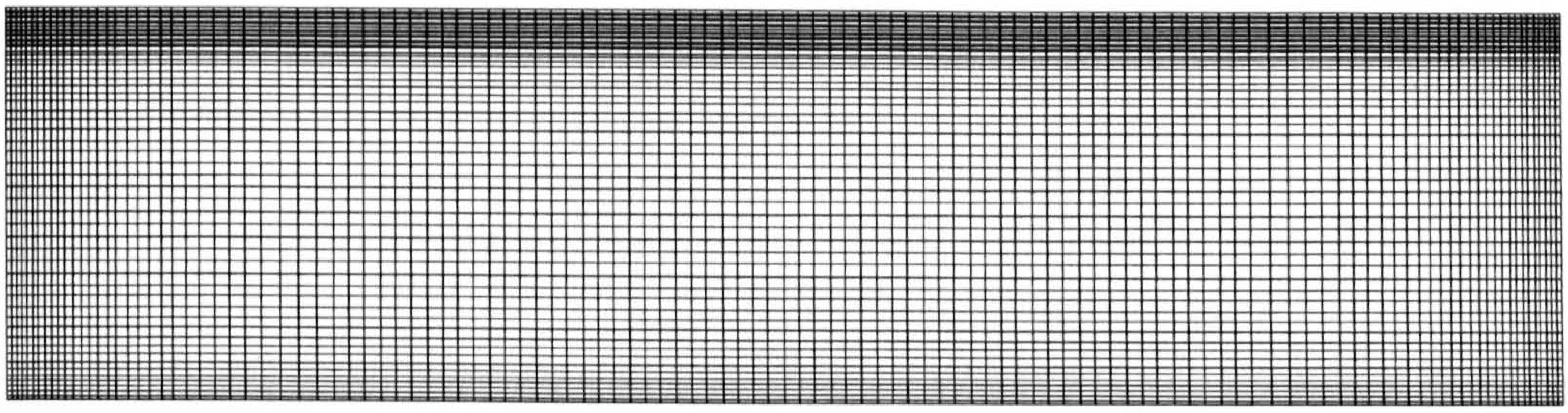

Figure 3.3: The main computational grid used for the parametric study (6000 cells).

Table 3.2: Physical properties of the fluid modelled.

Property	Value
Density (kg/m^3)	1.217
C_p (J/kg-K)	1004
Laminar Viscosity (kg/m-s)	1.802e-5
Thermal Expansion Coefficient (1/K)	3.408e-3
Thermal Conductivity (W/m-K)	0.02555
Absorption coefficient (1/m)	0

is impossible to produce a mesh that has a y^+ value greater than 30 with enough cells to resolve the flow, this is further addressed in the results section 3.5.5.

3.4.4 Physical Properties

The physical properties of air were set at their values for 291 K and 101.3 kPa, see Table 3.2.

3.4.5 Buoyancy Induced Instability

Air flows in naturally ventilated buildings are strongly affected by buoyancy. In a wind driven cross-flow ventilated room, as the temperature difference between the inflow air and the room air increases, or the pressure difference between the flow openings decreases, the effect of buoyancy on the air flow increases. When high level openings are used to promote air flow along the ceiling, the buoyancy force can cause the air flow to detach from the ceiling and fall to the floor.

When modelling buoyant flows, the momentum equation in the direction of gravity includes the body force resulting from buoyancy. Numerical problems arise as the energy equation becomes coupled to the momentum equations through the body force term. Sequential solution of the equations can then lead to numerical instabilities under certain circumstances. The rate of convergence of the solution is much slower when buoyancy is solved due to the fact that the momentum and energy solutions are coupled. McGuirk and Whittle (1991) comment on the convergence problems associated with buoyancy driven room air flows. One possible solution to the buoyancy induced instability problem is to seek a simultaneous solution of the momentum and energy equations. When the governing equations are solved sequentially there are three approaches to dealing with the buoyancy induced instability problem (in order of increasing effectiveness and computational cost):

1. Strong under-relaxation;
2. False time stepping;

Table 3.3: Cases modelled in the parametric study to investigate the effect of inlet velocity and the temperature difference between the inflow air and the ceiling.

Case	Inlet Velocity (ms^{-1})	Temperature Difference $T_{ceil} - T_{air}$ (K)
1-8	0.1	0, 2, 4, 6, 8, 10, 12, 15
9-16	0.25	0, 2, 4, 6, 8, 10, 12, 15
17-24	5	0, 2, 4, 6, 8, 10, 12, 15
25-32	0.75	0, 2, 4, 6, 8, 10, 12, 15
33-40	1	0, 2, 4, 6, 8, 10, 12, 15
41-48	1.5	0, 2, 4, 6, 8, 10, 12, 15
49-56	2	0, 2, 4, 6, 8, 10, 12, 15
57	5	0

3. Full transient solution.

Jones (1995) reports that for commonly used fully implicit numerical schemes it is necessary to restrict the time step, Δt, for buoyancy driven flows in order to resolve time scales of the order of the Brunt-Väisälä frequency, a natural frequency of oscillations of strongly stratified flows,

$$\Delta t < \left(\sqrt{g\beta\frac{\partial T_{n+1}}{\partial y}}\right)^{-1}. \tag{3.60}$$

All the CFD problems in the parametric study, except those where the inflow air and the ceiling are at the same temperature and heat transfer and buoyancy are not solved, use false time stepping. Time steps of 0.1 s were used for the momentum equations, as well as for k and ε, while a time step of 0.2 s was used for enthalpy. Under relaxation was not used on the variables for which false time stepping was used. Default under-relaxation was used on all other variables (CFX 1997b). Substituting the time step used for the enthalpy variable into Equation 3.60 shows that temperature gradients of up to approximately 750 K/m can be solved. The temperature gradients seen in the steady state parametric study outlined in Section 3.4.6 are well within this figure.

3.4.6 The steady state parametric study

Table 3.3 shows the simulations run in the parametric study. The emphasis of the parametric study was the investigation of the effect of two parameters:

1. The pressure difference between room openings. The actual inflow boundary used has a prescribed velocity rather than pressure (the pressure difference between openings increases with inflow velocity). The reason for setting velocity rather than pressure was discussed in Section 3.4.2.

2. The temperature difference between the inflow air and the ceiling.

3.4.7 Transient CFD model

This section describes how CFD was used to determine the the bulk air flow (capacity rate) parameters of the zonal model. The capacity rate is defined as

$$\rho \dot{v} c_p, \tag{3.61}$$

where ρ is the density of air (kg.m^{-3}), $\dot{v}$ is the volumetric flow rate between nodes (m^3.s^{-1}), c_p is the specific heat of air (J.kg^{-1}.K^{-1}). The capacity rates between nodes inside the main flow stream is known

$$\rho \dot{v}_{in} c_p, \tag{3.62}$$

where $\dot{v}_{in}$ is the volumetric flow rate through the inflow opening. The capacity rates between the nodes of the main flow stream and the two recirculating region nodes are an unknown parameter of the zonal model. CFD was used to determine the unknown mass flow rates so that the capacity rate parameters could be calculated.

There are two volumetric flow rates associated with each main flow stream zone, one to the lower recirculating region, $\dot{v}_{l,n}$, and one to the upper recirculating region, $\dot{v}_{u,n}$. $\dot{v}_{l,n}$ and $\dot{v}_{u,n}$ cannot be simply inferred from the results of a steady state CFD solution where the standard variables of velocity and temperature etc. are recorded. This is due to the fact that mass flow across the boundary between a recirculating region and each of the main flow stream zones is caused by mixing due to turbulent eddies rather than one way bulk air movement. If the later was the case, the air velocity normal to the boundary could be integrated along the length of the boundary to determine the mass flow. A CFD experiment was designed to calculate $\dot{v}_{l,n}$ and $\dot{v}_{u,n}$ which relies on the fact that contaminant dispersal in the room will depend on the entrainment from the recirculating region or regions into the main flow stream.

Contaminant dispersal was modelled using the scalar transport equations of the CFD software (CFX 1997b). An extra scalar was included in the simulation with a diffusivity set to a value equal to that of nitrogen in air. This value was chosen so that the properties of the contaminant were as close to those of air as possible. In (CFX 1997b) diffusivity is set using the quantity

$$\Gamma = \rho D \tag{3.63}$$

where ρ is the density of the carrier fluid (kg.m^{-3}), and D is the diffusivity ($m^2 s^{-1}$).

A transient solution method was employed to model the contaminant dispersal. The contaminant concentration at the first time step was set to zero throughout the computational domain. The contaminant was introduced at the inlet boundary at a constant rate by setting the scalar concentration across the boundary to a positive value. The time period modelled allowed the scalar to spread throughout the domain but left a large enough difference in concentration between the MFS zones and the recirculating zone(s) for a difference to be calculated. 140 time steps were used with smaller time steps close to the end of the simulation where the scalar concentration was used to calculate the mass flows between zonal model zones. This numerical technique is similar to how a tracer gas experiment could be used to determine mass transfer around the room, although the level of detail obtained numerically would not be practical to obtain experimentally.

A transient CFD simulation involving air flow, heat transfer, buoyancy and radiation is computationally demanding and unnecessary in this case. It is possible to obtain a steady state solution with a particular set of boundary conditions and then to use the output of this run as the starting point for the transient simulation. The flow regime is solved in the steady state simulation and it is possible to 'switch off' the hydrodynamic equation solver thereby 'locking' the flow in place for the transient simulations. The scalar dispersal is caused by the mixing of air of different concentration strengths and has nothing to do with the physical process of heat transfer, buoyancy or radiation (except through their affect on air flow regime), it is therefore possible to 'switch off' these solvers as well.

Calculating Mass Flow Between Nodes

The mass flow between the recirculating zone(s) and the main flow stream (MFS) zones is determined by examining the scalar concentration over three time steps in each of the control volumes used in the zonal model. The control volumes can be determined if the boundaries of the main flow stream are known, see Section 3.5.2.

After the MFS boundaries have been determined the mass flows can be calculated using equations for the scalar concentration change in each of the zonal model control volumes. In the following derivation of $\dot{v}_{l,n}$ the assumption that the MFS remains attached to the ceiling is made to simplify the explanation (i.e. $\dot{v}_{u,n} = 0$).

$$\begin{aligned} \text{contaminant change} &= \text{contaminant in} - \text{contaminant out} \\ V_n \frac{d\bar{c}_n}{dt} &= (\bar{c}_{w,n}\dot{v}_{in} + \bar{c}_l \dot{v}_{l,n}) - (\bar{c}_{e,n}\dot{v}_{in} + \bar{c}_n \dot{v}_{l,n}), \end{aligned} \tag{3.64}$$

rearranging for $\dot{v}_{l,n}$ gives

$$\dot{v}_{l,n} = \frac{\dot{v}_{in}(\bar{c}_{w,n} - \bar{c}_{e,n}) - V_n \frac{dC_n}{dt}}{\bar{c}_n - \bar{c}_l}, \tag{3.65}$$

where:

V_n	is the volume of MFS zone n (m^3);
$\bar{c}_n$	mean scalar concentration in MFS zone n ($kg\,m^{-3}$);
t	time (s);

$\bar{c}_l$	mean scalar concentration over the lower recirculating region ($kg\,m^{-3}$);
$\bar{c}_{w,n}$	mean scalar concentration over the west face cells of zone n ($kg\,m^{-3}$);
$\bar{c}_{e,n}$	mean scalar concentration over the east face cells of zone n ($kg\,m^{-3}$).

If a MFS zone that shares a border with the upper recirculating region rather than the lower region (i.e. after the flow detaches) Equation 3.65 can be altered to calculate $\dot{v}_{u,n}$ rather than $\dot{v}_{l,n}$ by replacing $\bar{c}_l$ with $\bar{c}_u$, the scalar concentration averaged over the upper recirculating region,

$$\dot{v}_{u,n} = \frac{\dot{v}_{in}(\bar{c}_{w,n} - \bar{c}_{e,n}) - V_n \frac{d\bar{c}_n}{dt}}{\bar{c}_n - \bar{c}_u}. \tag{3.66}$$

In Figure 3.11 zone 1 shares a border with the lower recirculating region while zones 3, 4 and 5 share a border with the upper recirculating region. Zone 2 however, shares a border with two recirculating regions. There is a mass flow between the MFS zone 2 and the lower recirculating region, $\dot{v}_{l,n}$, and from MFS zone 2 to the upper recirculating region, $\dot{v}_{u,n}$. Equations 3.68 and 3.69 are employed to solve the two unknown mass flows $\dot{v}_{l,n}$ and $\dot{v}_{u,n}$. Equation 3.68 is a scalar mass balance for zone n:

$$\begin{aligned} V_n \frac{dC_n}{dt} &= (\bar{c}_{w,n}\dot{v}_{in} + \bar{c}_l\dot{v}_{l,n} + \bar{c}_u\dot{v}_{u,n}) - (\bar{c}_{e,n}\dot{v}_{in} + \bar{c}_n\dot{v}_{l,n} + \bar{c}_n\dot{v}_{u,n}), \qquad (3.67) \\ &= \dot{v}_{in}(\bar{c}_{w,n} - \bar{c}_{e,n}) + \dot{v}_{l,n}(\bar{c}_l - \bar{c}_n) + \dot{v}_{u,n}(\bar{c}_u - \bar{c}_n), \qquad (3.68) \end{aligned}$$

where $\bar{c}_l$ is the mean scalar concentration in the lower recirculating region ($kg\,m^{-3}$), and $\bar{c}_u$ is the mean scalar concentration in the upper recirculating region ($kg\,m^{-3}$).

Equation 3.69 on the other hand represents the scalar decay in the lower recirculating region.

$$V_l \frac{d\bar{c}_l}{dt} = \sum_{i=1}^{n} \dot{v}_{l,i}(\bar{c}_i - \bar{c}_l), \tag{3.69}$$

where V_l volume of the lower recirculating region (m^3).

Rearranging Equation 3.69 gives the mass flow between the lower recirculating region and the MFS zone n:

$$\dot{v}_{l,n} = \frac{\sum_{i=1}^{n-1} \dot{v}_{l,i}(\bar{c}_i - \bar{c}_l) - V_l \frac{d\bar{c}_l}{dt}}{\bar{c}_l - \bar{c}_n}, \tag{3.70}$$

which can be substituted into Equation 3.68 to determine $\dot{v}_{u,n}$.

3.5 Results and Discussion

The results of the numerical calculations of air flow and heat transfer in cross-flow ventilated rooms are presented in this section. The 24 zonal model convective heat transfer parameters were found using the two-dimensional steady-state CFD parametric study.

The 26 bulk air convection capacity rates were then calculated from the transient scalar dispersal study. The results are presented in the following order:

- In Section 3.5.1 the pressure difference calculations between room openings are presented. An empirical relationship between inlet/outlet pressure difference and inlet velocity was derived that allows the zonal model to be linked with the many studies on wind-generated surface pressure distributions (Equation 3.77).
- Section 3.5.2 describes the velocity field and flow detachment position. A relationship between Archimedes number and the MFS detachment position is found. Five flow regimes are identified:

    1. Flow falls to floor on entry to room;
    2. Flow detaches in MFS zone 2;
    3. Flow detaches in MFS zone 3;
    4. Flow detaches in MFS zone 4;
    5. Flow remains attached to the ceiling through its path through the room.

- Section 3.5.3 discusses the heat transfer at room surfaces. A convective heat transfer coefficient is then derived for each of the 24 air-surface connections for each of the five flow regimes listed above.
- In Section 3.5.4 the mass flow between zonal model control volumes is determined. The zonal model capacity rates parameters are then derived for flow regimes 1–5.
- Section 3.5.5 then discusses the validity of the results with respect to the values of y^+ seen in the parametric study.

3.5.1 Pressure Difference Between Room Openings

We need to determine the static pressure difference between the inflow and outflow openings, ΔP_{io}, so that the zonal model can be linked to the many experimental studies on pressure distributions across the external walls of buildings, for example the wind tunnel experiments of Ernest (1991). The predicted static pressure difference, ΔP_{io}, will depend on the inlet velocity boundary condition, v_{in}, used in the CFD parametric study. Determining a correlation between ΔP_{io} and v_{in} will allow the zonal model to link studies that give pressure difference to the CFD study that uses inlet velocity.

To calculate the pressure difference between the room openings the static pressure was averaged along the cells at the inflow and outflow boundaries, and the difference taken. Figure 3.4 shows how pressure difference increases with inlet velocity for the iso-thermal cases. The temperature difference between the inflow air and the ceiling also affects the predicted pressure difference. Changes in pressure difference due to temperature

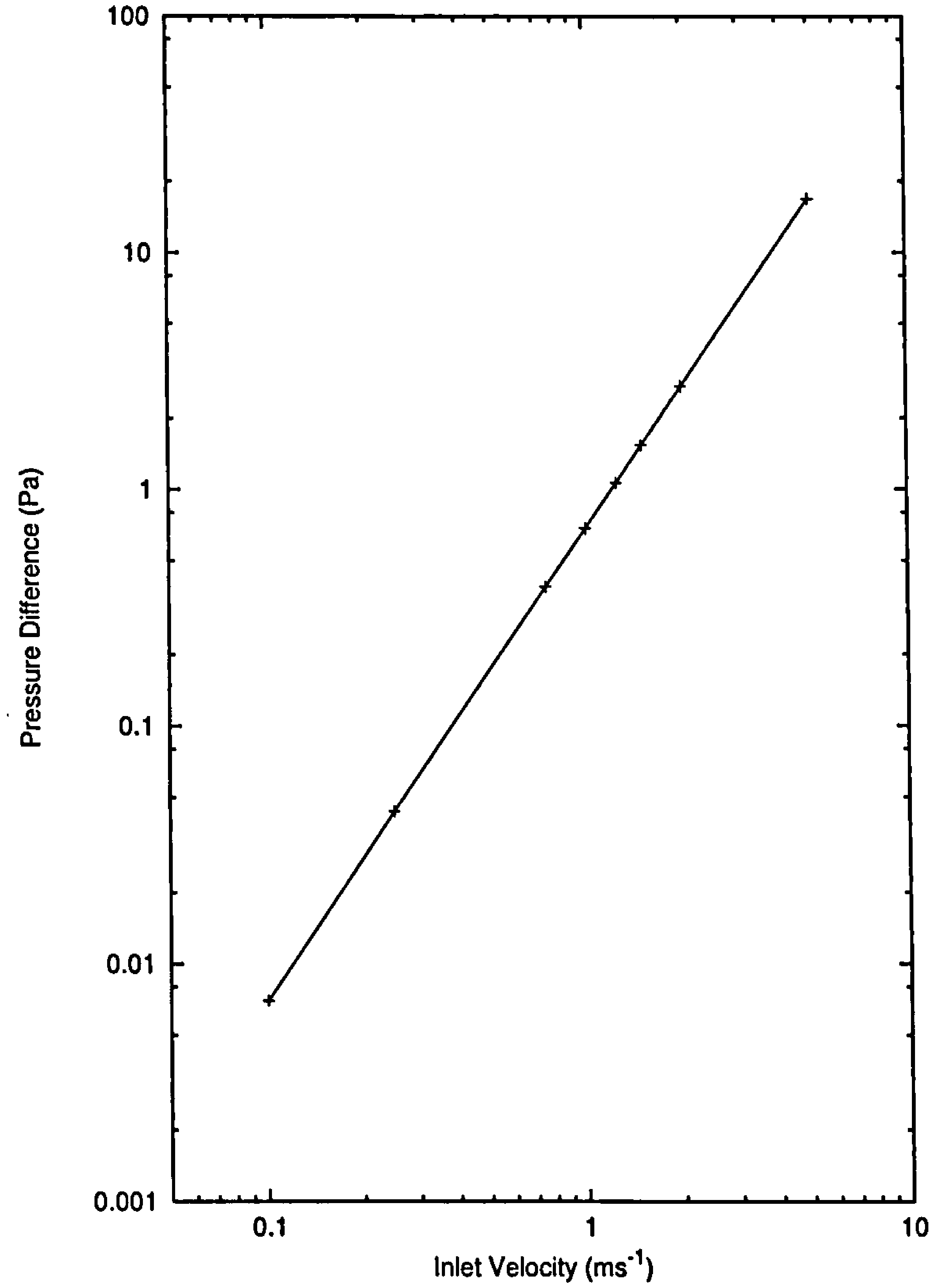

Figure 3.4: Pressure difference between the inlet and outlet openings versus inlet velocity for a 0 K temperature difference between inlet air and ceiling surface.

Table 3.4: The pressure difference coefficients for a variety of temperature differences.

Temperature Difference (K)	$\lvert C_{pi} - C_{po} \rvert$	uncertainty (±)
0	1.3478	0.0012
2	1.384	0.008
4	1.358	0.01
6	1.404	0.014
8	1.412	0.016
10	1.416	0.018
12	1.426	0.018
15	1.44	0.02

difference are small in comparison to changes due to inlet velocity. For example, when the temperature difference is 0 K and inlet velocity is increased from 1 ms^{-1} to 2 ms^{-1} the pressure difference between flow boundaries increases by 296 %. On the other hand, when the inlet velocity is 2 ms^{-1} and the temperature difference is increased from 0 K to 10 K the pressure difference is increased by 3 %. While the main flow stream remains attached to the ceiling, pressure difference increases with temperature difference. If the main flow stream detaches from the ceiling, the pressure difference decreases as the detachment point moves towards the inlet.

Equation 3.71 can be used for calculating the pressure difference between the room openings, ΔP_{io}, predicted by the CFD with respect to the velocity set at the inflow boundary

$$\Delta P_{io} = 0.5 \lvert C_{pi} - C_{po} \rvert \rho_{air} v_{in}^2, \tag{3.71}$$

where v_{in} is the inlet velocity, ρ_{air} is the density of air, and $\lvert C_{pi} - C_{po} \rvert$ is the inlet/outlet pressure difference coefficient and is a function of temperature difference between the inlet air and the ceiling surface.

Table 3.4 gives values for $\lvert C_{pi} - C_{po} \rvert$ for a number of temperature differences. The table shows that the value of $\lvert C_{pi} - C_{po} \rvert$ increases slightly with temperature difference. The uncertainty in $\lvert C_{pi} - C_{po} \rvert$ also increases with temperature difference. $\lvert C_{pi} - C_{po} \rvert$ is plotted against temperature difference in Figure 3.5. $\lvert C_{pi} - C_{po} \rvert$ and the uncertainty in $\lvert C_{pi} - C_{po} \rvert$ were found by least squares fitting. A third order equation has been fitted to $\lvert C_{pi} - C_{po} \rvert$ with respect to ΔT_{ci}

$$\lvert C_{pi} - C_{po} \rvert = a\Delta T_{ci}^3 + b\Delta T_{ci}^2 + c\Delta T_{ci} + d, \tag{3.72}$$

where the coefficients to Equation 3.72 are,

$$a = 0.0001 \tag{3.73}$$
$$b = -0.0016 \tag{3.74}$$
$$c = 0.0169 \tag{3.75}$$

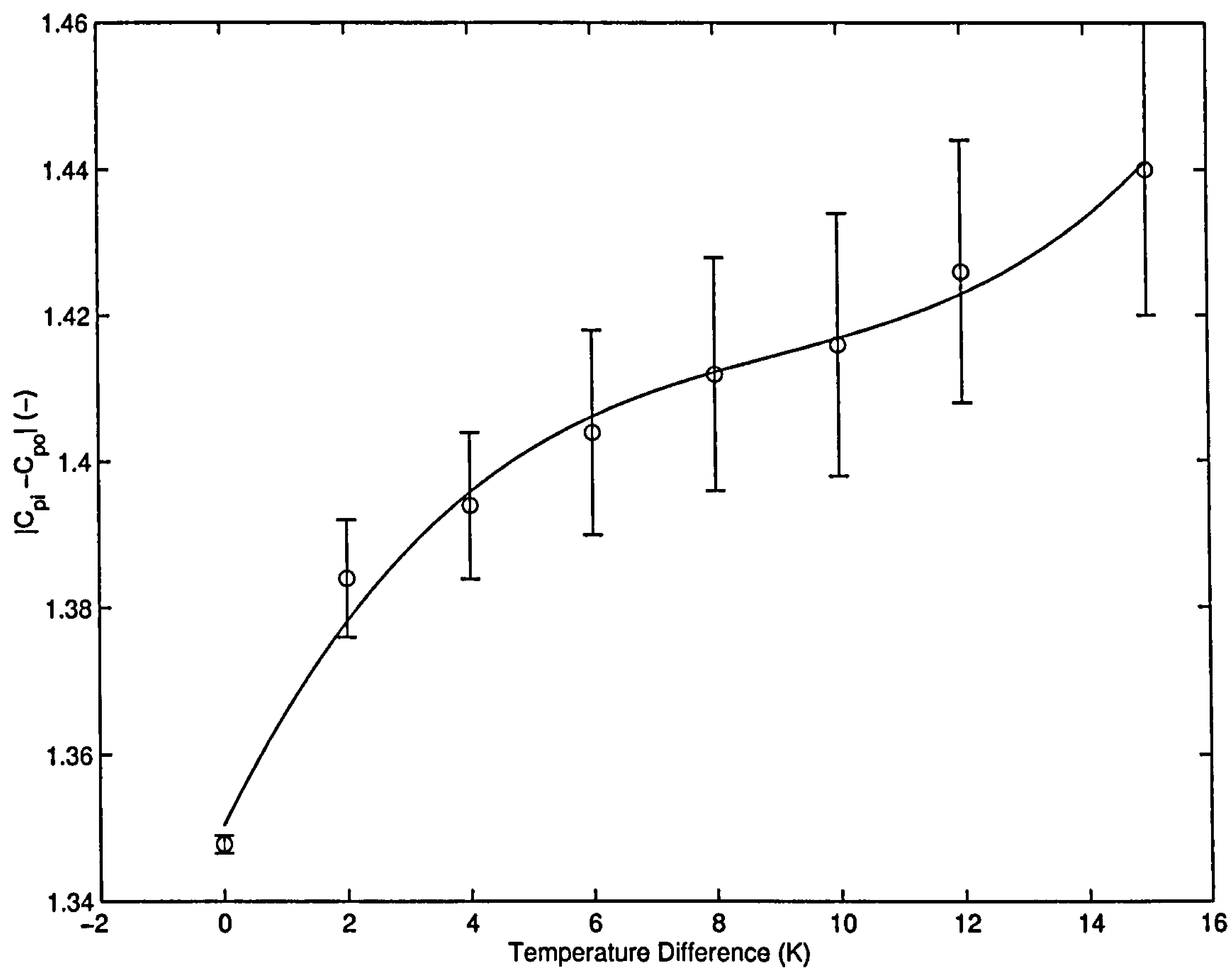

Figure 3.5: k versus the temperature difference between the inlet air and the ceiling surface.

$$d = 1.3504 \tag{3.76}$$

The correlation coefficient for Equation 3.72 is 0.9946.

Zonal Model Inlet Velocity Calculation

The pressure difference between the room openings can be determined using empirical correlations from other research on external pressure coefficients, i.e., (Ernest 1991), and the wind data from the weather set used. If the CFD study is to be used to set the other parameters of the model a way has to be found to convert the known pressure difference between the flow openings, ΔP_{io}, into a corresponding inlet velocity, v_{in}, the boundary condition used in the CFD model. Inlet velocity can be found from the pressure difference using the equation,

$$v_{in} = \sqrt{\frac{\Delta P_{io}}{0.5(0.0001\Delta T_{ci}^3 - 0.0016\Delta T_{ci}^2 + 0.0169\Delta T_{ci} + 1.3504)\rho_{air}}}. \tag{3.77}$$

3.5.2 Velocity Field and Flow Detachment

This section deals with flow detachment position and the boundaries of the control volumes for use within the zonal model.

The Main Flow Stream

The predicted velocity field can be seen in a number of vector plots, Figures 3.6–3.10. These figures have the main flow stream path superimposed on top of the vector plots.

The main flow stream (MFS) is defined as having the same horizontal mass flow, $\dot{m}$, throughout its path through the room—equal to the mass flow through the inlet, $\dot{m}_{in}$. As our CFD and zonal models are two dimensional $\dot{m}$ is actually a mass flow per unit length of the room facade.

The main flow stream boundaries can be found using the horizontal mass flow at vertical cross sections through the room. As a vertical section through a recirculating region has a total horizontal mass flow of zero, and the total horizontal mass flow through the MFS is $\dot{m}_{in}$, the mass flow for each vertical cross section through the room equals the mass flow through the flow boundaries, $\dot{m}_{in}$.

$$\dot{m} = \rho \int_{y_{floor}}^{y_{ceiling}} u(y)dy = \dot{m}_{in}, \tag{3.78}$$

where:

$y_{ceiling}$ is the y position of ceiling;

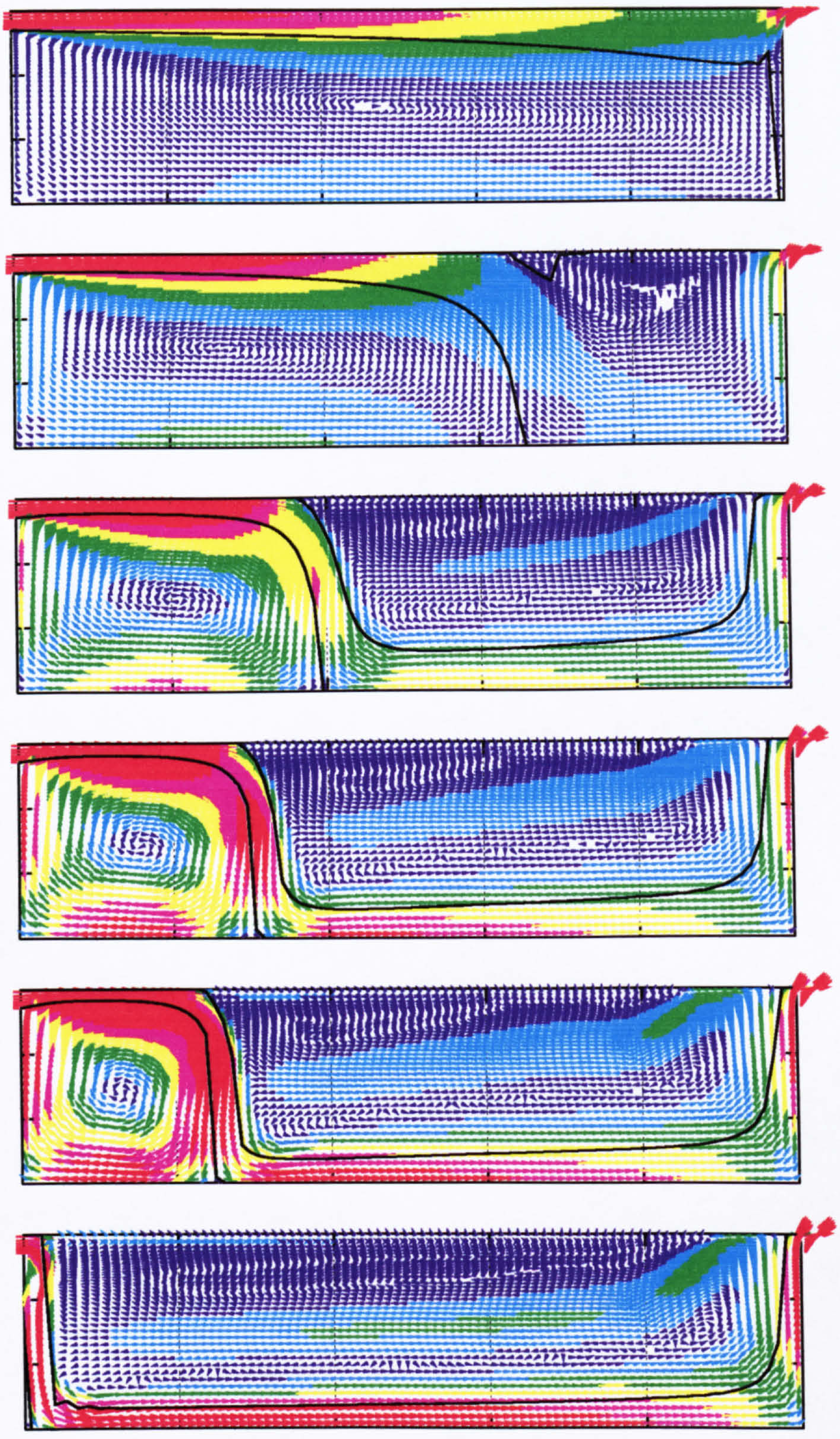

Figure 3.6: Vector plots for an inlet velocity of $0.25\,\mathrm{ms}^{-1}$ with the main flow stream path superimposed. The temperature differences between the inflow air and the ceiling are: 0 K (top); 2 K(second); 4 K(third); 6 K(fourth); 8 K(fifth); 10 K(bottom).

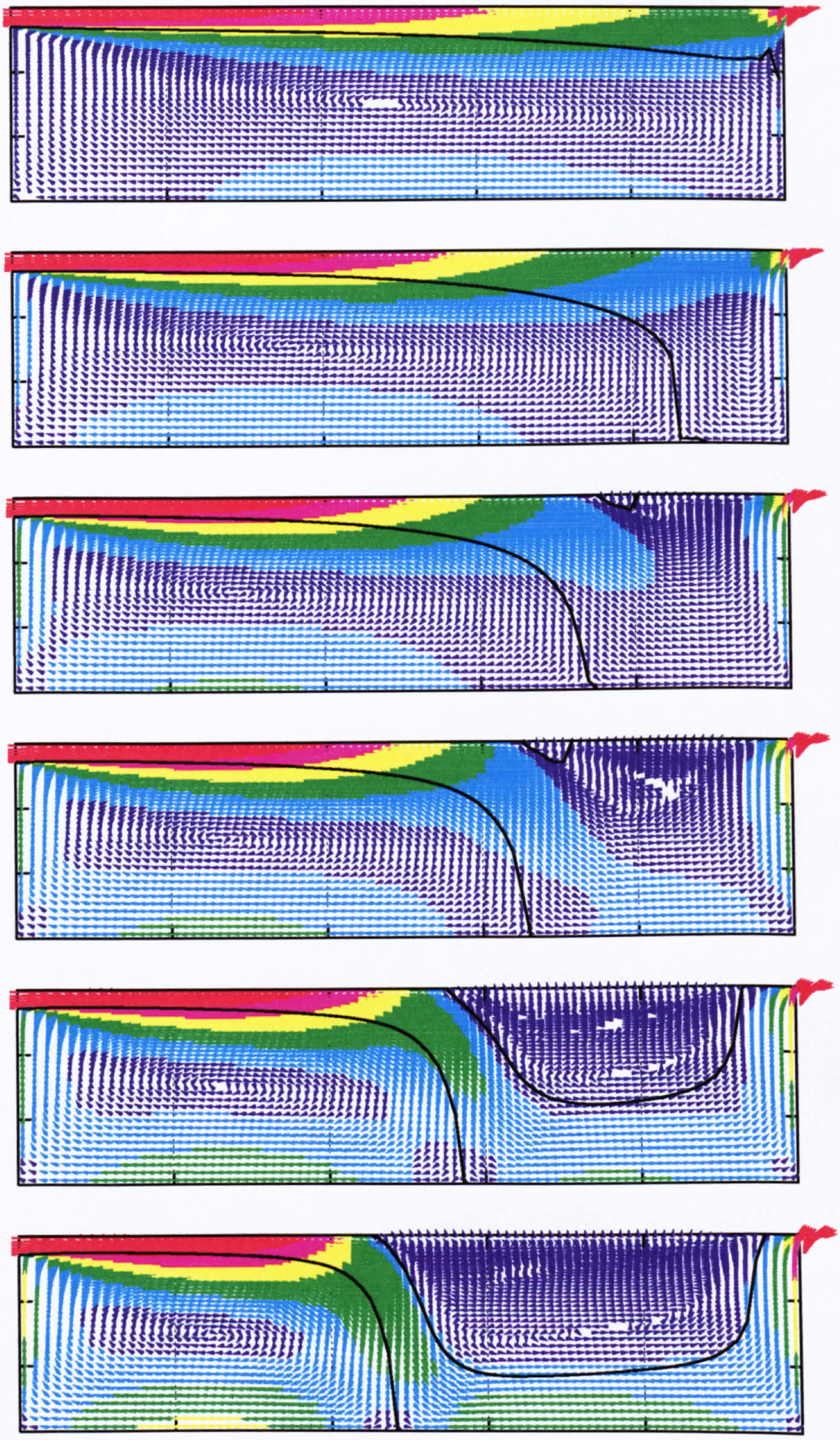

Figure 3.7: Vector plots for an inlet velocity of $0.5\,\mathrm{ms}^{-1}$ with the main flow stream path superimposed. The temperature differences between the inflow air and the ceiling are: 0 K (top); 4 K(second); 8 K(third); 10 K(fourth); 12 K(fifth); 15 K(bottom).

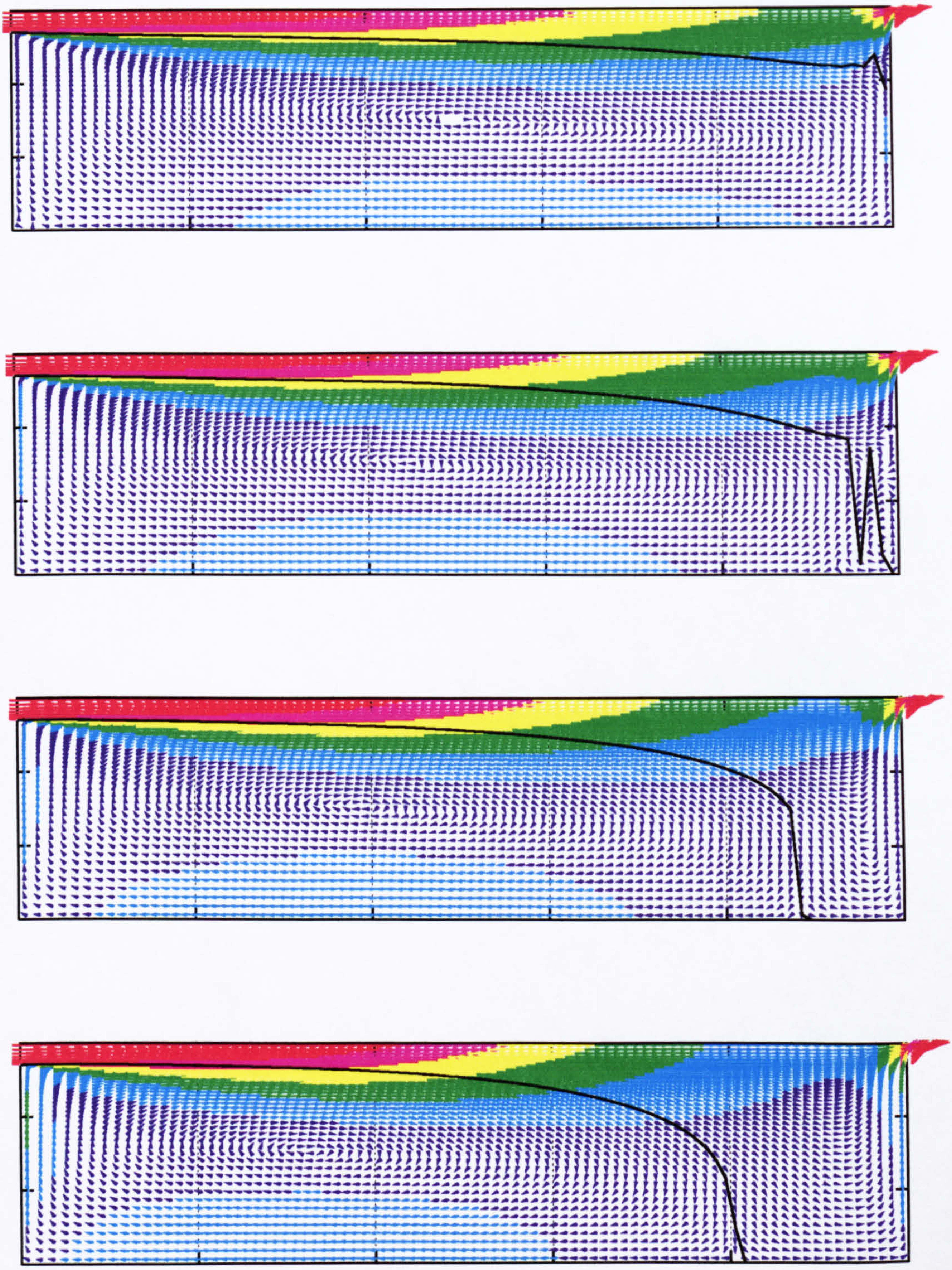

Figure 3.8: Vector plots for an inlet velocity of $0.75\,\mathrm{ms}^{-1}$ with the main flow stream path superimposed. The temperature differences between the inflow air and the ceiling are: 0 K (top); 4 K(second); 8 K(third); 15 K(bottom).

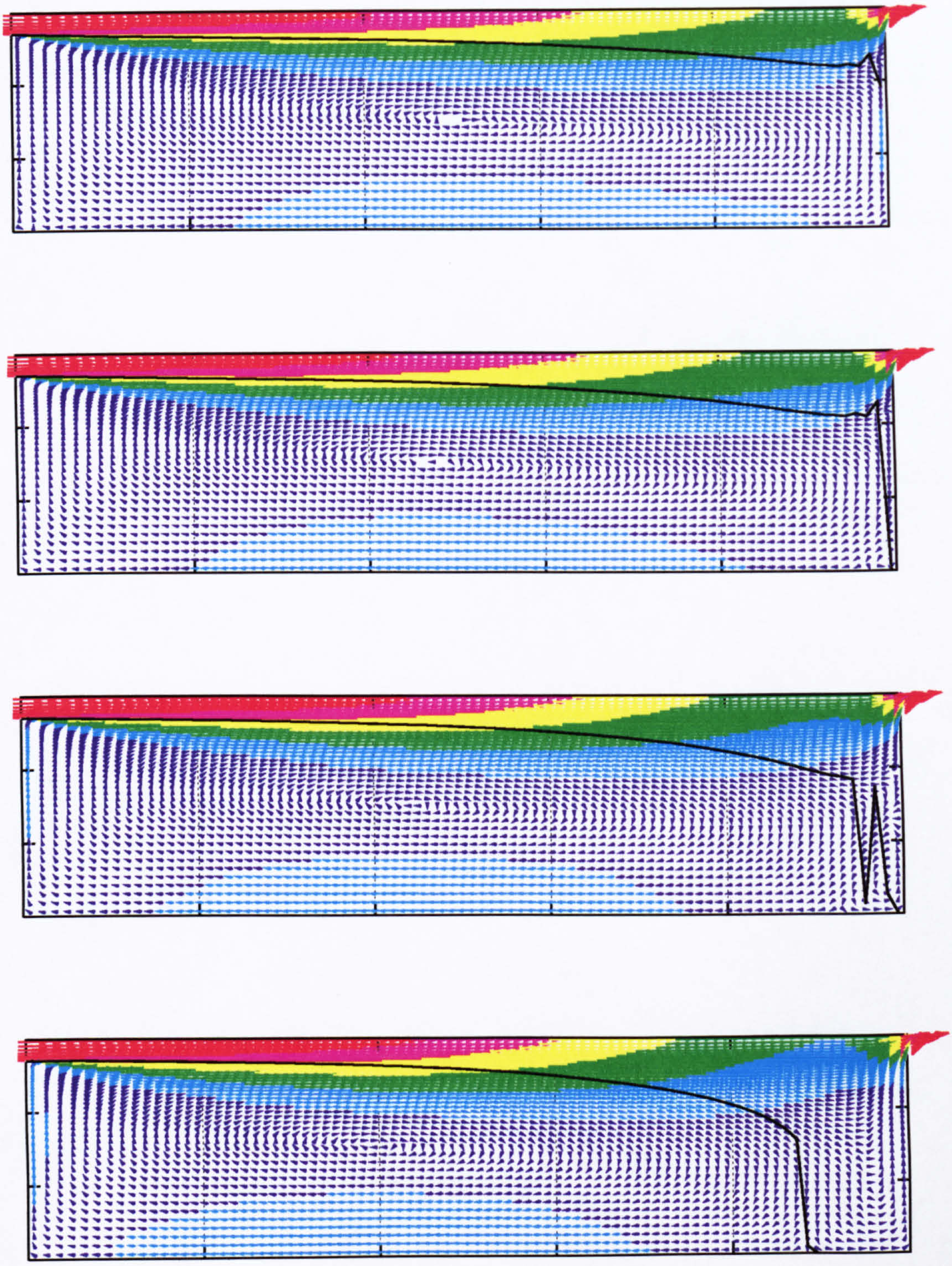

Figure 3.9: Vector plots for an inlet velocity of $1.0\,\mathrm{ms}^{-1}$ with the main flow stream path superimposed. The temperature differences between the inflow air and the ceiling are: 0 K (top); 4 K(second); 8 K(third); 15 K(bottom).

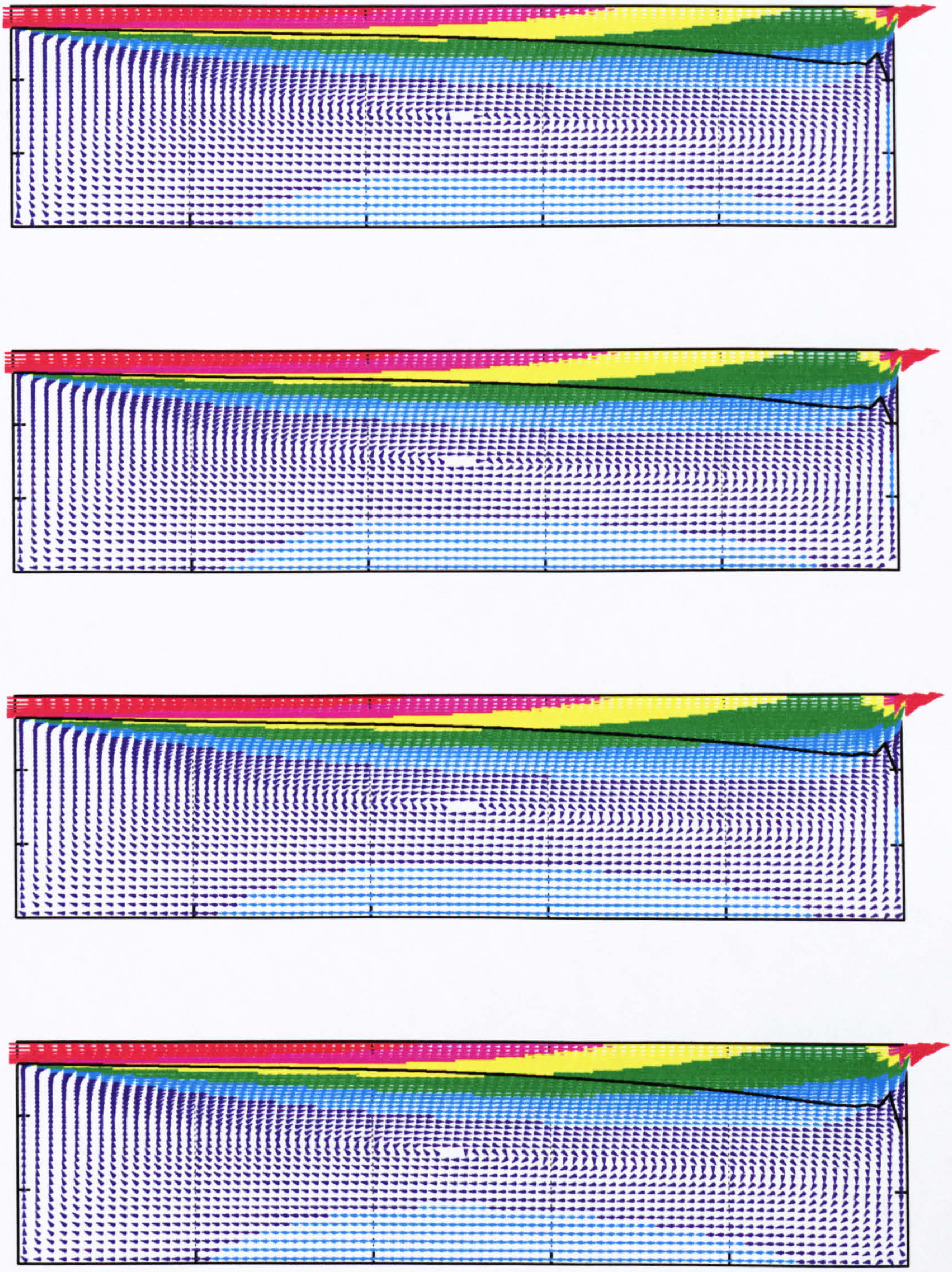

Figure 3.10: Vector plots for an inlet velocity of $2.0\,\mathrm{ms}^{-1}$ with the main flow stream path superimposed. The temperature differences between the inflow air and the ceiling are: 0 K (top); 4 K(second); 8 K(third); 15 K(bottom).

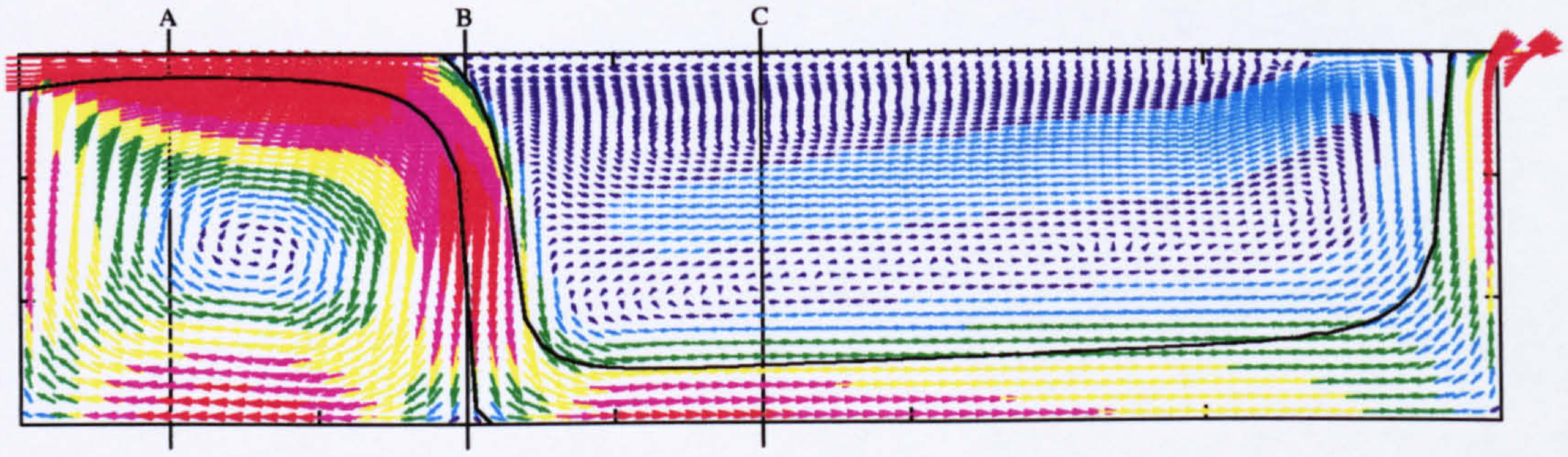

Figure 3.11: A main flow stream path that detaches from the ceiling.

y_{floor}	is the y position of floor;
u	is the horizontal component of air velocity;
ρ	is the density of air.

Figure 3.11 shows a MFS that detaches from the ceiling part way along its path through the room. Figure 3.12 shows the horizontal mass flow integrated from $y_{ceiling}$ to $y = 0$ along three slices through the room (A, B and C) shown in Figure 3.11.

A is a vertical section through the room where the main flow stream is attached to the ceiling.

B is a section where the main flow stream is neither attached to the ceiling nor the floor.

C is a section through the room where the main flow stream is attached to the floor.

In Figure 3.12 the boundaries of the main flow stream at each section are marked: the upper boundary with a cross; and the lower boundary with a square.

As shown in Figure 3.10, in the high velocity and low temperature difference cases, the main flow stream grows slowly in vertical size as it progresses across the room. At high velocities and high temperature differences, the main flow stream may widen to

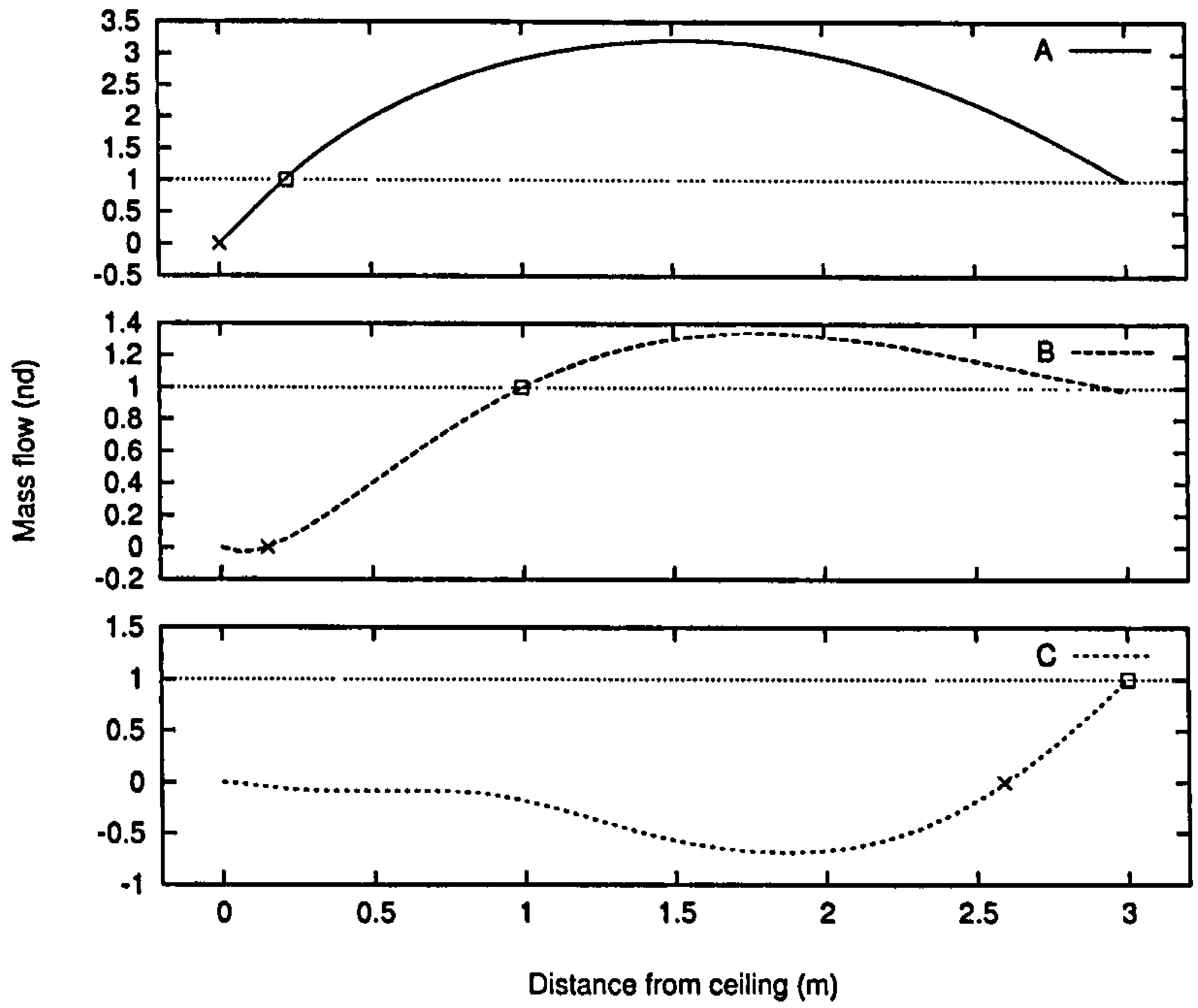

Figure 3.12: Cumulative horizontal mass flow along sections A, B and C. Mass flow is plotted in dimensionless form, i.e. $\frac{\dot{m}}{\dot{m}_{in}}$.

the height of the room close to the outflow boundary, see Figure 3.9 (bottom). In these cases, the flow next to the east wall is upwards rather than downwards and the edge of the recirculating region is moved towards the west wall. In these cases, there is one recirculating region in the bottom part of the room. When the flow detaches from the ceiling two recirculating regions exist, as shown in Figure 3.6 (third, fourth and fifth). The first recirculating region, next to the floor, is close to the inflow boundary. The second, which shares a boundary with the ceiling, is close to the outflow boundary. At low velocities and high temperature differences the main flow stream may travel down the west wall, along the floor, and up the far wall, see Figure 3.6 (bottom). Again there is one recirculating region, this time against the ceiling.

Detachment Position

The flow fields can be split into five distinct cases:

1. The main flow stream immediately detaches from the ceiling and falls to the floor upon entry to the room. This can occur when the inlet velocity is low ($\leq 0.25\,\text{ms}^{-1}$) and the temperature differnece between inlet flow and the room is sufficiently large.
2. The main flow stream detaches in MFS zone 2. This occurs at inlet velocities $\leq 0.5\,\text{ms}^{-1}$ when the temperature difference between in the inflow air and the ceiling is large enough for the buoyancy forces to overcome the pressure forces caused by the Coanda effect.

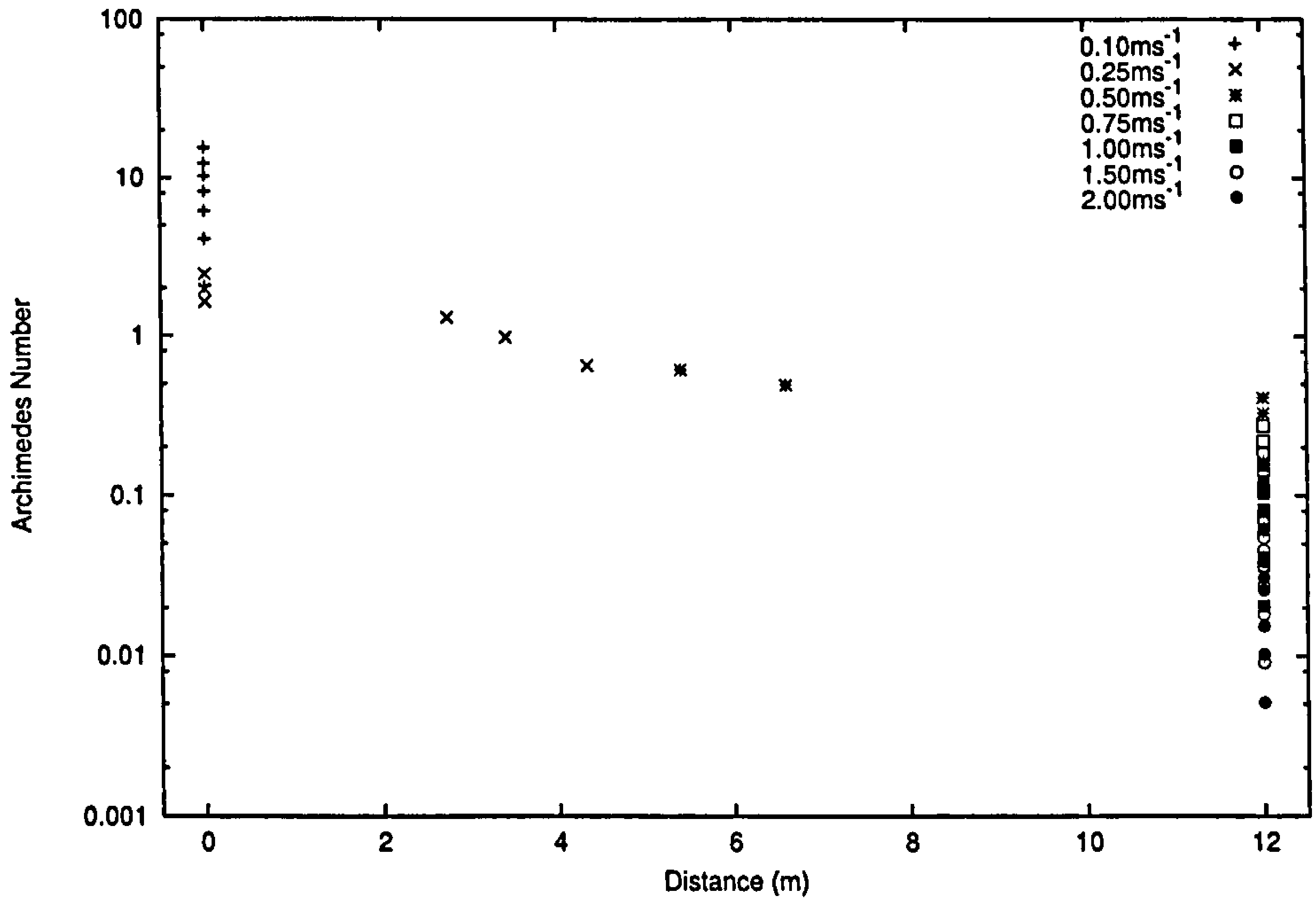

Figure 3.13: Distance from inflow boundary that detachment occurs plotted against Archimedes number.

3. Flow detaches in MFS zone 3;
4. Flow detaches in MFS zone 4;
5. The main flow stream remains attached to the ceiling throughout its path through the room. This occurs at high inlet velocities, greater than $0.75\,\mathrm{ms}^{-1}$, at all thermal boundary conditions used in this work[3]. It also occurs at lower inlet velocities when the temperature difference between the inflow air and the ceiling is not large enough for the buoyancy forces to overcome the pressure forces caused by the Coanda effect that acts across the main flow stream which resembles a wall jet.

Archimedes number, the ratio of buoyancy to inertia forces, can be used to determine whether the main flow stream detaches from the ceiling or not. Figure 3.13 plots the MFS detachment point (in meters from the inflow boundary) against Archimedes number, Ar,

$$Ar = \frac{g\beta\Delta Tl}{v^2}, \tag{3.79}$$

where:

g is the gravitational acceleration;

β is the volumetric expansion factor ($= -\frac{1}{\rho}\frac{\partial\rho}{\partial T}$);

---

[3] The ceiling and inflow air temperatures are set at a constant value, the other room surfaces are adiabatic.

ΔT is the characteristic temperature difference;

l is the characteristic dimension;

v is the characteristic velocity.

The values used to calculate Archimedes number were taken from the boundary conditions for each case. The characteristic temperature difference, ΔT, was taken to equal the temperature difference between the inflow air and the ceiling surface, ΔT_{ci}. The inflow opening area per unit length, $\frac{A_{in}}{l}$, was used as the characteristic dimension. The velocity at the inlet boundary, v_{in}, was used as the characteristic velocity. For an ideal gas, the volumetric expansion factor, β, is defined as

$$\beta = \frac{1}{T}, \tag{3.80}$$

where T is a characteristic absolute temperature. The inflow air temperature, T_{in}, was used as the characteristic temperature when calculating the Archimedes number. Thus, the Archimedes number is defined as

$$Ar = \frac{1}{T_{in}} \frac{g \Delta T_{ci}}{v_{in}^2} \frac{A_{in}}{l}. \tag{3.81}$$

At Archimedes number greater than 1.6 the flow does not attach to the ceiling. This is indicated by those points in a vertical line at a distance of zero from the inflow boundary. The main flow stream remains attached to the ceiling throughout its path through the room when the Archimedes number is below 0.42 (those points at 12 metres from the inflow boundary). At Archimedes numbers between 0.42 and 1.6 the main flow stream detaches some where between the inflow and outflow boundary. It can clearly be seen that larger Archimedes number flows detach earlier than flows with smaller Archimedes number.

Zonal Model Flow Regime Calculation

Figure 3.14 shows a first order fit of Archimedes number versus detachment distance from inlet for those cases that detach from the ceiling. Using this fit the Archimedes number range for each of the five flow regimes was calculated—these ranges are given in Table 3.5. Equation 3.81 can be used to calculate Archimedes number and then the flow regime can be looked up from Table 3.5. Once the flow regime is found the convective heat transfer and capacity rate parameters can be determined. The method to calculate the convective heat transfer and capacity rate parameters is discussed later in this chapter.

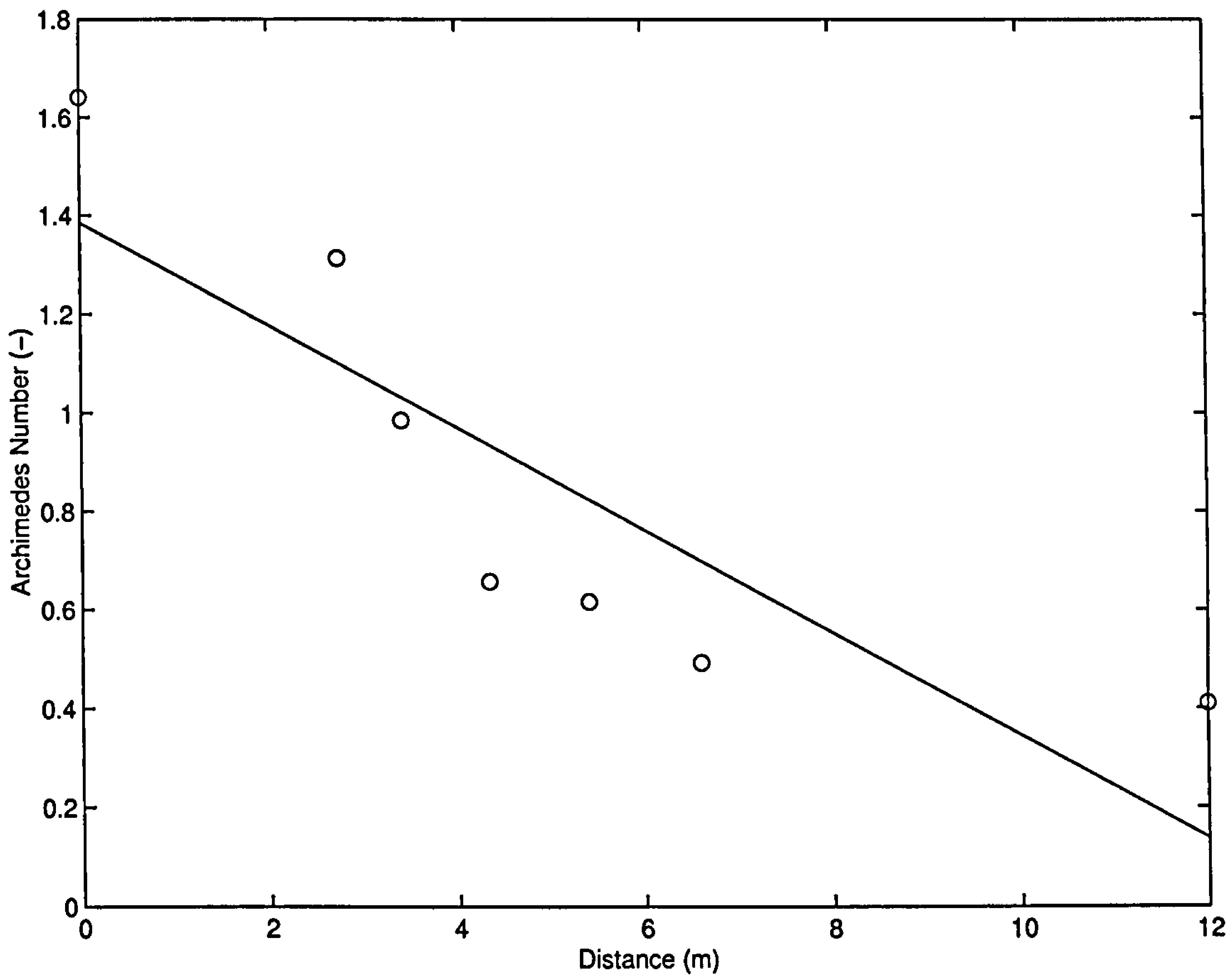

Figure 3.14: A first order fit of Archimedes number versus detachment distance from inlet.

Table 3.5: Detachment position related to Archimedes number (first order fit).

Flow Regime	Description	Relationship
1	flow falls to floor on entry to the room	$Ar > 1.14$
2	flow detaches in zone 2	$0.89 < Ar < 1.14$
3	flow detaches in zone 3	$0.64 < Ar < 0.89$
4	flow detaches in zone 4	$0.39 < Ar < 0.64$
5	flow remains attached to ceiling	$Ar < 0.39$

3.5.3 Convective Heat Transfer Coefficients

This section deals with convective heat transfer coefficients parameters of the zonal model. Net convective heat transfer to each zonal model surface node is calculated along with the temperatures of the control volumes and surface nodes. The convective heat transfer coefficients are then compared to experimentally derived values.

Figure 3.15 shows how the convective heat flux predicted at the room surfaces varies with the temperature difference between the inflow air and the ceiling. The 7 graphs represent inlet velocities from $2\,\mathrm{ms}^{-1}$ (top left) to $0.1\,\mathrm{ms}^{-1}$ (bottom right). As the inlet velocity decreases so does the predicted convective heat transfer.

At high inlet velocities, greater than or equal to $0.75\,\mathrm{ms}^{-1}$, the increase in convective heat transfer rate with respect to temperature difference is close to linear. At these inlet velocities, the main flow stream remains attached to the ceiling. As the main flow stream travels through the room it entrains air and slows down. As the velocity next to the ceiling decreases so does the predicted convective heat transfer rate. The graphs show that the convective heat transfer rate does decrease from C1 to C5 (the position of C1 to C5 are shown in Figure 2.4). Although, the decrease between C4 and C5 is smaller than the decrease between other ceiling nodes because the main flow stream increases in velocity before exiting through the outflow opening. The convective heat transfer rate at the room surfaces that bound the recirculating region, the floor, and the west and east walls, is significantly lower than that predicted at the ceiling for high inlet velocities. The difference between the ceiling prediction and the prediction for the other surfaces increases with inlet velocity.

At low inlet velocities, less than or equal to $0.5\,\mathrm{ms}^{-1}$, the convective heat transfer rate is effected by the detachment of the main flow stream from the ceiling. For an inlet velocity of $0.5\,\mathrm{ms}^{-1}$, the main flow stream detaches at C3 at temperature differences of 12 K and 15 K. This explains the dip in the predicted heat transfer rate at C3, as shown in Figure 3.15 (third left). At an inlet velocity of $0.25\,\mathrm{ms}^{-1}$, the convective heat transfer rate at C1 dips at a temperature difference of 10 K. The dip corresponds to a case where the main flow stream descends to the floor upon entry to the room.

At an inlet velocity of $0.1\,\mathrm{ms}^{-1}$, the convective heat transfer rate at the ceiling is lower than for the other room surfaces. This is due to the fact that the main flow stream descends to the floor upon entry to the room. Therefore, air velocities are lower next to the ceiling in comparison with the other surfaces. C5 has a higher convective heat transfer rate than the other ceiling zones because the main flow stream attaches to the ceiling before exiting through the outflow opening.

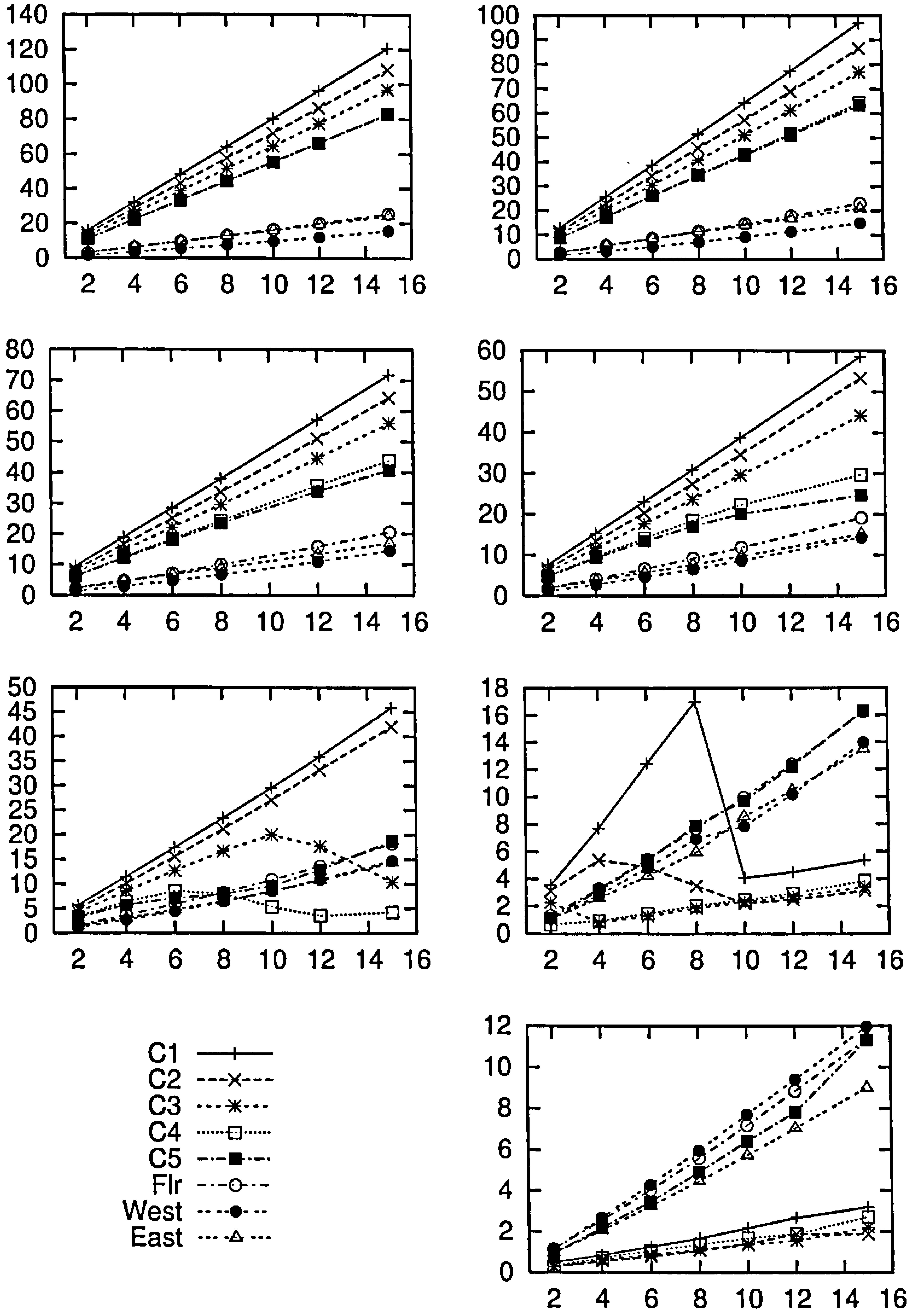

Figure 3.15: The convective heat flux predicted at the room surfaces (y-axis in Wm^{-2}) versus the temperature difference (x-axis in K) between the inflow air and the ceiling for a particular inlet velocity: $2\,ms^{-1}$ (top left); $1.5\,ms^{-1}$ (top right); $1\,ms^{-1}$ (second left); $0.75\,ms^{-1}$ (second right); $0.5\,ms^{-1}$ (third left); $0.25\,ms^{-1}$ (third right); $0.1\,ms^{-1}$ (bottom right).

Convective Heat Transfer Coefficients

The convective heat transfer coefficients at each of the surface nodes of the zonal model were calculated using a convective heat transfer rate per unit area, q_c, a surface temperature, T_s, and an air temperature, T_a,

$$h_c = \frac{q_c}{T_s - T_a}. \tag{3.82}$$

T_s was calculated by averaging the wall temperature prediction over the surface that corresponds to the surface nodes in the zonal model. In the same way, convective flux was averaged to determine q_c. T_a was calculated by averaging the temperature fields over areas of the CFD computational domain that correspond to the zonal model control volumes. For example, when the main flow stream remains attached to the ceiling, the convective heat transfer coefficient at the floor would depend on the temperature of the lower recirculating region, the temperature of the floor and the convective heat flux at the floor. Hence,

$$h_c = \frac{\frac{\sum_{i=s} q_i A_i}{A_{sn}}}{\frac{\sum_{i=s} T_i A_i}{A_{sn}} - \frac{\sum_{i=n} T_i V_i}{V_{an}}}, \tag{3.83}$$

where:

q_i	is the convective heat flux per unit area through CFD cell i;
A_i	is the surface area of CFD cell i;
A_{sn}	is the total surface area corresponding the zonal model node;
T_i	is the temperature in CFD cell i;
V_i	is the volume of CFD cell i;
V_{an}	is the volume of the zonal model air node;
$\sum_{i=s}$	sum over cells corresponding to surface node;
$\sum_{i=n}$	sum over cells corresponding to air node.

In this way CFD allows you to determine convective heat transfer coefficients based on values averaged over the whole of the zonal model control volume. This would be difficult to do experimentally as the density of data obtained via experimental measurement is usually much lower than that obtained from CFD simulations. Hence, convective heat transfer coefficients found experimentally are much more likely to be derived from point measurements.

Figure 3.16 shows how the convective heat transfer coefficients varies with the temperature difference between the inflow air and the ceiling for inlet velocities from

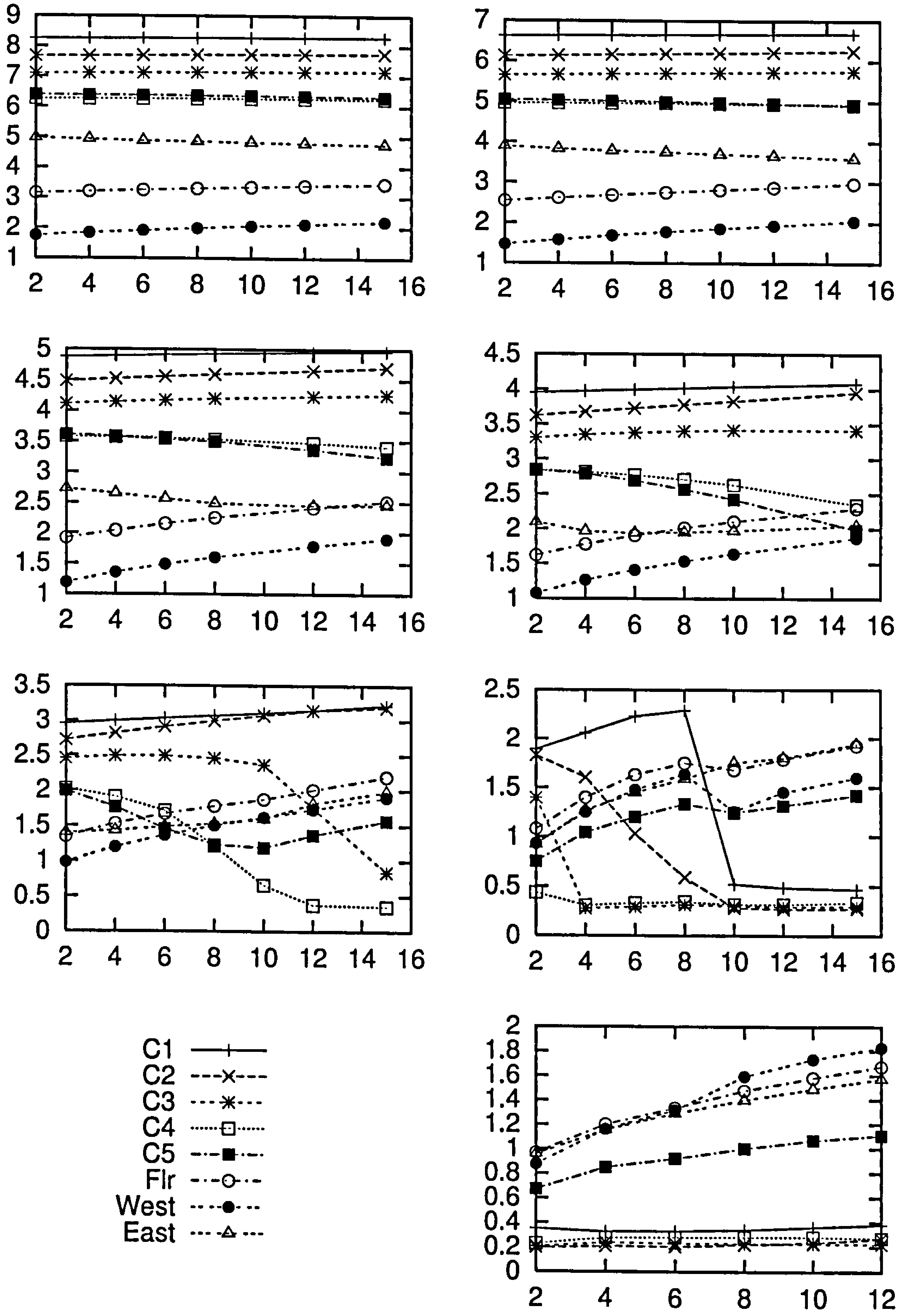

Figure 3.16: The predicted convective heat transfer coefficients at the room surfaces (y-axis in $\mathrm{Wm^{-2}K^{-1}}$) versus the temperature difference between the inflow air and the ceiling (x-axis in K) for a particular inlet velocity: $2\,\mathrm{ms^{-1}}$ (top left); $1.5\,\mathrm{ms^{-1}}$ (top right); $1\,\mathrm{ms^{-1}}$ (second left); $0.75\,\mathrm{ms^{-1}}$ (second right); $0.5\,\mathrm{ms^{-1}}$ (third left); $0.25\,\mathrm{ms^{-1}}$ (third right); $0.1\,\mathrm{ms^{-1}}$ (bottom right).

$0.1\,\mathrm{ms}^{-1}$(bottom right) to $2\,\mathrm{ms}^{-1}$(top left). At high inlet velocities, 1.5 and $2.0\,\mathrm{ms}^{-1}$, the predicted heat transfer coefficients at each surface varies very little with temperature difference. At inlet velocities of 0.75 and $1.0\,\mathrm{ms}^{-1}$, the predicted heat transfer coefficients at C4 and C5 decrease with temperature difference while the floor and west wall surfaces increase. At velocities below $0.75\,\mathrm{ms}^{-1}$, where the main flow stream can detach from the ceiling, the predicted heat transfer coefficients vary more markedly. At $0.1\,\mathrm{ms}^{-1}$, the ceiling surface is next to a recirculating region that has lower air velocities than the main flow stream. Thus, the convective heat transfer rates are lower for the ceiling than for the floor and walls.

The convective heat transfer coefficient parameters for the ceiling nodes are much lower if the flow detaches from the ceiling, see Figure 3.16 (bottom right). In this case the air is thermally stratified with warm air next to the ceiling. The low convective heat transfer coefficient is due to:

1. The low air speeds next to the ceiling. Convective heat transfer coefficients are proportional to local air speed, therefore, low air speed means low convective heat transfer.
2. Thermal stratification means that the average air temperature over the volume that makes up the zonal model node next to the ceiling (the upper recirculating region) is lower than the air directly in contact with the ceiling. Therefore, the low convective heat transfer coefficients in this case are due partly to the modelling decision to represent the recirculating region as one large zone. This may limit the accuracy of the model, particularly in the case of the upper recirculating zone where thermal stratification may be an important factor.

Zonal Model Surface Convective Heat Transfer Parameters

Table 3.6 gives empirical relationships that have been derived for the surface convective heat transfer parameters. These empirical relationships use the inlet velocity found from Equation 3.77 and the detachment position from Table 3.5. Figure 3.17 is a plot of the convective heat transfer coefficient empirical relationships derived from the parametric study for use within the zonal model. The convective heat transfer coefficient empirical relationships in Table 3.6 are given in the form of coefficients of the equation:

$$h_c = av_{in} + b. \tag{3.84}$$

The floor, east and west nodes have a minimum value of $1.5\,\mathrm{W/m^2\text{-}K}$ which should be used if Equation 3.84 predicts a lower value. To convert the convective heat transfer coefficient in Table 3.6 into a zonal model parameter it must be multiplied by the area of the surface that the coefficient applies to.

Table 3.6: Convective heat transfer coefficient empirical relationships for the flow regimes given in Table 3.5.

	Flow Regime 1	Flow Regime 2	Flow Regime 3	Flow Regime 4	Flow Regime 5
C1	a=0.0, b=0.3	a=3.4, b=1.45	a=3.4, b=1.45	a=3.4, b=1.45	a=3.4, b=1.45
C2	a=0.0, b=0.2	a=3.2, b=1.3	a=3.2, b=1.3	a=3.2, b=1.3	a=3.2, b=1.3
C3	a=0.0, b=0.2	a=0.0, b=0.2	a=3.0, b=1.0	a=3.0, b=1.0	a=3.0, b=1.0
C4	a=0.0, b=0.3	a=0.0, b=0.3	a=0.0, b=0.3	a=2.8, b=0.65	a=2.8, b=0.65
C5	a=0.0, b=1.0	a=0.0, b=1.0	a=0.0, b=1.0	a=0.0, b=1.0	a=2.8, b=0.65
flr	a=1.08, b=1.25, min=1.5	a=1.08, b=1.25, min=1.5	a=1.08, b=1.25, min=1.5	a=1.08, b=1.25, min=1.5	a=1.08, b=1.25, min=1.5
east	a=2.4, b=0.2, min=1.5	a=2.4, b=0.2, min=1.5	a=2.4, b=0.2, min=1.5	a=2.4, b=0.2, min=1.5	a=2.4, b=0.2, min=1.5
west	a=0.26, b=1.48, min=1.5	a=0.26, b=1.48, min=1.5	a=0.26, b=1.48, min=1.5	a=0.26, b=1.48, min=1.5	a=0.26, b=1.48, min=1.5

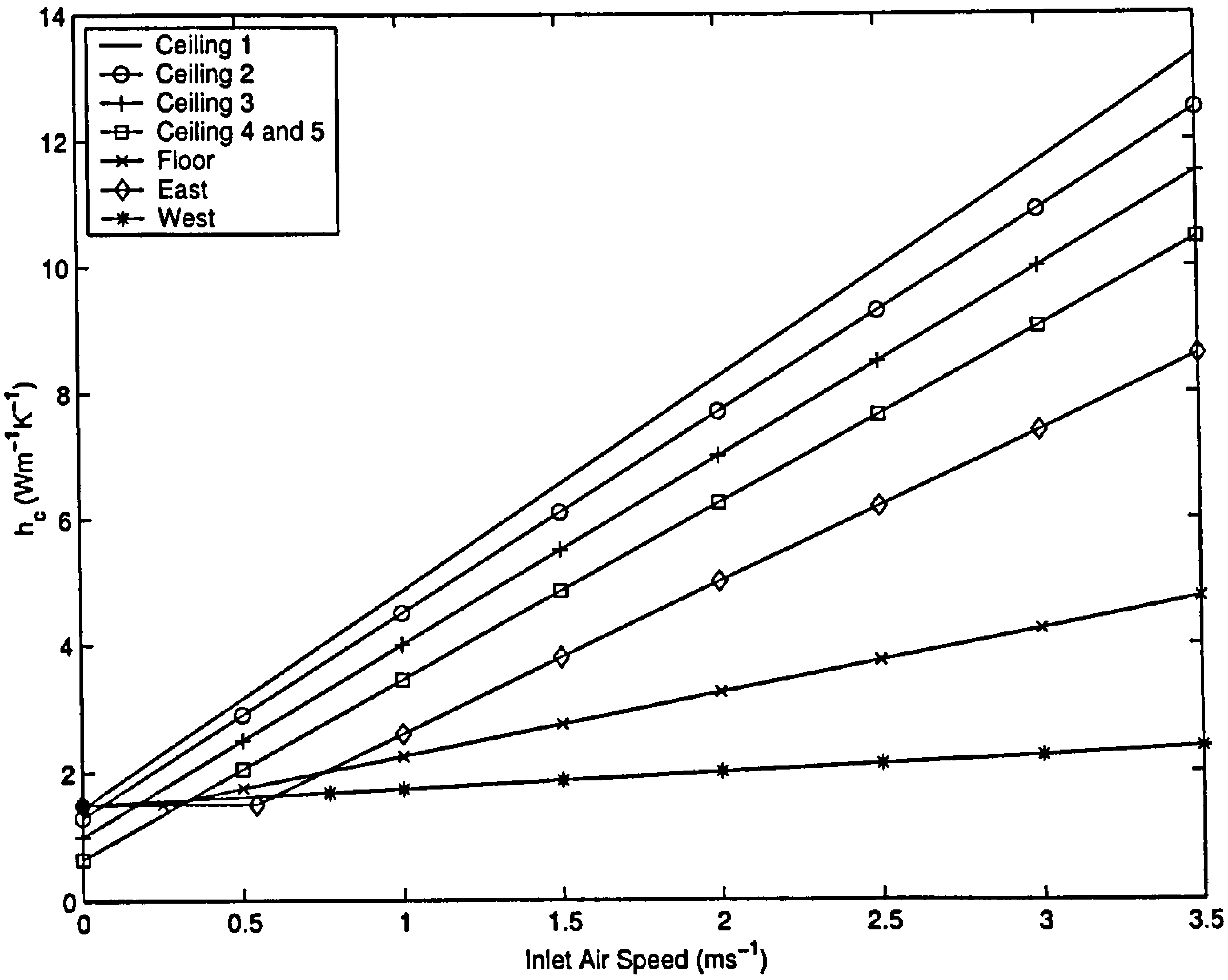

Figure 3.17: The convective heat transfer coefficients taken from the numerical results for the zonal model.

Care must be taken when comparing the heat transfer coefficients derived from the numerical work with those from other studies because of the different methods of determining the reference air temperature, T_a. The detailed field data from the CFD results has allowed T_a to be the area weighted average of the cells that cover the volume that corresponds to the zonal model node in question. Typically, in other research the reference temperature is the average of much fewer measurements. It may also be taken in a different location, i.e., the outflow temperature (Spitler, Perdersen, and Fisher 1991).

If a correlation between local air velocity and convective heat transfer coefficient is required a reference velocity, v_{ref}, must be determined. Studies have differing methods of determining this velocity. Experimentally it is often the nearest velocity measurement that is used. Spitler, Perdersen, and Fisher (1991) use a dimensionless number termed the jet momentum number, J,

$$J = \frac{\dot{V} U_o}{g V_{room}}, \tag{3.85}$$

where:

$\dot{V}$	is the volumetric flow rate ($\mathrm{m^3 s^{-1}}$);
U_o	is the inlet velocity ($\mathrm{ms^{-1}}$);
g	is the acceleration due to gravity ($\mathrm{ms^{-2}}$);
V_{room}	is the room volume ($\mathrm{m^3}$).

In this study the inlet velocity is used as the reference velocity for the correlation between heat transfer coefficient and velocity. Another possible velocity that could have been used would be the average velocity over the volume of the zone in question. This would be easy to determine from the CFD output but was not done as the inlet velocity was considered sufficient and easier to incorporate into the zonal model.

Figure 3.18 shows the ceiling convective heat transfer coefficient empirical relationships compared with data from the literature (only ceiling nodes C1 and C5 are shown for clarity). Comparison data is taken from 4 sources:

1. Spitler, Perdersen, and Fisher (1991);
2. Chandra and Keresteciogl u (1984);
3. Awbi and Hatton (2000);
4. ASHRAE fundamentals (1997).

To compare the coefficients with those of Spitler et al., the jet momentum number, J, used and given in Equation 3.85 has been converted into an inlet velocity for the

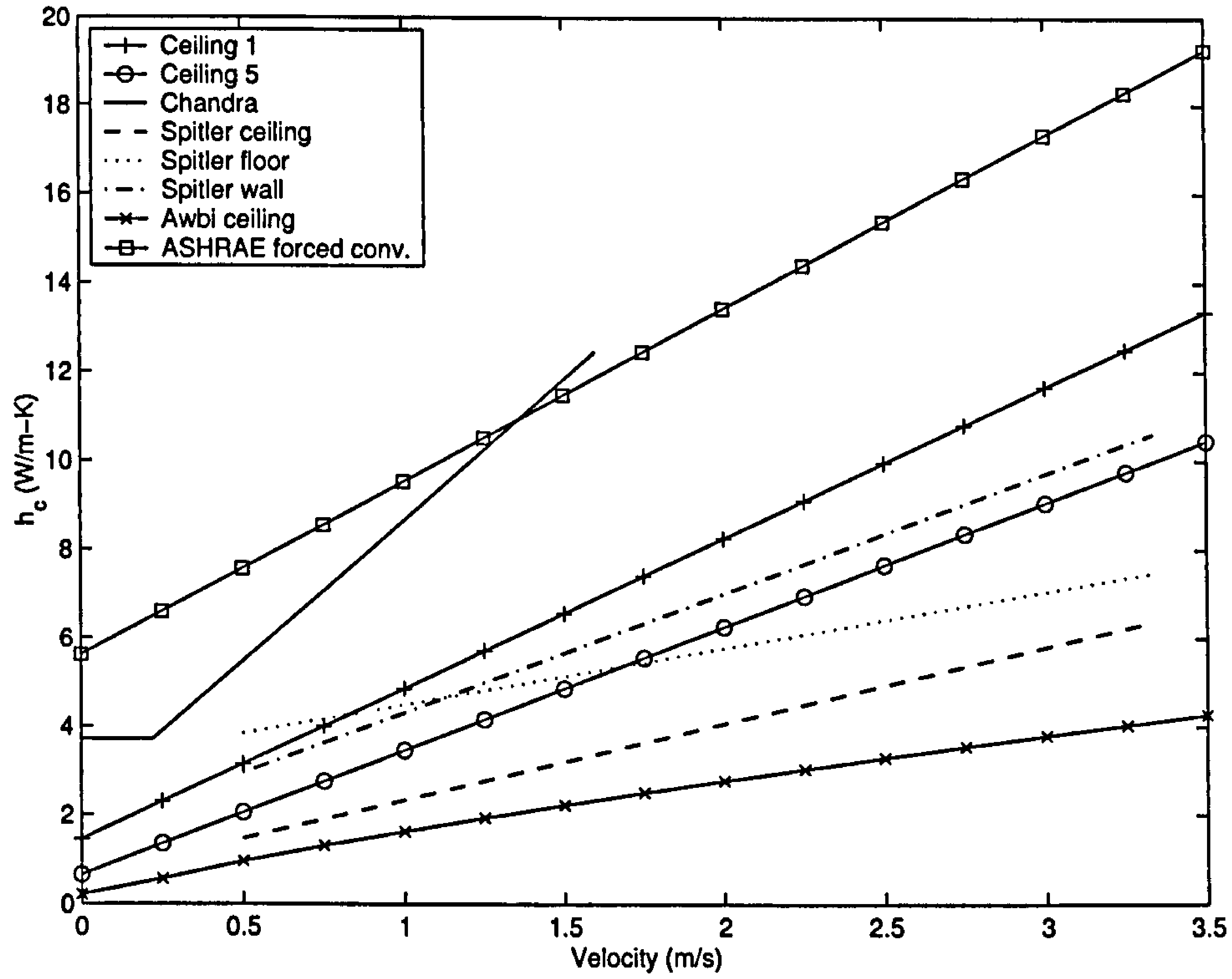

Figure 3.18: The ceiling convective heat transfer coefficient empirical relationships compared with data from the literature.

Table 3.7: Correlations for convective heat transfer coefficient, h_c ($\mathrm{Wm^{-2}K^{-1}}$), (Spitler, Perdersen, and Fisher 1991).

Surface	Correlation	Limits
Ceiling	$h_c = 0.6 + 56.4\,J^{0.5}$	$0.002 < J < 0.011$
Walls	$h_c = 1.6 + 92.7\,J^{0.5}$	$0.002 < J < 0.011$
Floor	$h_c = 3.2 + 44.0\,J^{0.5}$	$0.002 < J < 0.011$

geometry used in the numerical analysis. Spitler et al. give correlations between J and convective heat transfer coefficient when a side wall inlet opening is used, see Table 3.7. Although, the correlations cannot be applied with any accuracy to geometries different to the experimental room used by Spitler et al., they are closer to the coefficients derived from the numerical work than those of Chandra and Kerestecioglu. This is due to the fact that Spitler et al. use J which is related to the inlet velocity for their correlation while Chandra and Kerestecioglu use a reference velocity 10 mm away from the side wall surface. The ceiling node curves from the numerical work closely follow the side wall and floor correlation of Spitler et al.. As Spitler et al. used a side wall inflow opening, the incoming air flowed along the floor rather than the ceiling. Therefore, their floor correlation is more applicable to the ceiling coefficients of the numerical work.

Awbi and Hatton examine convective heat transfer coefficients when a wall jet is present over the ceiling, wall and floor surfaces. The convective heat transfer coefficient, h_c, is defined as having a component due to natural convection, h_{cn}, and a component due to forced convection, h_{cf}:

$$h_c^{3.2} = h_{cn}^{3.2} + h_{cf}^{3.2}. \tag{3.86}$$

An expression for h_{cn} and h_{cf} is then given by Awbi and Hatton for the ceiling, wall and floor surfaces. The expressions for h_{cn} and h_{cf} for the ceiling surface are given as:

$$h_{cn} = \frac{0.704}{D^{0.601}}(\Delta T)^{0.133}, \tag{3.87}$$

and

$$h_{cf} = 1.35(W)^{0.074}U^{0.772}, \tag{3.88}$$

where D is the hydraulic diameter of the ceiling (m), ΔT is the air to surface temperature difference (K), W is the width of the nozzle opening (m), and U is the jet velocity ($m\,s^{-1}$). To compare this correlation to the CFD study, values have to be assigned to the variables D, ΔT and W. The hydraulic diameter, D, of the ceiling in the 2D CFD model is the width of the room between the inflow and outflow boundaries, i.e., 12 m. The solution of h_c for the ceiling surface is not sensitive to ΔT therefore a value of 7.5 K, the median temperature range used in the CFD study, is assumed. W is assumed to be 12 m as the window opening is the whole width of the room facade. The ceiling convective heat transfer coefficient correlation of Awbi and Hatton gives values below those from the CFD study and the other correlations found in the literature and presented here.

Figure 3.19 shows the floor and wall convective heat transfer coefficient empirical relationships compared with data from the literature. Again the ceiling, floor and wall empirical relationships are nearest to the correlations of Spitler et al..

The relationship between convection coefficient and velocity can be compared using two factors: the gradient; and the intersection. The gradient of the numerical curves for the ceiling and east wall nodes lie between those of Spitler et al. and the ASHRAE

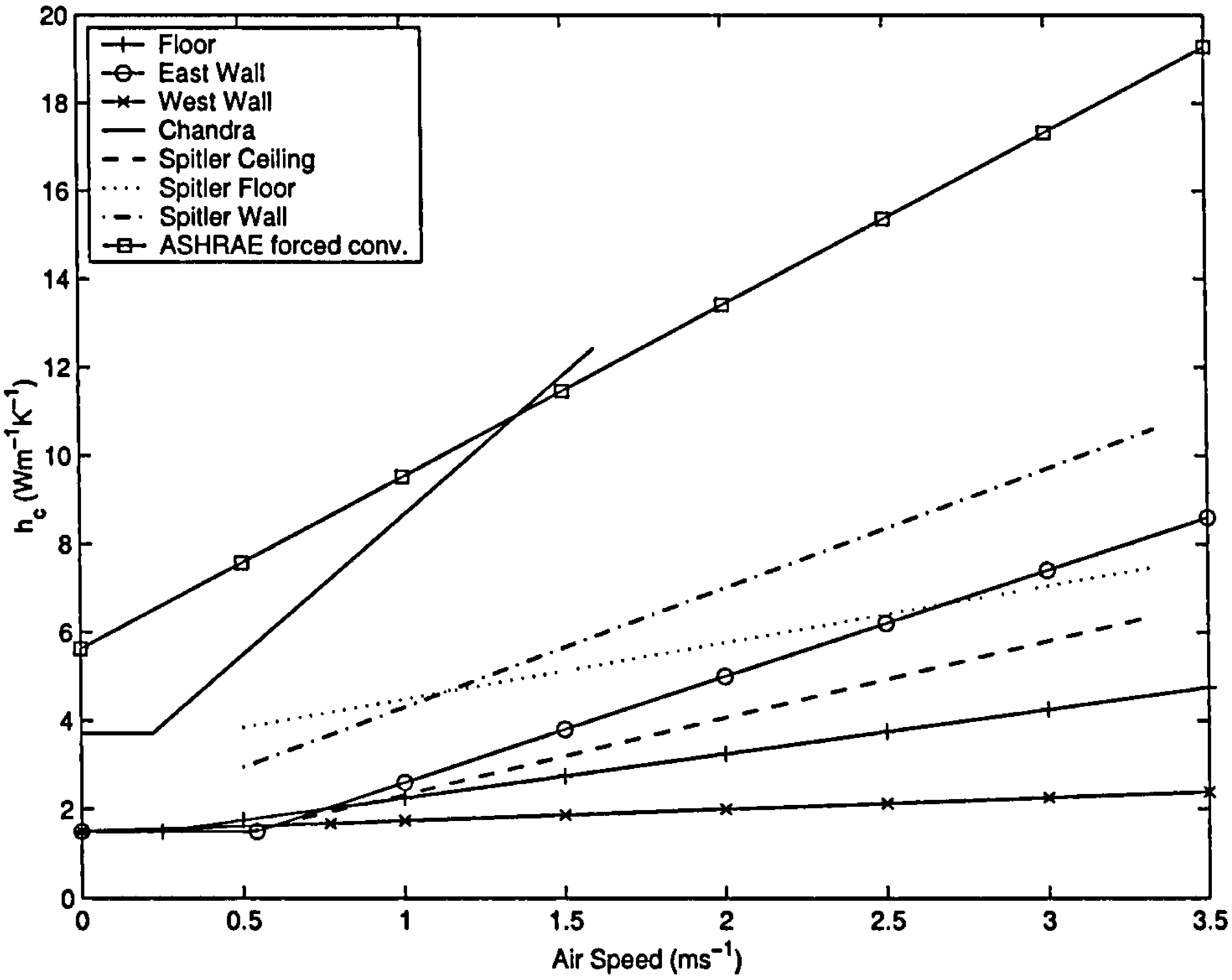

Figure 3.19: The floor and wall convective heat transfer coefficient empirical relationships compared with data from the literature.

forced convection curve which have a smaller gradient, and that of Chandra and Kerestecioglu which has a larger gradient. The floor and particularly the west wall node has a smaller gradient than all the correlations derived experimentally but are close to the gradient of the ceiling and floor correlation of Spitler et al.. The intersection points compare most favourably with those of Spitler et al.. The curve from Chandra and Kerestecioglu consists of two sections: one above 0.5 mph (0.22 m/s) which is derived experimentally; and one below 0.5 mph which is an assumed constant value. The error in the coefficient value was too high below 0.5 mph for a correlation to be calculated by Chandra and Kerestecioglu. If the experimentally derived curve of Chandra and Kerestecioglu was extrapolated it would intersect just above the numerical curves and those of Spitler.

In summary, the CFD has been used successfully to determine zonal model convective heat transfer coefficients, these coefficients fall within a range of correlations used in practice and obtained from experimental data.

3.5.4 Mass Flows

This section deals with the mass flow rates between air nodes in the zonal model. The mass flow rates are presented in a dimensionless form, divided by the total mass flow rate through the inflow boundary.

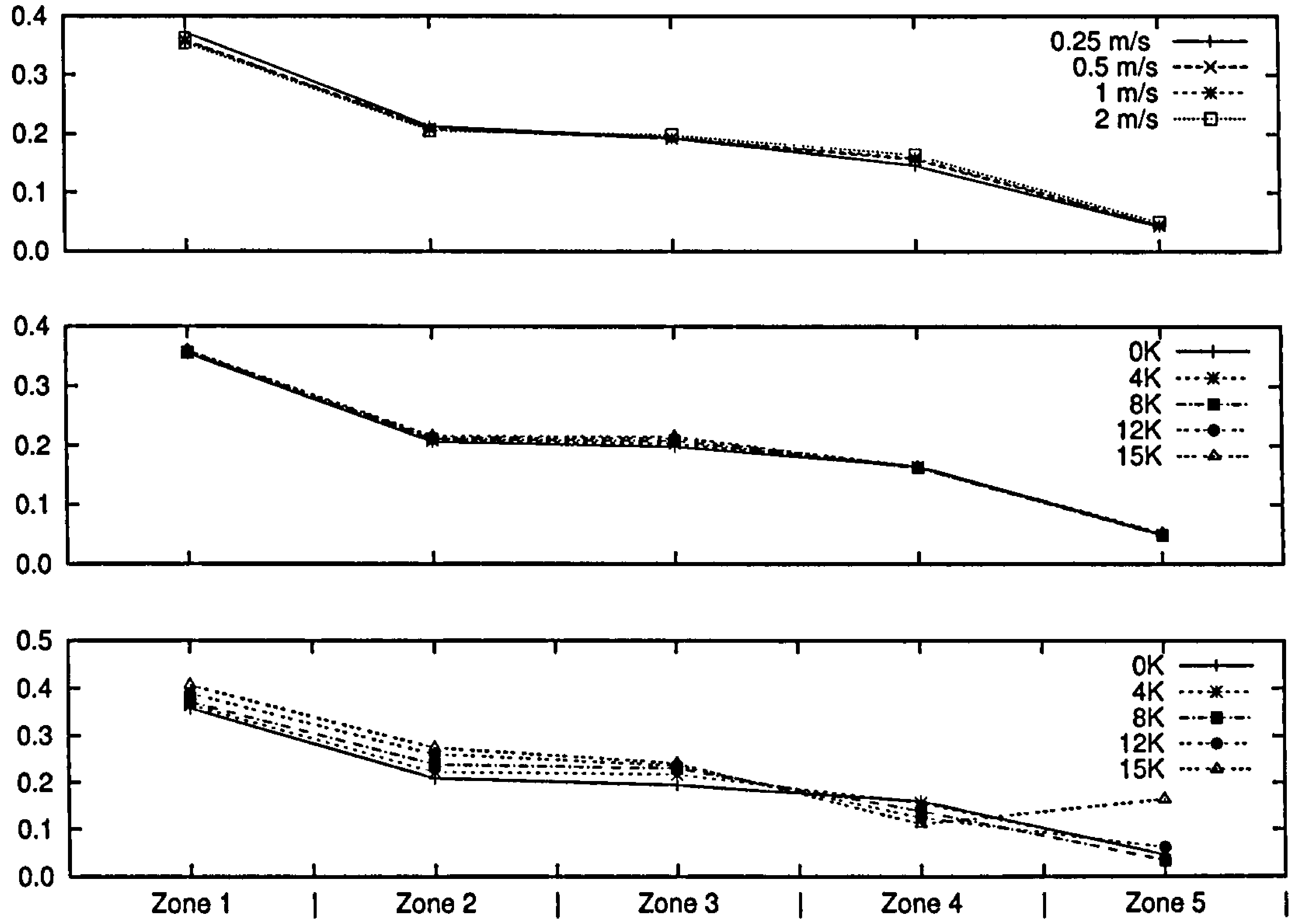

Figure 3.20: Dimensionless mass flows ($\dot{m}_{l,n}/\dot{m}_{in}$) from the recirculating region into the main flow stream: temperature difference of 0 K (top); inlet velocity of 2 ms^{-1} (middle); inlet velocity of 1 ms^{-1} (bottom).

The mass flow between zones used in the zonal model was examined using a transient scalar concentration study. Of interest was the air exchange due to turbulent mixing at the interface between recirculating regions and the zones that comprise of the main flow stream. By definition the mass flow from one main flow stream zone to another is equal to the mass flow through the room openings[4]. Defining the main flow stream in this way means that the mass flow between a recirculating region and a main flow stream zone must be balanced by a mass flow of the same value from the main flow stream zone to the recirculating region for conservation of mass to be obeyed, see Section 2.3.1.

If the main flow stream remains attached to the ceiling then the entrainment rate into the MFS decreases towards the outlet opening. Figure 3.20 shows dimensionless mass flows, $\frac{\dot{m}_{l,n}}{\dot{m}_{in}}$, from the recirculating region into the MFS. It can be seen from Figure 3.20 (top) that the effect of inlet velocity on the dimensionless mass flow is insignificant.

At high inlet velocities, temperature difference has little effect on the entrainment of air from the recirculating region into the main flow stream. Figure 3.20 (middle) shows that with an inlet velocity of 2 ms^{-1}, temperature differences from 0 K to 15 K have little effect on the dimensionless mass flows.

Temperature difference has a more significant effect on the mass flow prediction with

---

[4] The definition of the main flow stream is a modelling decision and is discussed in Section 2.3.1.

Table 3.8: Dimensionless mass flow rates for flow regimes (1–5) given in Table 3.5.

	Flow regime				
Dimensionless mass flow	1	2	3	4	5
$m_{l,1}$	0.0	1.0	1.0	1.0	0.36
$m_{l,2}$	0.0	4.6	0.27	0.27	0.21
$m_{l,3}$	0.0	0.0	4.6	0.27	0.20
$m_{l,4}$	0.0	0.0	0.0	4.6	0.16
$m_{l,5}$	0.0	0.0	0.0	0.0	0.05
$m_{u,1}$	0.16	0.0	0.0	0.0	0.0
$m_{u,2}$	0.18	0.30	0.0	0.0	0.0
$m_{u,3}$	0.28	0.27	0.30	0.0	0.0
$m_{u,4}$	0.32	0.27	0.27	0.30	0.0
$m_{u,5}$	1.5	1.5	0.5	0.5	0.0
$m_{in,ma}$	1.0	1.0	1.0	1.0	1.0
$m_{ma,mb}$	1.0	1.0	1.0	1.0	1.0
$m_{mb,mc}$	1.0	1.0	1.0	1.0	1.0
$m_{mc,md}$	1.0	1.0	1.0	1.0	1.0
$m_{md,me}$	1.0	1.0	1.0	1.0	1.0
$m_{me,out}$	1.0	1.0	1.0	1.0	1.0

an inlet velocity of $1\,\mathrm{ms}^{-1}$, Figure 3.20 (bottom). In the first three zones, the mass flows increase with temperature difference. At zone 4, the order reverses with the largest temperature difference having the smallest mass flow. The dimensionless mass flow in zone 5 is larger than zone 4 for a temperature difference of 15 K. This increase in dimensionless mass flow is in contrast to the general downward trend and occurs when the main flow stream widens to the height of the room within the first half of the zone in question, see Figure 3.9 (bottom).

Zonal Model Capacity Rate Parameters

Dimensionless mass flow rates for flow regimes 1–5 are given in Table 3.8. To convert the dimensionless mass flow rate into a capacity rate it is multiplied by the mass flow through the inlet, $\dot{m}_{in}$, and the heat capacity of air, c_p.

3.5.5 Effect of y^+ Values

It is accepted that in momentum driven zero pressure gradient boundary layer flows that the flow is laminar where $y^+ < 11.6$ and fully turbulent where $y^+ > 30$. Between these values there is a transition region where u^+ is neither described by a linear or 'log law' function. When a wall function is used, the usual intention is that the first node adjacent to wall surfaces is positioned in the fully turbulent zone ($30 < y^+ < 300$). This can be difficult when low velocities are prevalent, such as in room air flow. The meshes used in this work were produced with the requirements:

1. Sufficient cells to resolve important aspects of the flow;
2. y^+ values above 30.

When it was not possible to fulfill both requirements resolving the flow field was given priority, i.e., there were a minority of low velocity cases where the grid could not be made coarse enough to satisfy $y^+ > 30$ and resolve the jet as it entered the room through the inflow boundary—for these cases y^+ was below 30.

In the majority of the simulations where the main flow stream remains attached to the ceiling (cases 17-22 and 25-57, see Table 3.3) y^+ values were above 30 except in the bottom corners of the room where the air velocity is low. This deficiency is minor and unavoidable in recirculating flows on structured meshes.

At an inlet velocity of $0.5\,\mathrm{ms}^{-1}$ where the flow detaches (cases 23 and 24), y^+ values were greater than 30 for the majority of near wall cells. The exception to this were cells along the ceiling after flow detachment where y^+ fell into the range associated with the laminar subregion. This is also unavoidable due to the structured mesh used and the very low velocities in the thermally stratified region after flow detachment.

At inlet velocities of $0.1\,\mathrm{ms}^{-1}$ and $0.25\,\mathrm{ms}^{-1}$ (cases 1-16) y^+ values at the ceiling fell within the transition region ($11.6 \leq y^+ \leq 30$) before flow detachment and within the range associated with the laminar subregion after flow detachment. For the walls and floor y^+ values fell within the transition region ($11.6 \leq y^+ \leq 30$) before flow detachment but were greater than 30 after.

This means there are serious questions over the convective heat transfer prediction at the ceiling for 16 of the 57 cases in the parametric study. Values over much of the surfaces in these cases fall in the range associated with the transition zone in conventional boundary layers. The wall functions are implemented in the code used here (CFX 1997b) in such a way that a linear function is applied where $y^+ < 11.6$ and the usual 'log law' applied where $y^+ > 11.6$. This arguably results in an over-prediction of u^+ where y^+ falls in the transitional range.

If the results of the parametric study are examined it is possible to determine whether low y^+ values effect the correlations obtained. Results presented in Section 3.5.4 suggest that low y^+ values had little effect on the predicted dimensionless mass flows calculated for use in the zonal model capacity rate parameters. Values obtained from case 9 ($v_{in} = 0.25\,\mathrm{ms}^{-1}$ and $\Delta T_{ci} = 0\,\mathrm{K}$) which had y^+ values associated with the transition zone did not differ from those obtained from cases where y^+ was greater than 30, see Figure 3.20 (top) where the $0.25\,\mathrm{ms}^{-1}$ case has y^+ values below 30.

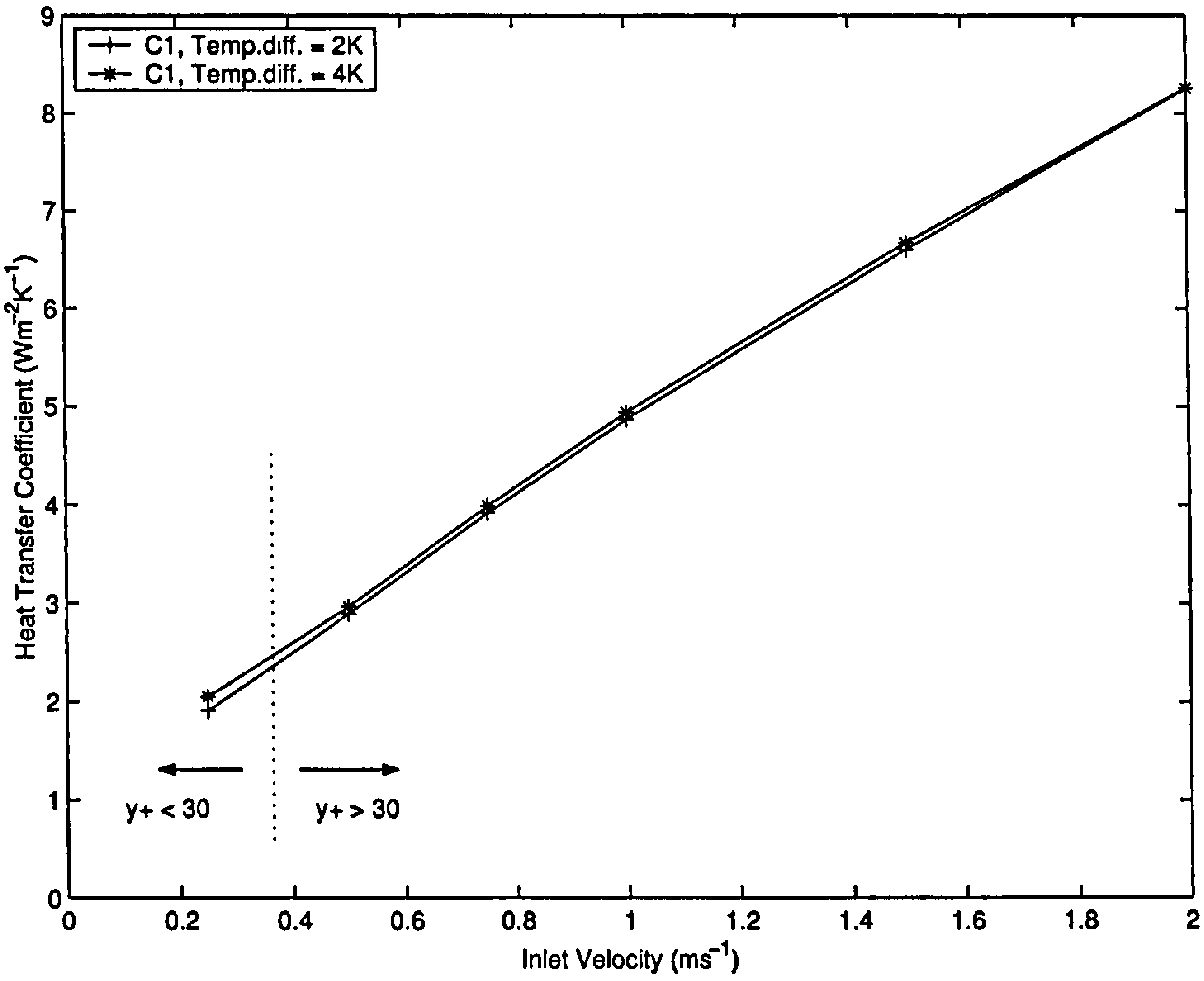

Figure 3.21: Predicted heat transfer coefficient for ceiling node C1 in cases with y^+ values above and below 30.

It is harder to determine whether the heat transfer coefficient predictions were effected by low y^+ values because their value depend on the flow regime, i.e., whether the flow detaches or not. Although, it is possible to compare like with like if the heat transfer at ceiling nodes where the MFS is attached to the ceiling are examined. In Figure 3.21 the predicted heat transfer coefficient for ceiling node C1 in cases with y^+ values above and below 30 are compared. Note that the trend of h_c versus inlet velocity holds where y^+ values are above and below 30.

The fact that correlations from simulations with y^+ values above and below 30 agree is very encouraging and implies that the placement of the near wall node had little effect on the zonal model parameters extracted from the CFD results.

3.6 Conclusions

1. By examining the CFD results from simulations across the range of boundary conditions applied, it is clear that flow regime (the path of the flow through the room) has a dramatic impact on the predicted zonal model parameters. A zonal model that allows flow detachment to be modelled is clearly essential if the thermal environment is to be treated well. Therefore, it can be said that the CFD results support the choice to consider the main flow stream separately from the

recirculating air zones.

2. CFD results allow the calculation of convective heat transfer coefficients based on area weighted values of q_s and T_s (over the area corresponding to the surface node), and volume weighted values of T_a (over the volume corresponding to the model zones). This is difficult to do experimentally as the density of data obtained via experimental measurement is usually much lower than that obtained from CFD simulations, and are likely to be derived from point measurements of heat flux, air temperature, and surface temperature. The convective heat transfer coefficients predicted by the numerical work compare favourably with experimentally derived values in the literature, and fall within a range of correlations used in practice. The numerical correlations compare most favourably with experimental results that use the inlet velocity as the reference velocity in the correlation calculation. This is not surprising as inlet velocity was used in the correlation from the numerical data.

3. There are two types of capacity rate parameters in the zonal model:

   (a) Mass flows between main flow stream zones;
   (b) Mass flows between the main flow stream zones and the recirculating regions.

   The mass flows between main flow streams zones are known, and equal the mass flow through the inlet. This leaves the mass flows between the main flow stream zones and the recirculating regions to be determined. A simple integration of air velocity along the zone boundaries could not be used, as mass exchange was due to turbulent mixing rather than bulk air flow. Transient CFD simulations have allowed these mass flows to be determined by examining the dispersion of an extra scalar throughout the computational domain—the numerical equivalent of a tracer gas experiment.

4. The standard k-ε turbulence model is known to over-predict turbulence levels in these low-Reynolds flows. Therefore, it is expected that these mass flows are over-predicted by the model. It would have been of interest to compare the mass flows predicted using other turbulence models, such as, the low-Reynolds k-ε turbulence model, and the Reynolds stress model. Considerable efforts were made to use the low-Reynolds k-ε turbulence model but a converged solution could not be attained.

5. A check was made to see if y^+ values effected the parameter values obtained from the CFD results. It was found that heat transfer coefficients and mass flows obtained from simulations with $y^+ \geq 30$ agreed with results from simulations with $y^+ \leq 30$.

6. A number of empirical relationships have been found from the CFD study that can be used to determine zonal model parameter values in the form of:

- 24 surface convective heat transfer parameters, equal to a convective heat transfer coefficient multiplied by the surface area that the node represents, and
- 26 capacity rate parameters, equal to the heat capacity of air multiplied by a mass flow rate between two air nodes.

7. A procedure for setting the zonal model parameters has been defined:
   (a) The pressure difference between the inlet and outlet is found from empirical correlations from studies on wind-generated surface pressure distributions such as that of Ernest (1991);
   (b) The average temperature of the ceiling nodes is calculated;
   (c) The temperature difference between in inflow air and the ceiling is calculated;
   (d) Pressure and temperature difference are used in Equation 3.77 to calculate the inlet velocity;
   (e) Temperature difference and inlet velocity are used in Equation 3.81 to calculate Archimedes number;
   (f) Table 3.5 can be used to find at which ceiling node the flow detaches using the Archimedes number;
   (g) Inlet velocity and flow detachment position are used with Table 3.6 to find the convective heat transfer parameters;
   (h) Inlet velocity and flow detachment position are used with Table 3.8 to calculate the capacity rate parameters.

Appendix B gives the calculation procedure in a general form which may be used to implement the zonal model in another thermal modelling program.

CHAPTER 4

Experimental Procedure

4.1 Objectives

A review of the current literature showed that very few measurements had been published concerning flow regime and convective heat transfer at the ceiling in naturally ventilated spaces. Chandra and Kerestecioglu (1984) examine convective heat transfer at vertical wall surfaces in a naturally ventilated room. Spitler, Perdersen, and Fisher (1991) examine convective heat transfer at the ceiling, floor and walls in a mechanically ventilated room. Khalifa and Marshall (1990), Awbi (1998) and Awbi and Hatton (1999) examine convective heat transfer coefficients for natural convection while Awbi and Hatton (2000) examines convective heat transfer coefficients for mixed convection.

The existing literature does not explicitly address:

- Heat transfer coefficients when high level openings are used to promote wind driven air flow along the ceiling; or
- The flow path taken by the inflow air for particular thermal boundaries and flow rates.

For these reasons experimental measurements were taken in a night-time cross-flow ventilated room with three primary purposes in mind:

1. To gain understanding of the physical processes involved in natural ventilation, particularly of interest were flow regime and convective heat transfer at the ceiling;
2. To provide data that can be used to determine the structure and parameters of the zonal model. Due to the tentative nature of the CFD results it was felt important enough to seek experimental evidence for the flow regimes postulated in the zonal model;

3. To provide boundary conditions for, and checking the results of, CFD simulations (although not being detailed enough to allow full validation).

One of the key tasks in the development of a room heat transfer model is the determination of the parameters associated with convective heat transfer. Surface-air convection parameters can be determined from numerical experiments by performing a heat balance between surface and air nodes of the CFD model which relate to zones of the simplified model. However, in view of the uncertainties regarding the accuracy of the numerical convective heat transfer calculations, experimental data was sought that allowed a similar heat balance to be performed with the experimental data which could verify (or not) the numerical one. For this purpose, distributions of radiative and convective heat fluxes were measured.

A similar approach of performing a heat balance calculation on measured air temperature values to determine bulk air flow parameters for the simplified model could also take place. This approach was used by Rees (1998) for displacement ventilation. In the zonal model proposed by Rees the positions of the nodes and the network representing the bulk airflow are fixed. In the zonal model presented here, the bulk airflow network changes with boundary conditions that can change rapidly with time. Due to the difficulty in determining which of the five zonal model flow regimes exists in the experimental room, and the fact that the flow regime can change during the air temperature data sampling/collection period, this approach to determine bulk air flow parameters was not used here.

For a complete experimental study to generalise the model, data from many different weather conditions and room geometries would be necessary. This was not within the scope of this work and CFD was used to explore these issues parametrically.

This chapter discusses the methodology used to make experimental measurements of night-time cross-flow ventilation, the experimental apparatus used, and the results obtained. Calibration of the measurement systems is discussed in Appendix C. Chapter 5 describes modelling the experimental room numerically using computational fluid dynamics.

4.2 Background

4.2.1 Convective Heat Transfer

Models predicting convective heat transfer in buildings rely entirely on correlations of experimental data. The convective heat transfer coefficients used in hourly building analysis programs were correlated from experimental data obtained in the 1930's. These experimental data were obtained from flat plate experiments in still air. Therefore, their use in systems with a variety of air flow rates is questionable. More realistic data is available (Chandra and Keresteciogiu 1984; Spitler, Perdersen, Fisher, Menne, and Cantillo 1991; Spitler, Perdersen, and Fisher 1991) that has not as yet been incorporated into thermal analysis codes offered to the general practitioner.

4.2.2 Full-Scale Investigations

Full-scale field studies of indoor air motion have been used to evaluate existing buildings (Caudill and Reed 1952; Chand, Sharma, and Krishak 1989). Smith (1951) used full-scale and model scale comparisons to establish the feasibility of using small scale models to predict flow patterns within buildings. Other research (Chandra, Kerestecioglu, Fairey, and Cromer 1982; Gandamer and Barnaud 1989) has found good agreement between indoor velocities obtained from scale models in boundary layer wind tunnels and full-scale building measurements.

4.2.3 Wind Tunnel Tests

Interior Building Geometry

A number of studies have been conducted on the effect of ceiling height (Warsi and Chand 1967; Chand, Sharma, and Bhargava 1978; Caudill and Reed 1952) which together show that ceiling height (when the external geometry is unchanged) has little effect on indoor air flows.

Givoni (1969) investigated the effects of 6 different partition types for a normal wind incidence. Chand, Sharma, and Bhargava (1977) tested partitions designed to increase the air flow near the floor while reducing velocities higher up. Ernest (1991) investigated 3 different partition types at three locations within the space for wind angles from 0^o to 90^o.

Exterior Building Geometry

Chand, Sharma, and Bhargava (1977) present a series of tests on the effect of building shape on indoor air motion. The various building shapes investigated (L-shape, U-shape, H-shape and T-shape) were compared with the performance of the square floor plan. He found that indoor air velocity could be +/- 50 % of the level obtained for the square plan building. Ernest (1991) investigated more building shapes including a Z-shaped floor plan and two rectangular buildings at wind angles between -90^o and 90^o. The effect of horizontal overhangs and vertical wing-walls has been examined by a number of studies (Chand and Krishak 1971; Sobin 1983; Givoni 1969; Chand, Sharma, and Bhargava 1977; Chandra 1983; Ernest 1991). These studies show that external projections are an important parameter affecting indoor air motion, particularly when the wind angle is oblique.

Window Design

The effect of window size was investigated by a number of studies (Givoni 1962; Chand and Krishak 1969; Sobin 1983; Ernest 1991). These studies show that while indoor air motion increases with window size, the rate of increase levels off above a certain wall porosity (wall porosity is defined as the ratio of the window area to the wall area). This threshold was found to be between 20 % and 30 % of the windward wall area. The horizontal position of the window was found to have an effect on indoor air motion

Building orientation with respect to wind direction

Building orientation with respect to wind direction has been studied by a number of researchers (Givoni 1962; Sobin 1981; Sobin 1983; Chand and Krishak 1969; Chand, Sharma, and Bhargava 1977; Warsi and Chand 1967). Ernest (1991) concludes that these studies in aggregate prove inconclusive about the effects of wind direction, and suggested that building orientation with respect to wind direction cannot be studied independently of other design variables.

Upwind Obstructions

Despite the fact that most buildings are surrounded by other objects, relatively few studies have addressed the effect of upwind obstructions on indoor air motion. Chand, Krishak, and Sharma (1975) used two building configurations to study the effect of upwind obstructions. Ernest (1991) combines wind tunnel tests on upwind obstructions with investigations on building geometry and orientation.

Static pressure data

The overall external pressure field around the building may be affected by the presence of openings in the structure. This means that pressure data taken around sealed models may differ significantly to pressure levels when there are openings to the air flow. This effect was investigated by Snyckers (1970), who found that the presence of fairly large openings (wall porosity of 12 %) did not significantly affect the surface pressure distribution patterns except in the immediate vicinity of the openings.

Pressures measured on window areas of sealed models may be different from those measured at the openings of porous models. Poreh, Cermak, and Peterka (1982) found that the total pressure measured at an open inlet was slightly larger than the pressure measured on a sealed model at the same location. To account for this pressure measurements are needed at the windows of porous models which are difficult to measure directly, especially for oblique wind directions, and very little published data are currently available. However, studies that have addressed this issue have shown that the use of pressures measured on sealed models lead to errors of less than 10 % for predicted flow rates (Aynsley 1988).

In another study it was found that for buildings with wall porosities lower than 25 % and wind angles below 45 %, internal air flow rates could be predicted to within 10 % from external surface pressure distributions measured on sealed models (Vickery and Karakatsanis 1987).

4.2.4 Implications of Previous Work

The overall external pressure field around the building may be affected by the presence of openings in the structure. This means that pressure data taken around sealed models may differ significantly to pressure levels when there are openings to the air flow (Snyckers 1970; Aynsley 1988; Poreh, Cermak, and Peterka 1982; Vickery and Karakatsanis 1987). However, studies that have addressed this issue have shown that the use of pressures measured on sealed models lead to errors of less than 10 % for predicted flow rates (Aynsley 1988). This means that the zonal model can be coupled to the research of others on pressure distributions around buildings, even though the CFD predictions are driven by the total pressure at the inflow boundary rather than the static pressure as measured by sealed model testing. Results will be sufficiently accurate as long as wall porosities remain below 25 %. The design implications of a limitation on porosity are not that great as most buildings are within this limit.

There is much research using wind tunnel experiments in the area of external pressure coefficients and internal flows due to pressure differences between room openings (Givoni 1965; Sobin 1981; Sobin 1983; Chand, Sharma, and Bhargava 1978; Ernest 1991). This research ignores the effects of buoyancy forces on internal flows, brought about by the incoming air being at a lower temperature than the room air.

Review of the literature showed that the ceiling convective heat transfer coefficients are largely ignored, although, there are correlations for forced convection at vertical plates (ASHRAE 1997; McAdams 1954; Chandra and Kerestecioglu 1984). Spitler, Perdersen, and Fisher (1991) determine ceiling convective heat transfer coefficients but have different inlet configurations to the high level inlet of interest in this study. In their study they also use the outlet temperature to define the air reference temperature for the calculation of convective heat transfer coefficients. For these reasons it was considered necessary to conduct an experiment to determine convective heat transfer coefficients at the ceiling. Data collected are also used to:

- Support the choice of zonal model structure;

- To provide boundary conditions for further three-dimensional CFD simulations presented in Chapter 5;
- To check whether the CFD models are giving reasonable results, although, the experimental data are not sufficient for full validation.

For these ends the following measurements are taken:

- Internal air speed;
- External air velocity;
- Wall, ceiling and floor temperature;
- Air temperature;
- Ceiling heat flux.

Flow regime inside the experimental room is also explored using a laser and joss-stick smoke;

4.3 Experimental Method

4.3.1 Experimental Room

The experiment outlined in this document consisted of measurements taken under night-time cross-flow conditions. The criteria involved in choosing the experimental room included:

- A high thermal mass ceiling;
- The possibility of cross ventilation;
- Windows designed for night-time cross-flow ventilation that would induce air flow across the ceiling;
- A window that faced the prevailing wind direction.

The room found that most closely met the requirements, and that was available, was a student bedroom in the David Collett residence hall at Loughborough University. The room is of a size representative of a one-person office and has internal dimensions of 3.95 m long, 2.55 m wide and 2.41 m high. The room is not symmetrical, and a 870 by 760 mm area that included a sink was sectioned off with hardboard to make the room geometry simpler, and easier to model using CFD, see Figures 4.2 and 4.3. The door

Figure 4.1: Outside view of David Collett residence. Experimental room is in the middle of photo with ultrasonic anemometer protruding from window.

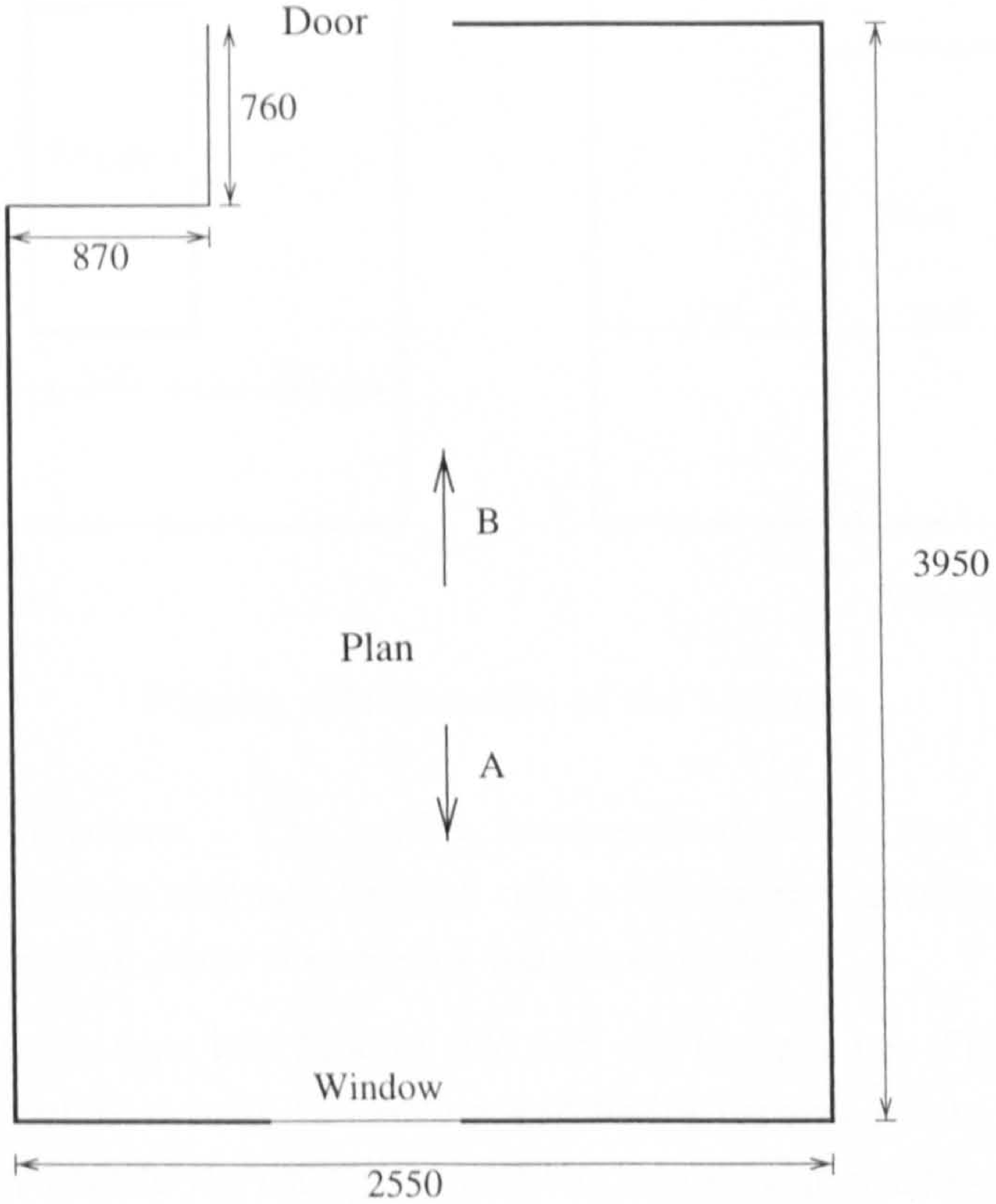

Figure 4.2: A plan of the bedroom in David Collett

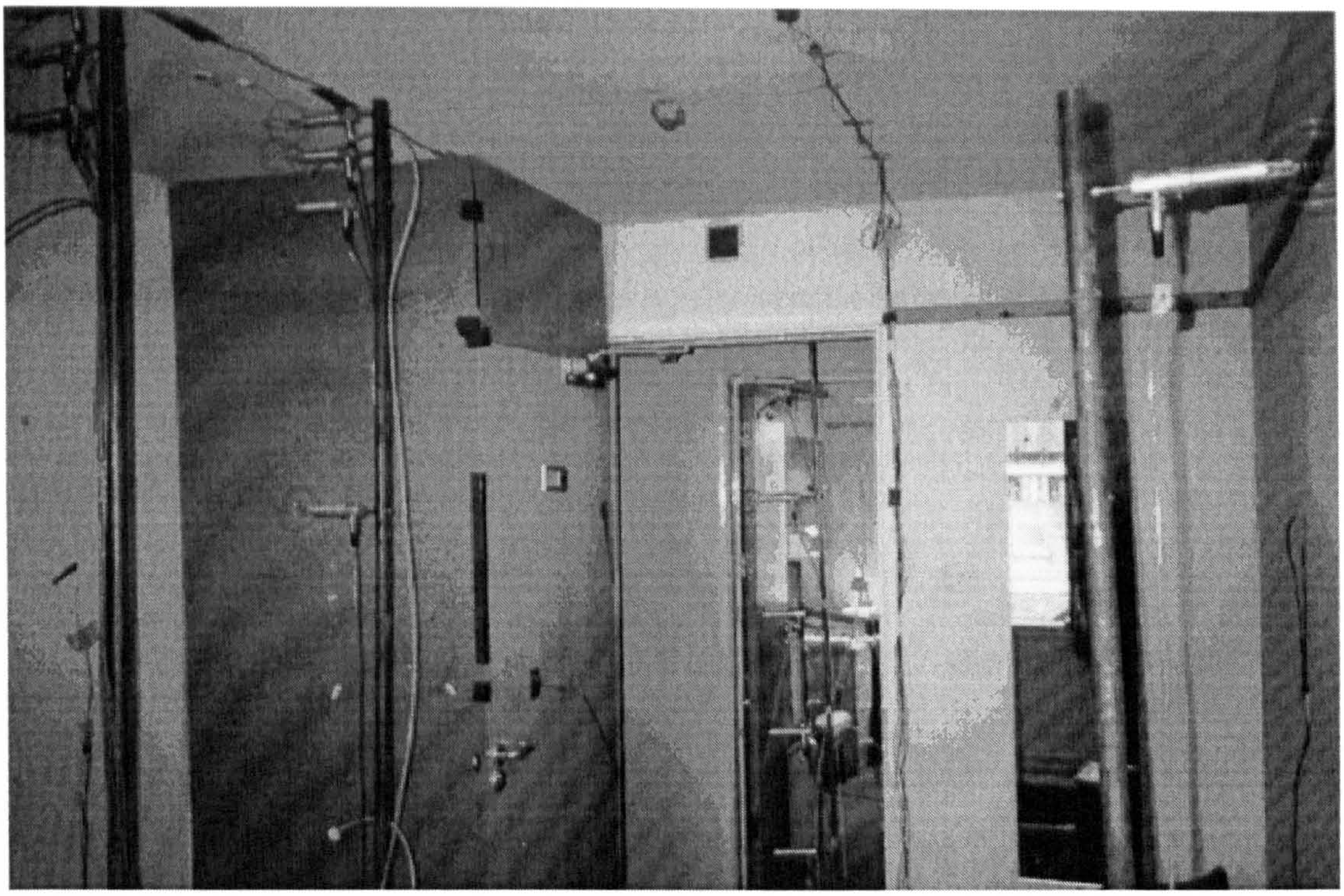

Figure 4.3: Inside view of the experimental room towards the door.

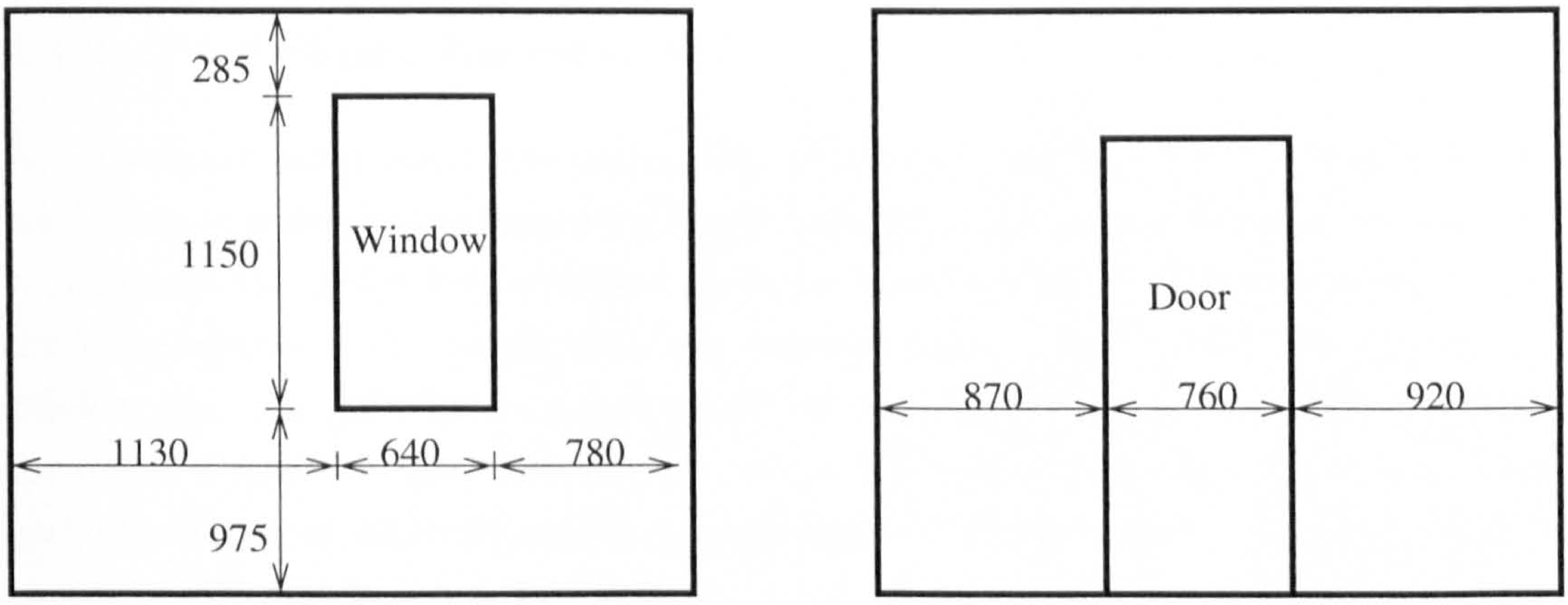

View A

View B

Figure 4.4: Elevation of the bedroom

and window are off-centre. The window faces approximately west and the ceiling is constructed of a concrete slab and finished with a thin layer of plaster. The floor is also concrete but is carpeted while the interior walls are plastered.

The openable window area was 1150 by 640 mm, see Figure 4.4. The existing window in the room was not flush with the ceiling and had a vertical pivot, both unhelpful in promoting air flow next to the ceiling. Therefore the openable window area was removed and replaced with a wooden frame that allowed a hopper to be attached to simulate a bottom hung pivoting window, see Figure 4.5.

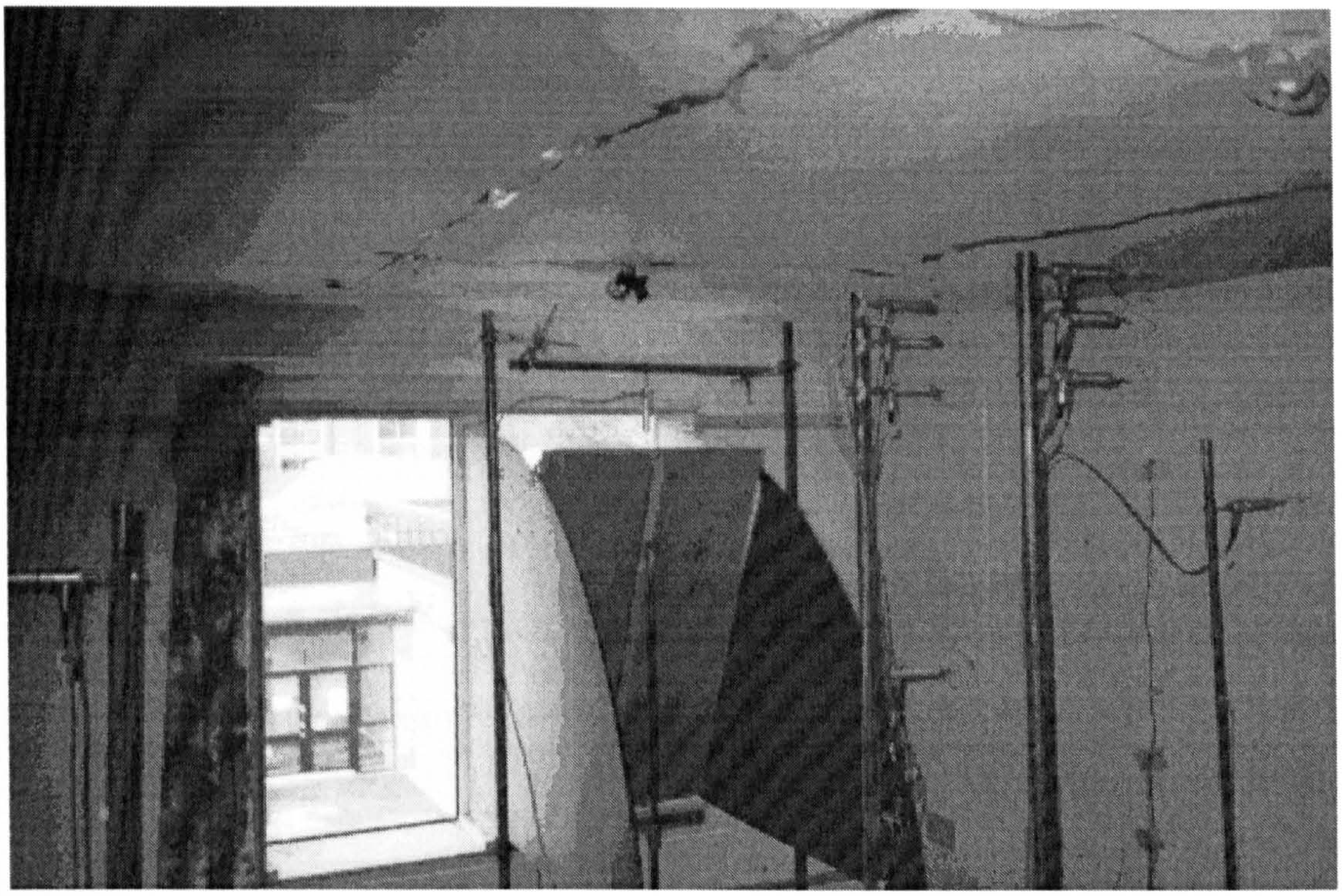

Figure 4.5: View inside the experimental room and the hopper.

4.3.2 Preliminary Experiment

A preliminary experiment was undertaken to examine air flow paths under cross-flow conditions in order to help place experimental equipment in suitable locations in order to maximise the useful data obtained from the experimental procedure. During the day the temperature of the ceiling slab was elevated using a fan heater. The half of the window with the glass left in was screened off to minimised the external light entering the room. A laser and joss-stick smoke were used to help visualise flow paths in the room with the hopper at different angles. A hand held anemometer was used to determine air speeds at different locations in the room.

The smoke and a hand held anemometer experiments showed that it was possible to get at least two flow regimes:

1. In the first flow regime the main flow path is across the ceiling. Near to the door the flow detaches from the ceiling due to wall obstruction above the door. The flow then leaves the room mostly at the top of the door opening.
2. In the second flow regime the flow went along the ceiling for only part of the room depth before rapidly dropping to the floor. Then the flow travels along the floor and exits at the bottom of the door opening.

In both cases flow was biased towards the northern wall. As the window is off-centre the flow is more likely to attach to the nearer north wall surface due to the Coanda effect.

Along this wall there was a strong downward flow whether the flow through the middle of the room remained attached to the ceiling or not. This was due to the hardboard section, shown in Figure 4.3, forcing the flow downwards and around the corner made by the north wall and the hardboard section. When the flow rounded the edge of the hardboard section it was hard to determine whether the flow joined air leaving the room through the door or air forming a recirculating region with flow back towards the west wall. In reality the flow probably fluctuated between the two but the smoke visualisation was not sensitive enough to pick up other flow features. Flow along the floor was generally complicated with evidence of cells of recirculating air along with flow through the bottom half of the door opening.

4.3.3 Experimental Equipment

Air Speed and Air Temperature Measurements

Air speed and temperature measurements were made using a Dantec 'Multichannel Flow Analyser'. This system consists of a flow analyser (type 54N10) linked to a personal computer and 24 air flow transducers (type 54R10) (Dantec 1993b; Dantec 1993a).

The 54R10 air flow transducer is a combined omnidirectional air speed and temperature sensor designed specifically for measuring room air flows within the velocity range 0.05–5.0 ms^{-1} and works on the hot sensor anemometer principle. The air speed sensor of the transducer consists of a 3 mm glass sphere coated with a thin film of nickel and a protective quartz outer coating. The Nickel film has a double spiral formed in it so that it can act as an electrical conductor. This sphere is connected electrically to one arm of a Wheatstone bridge, whose opposite arm contains an identical, non-heated, sphere for automatic temperature compensation. The hot sphere is maintained at a constant 30 K above the surrounding air by a heating current passing through the nickel conducting layer, independent of variations in flow velocity or temperature. The power supplied to heat the sphere is then a function of the air speed. The temperature sensor of the transducer is a thermistor approximately 0.5 mm in diameter.

The flow analyser drives each of the transducers, sampling a velocity reading twice a second. These data are stored over a preset sampling interval and the mean and RMS velocity calculated at the end of each interval. A personal computer is used to control the flow analyser and download, process, display and log velocity and temperature measurements. The sampling period chosen can be varied depending on the nature of the fluctuations in the flow. In this case, a sampling time of 60 s was used with a 30 s pause between samples to capture some of the dynamics of air flow driven by natural ventilation.

The anemometers were mounted on vertical stands to allow measurement of the room air vertical temperature and velocity distribution. Figure 4.6 shows were the stands were

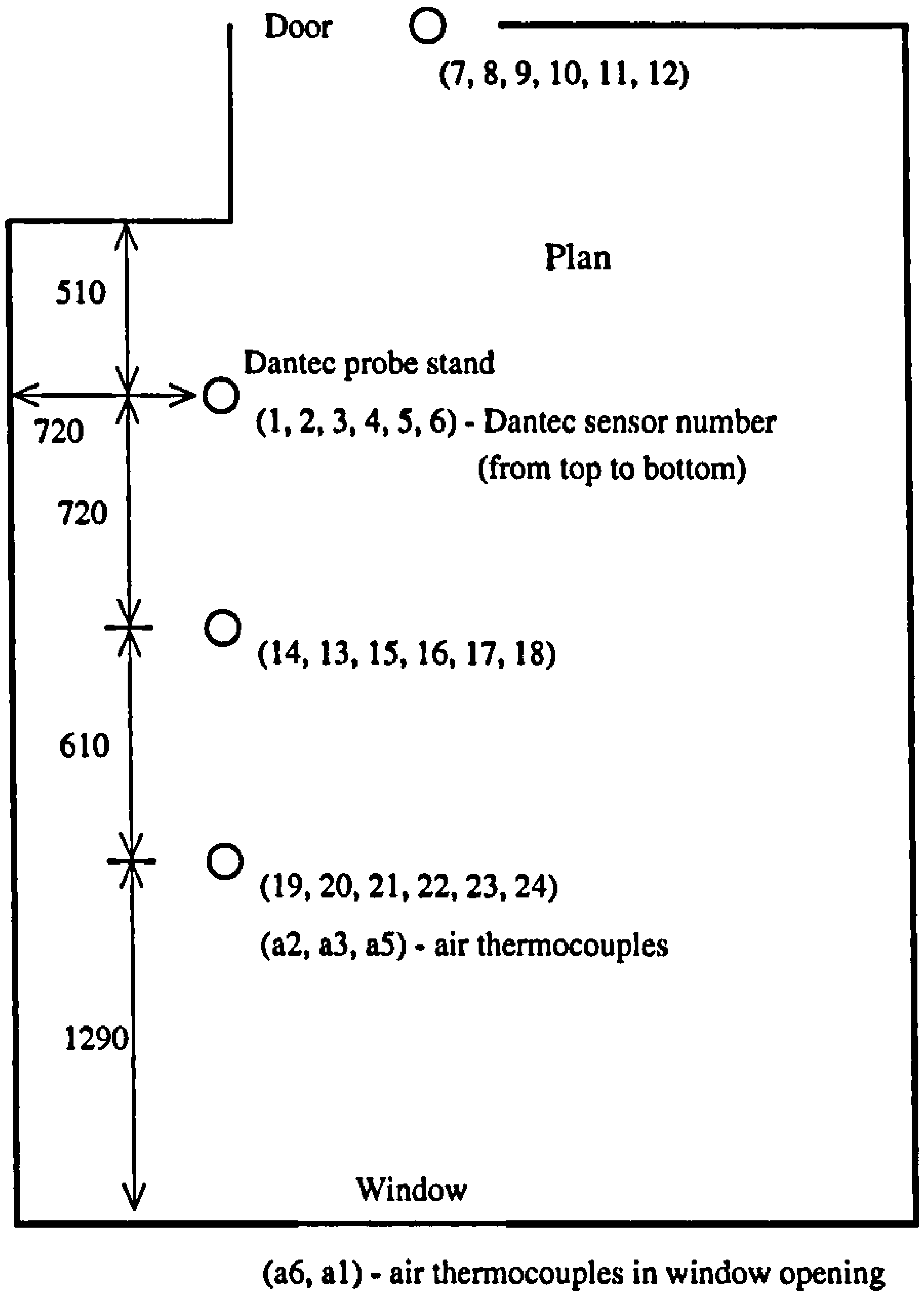

Figure 4.6: The positioning of the anemometer stands

positioned within the room. Sensors were closely spaced near the floor and ceiling where the air velocity gradients were expected to be greatest, see Figure 4.7. One anemometer was used in the hopper opening to get an inlet velocity throughout the experiment while six anemometers were mounted on a vertical stand place in the doorway to determine the exit position of the flow, see Figure 4.8.

Air Velocity Measurements

Outside air speed and direction measurements were taken with an ultrasonic anemometer (Gill 1991). The logging ultrasonic anemometer consists of a sensing head with six ultrasonic transducers arranged in three pairs, surmounting a cylindrical electronic base housing. The on-board electronics provide all ultrasonic processing and vector computations required to calculate wind data in either a magnitude, direction and vertical speed format (MET mode), or a 'UVW' format. This information is logged within the anemometer until it is transmitted on request to the PC.

The anemometer works by a pair of transducers acting alternately as transmitter and receiver, sending pulses of high frequency ultrasound between themselves. The times of flight in each direction are measured from which a vector component of air flow resolved along the line of the pair of transducers may be inferred. A computer program supplied

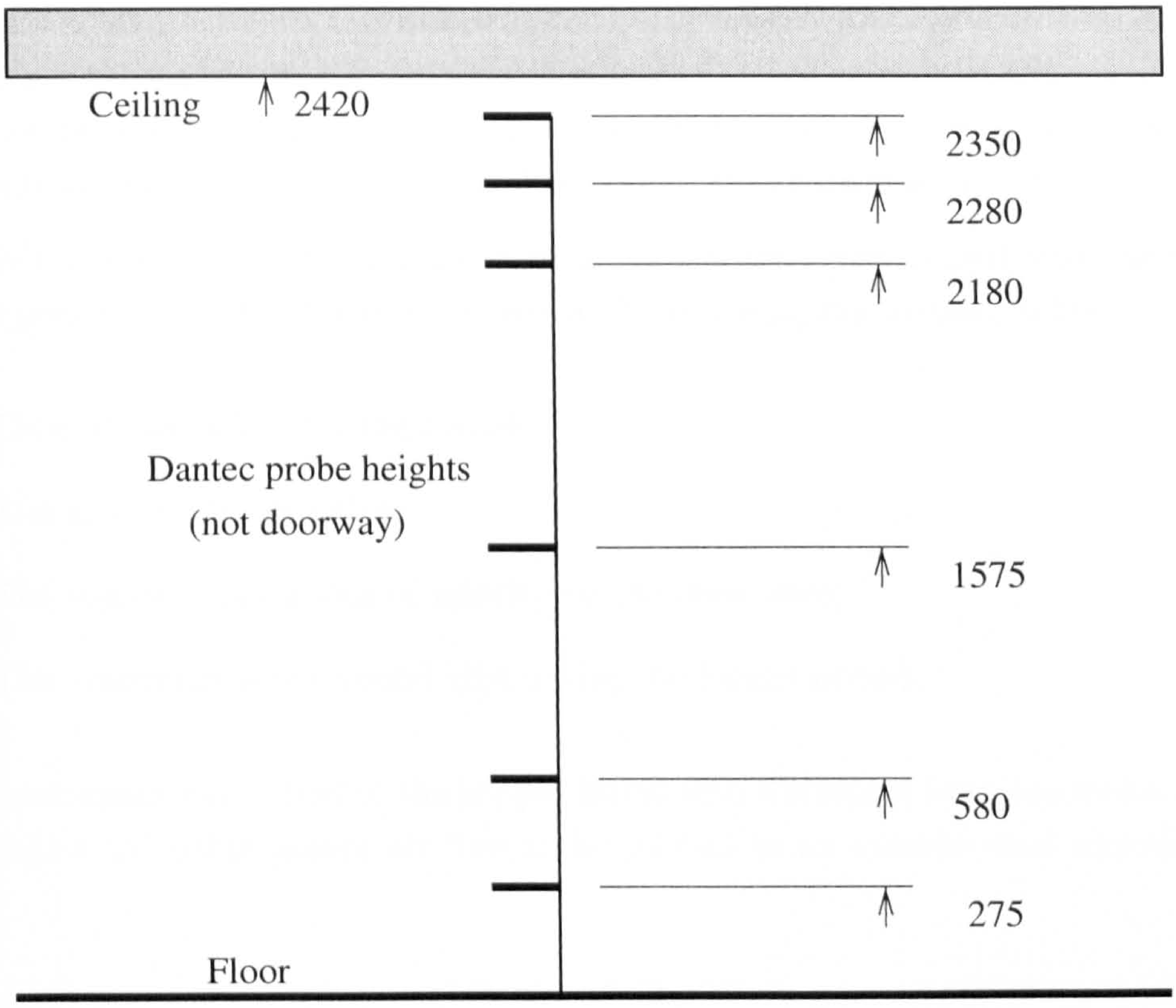

Figure 4.7: The vertical positioning of the anemometer in the room

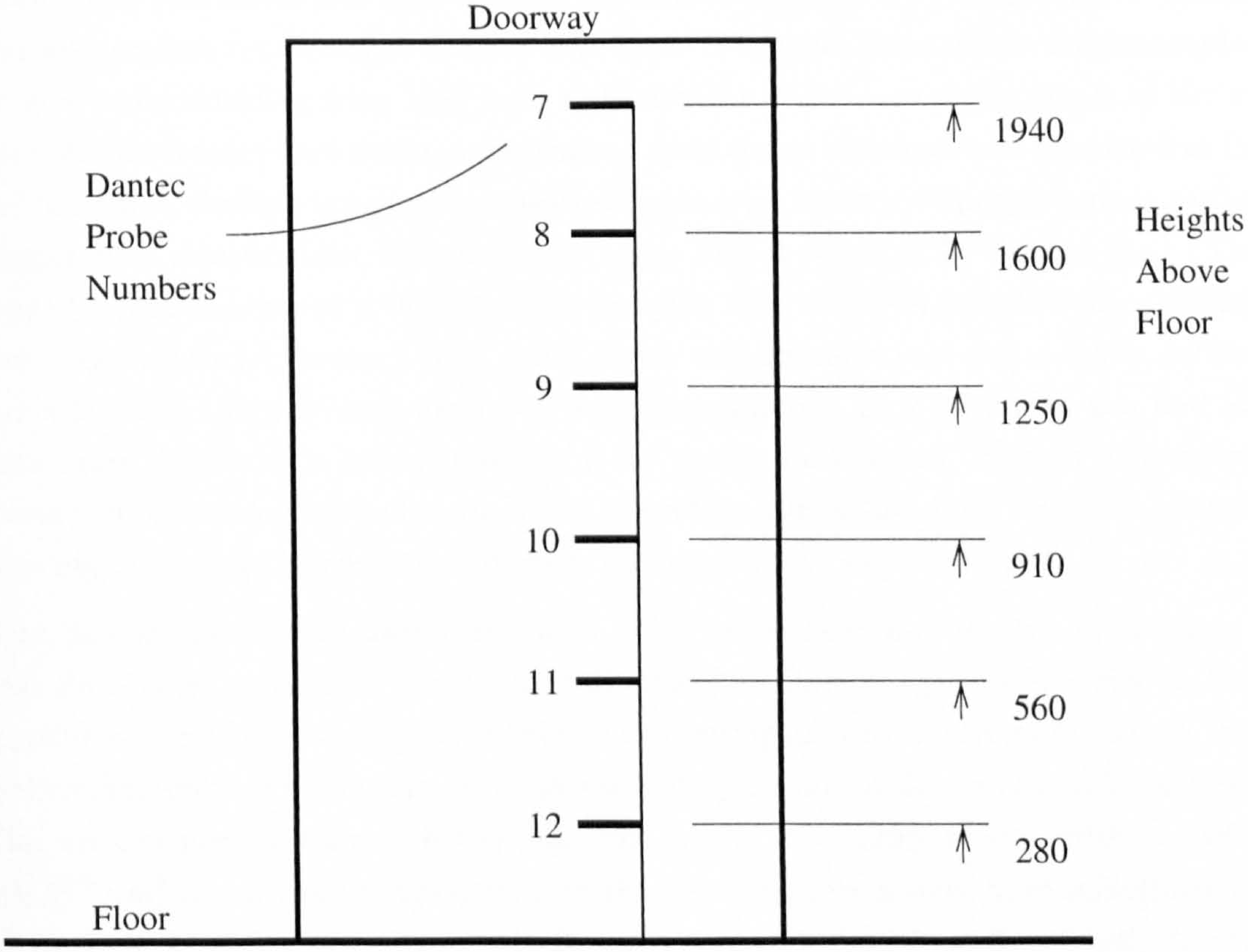

Figure 4.8: The vertical positioning of the anemometer in the doorway

by the manufacturer allows the user to switch between MET and UVW modes, save data to disk and to display data in either a tabular or a graphical form. When a sampling period of 10 seconds is used the manufacturer quotes the wind speed accuracy of the ultrasonic anemometers to be ±3%, and the direction accuracy to be $\pm 3^{o}$.

For this experiment the two ultrasonic anemometers used were logged over one minute sample periods using the UVW mode where the following are written to file:

- Time at the end of the log period;
- The u, v and w velocities;
- The standard deviations of velocity on the three axes;
- The maximum three second gust during the logged period.

The anemometer was bolted to the hopper frame with the sensor head one meter outside the window to enable indoor air flow to be related to an outside wind direction and speed.

Surface Temperature and Heat Flux Measurements

Twenty four thermocouples were used for the surface temperature measurements. The air and wall surface temperature sensors were type 'T' copper-constantine thermocouples. To give some shielding from long wave radiation the thermocouple junctions of the air temperature sensors were contained within an open ended stainless steel tube fixed at the end of a shaft. Surface temperature measurements were made with purpose made surface temperature measurement thermocouples (type SAF-1 supplied by Omega Inc.). This type of sensor consists of a thermocouple junction that has been flattened after welding and is sandwiched between a high conductivity self adhesive pad and a fabric backing material. The thermocouple assembly was approximately 25 × 20 mm in size and less than 1 mm thick with a junction area of a few square millimetres. Surface temperature thermocouples were distributed to divide the walls, ceiling and floor into four quarters allowing an average temperature for each room surface to be determined.

Heat flux measurements were made with 'TNO' type heat flux meters. This type of heat flux meter consists of many thermocouple junctions connected in series (a thermopile) and packed together in a thin plastic encapsulating material of known thermal conductivity. The sensors were approximately 20 mm in diameter and 2 mm thick. This arrangement of thermocouple junctions results in a signal of the order of tens of $mV.W^{-1}.m^{2}$ which can be measured directly. The heat flux meters have sufficiently low thermal conductivity so as to not significantly alter the conducted flux locally to their attachment point.

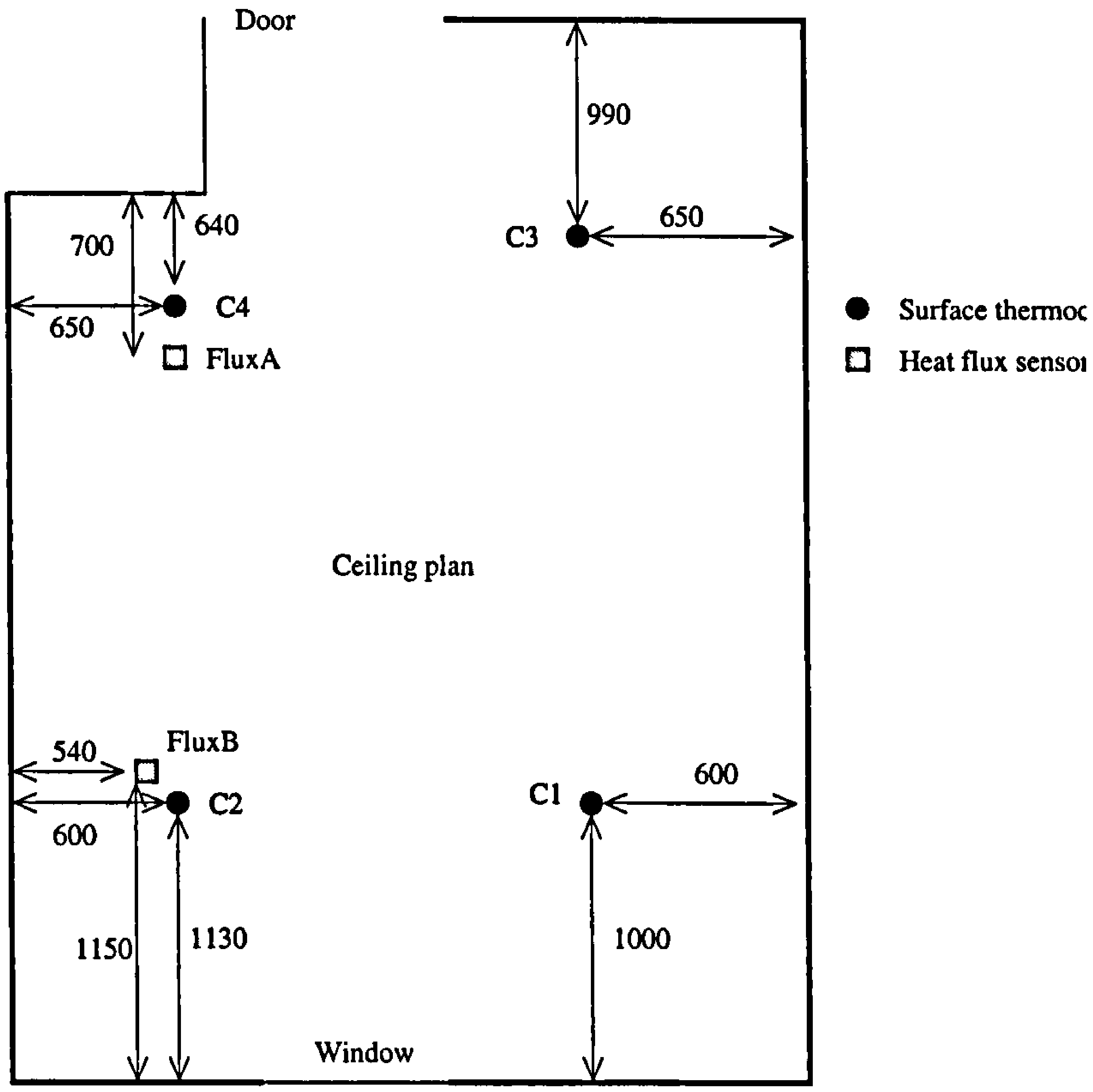

Figure 4.9: The thermocouples/heat flux meters on the ceiling

The two heat flux meters were paired up with two of the ceiling thermocouples allowing a ceiling temperature to be measured along side a heat flux measurement. Using a ceiling temperature and heat flux measurement pair, along with a nearby air temperature measurement, a convective heat transfer coefficient for the ceiling slab could be calculated (after the radiant heat flux component had been removed). Figure 4.9 shows the placement of heat flux meters and surface thermocouples on the ceiling. The flux meters were situated along the north side of the room because more air flowed along the north wall in comparison to the south wall, see Section 4.3.2.

The main component of the data logging system for the thermocouples was a multiplexer/signal conditioning card with 32 input channels connected into an 8 channel 12 bit analogue-to-digital converter card mounted in one of the ISA expansion slots of a personal computer. The multiplexer cards are designed for use with thermocouples and consist of 32 double ended inputs connected through some simple input circuitry and pre-amplifiers into two 16 channel multiplexers each of which is connected into an amplifier. The gain of the amplifiers on the signal processing card can be pre-set in the range 10–800 depending on the range of the thermocouple voltage expected. The thermocouple voltages generated in this case were expected to be relatively small and so the gain was set at its maximum. The gain of the A/D card is fixed to give an input voltage range of ±5 V so that, for the 'type T' thermocouples used here, the full range of the input voltage corresponds to a temperature range of 140 K. The analogue-to-digital converter was of the 12 bit type (i.e. the input voltage scale is mapped onto 0–4096 digital output) so that the resulting resolution of the system was 0.07 K/bit.

The personal computer used ran a real time data logging and display program developed by Rees (1998). This program scans a pre-configured number of input channels, 96, every second. Data from each channel is averaged over a longer period before being logged. An averaging period of one minute was used during the cross-flow ventilation experiment. The raw thermocouple data is then processed using methods described in (Rees 1998) and multiplied by a calibration factor described in Appendix C to give a resulting thermocouple temperature. Data from selected channels could be displayed in real time on the screen as a time series temperature graph as well as logged to text files.

The heat flux meters were connected to two of the channels of the thermocouple signal processing/multiplexer card and were logged using the same software. The heat flux meters gave a maximum output of the order of ±2 mV in these experiments and so could be used at the same gain as the thermocouples. The output voltage from the heat flux meters was read through the A/D card and converted to a heat flux reading by a linear relationship between voltage and heat flux supplied by the manufacturer. Heat flux data was averaged and logged in the same way as the temperature measurements.

4.3.4 The Experiment Proper

The experimental equipment was available for two weeks. During this time one nights worth of data was collected due to the time required to setup the equipment and equipment failure problems. After the air flow equipment was set-up, the ceiling slab temperature was elevated using the fan heater and measurements were recorded over the following night between 11 p.m. and 8 a.m. Breaks in the data were due to equipment failure.

4.4 Results

4.4.1 Wind data

Figure 4.10 shows the hourly wind data collected at the local site weather station approximately 100 m on the leeward side of the test room. The beginning of the night was calm. After 3.00 a.m. the wind speed increased, except for a calm period between six and seven in the morning, it averaged over 1 ms^{-1} for the rest of the night.

Figure 4.11 shows the wind data recorded by the ultrasonic anemometer positioned 1 m outside the bedroom window. The minute long data samples were averaged over each hour to enable a comparison with the weather station data. The wind speed outside

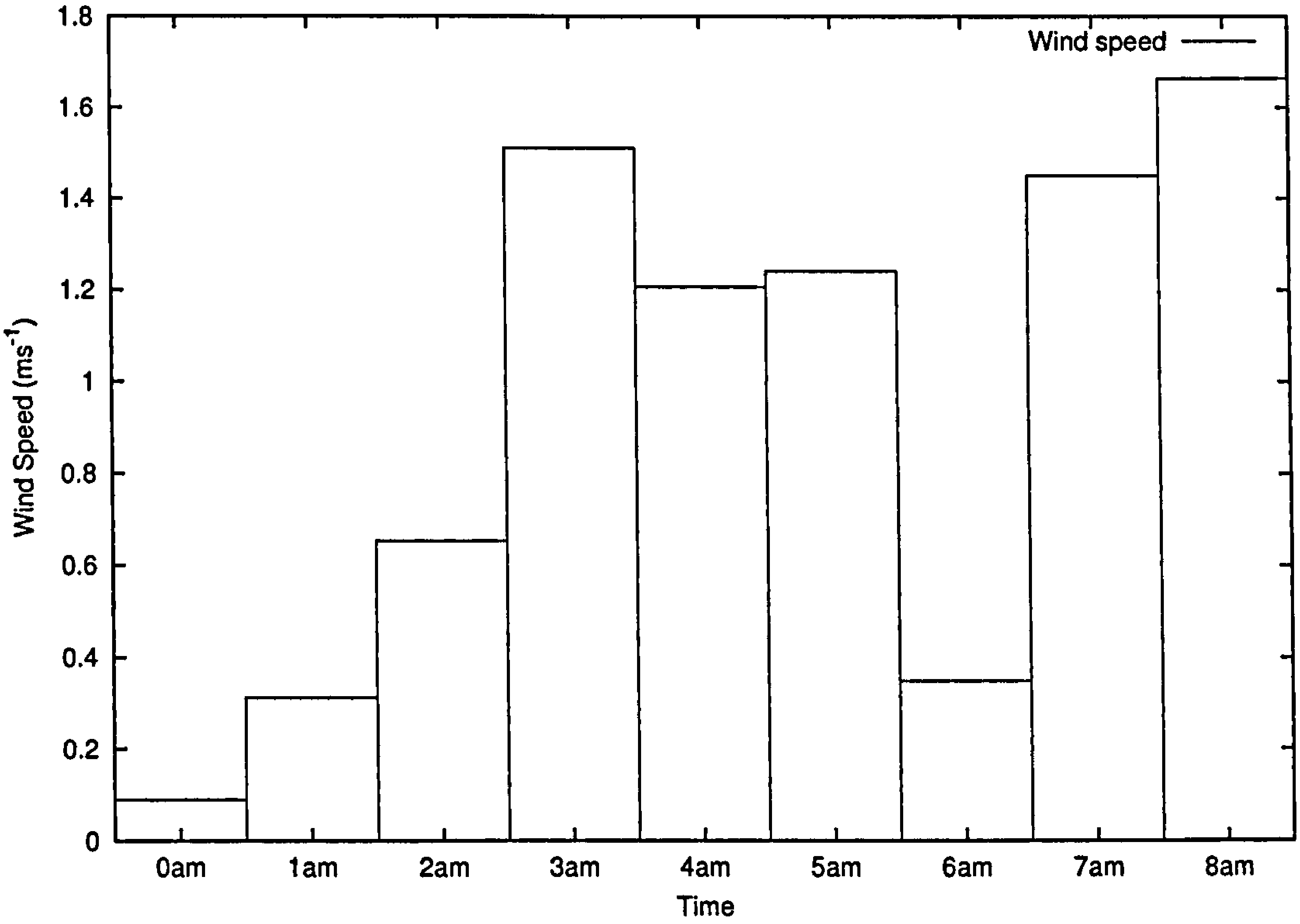

Figure 4.10: Local site weather station wind data.

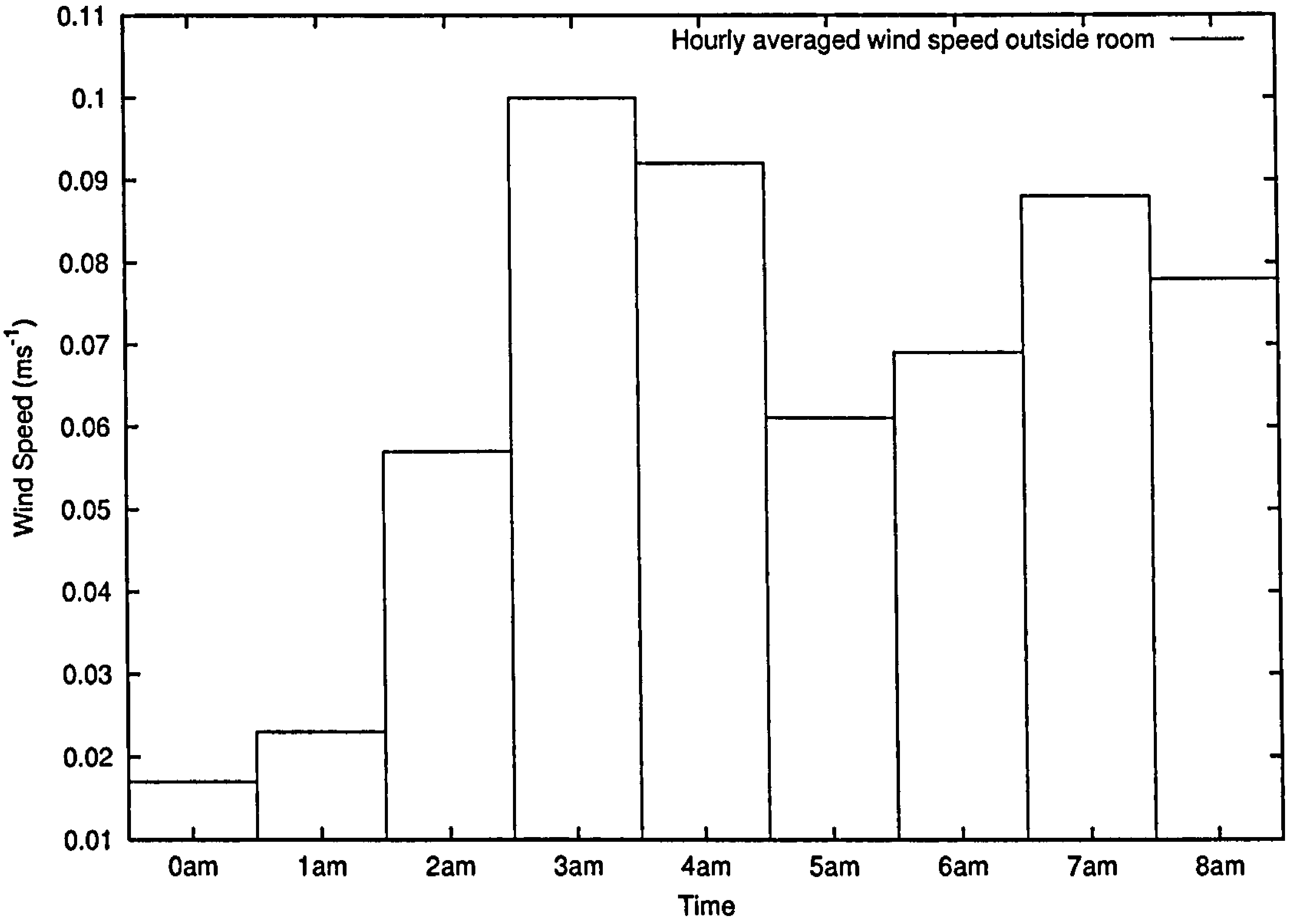

Figure 4.11: Hourly averaged wind speed outside the experimental room.

the room corresponds well with that near the weather station, the correlation coefficient is 0.85. As expected the overall wind speeds are much lower near the David Collett building compared with the more exposed site at the weather station. In both cases, lower wind speeds are seen at the beginning of the night and at around six in the morning. Differences in the form of the wind speed curves could be attributable to the complex building geometry around the experimental site.

Figure 4.12 shows the U, V and W components of the wind velocity recorded by the ultrasonic anemometer. U is in the direction of North, parallel to the plane of the window; V is the axis through the room, from the window to the door; W is the vertical component. The U velocity is generally positive as the wind is blowing from the South. The V component through the building is more steady and is almost entirely in a positive direction. Like the V component W also fluctuates greatly. Near to the building the dynamic pressure of the V component of the wind is converted to a static pressure, hence the lower velocity in this direction.

4.4.2 Room Air Speed and Air Temperatures

Figure 4.13 shows that the air speed at the top of the hopper. Air speeds increase at 3.00 a.m. and decrease at 6.00 a.m. Gaps in the data are due to the Dantec logging equipment failing during the night. The hourly averaged air speeds in the hopper are shown in Figure 4.14. When these averaged speeds are compared with those in Figures 4.11 and 4.10, it can be seen that the air speed at the top of the hopper follows changes in outside air speed closely (although, there is missing Dantec data which makes a direct comparison difficult at hours 4, 5 and 7). The hopper air speed measurement has a correlation coefficient of 0.94 with the weather data, and 0.97 with the air speed measurement from the ultrasonic anemometer. The data for hour 5 a.m. is not used in the correlations due to the lack of anemometer data at this time.

Figure 4.15 shows the temperature recorded by the Dantec sensor in the hopper plotted along side the outside temperature measured at the local site weather station. The temperature of the room air is found by averaging the Dantec anemometer measurements, this average is also plotted in Figure 4.15. When the wind speed is large the air temperature in the hopper approaches that of the weather station; the sensor 'sees' mostly outside air. As the outside wind speeds falls, the hopper temperature measurement approaches the average room air temperature; the sensor 'sees' mostly room air (see also Figure 4.16).

Figure 4.16 shows the air speed at heat flux meter sites A (nearest the door) and B (nearest the hopper), as well as in the hopper. Hopper air speed before 3.00 a.m. is small and the air speeds in question are not high enough for the flow to attach to the ceiling; instead the air might fall to the floor and mix with the room air. This theory is supported by the velocity profiles plotted in Figure 4.17. The Dantec sensors used were

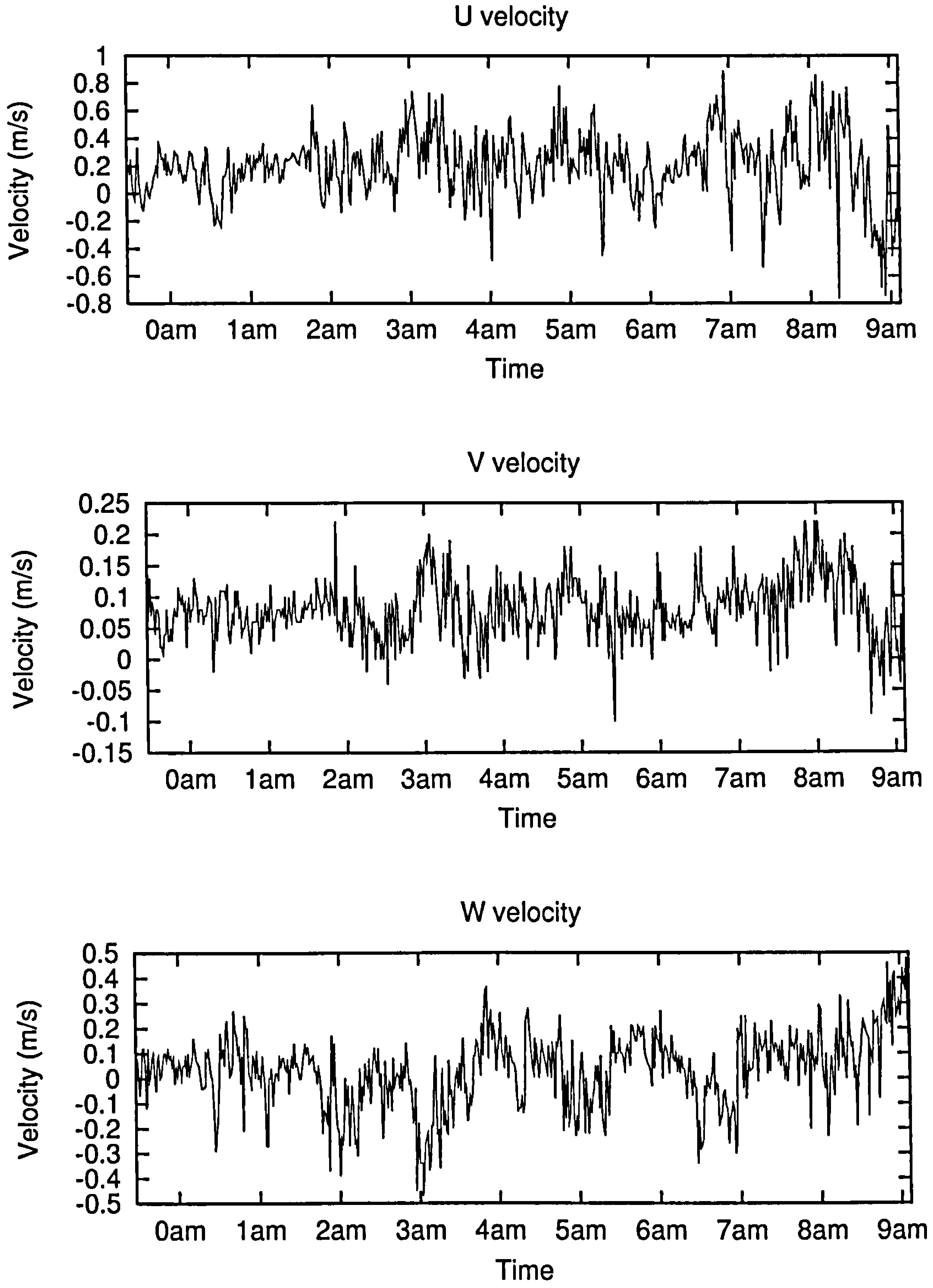

Figure 4.12: Air velocity from the ultrasonic anemometer positioned outside the experimental room.

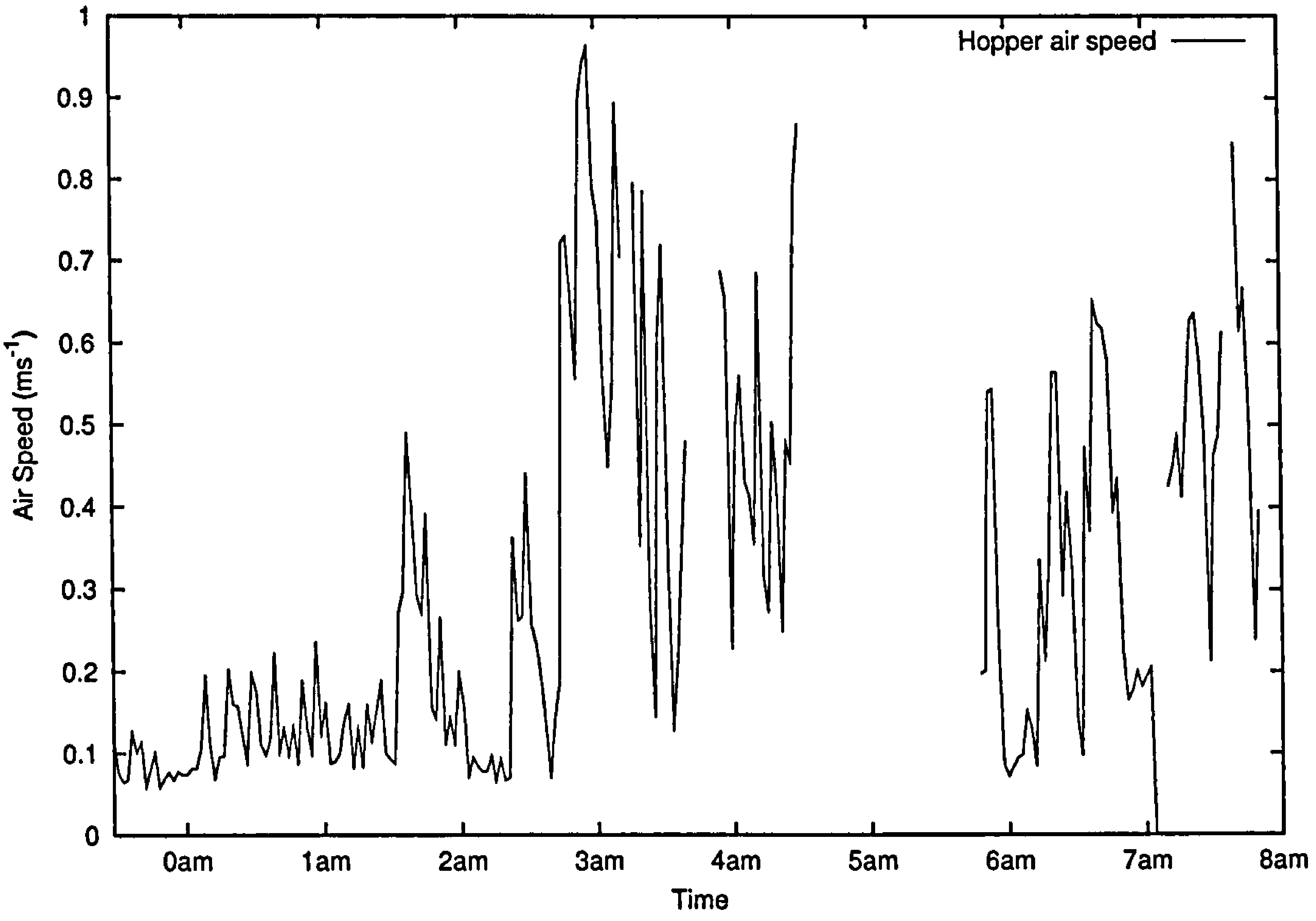

Figure 4.13: Air speed in the hopper opening.

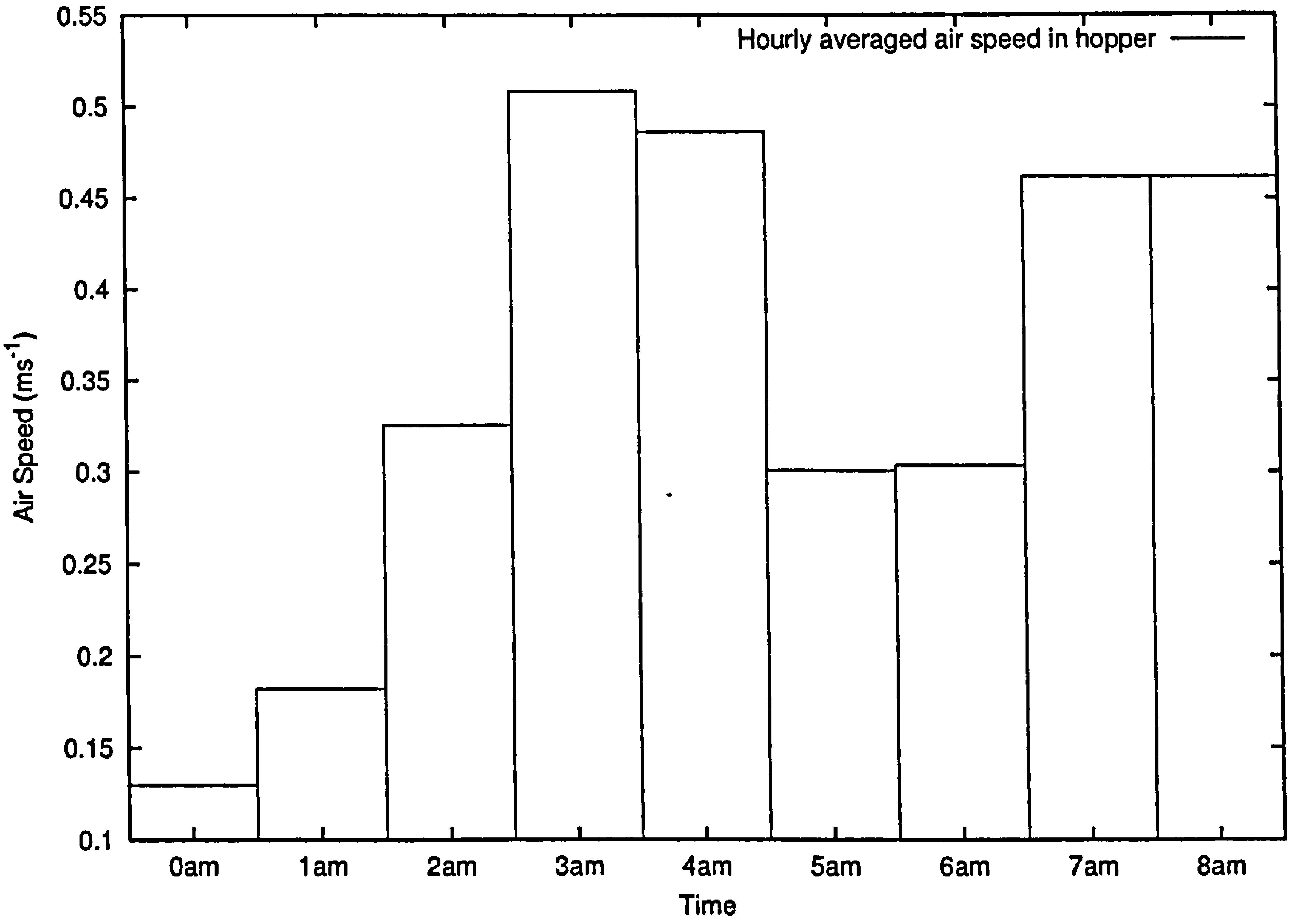

Figure 4.14: The air speed in the hopper opening averaged over hourly intervals.

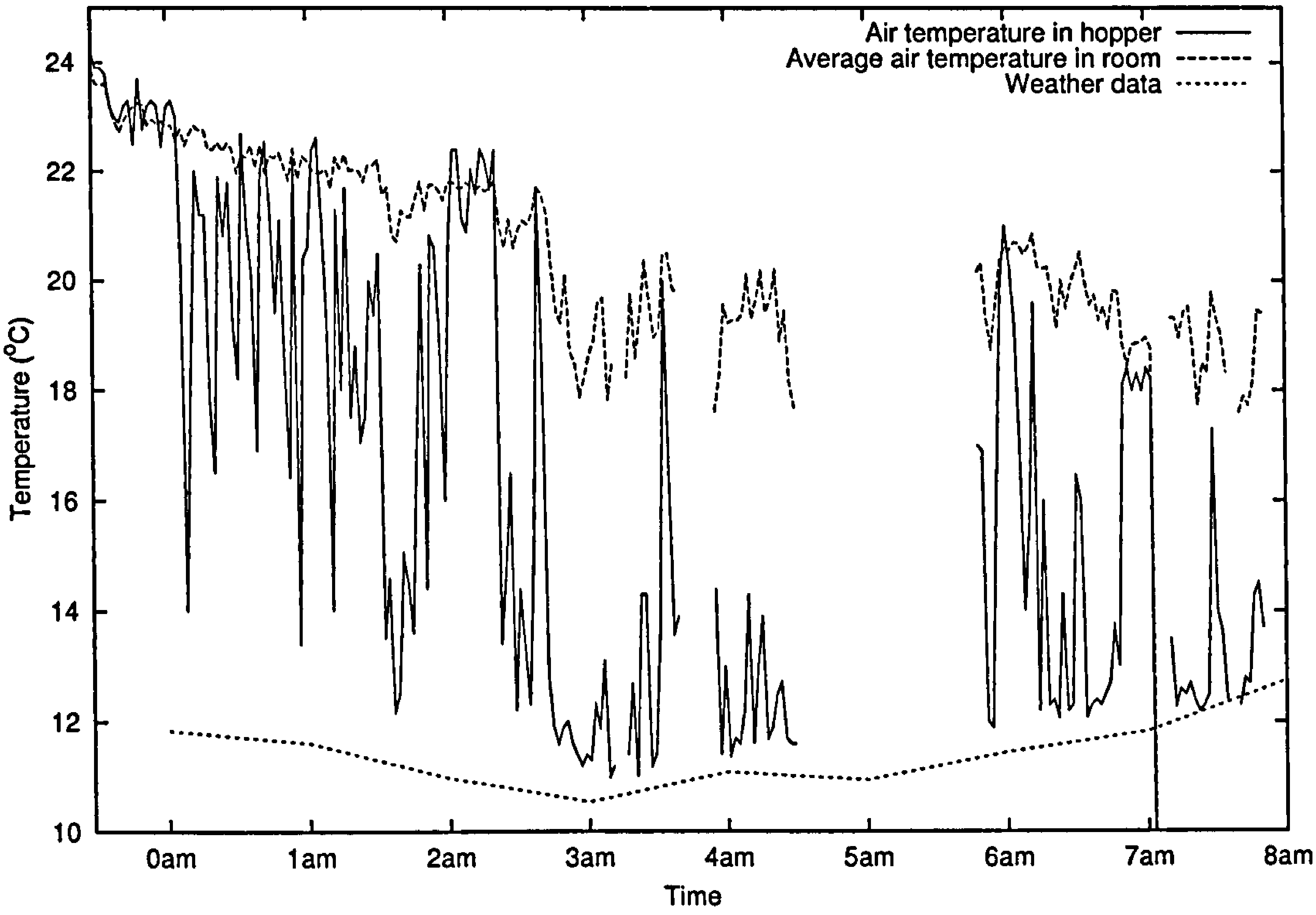

Figure 4.15: Air temperature in the hopper.

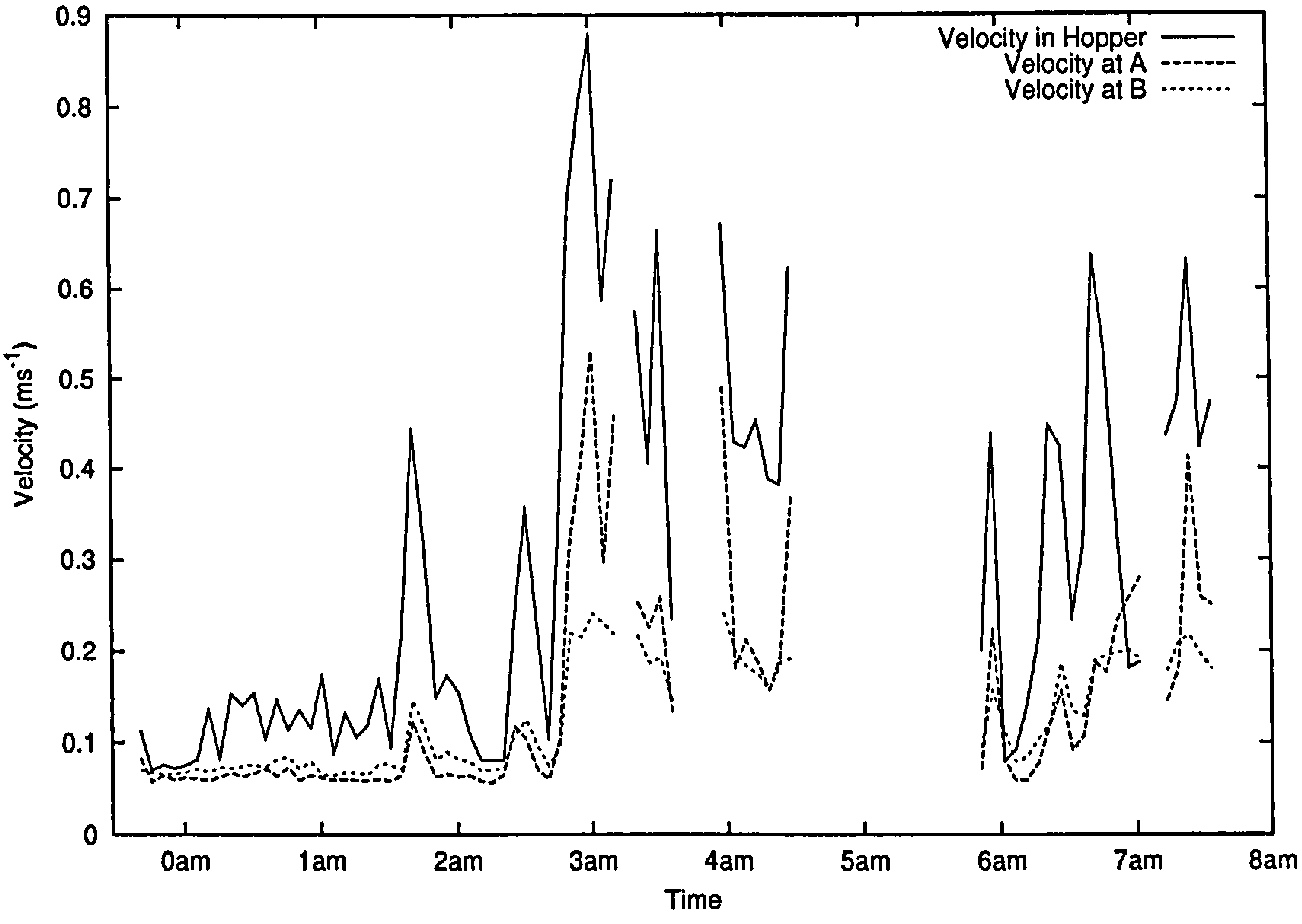

Figure 4.16: Air speed at heat flux meter sites A and B, and in the hopper.

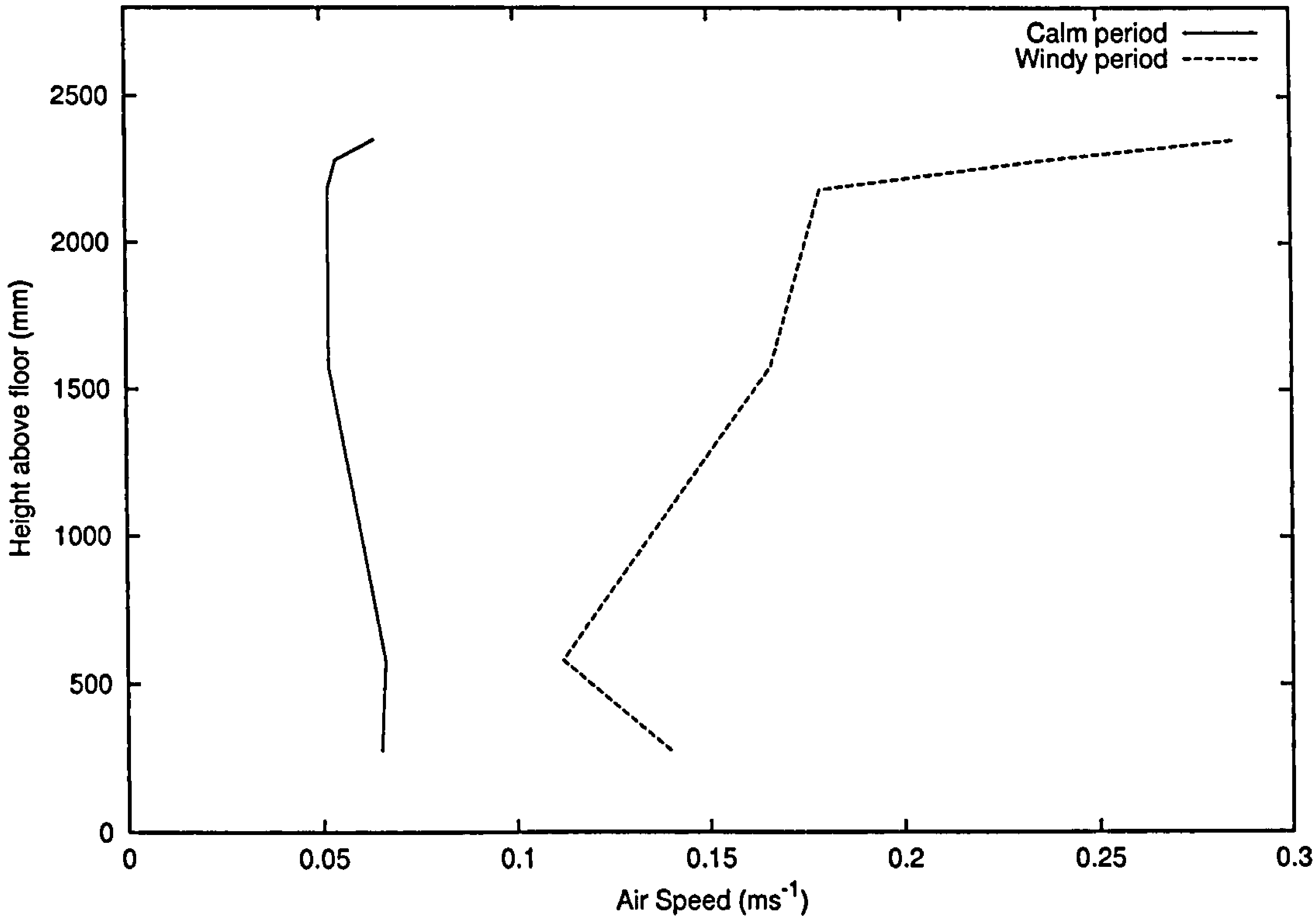

Figure 4.17: Air speed profile at sensor site B.

Table 4.1: Correlation between hourly averaged air speed at various locations and the weather data.

Measurement	Correlation
Ultrasonic anemometer	0.85
Hopper air speed	0.94
Dantec sensor 19	0.97
Dantec sensor 1	0.94

Ch19–24 on the anemometer stand at site B, nearest the hopper. In the calm period, the velocity profile is almost constant over the height of the room. After 3.00 a.m. there is a large velocity profile near to the ceiling showing that the air flow attaches.

Correlation data between various hourly averaged air speed measurements taken is given in three tables:

- Table 4.1 gives the correlation between hourly averaged air speed at various locations and the weather data;
- Table 4.2 gives the correlation between hourly averaged air speed at various locations and the ultrasonic anemometer;
- Table 4.3 gives the correlation between hourly averaged air speed at various locations and the hopper air speed.

Table 4.2: Correlation between hourly averaged air speed at various locations and the ultrasonic anemometer.

Measurement	Correlation
Hopper air speed	0.97
Dantec sensor 19	0.93
Dantec sensor 1	0.92

Table 4.3: Correlation between hourly averaged air speed at various locations and the hopper air speed.

Measurement	Correlation
Dantec sensor 19	0.98
Dantec sensor 1	0.95

It can be seen from Table 4.1 that the weather site air speed data correlates very well with the anemometer measurements in the hopper, and at the ceiling at flux meter sites A and B. The weather site air speed correlates slightly less well with the outside air speed measured with the ultrasonic anemometer. This may be due to the sensitivity of the ultrasonic anemometer measurements to instantaneous changes of the prevailing wind direction or other local effects associated with the obstruction that the building presents to the air flow.

Table 4.2 shows that the ultrasonic anemometer data, and hence, the wind speed 1 m outside the room, correlates well with the hopper and ceiling air speeds. Table 4.3 shows that the hopper air speeds correlate well with both of the ceiling air speeds.

Figures 4.18 and 4.19 show an air speed ratio at heat flux meter sites A and B respectively. The ratio is calculated by dividing the air speed next to the ceiling by the air speed at midheight, (i.e., Sensor 1/Sensor 5 at site A, and Sensor 19/Sensor 23 at site B). The ratio was calculated to see if it could be used as an indication of whether the flow attaches to the ceiling or falls to the floor on entry to the room.

The air speed ratio at heat flux meter site B is approximately equal to 1 during calm periods when the flow can be assumed to be detached from the ceiling at site B. The picture is more complicated at heat flux meter site A. Here the air speed ratio can be greater than 2 during the calm period. This is due to the fact that air near the ceiling at A is entrained back towards the hopper into the descending main flow stream.

The air speed ratios were also averaged over each hour to see if a correlation could be found between the ratios and the hopper air speed. The hourly averaged air speed ratio at A and B are shown in Figures 4.20 and 4.21 respectively. Table 4.4 shows the correlations between the air speed ratios and the hopper air speed. The fact that the correlation coefficients are high for both air speed ratios shows that in general an increase in air speed in the hopper will increase the air speed near the ceiling more than in the middle of the room.

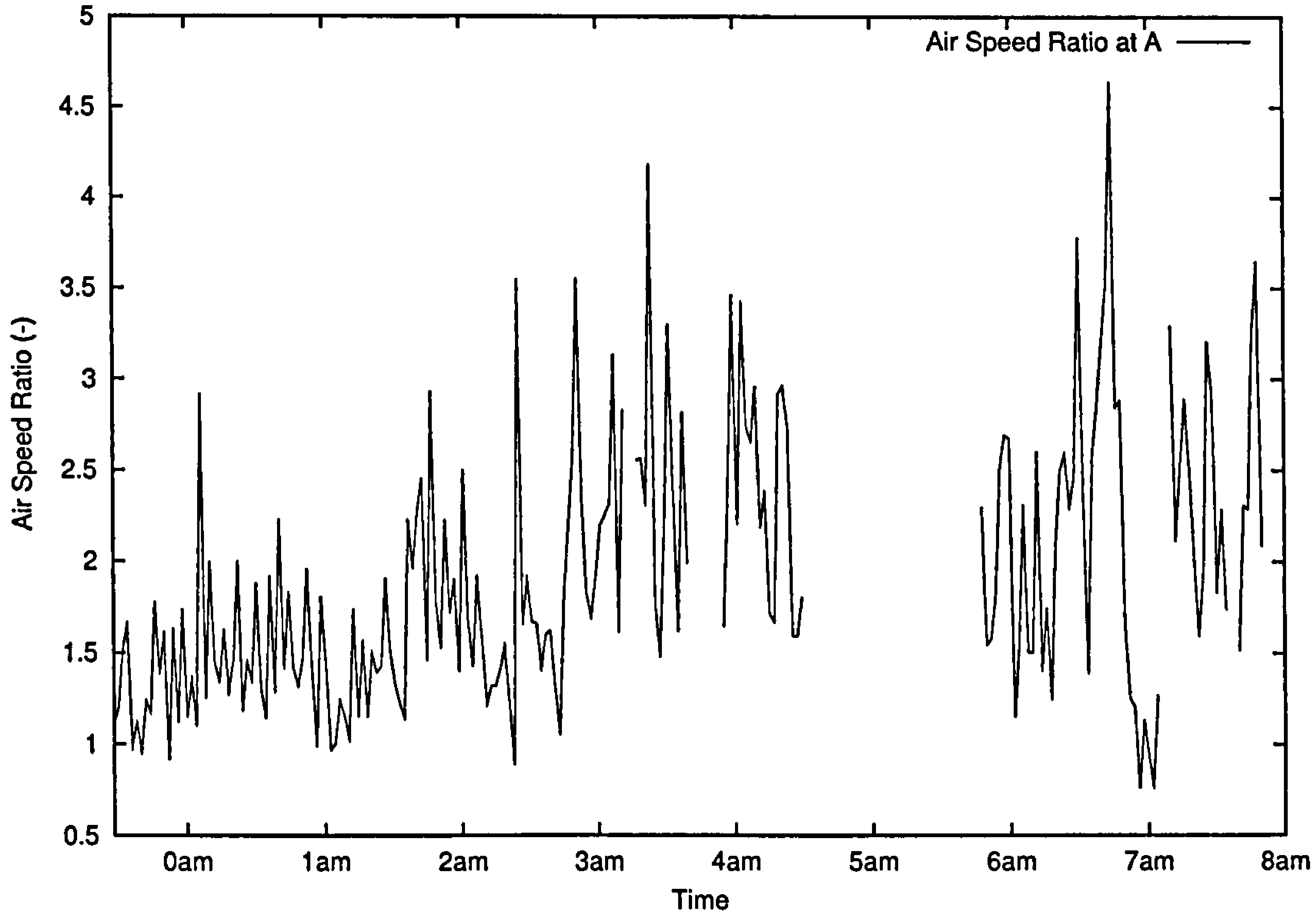

Figure 4.18: Air speed ratio at heat flux meter site A.

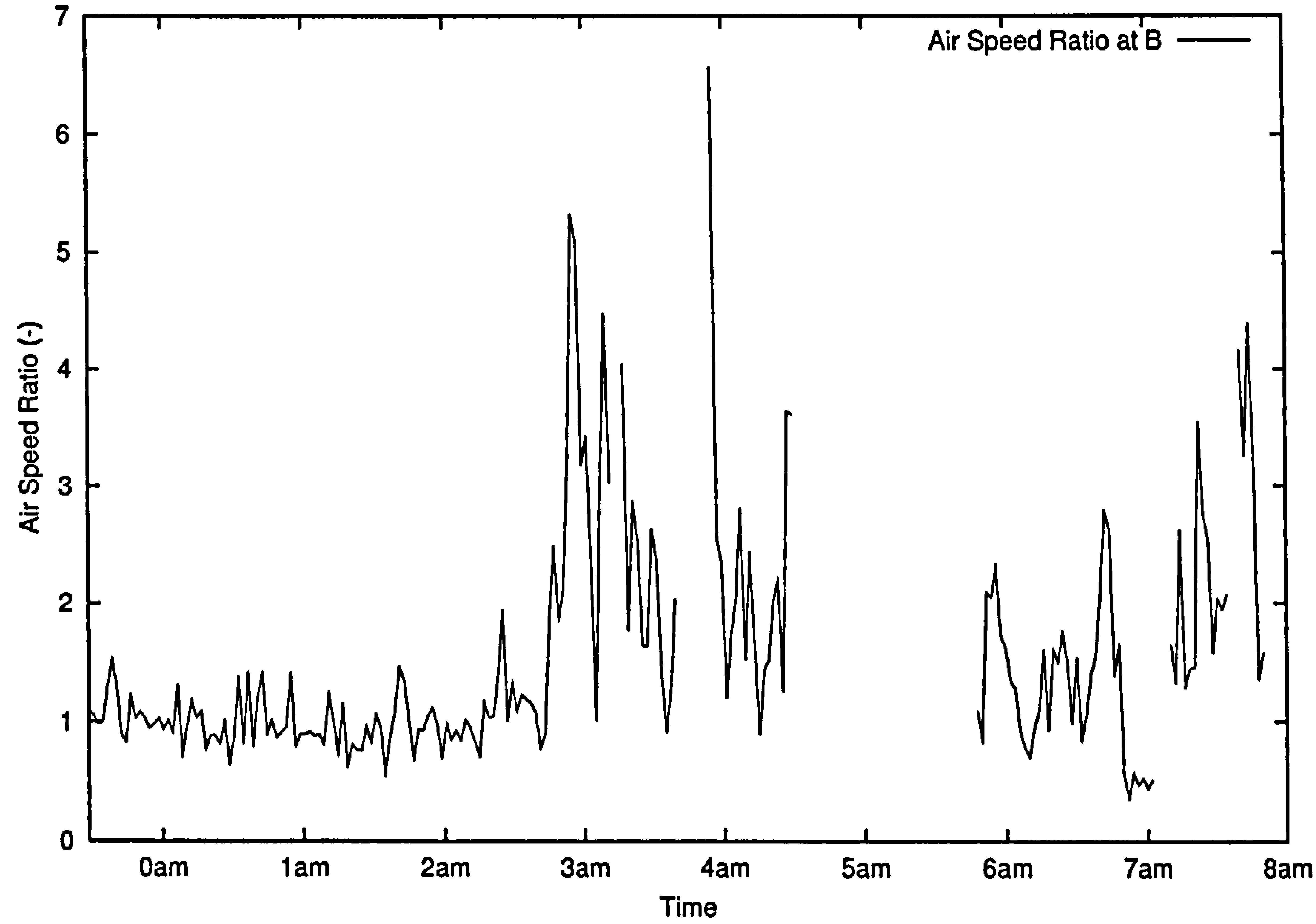

Figure 4.19: Air speed ratio at heat flux meter site B.

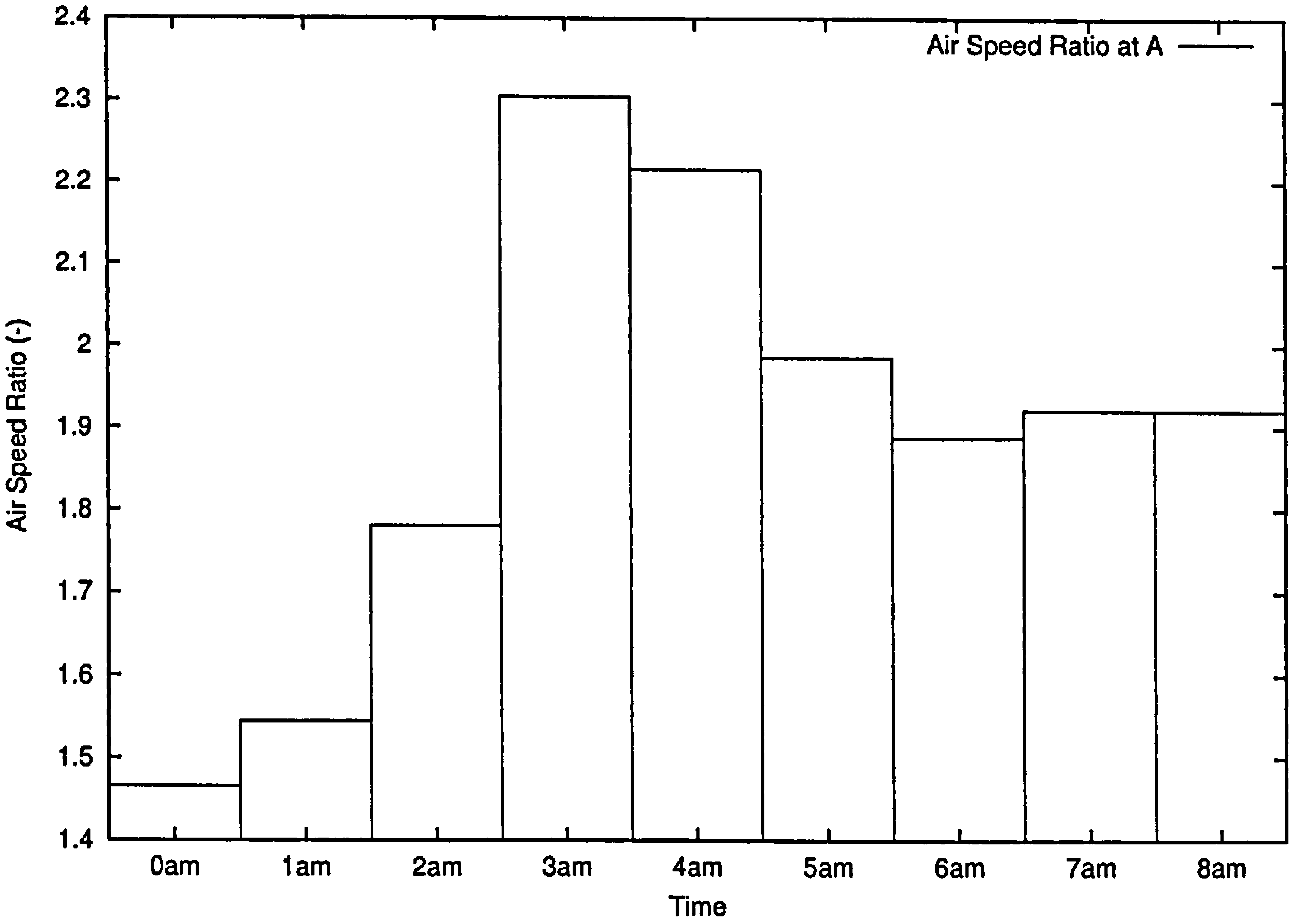

Figure 4.20: Air speed ratio at heat flux meter site A.

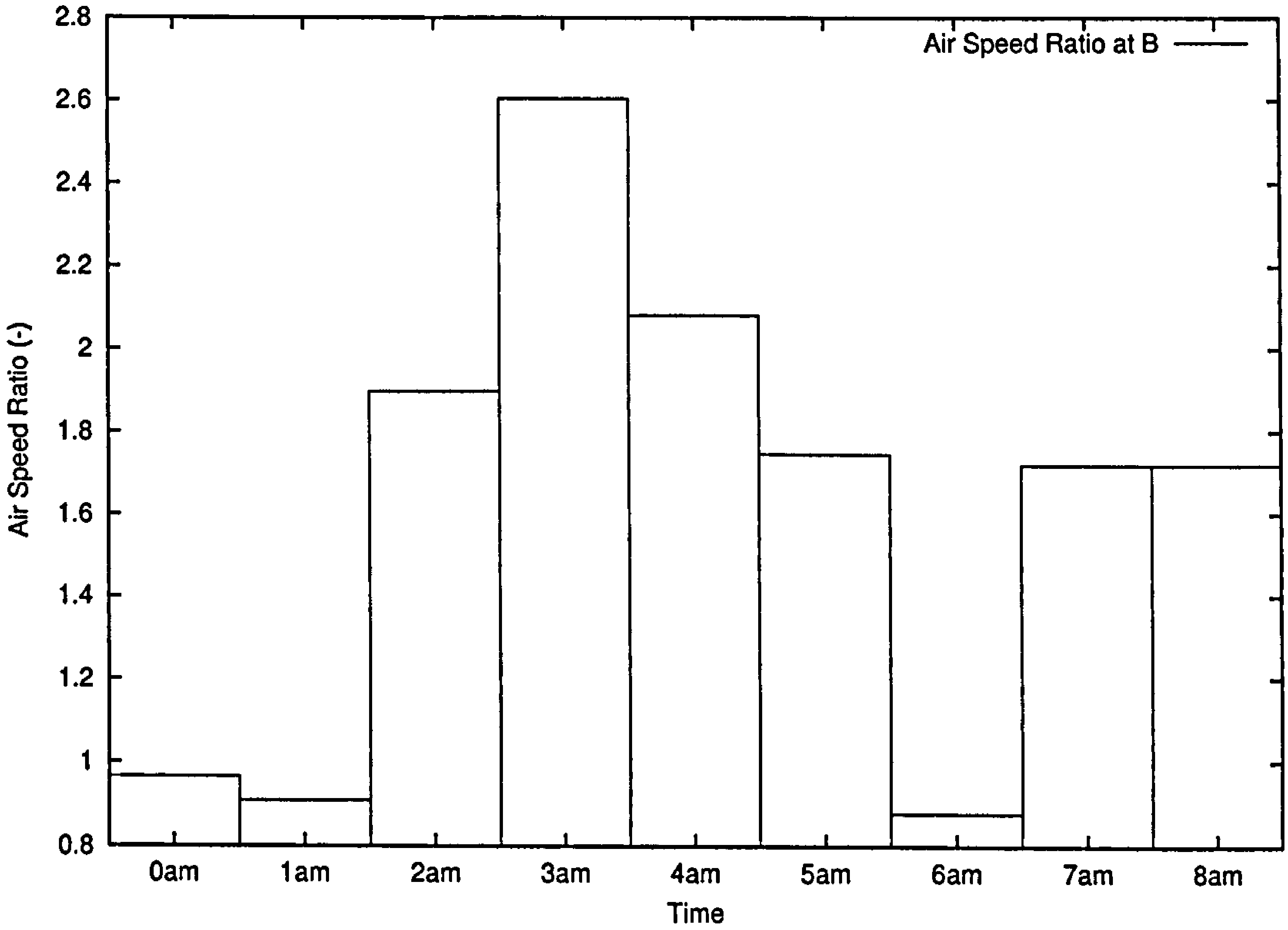

Figure 4.21: Air speed ratio at heat flux meter site B.

Table 4.4: Correlation data for the hourly averaged hopper air speed.

Measurement	Correlation
Air speed ratio A	0.92
Air speed ratio B	0.84

The hourly averaged air speed ratio at B is actually below 1 for the hours of 12 p.m., 1 a.m. and 6 a.m., thus, the air speed at midheight is larger than at the ceiling. This can be attributed to the acceleration of the main flow stream as it falls to the floor.

Existing thermal analysis programs use reference weather data sets and they have relatively crude methods of transposing these data to what would be expected at the building, i.e., a reduction of local air speeds due to external obstructions seen in urban and suburban spaces when compared to the countryside environment. This study shows that there can be good correlation between local internal and external hourly averaged air speeds and remote external air speed measurements.

4.4.3 Detachment Point

Next, we examine if the relationship between Archimedes number (Ar) and detachment point derived from the two-dimensional CFD parametric study is supported by the results from the experimental measurements presented in this chapter. Archimedes number is given by Equation 3.81 derived in Chapter 3 and repeated below,

$$Ar = \frac{1}{T_{in}} \frac{g\Delta T_{ci}}{v_{in}^2} \frac{A_{in}}{l},$$

where:

g	is the gravitational acceleration;
T_{in}	is the temperature of the air in the hopper;
ΔT_{ci}	is the temperature difference between the inflow (hopper) air and the ceiling;
$\frac{A_{in}}{l}$	is the area of the window per unit length of facade;
v_{in}	is the hopper air speed.

Figure 4.22 shows Archimedes number plotted against time during the experiment. At the beginning of the night and again at around 6 a.m. Archimedes number is large, sometime above 1.14 which is the point where the 2D CFD study suggests the main flow stream will fall on entry to the room. During the higher velocity periods of the night at around 3 a.m. Archimedes number is below 0.39, the point where the 2D CFD study

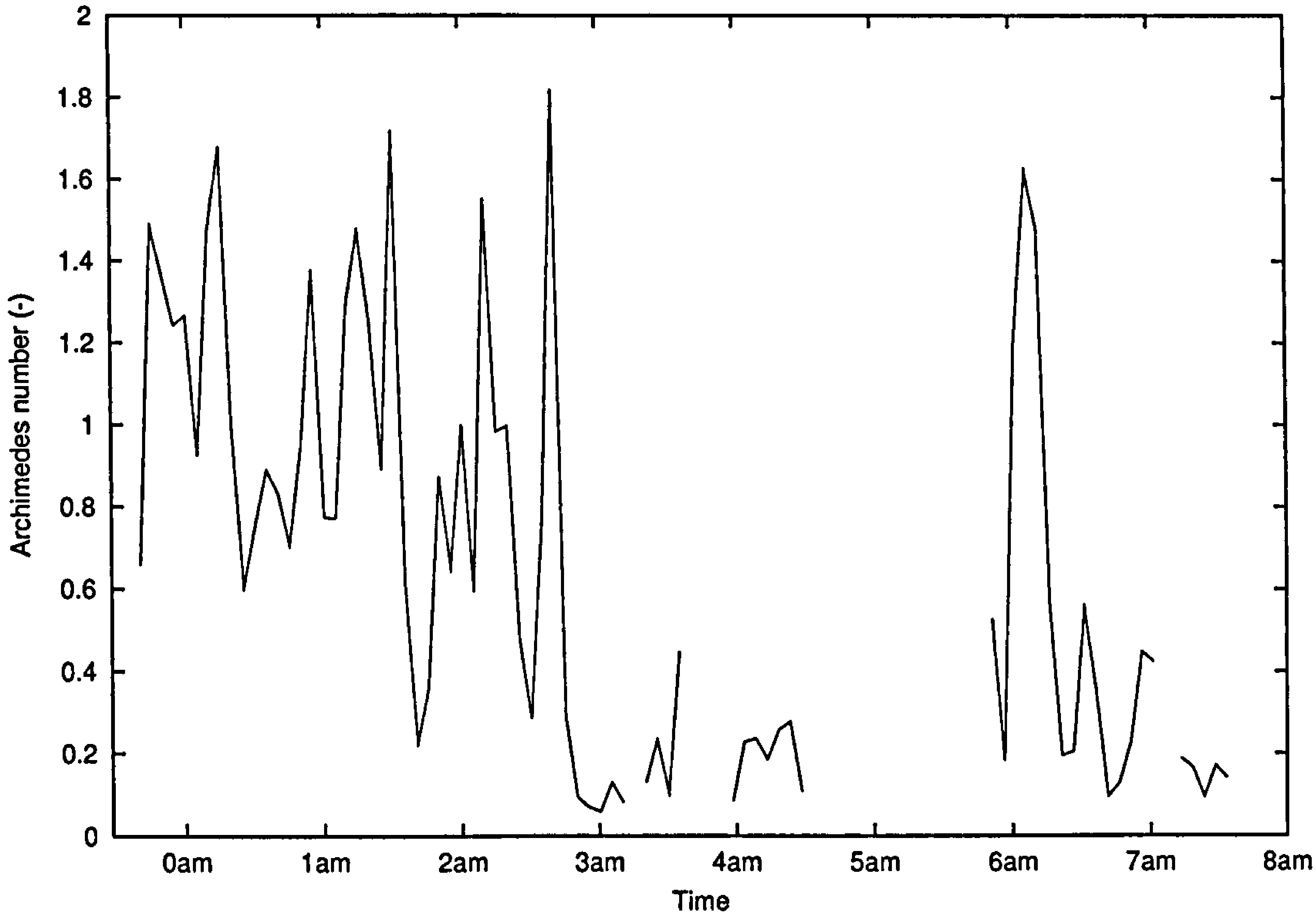

Figure 4.22: Archimedes number versus time during experiment.

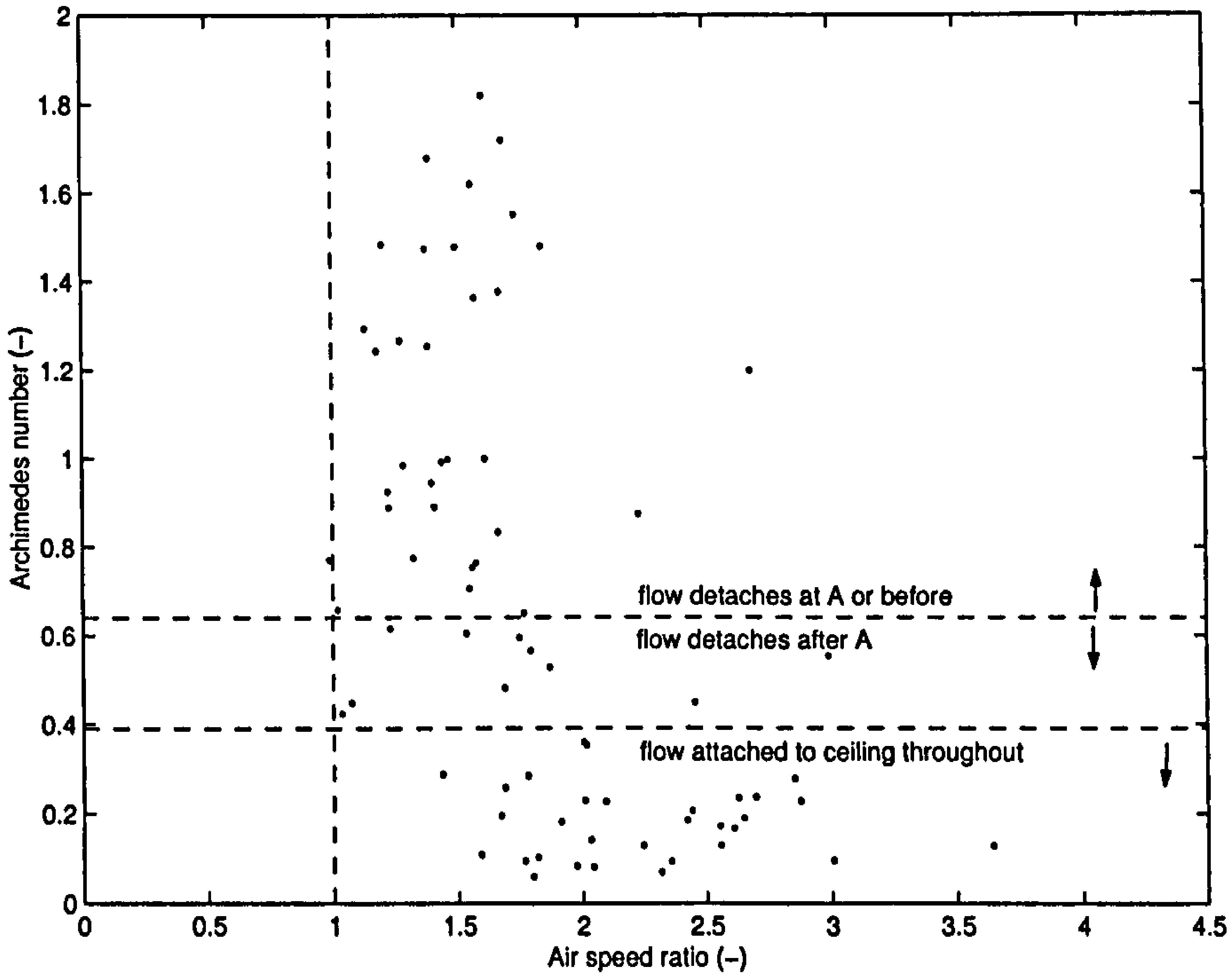

Figure 4.23: Archimedes number versus air speed ratio at heat flux meter site A.

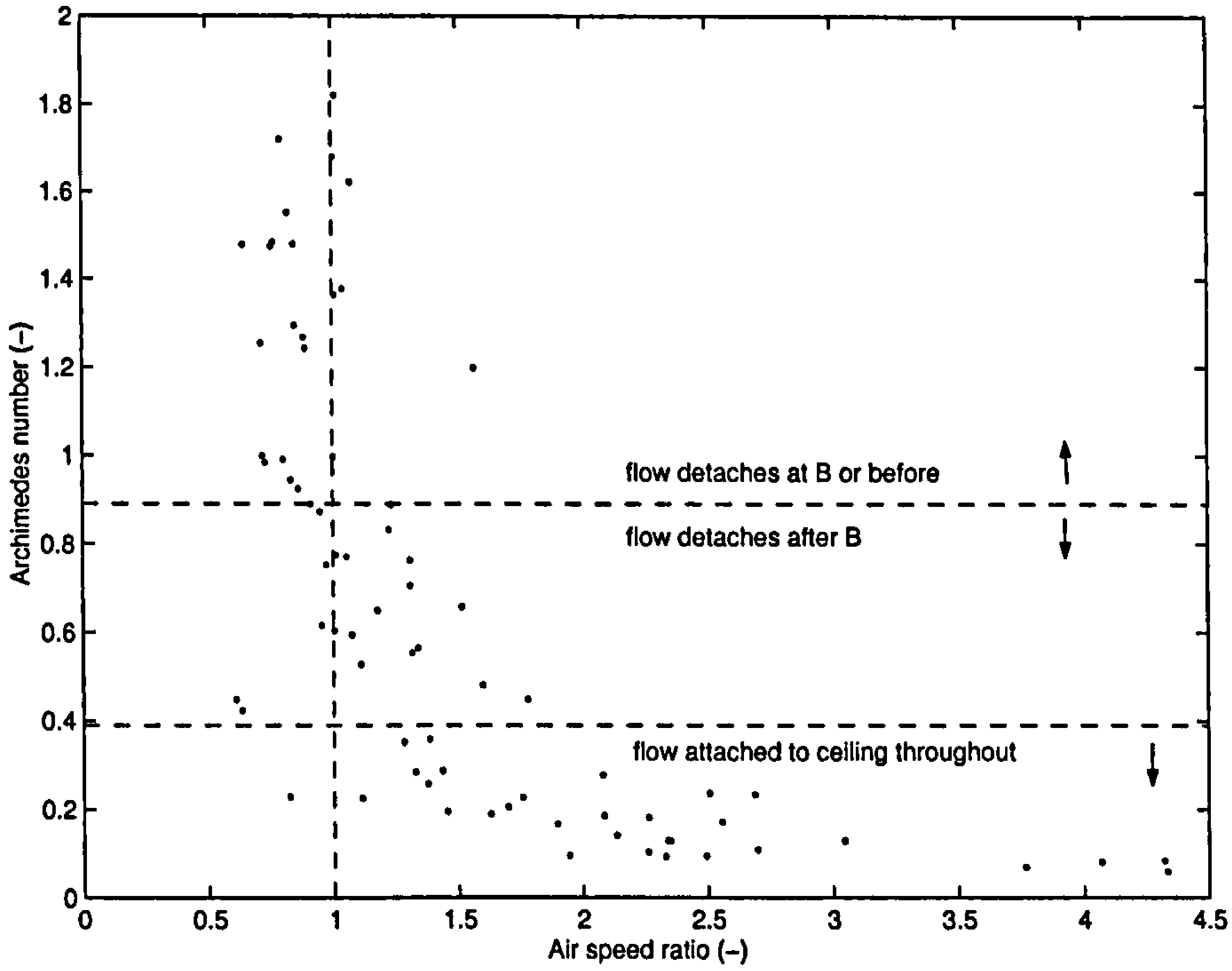

Figure 4.24: Archimedes number versus air speed ratio at heat flux meter site B.

suggests the main flow stream will remain attached to the ceiling throughout the room width.

Figures 4.23 and 4.24 show Archimedes number plotted against air speed ratio and sites A and B respectively. When the air speed ratio is above 2 at sites A and B the Archimedes number is nearly always less than 0.39 the point where the 2D CFD study suggests the main flow stream will remain attached to the ceiling throughout the room width. This shows there is good correlation between high air speed ratios and attached ceiling flow.

When the air speed ratio is less than or equal to 1 the flow detachment position should be close to the anemometer stand in question. Figure 4.23 shows there are very few times when the air speed ratio at site A is less than or equal to 1 suggesting the flow does not detach at this point very often. Figure 4.24 shows there are many times when the air speed ratio at site B is less than or equal to 1. The majority of these instances occur at Archimedes numbers above 0.89 (the point where the 2D CFD study suggests the main flow stream will detach close to site B).

These findings suggest that air speed ratio is a good indicator of flow regime and that the correlation between Archimedes number and detachment position postulated in Chapter 3 from CFD simulation results agrees well with the experimental measurements.

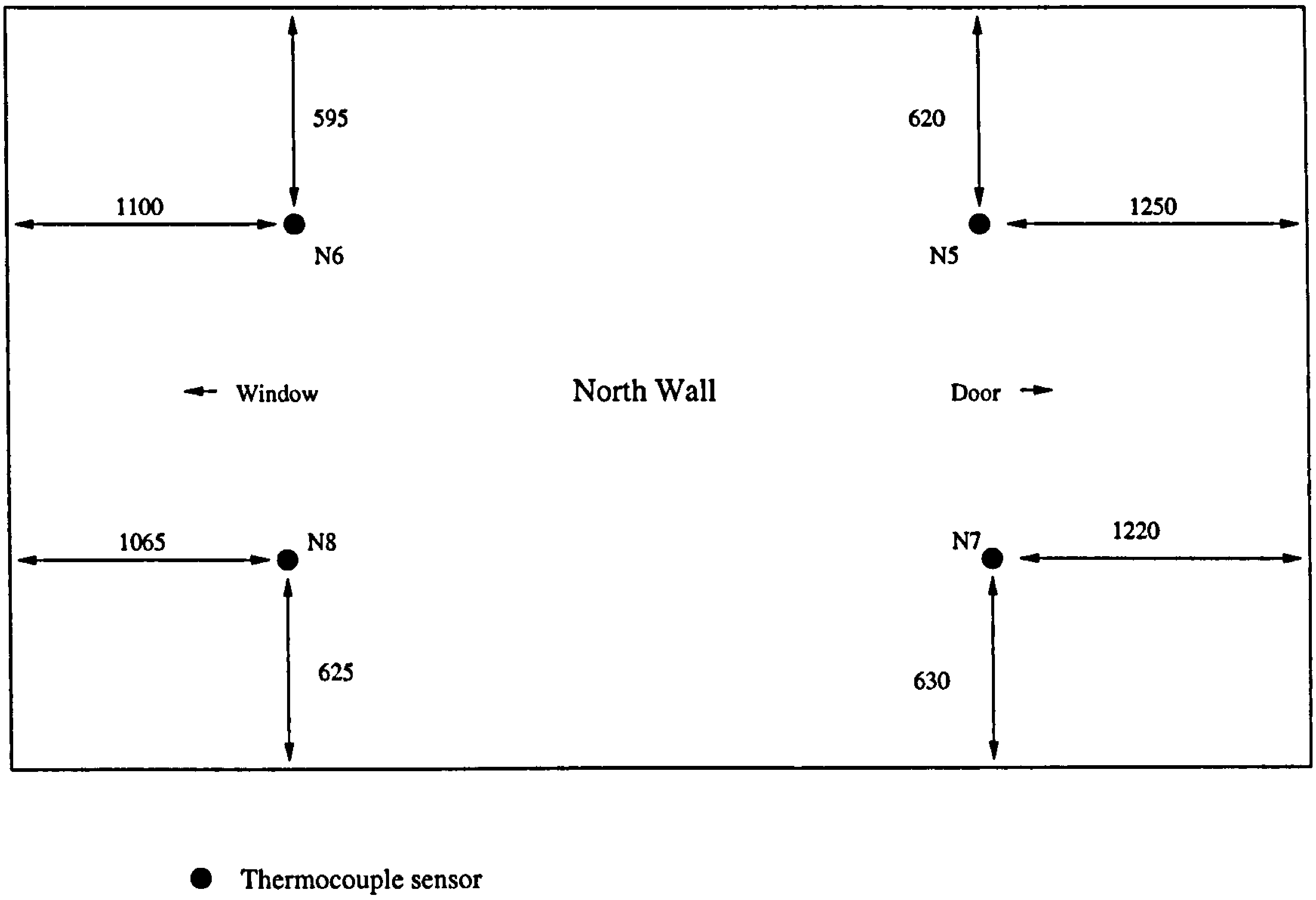

Figure 4.25: North wall thermocouple placement.

4.4.4 Room Temperatures

In this section the ceiling temperature at heat flux meter sites A and B are compared to the temperatures of various surfaces, nearby air temperatures, and the radiant temperature seen by the heat flux meter in question.

The radiant temperature was calculated using the surface thermocouple temperature measurements and a view factor that corresponds to the area that the measurement was supposed to represent. For example, the temperature measurement from each of the four thermocouples on the north wall (Figure 4.25 shows the north wall thermocouple placement) is assumed to equal the temperature of 1/4 of the north wall. The radiant temperature is then calculated by using,

$$T_r = \Sigma(f_i T_i), \tag{4.1}$$

where:

T_r is the radiant temperature seen by the heat flux meter (K).

f_i is the view factor from a point that represents the ceiling heat flux meter and the area of surface i;

T_i is the temperature of surface i (K).

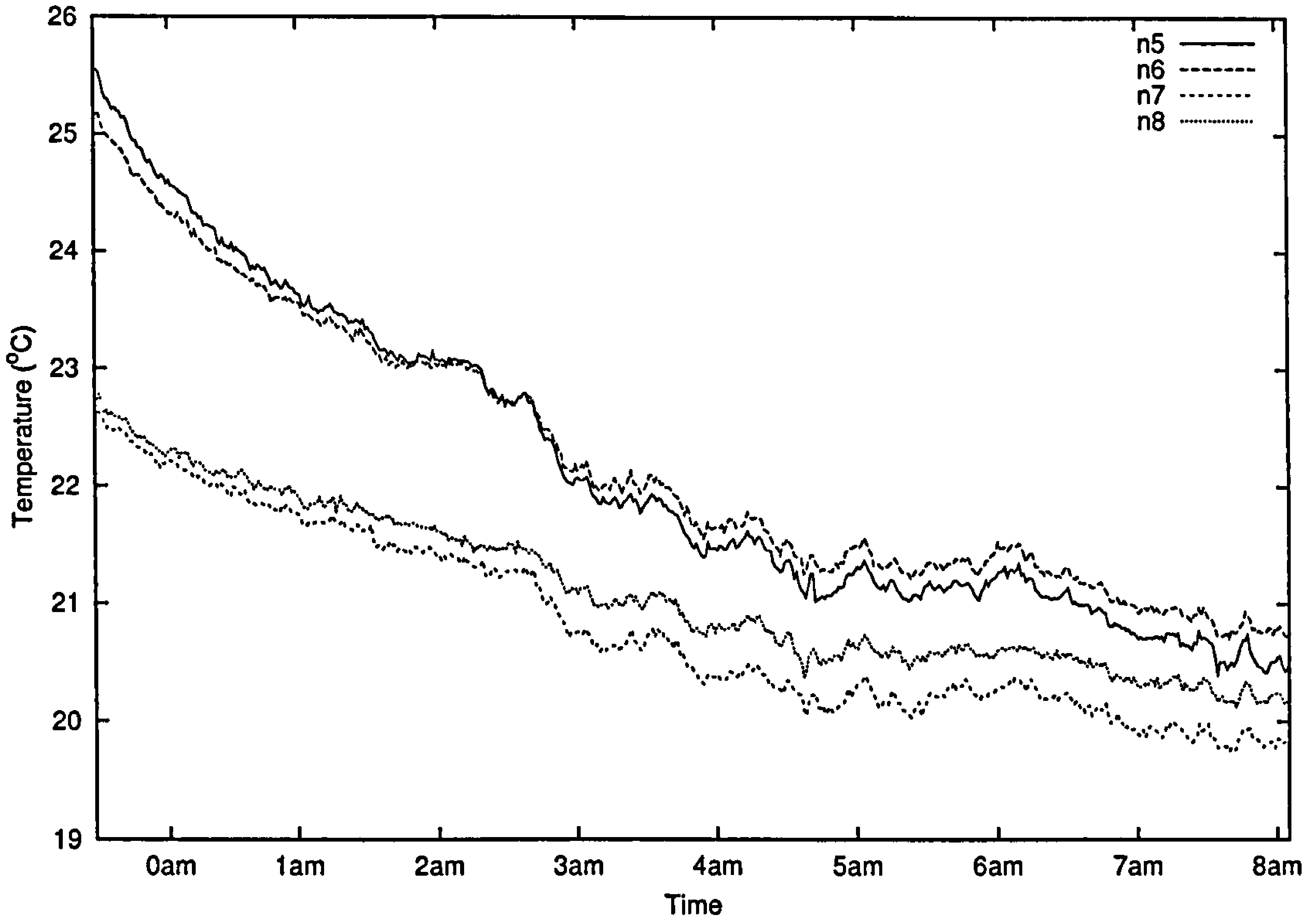

Figure 4.26: North wall temperature.

There are four temperature measurements taken on each of the 5 surfaces that the heat flux meters can "see", i.e., the floor surface, and the north, south, east and west walls. This means the summation given in Equation 4.1 is performed over a total of 20 surface areas.

There is an error in the radiative heat transfer calculation due to the fact that only four temperature measurements were taken on each surface. This is particularly the case with the vertical surfaces where there is a large thermal stratification. Figure 4.26 shows the temperature measurements on the north wall, it can be seen that the temperature at N5 and N6 (~1790 mm above the floor) is higher than at N7 and N8 (~630 mm above the floor).

Figure 4.27 and 4.28 show the temperature of the ceiling, compared with the radiant temperature and the air temperature, at heat flux meter sites A and B respectively. The ceiling temperature was approximately 1 K above the radiant temperature throughout the night at both heat flux meter sites.

The surface temperature measurements are now used to derive the radiative heat flux component of the total heat flux measured by the heat flux meters.

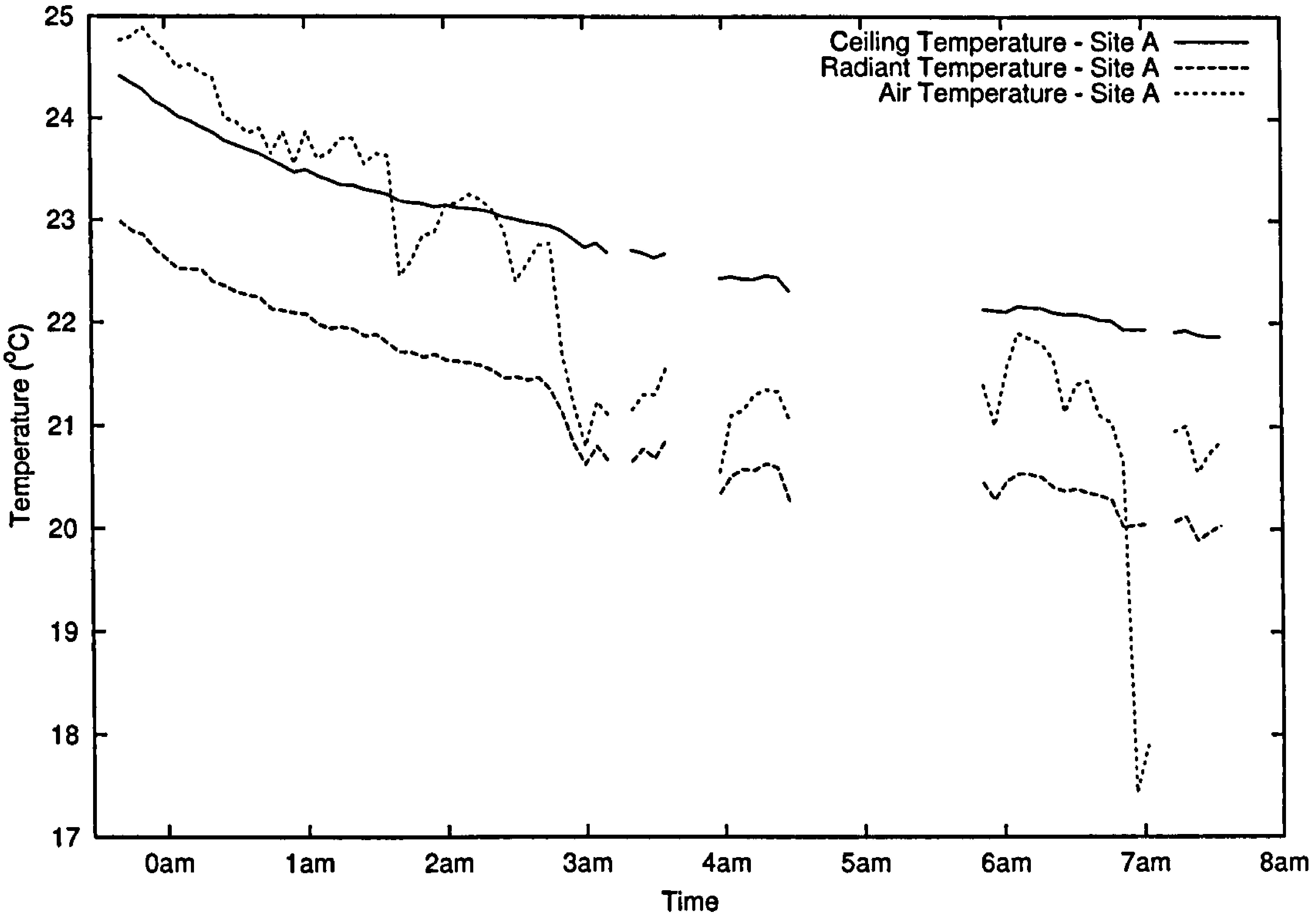

Figure 4.27: Ceiling temperature, radiant temperature, and the air temperature at heat flux meter site A.

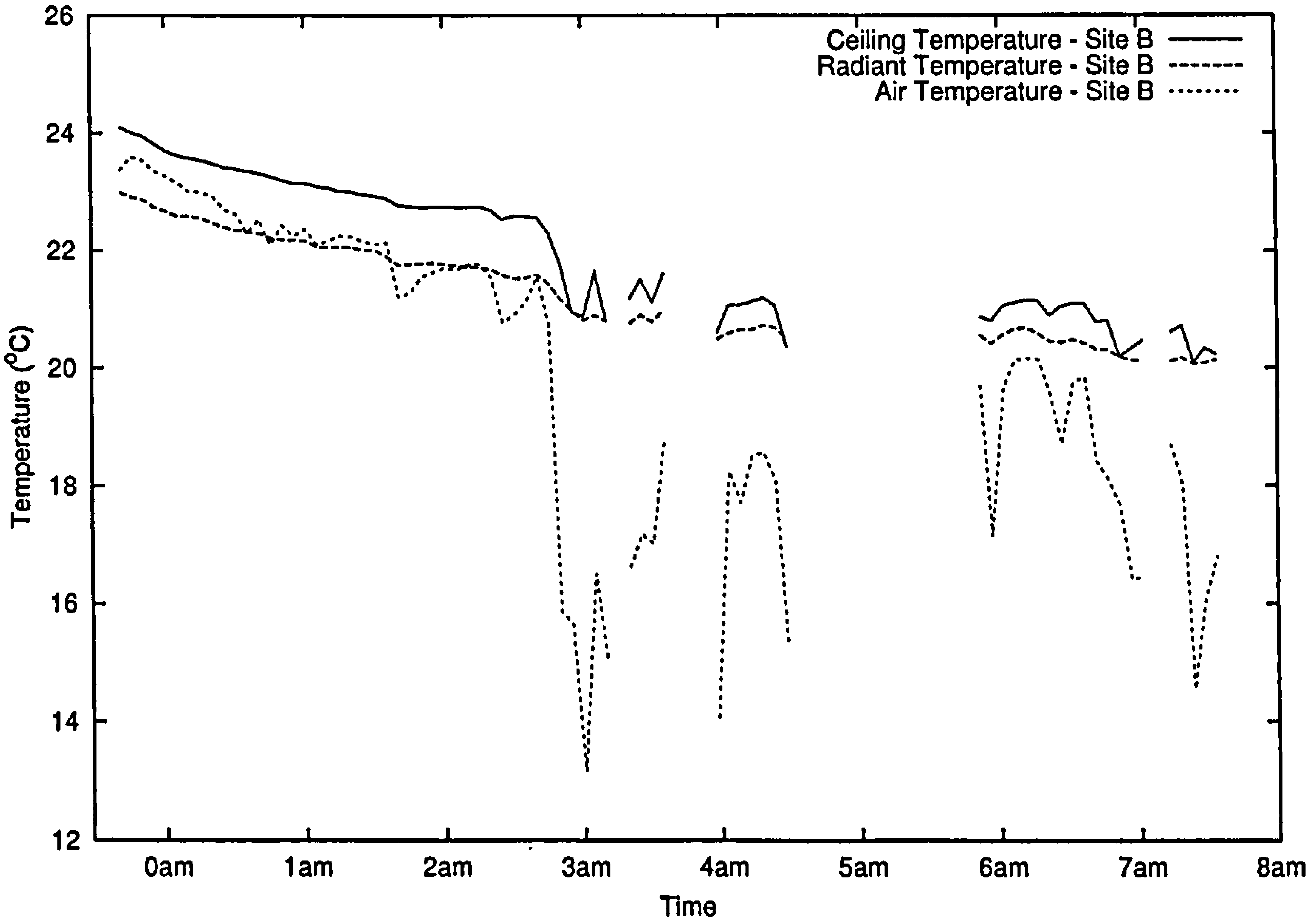

Figure 4.28: Ceiling temperature, radiant temperature, and the air temperature at heat flux meter site B.

4.4.5 Heat Flux

In order to determine the convective heat transfer coefficient at the ceiling, the original purpose behind the experiment, the convective heat flux per unit area, q_c, must be found from the total heat flux measurement, q_t, and the radiative heat flux, q_r,

$$q_c = q_t - q_r. \tag{4.2}$$

The radiative heat transfer is found from,

$$q_r = \varepsilon\sigma\Sigma(f_i\,(T_c^4 - T_i^4)), \tag{4.3}$$

where:

f_i	is the view factor from the ceiling and surface i;
T_c	is the ceiling temperature (K);
T_i	is the temperature of surface i (K);
ε	is the emissivity of the ceiling; and
σ	is the Stefan Boltzmann constant ($5.670e^{-8}\,\mathrm{Wm^{-2}K^{-4}}$).

Figures 4.29 and 4.30 show the total, radiative and convective heat flux components at heat flux meter site A and site B respectively. The absolute value of heat flux, as well as the fluctuations in heat flux, are greater at flux meter site B due to the higher air speeds nearer the window.

There is a marked difference between the flux curves before and after 3 a.m. Before 3 a.m. during the low air speed period when flow detaches on entry to the room radiative heat transfer dominates at both sites, being approximately $7.5\,\mathrm{Wm^{-2}}$. During the 3-5 a.m. and 7 a.m. high speed episodes convective heat transfer increases, and dominates at site B.

The correlation between high convective heat flux and high near ceiling air speeds is good. The convective heat flux is now used to derive convective heat transfer coefficients at both sites A and B.

4.4.6 Heat Transfer Coefficients

The convective heat transfer coefficient, h_c, is found from

$$\begin{aligned} h_c &= \frac{q_c}{T_c - T_a} && (4.4)\\ &= \frac{q_t - \varepsilon\sigma\Sigma(f_i\,(T_c^4 - T_i^4))}{T_c - T_a}, && (4.5) \end{aligned}$$

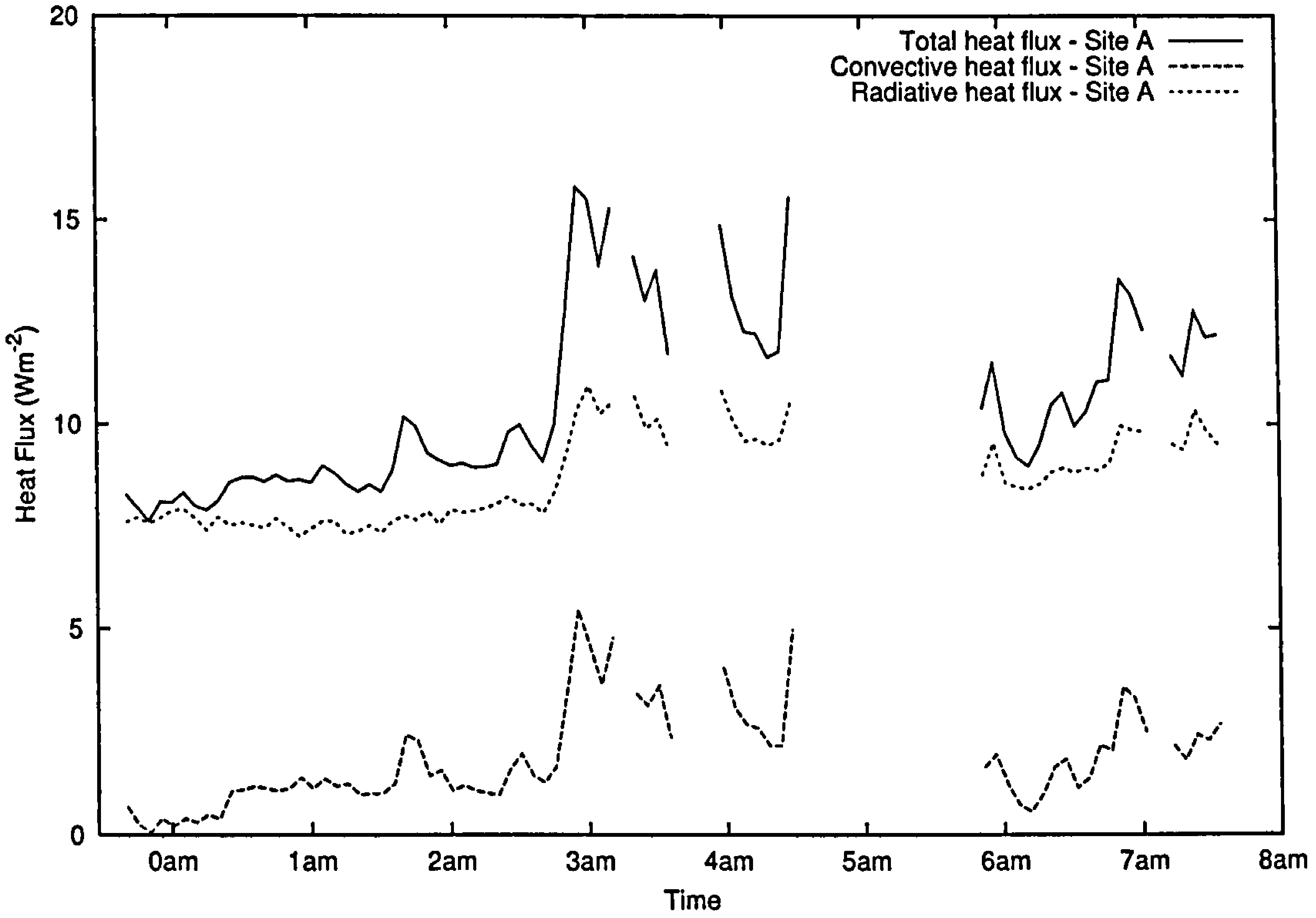

Figure 4.29: Ceiling heat flux at flux meter site A.

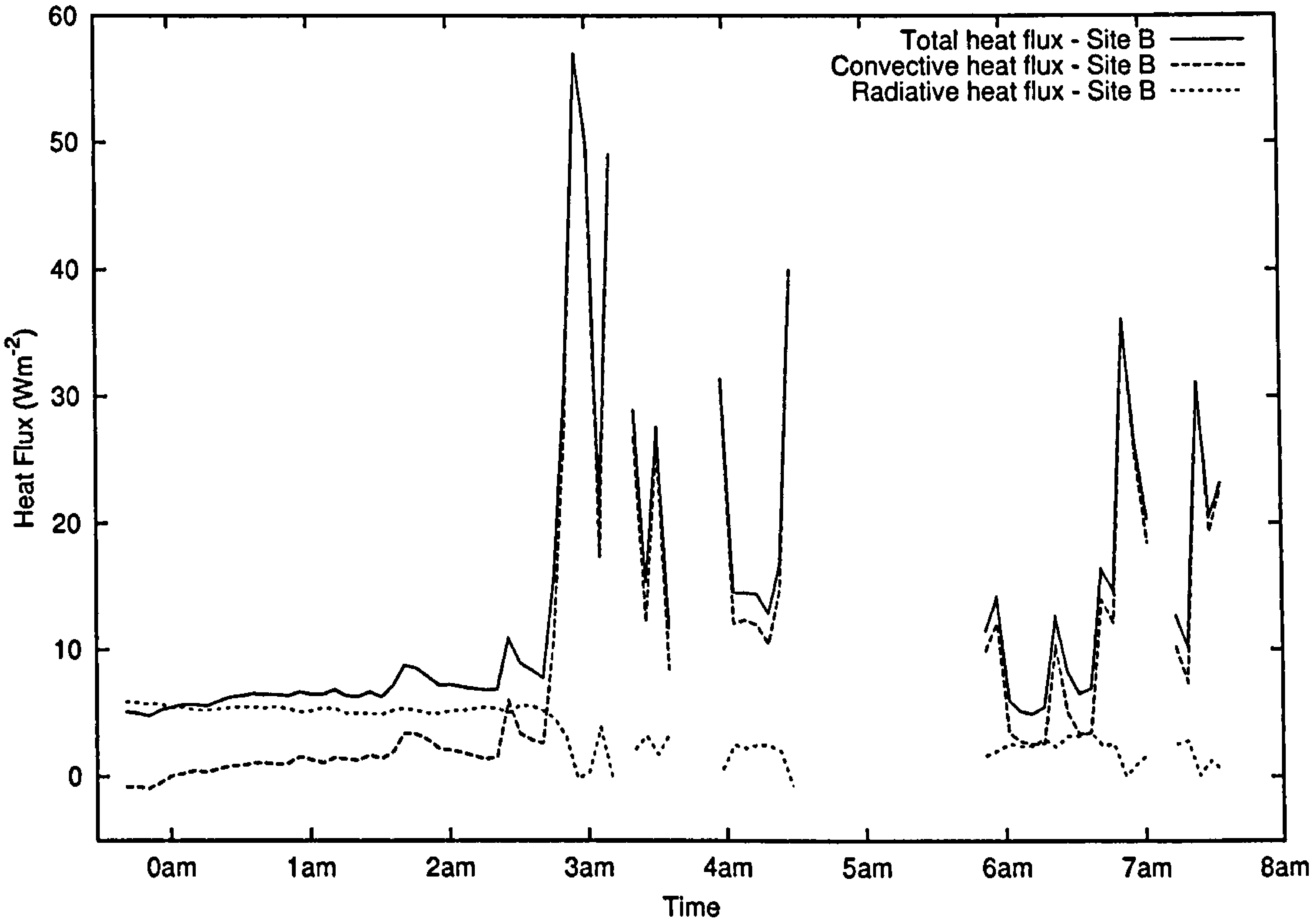

Figure 4.30: Ceiling heat flux at flux meter site B.

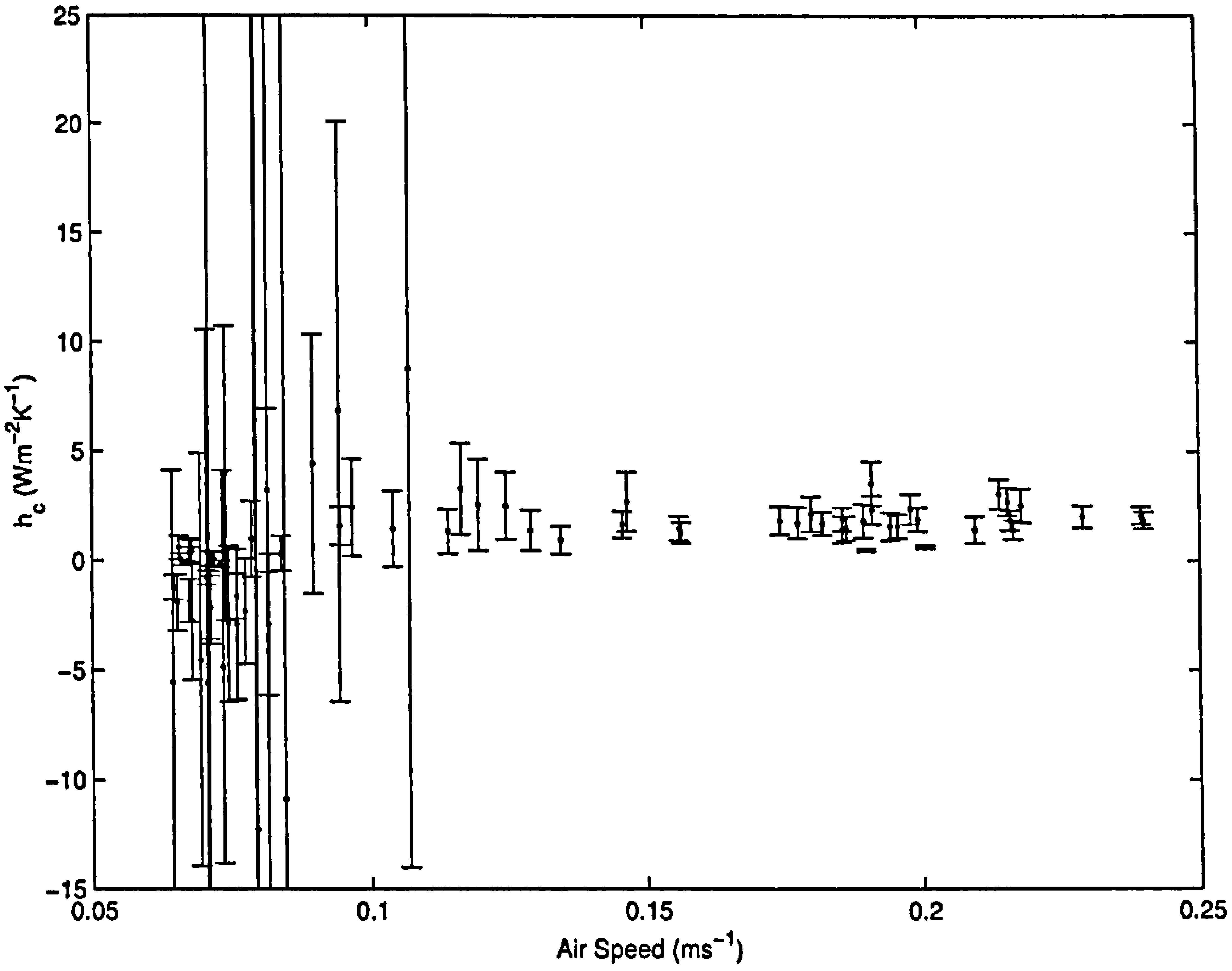

Figure 4.31: Convective heat transfer coefficient versus local air speed at heat flux meter site A plotted along with the estimated uncertainty.

Table 4.5: The uncertainty in the different experimental equipment.

Measurement	Error
Heat flux	$\pm 0.15 \mathrm{W.m}^{-2}$
Air temperature	$\pm 0.5\,\mathrm{K}$
Air speed	$\pm 5\%$ (min $\pm 0.01\,\mathrm{ms}^{-1}$)
Surface temperature	$\pm 0.181\,\mathrm{K}$

where T_a is the air temperature measurement from the nearby anemometer.

The calculated heat transfer coefficients at sites A and B and the estimated uncertainty in the calculation are plotted in Figures 4.31 and 4.32 respectively. The experimental measurement uncertainties assumed are given in Table 4.5 and are discussed in detail in Appendix C.

The uncertainty in the calculated heat transfer coefficient at low air speeds is larger, this is particularly the case a heat flux meter site A, see Figure 4.31. There is no data below $0.05\,\mathrm{ms}^{-1}$ because the omnidirectional anemometers used are only able to measure between $0.05\,\mathrm{ms}^{-1}$ and $5\,\mathrm{ms}^{-1}$. This has caused bunching of the data at a local air speed below $0.1\,\mathrm{ms}^{-1}$. The uncertainty in the air temperature measurement has a large effect on the calculated heat transfer coefficient when the difference between the air and ceiling temperature is small. Small differences in air/ceiling temperature coincided

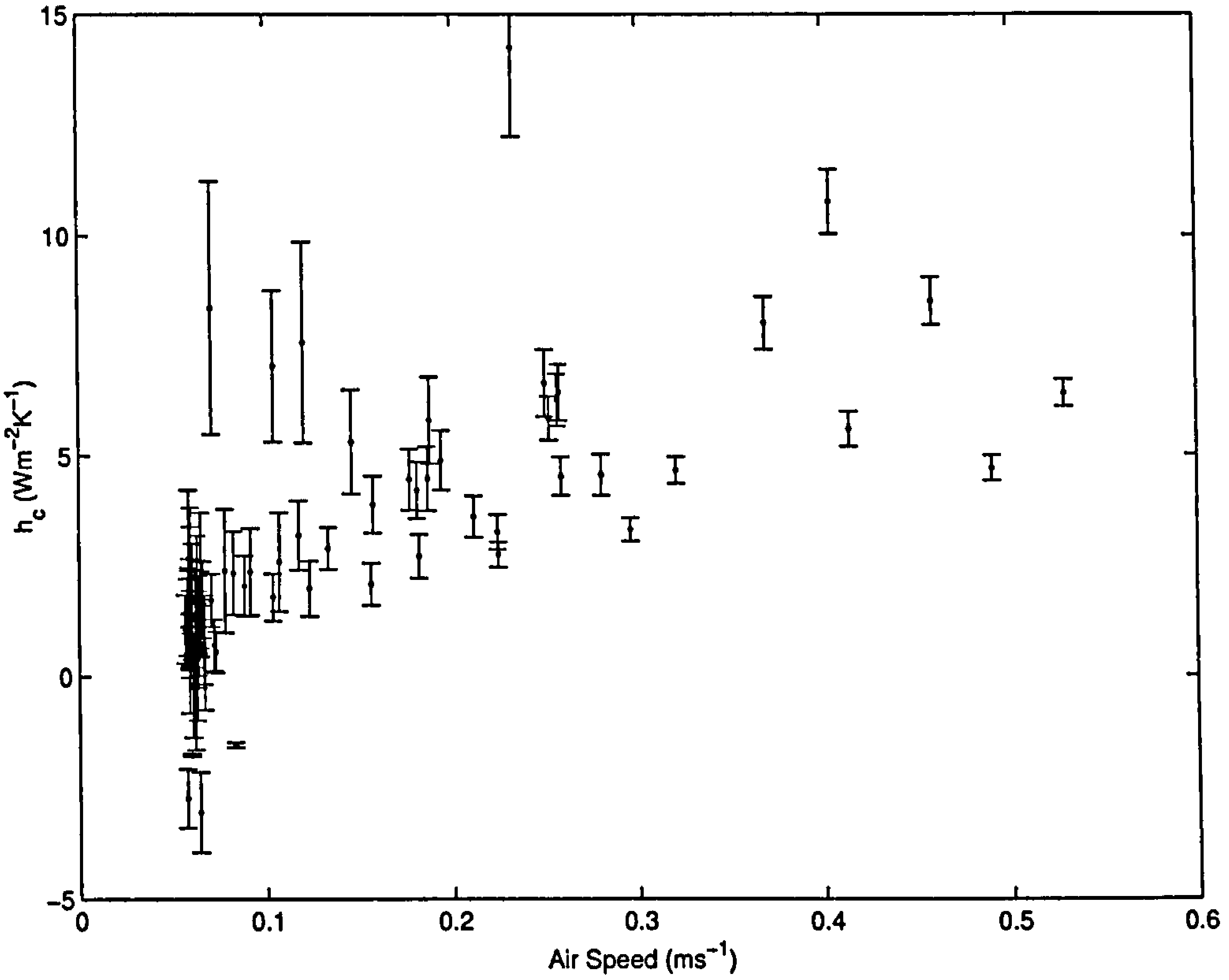

Figure 4.32: Convective heat transfer coefficient versus local air speed at heat flux meter site B plotted along with the estimated uncertainty.

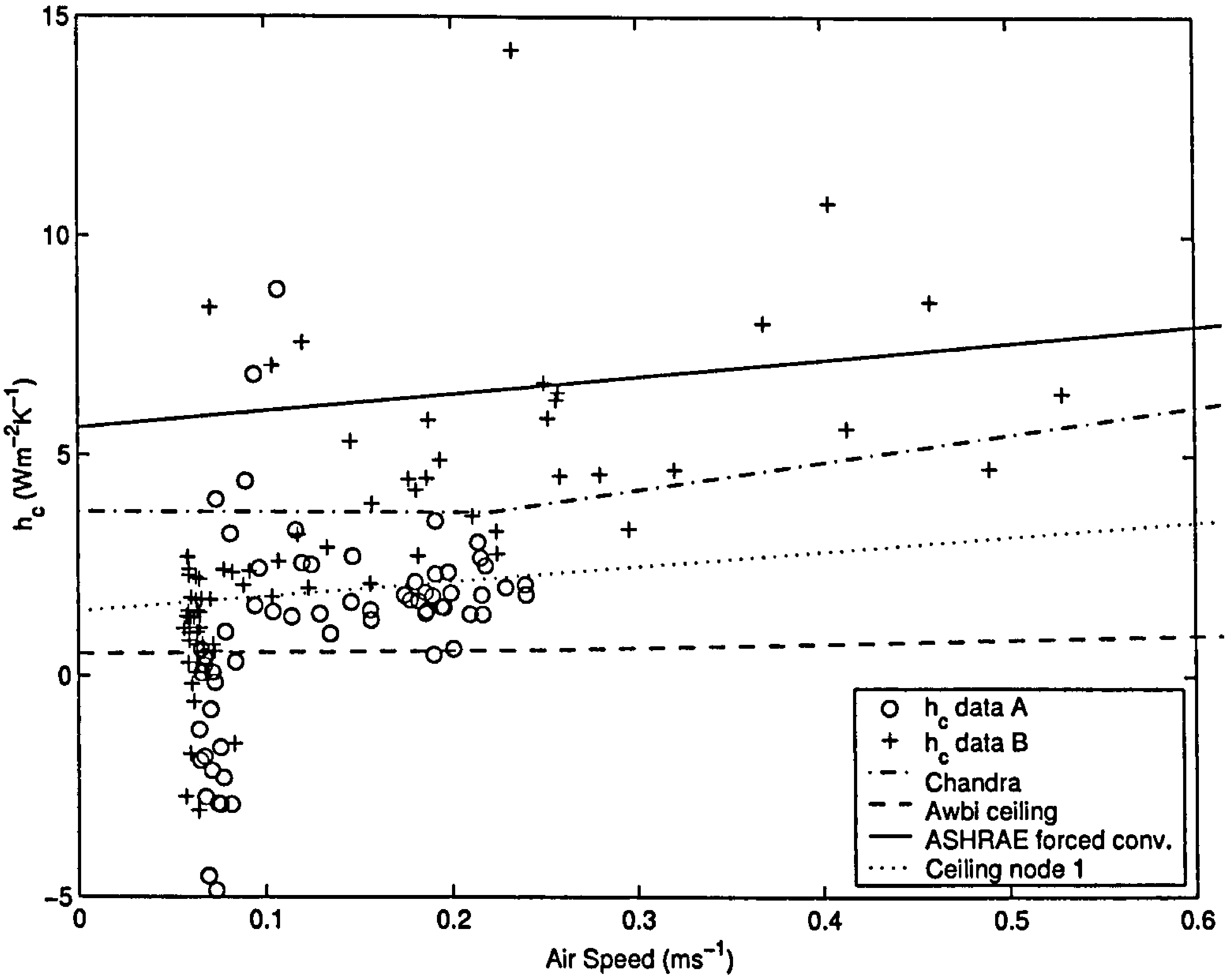

Figure 4.33: Convective heat transfer coefficient versus local air speed compared with correlations (see Chapter 3).

with low air speeds when the temperature measurement of hot wire anemometers are at their most suspect, thus, compounding the uncertainty in convective heat transfer coefficient calculation.

Figure 4.33 shows the convective heat transfer coefficient versus local air speed compared to correlations found in the literature and to the CFD results in Chapter 3. There are four curves drawn over the h_c data:

1. The ASHRAE forced convection correlation for air speeds below 5 ms^{-1} (ASHRAE 1997; McAdams 1954);
2. A correlation for unfinished wallboard from Chandra and Kerestecioglu (1984);
3. A correlation for mixed convection at the ceiling from Awbi and Hatton (2000);
4. The correlation derived from the numerical work for ceiling node *C1* (see Section 3.5.3).

Awbi and Hatton (2000) define the convective heat transfer coefficient, h_c, as having a component due to natural convection, h_{cn}, and a component due to forced convection, h_{cf}:

$$h_c^{3.2} = h_{cn}^{3.2} + h_{cf}^{3.2}. \tag{4.6}$$

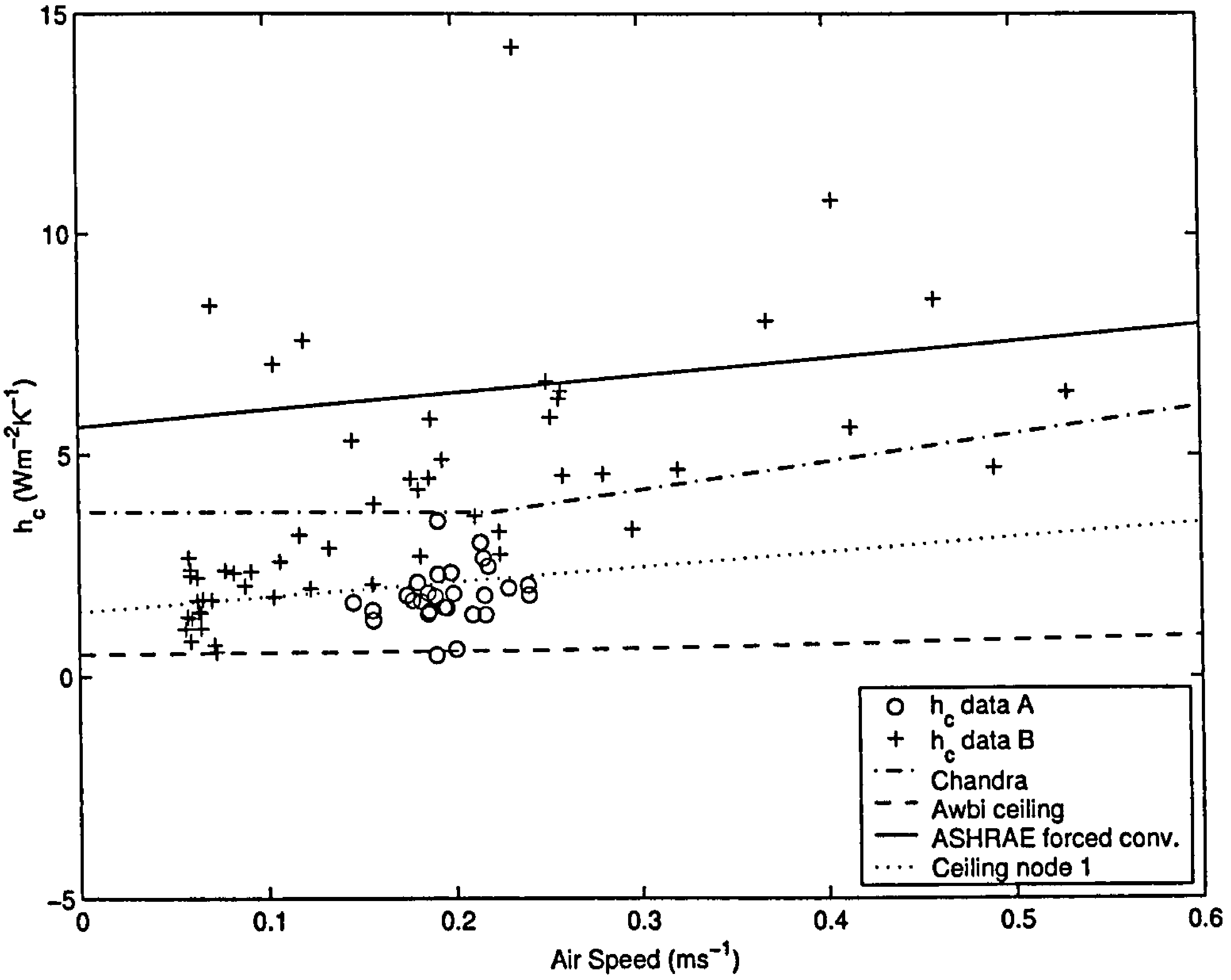

Figure 4.34: Convective heat transfer coefficient versus local air speed compared with correlations when data at instances where the difference between the ceiling temperature and the local air temperature is less than 0.75 K are ignored.

h_{cn} and h_{cf} for the ceiling surface are given as:

$$h_{cn} = \frac{0.704}{D^{0.601}}(\Delta T)^{0.133}, \tag{4.7}$$

and

$$h_{cf} = 1.35(W)^{0.074}U^{0.772}, \tag{4.8}$$

where D is the hydraulic diameter of the ceiling (m), ΔT is the air to surface temperature difference (K), W is the width of the air supply opening (m), and U is the jet velocity ($m\,s^{-1}$). To compare this correlation to the experimental study, values have to be assigned to the variables D, ΔT and W. The hydraulic diameter of the ceiling, D, is 3.1 m. The solution of h_c for the ceiling surface is not sensitive to ΔT therefore a value of 2.5 K, a typical value seen during the experiment, is assumed. W, the width of the window opening, is 0.64 m.

If data at instances where the difference between the ceiling temperature and the local air temperature is less than 0.75 K are ignored the spread of calculated heat transfer coefficients at low air speeds is largely eliminated, see Figure 4.34. The figure of 0.75 K was chosen as it is high enough to be larger than the accuracy of the air temperature measurement while small enough not to exclude too many points. When the filtering

Table 4.6: Coefficients to Equation 4.9 when h_c is fitted with respect to local air speed or hopper air speed.

Data Set	Reference velocity	a	b	Correlation coefficient
A	local	4.97	1.28	0.17
B	local	12.94	1.83	0.60
A and B	local	11.75	1.33	0.50
A	hopper	2.47	1.00	0.64
B	hopper	7.19	1.53	0.58
A and B	hopper	3.94	1.87	0.36

had been applied 74 data points where reduced to 28 for heat flux meter site A, while 74 points were reduced to 55 for site B.

Two first order equations have been fitted to h_c with respect to air velocity, v,

$$h_c = a * v + b, \tag{4.9}$$

one with local air speed (from anemometer nearest heat flux meter sites) used as the reference velocity, the second using the hopper air speed. Three data sets are used:

1. Measurements from heat flux meter site A;
2. Measurements from heat flux meter site B;
3. Measurements from heat flux meter sites A and B.

The coefficients to Equation 4.9 are given in Table 4.6. Figure 4.35 shows the convective heat transfer correlations with respect to the local air speed, while Figure 4.36 shows the correlations with respect to the hopper air speed.

The experimental measurements taken show convective heat transfer coefficient does increase slowly with local air velocity. The spread in the data is to be expected considering the low air speeds present. Chandra and Kerestecioglu only considered data points with velocities over 0.5 mph or 0.22 ms^{-1}. In this study there was only 20 instances when the local air speed was greater than the 0.22 ms^{-1}, 3 at heat flux meter site A and 17 at site B. Also, their correlation was for vertical surfaces and therefore would not be effected by a thermally stratified boundary layer between the surface and the air temperature measurement location as was the case in this study at low air velocities where the incoming air does not attached to the ceiling.

Given the level of spread in calculated values of convective heat transfer coefficient we do not expect the correlation coefficient to be too high. It is encouraging to find that within the range of speeds of the present experiment the experimental data correlations provide equally satisfactory fit as the correlations of Chandra and Kerestecioglu, Awbi

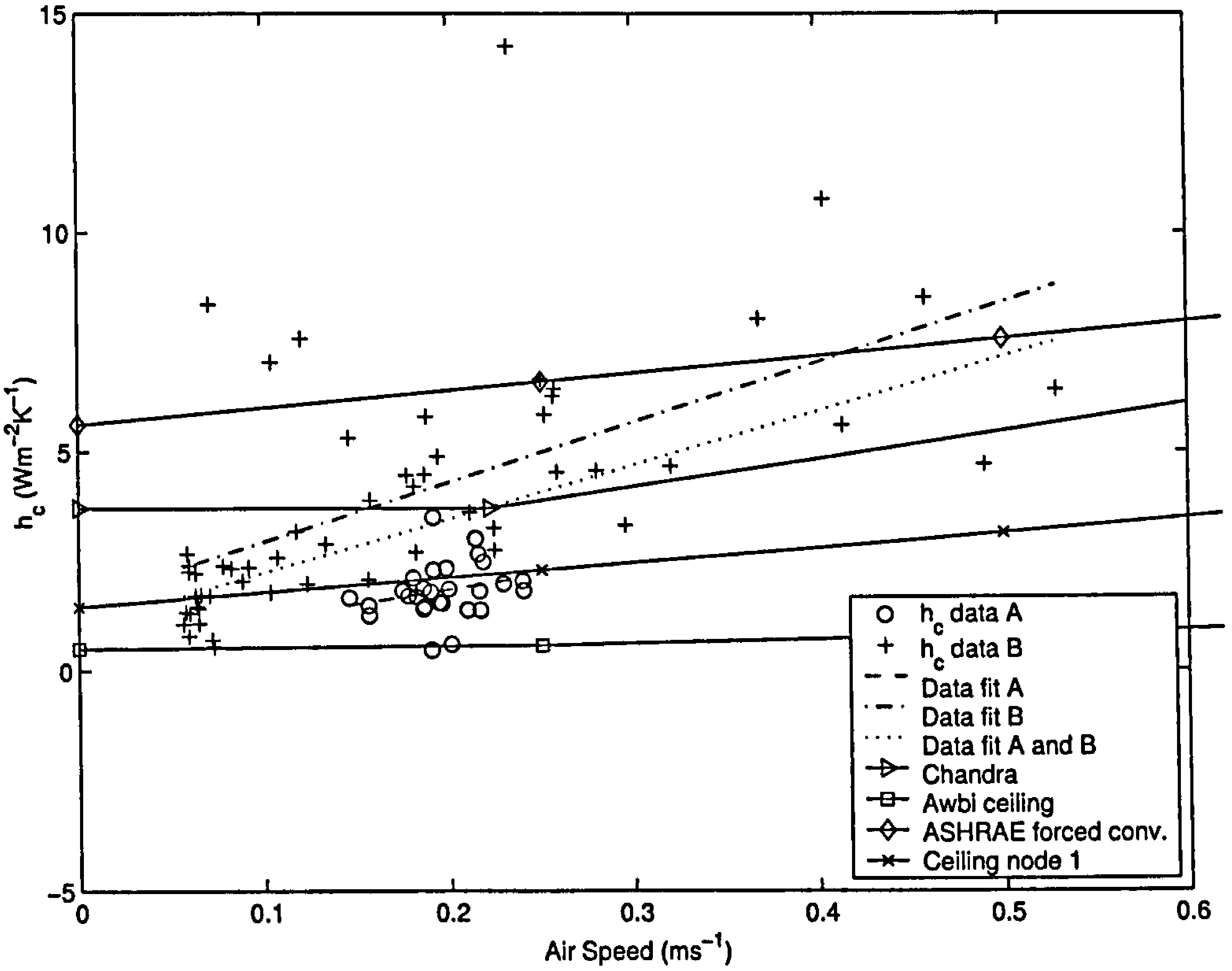

Figure 4.35: Convective heat transfer coefficient versus local air speed compared with correlations from the literature and the CFD simulations in Chapter 3.

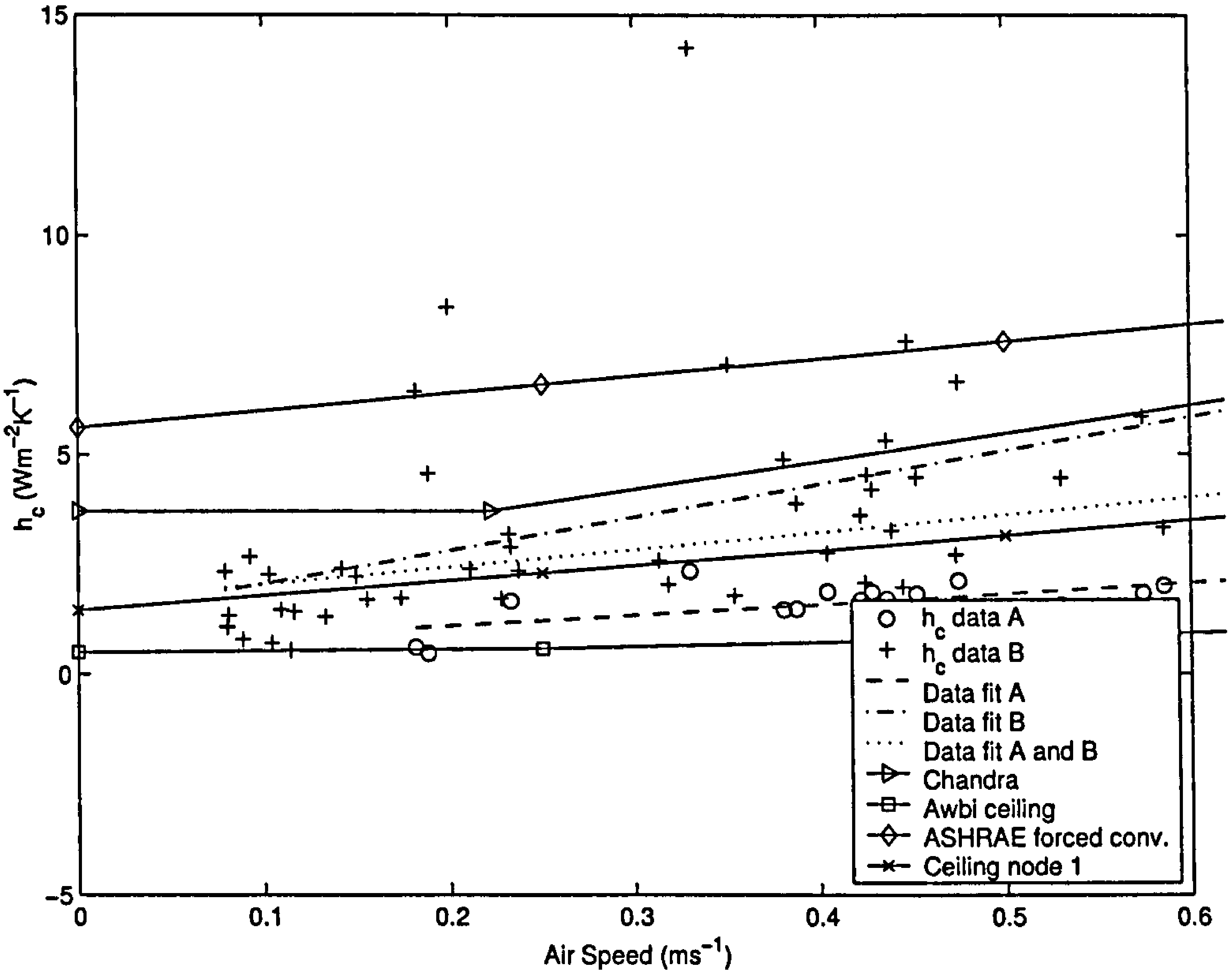

Figure 4.36: Convective heat transfer coefficient versus hopper air speed compared with correlations from the literature and the CFD simulations in Chapter 3.

and Hatton, and the ASHRAE forced convection correlation. Furthermore the correlation emerging from the CFD work in Chapter 3 is sufficiently close to the experimental data (within the spread of data) to serve as input for the zonal model.

4.5 Conclusions

The experimental findings of cross-flow night-time ventilation are summarised below:

1. The flow visualisation experiment using a laser and smoke supported by hand-held anemometer readings described in Section 4.3.2 showed that it was possible to get at least two flow regimes in the experimental room.

   (a) In the first flow regime the main flow path is across the ceiling. Near to the door the flow detaches from the ceiling due to wall obstruction above the door. The flow then leaves the room mostly at the top of the door opening.

   (b) In the second flow regime the flow went along the ceiling for only part of the room depth before rapidly dropping to the floor. Then the flow travels along the floor and exits at the bottom of the door opening.

   This finding provides support for the decision to include a method to model the impact of whether the flow remains attached to the ceiling or not within the zonal model.

   In both cases flow was biased towards the northern wall. As the window is off-centre the flow is more likely to attach to the nearer north wall surface due to the Coanda effect. Along this wall there was a strong downward flow whether the flow through the middle of the room remained attached to the ceiling or not. This was due to the hardboard section, shown in Figure 4.3, forcing the flow downwards and around the corner made by the north wall and the hardboard section.

2. Indoor air velocities close to the ceiling correlated well with a number of air speed measurements taken:

   (a) The wind speed data from the weather station;

   (b) Wind speed data from the ultrasonic anemometer 1 m outside the experimental room;

   (c) Air speed in the hopper.

3. Current practice within thermal analysis and building airflow programs is to use weather data sets typically collected in rural settings, airports etc., and then to use rough correlations to derive a 10 m air velocity in an urban or suburban setting depending on the site of interest. The fact that indoor air velocities close to the

ceiling correlated well with wind speed data from a weather station remote from the experimental site shows that it is not necessary to have an accurate inflow opening air velocity to determine indoor air speeds.

4. Ratios were taken of the air speed next to the ceiling and near to the floor to see if a flow regime could be inferred. It was possible to determine where the main flow stream path was from the omnidirectional anemometer data collected using the air speed ratio—the ratio between the air speed near the ceiling and at midheight. Air velocity rather than speed measurements collected inside the experimental room would also have helped in this respect.

5. The correlation between Archimedes number and detachment position postulated in Chapter 3 from CFD simulation results was found to agree well with the experimental measurements.

6. Convective heat transfer coefficients were measured and the uncertainty in the ceiling convective heat transfer coefficient was estimated.

    (a) The uncertainty in the radiative heat flux calculation, and therefore in turn, the uncertainty in the calculation of convective flux (from the total flux measurement) was substantial. Studies that have produced more successful correlations with air speed limit the uncertainty in the radiative heat flux calculation by keeping all the surfaces at the same temperature (Spitler, Perdersen, and Fisher 1991; Chandra and Kerestecioglu 1984). In the study of Spitler et al. problems associated with the measurement errors of heat flux transducers were avoided as the total heat flux through the surface panels used could be determined by the voltage supplied to each panel to keep its temperature constant.

    (b) The spread of calculated convective heat transfer coefficient at air speeds below 0.1 m/s was substantial. This was due partly to the fact that these low air speeds were at and beyond the measurement capabilities of the anemometers used.

    (c) The uncertainty in the air temperature measurement was large. The hot wire anemometers had an accuracy of ±0.5 K. The air temperature measurement uncertainty is unquantified but larger at air speeds below 0.1 m/s.

The uncertainty in the air temperature measurement had a large effect on the calculated heat transfer coefficient when the difference between the air and ceiling temperature was small. Small differences in air/ceiling temperature coincided with low air speeds when the temperature measurement of hot wire anemometers are at their most suspect. Thus, the uncertainty in convective heat transfer coefficient was compounded at air speeds below 0.1 m/s.

7. The experimental procedure obtained the measurements needed to provide the boundary conditions for a CFD model as well as data to check the CFD results. The convective heat transfer coefficients calculated in this study were of the same order of magnitude as the correlations of Chandra and Kerestecioglu (1984), Awbi and Hatton (2000), and the ASHRAE forced convection correlation for air speeds below $5\,\mathrm{ms}^{-1}$ (ASHRAE 1997; McAdams 1954). The measured convective heat transfer coefficients are sufficiently close to the correlation indicated by the CFD work reported in Chapter 3 to give confidence in the use of CFD models as input to the zonal model. A more detailed CFD analysis of the experimental room is presented in Chapter 5.

CHAPTER 5

CFD Analysis of the Experimental Room

5.1 Objectives

A CFD model of the experimental room was developed in order to compare numerical results with experimental data from the work outlined in Chapter 4. This CFD model allows:

- Validation of the CFD approach taken in Chapter 3;
- Validation of observed and computed flow patterns;
- Provide further support for the structure the zonal model.

These objectives are achieved by the comparison of measured and computed temperature and velocity distributions, establishing the feasibility of extracting complementary pieces of information from experimental work and CFD to feed into the zonal model.

5.2 Modelling Method

5.2.1 Geometry and grid

The room geometry was modelled using the dimensions of the room given in Section 4.3 in Gambit (FLUENT 1999b) (the meshing software from FLUENT Incorporated) and an unstructured grid was produced for use with FLUENT-5 (FLUENT 1999a). The model geometry and the initial grid used with 63347 cells is shown in Figures 5.1 and 5.2 respectively. Two finer grids were also used with 203445 and 506776 cells, the second of these is shown in Figure 5.3.

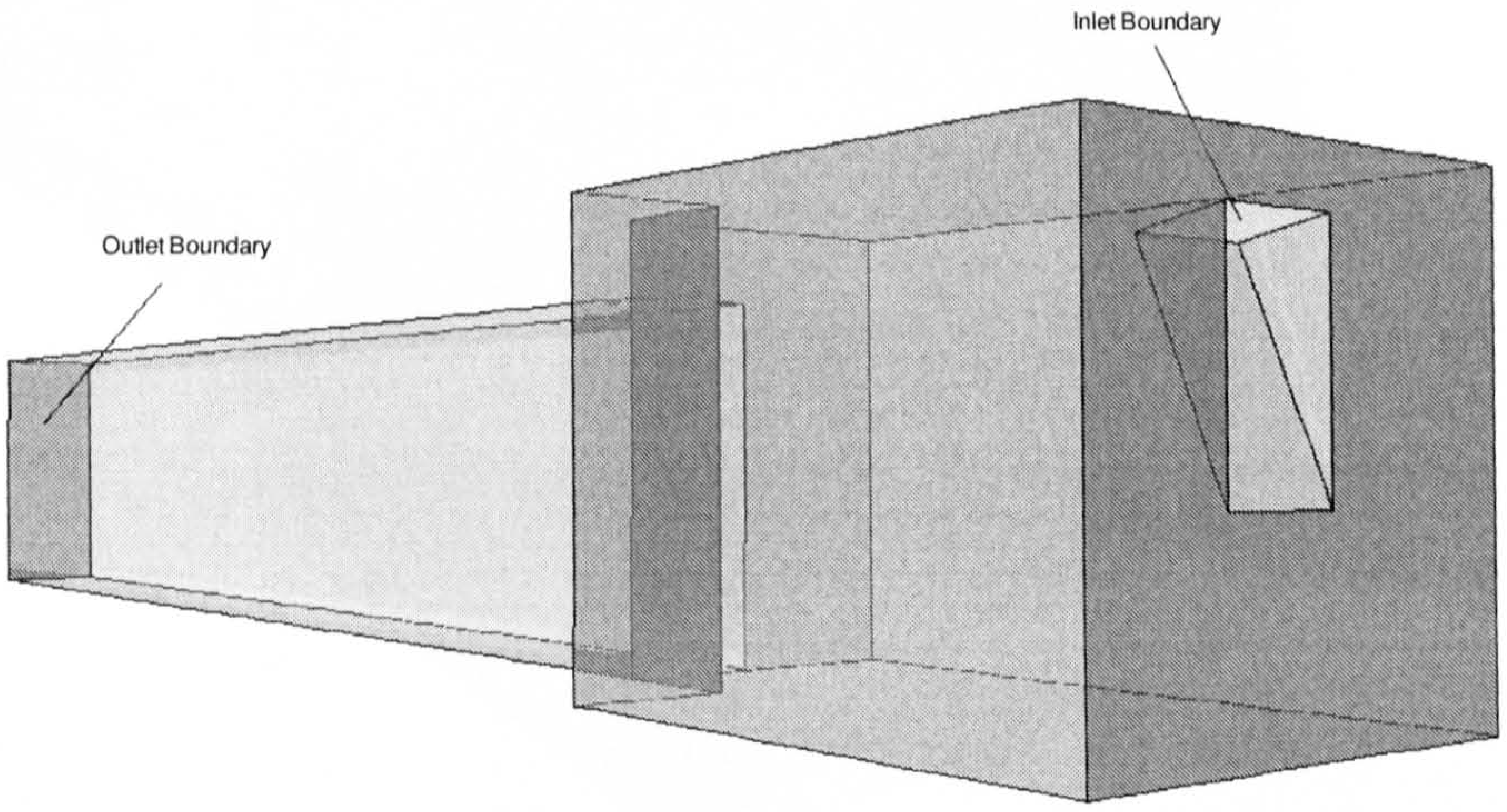

Figure 5.1: 3D CFD model geometry of the experimental room.

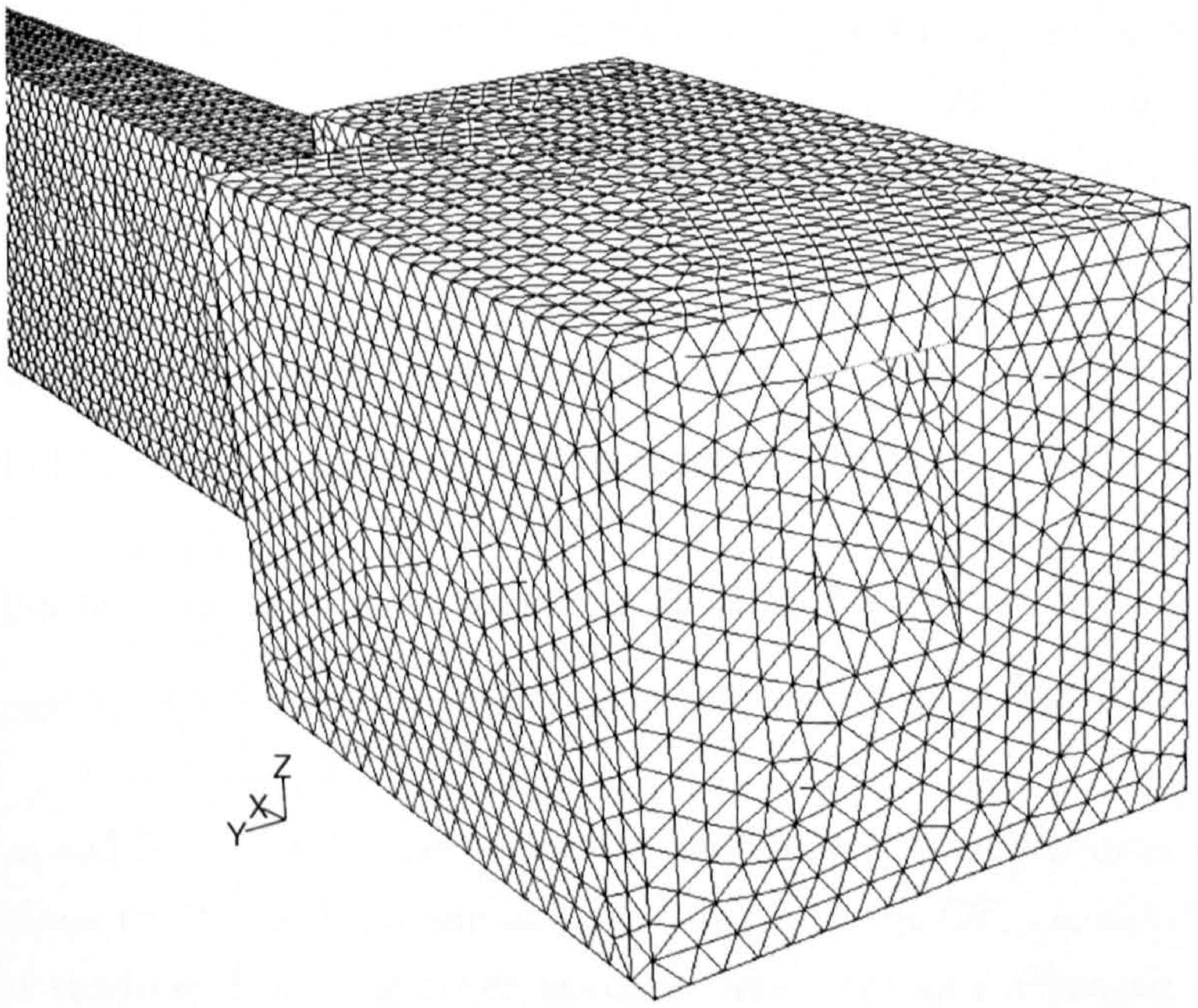

Figure 5.2: Initial coarse grid used for the simulations, 63347 cells.

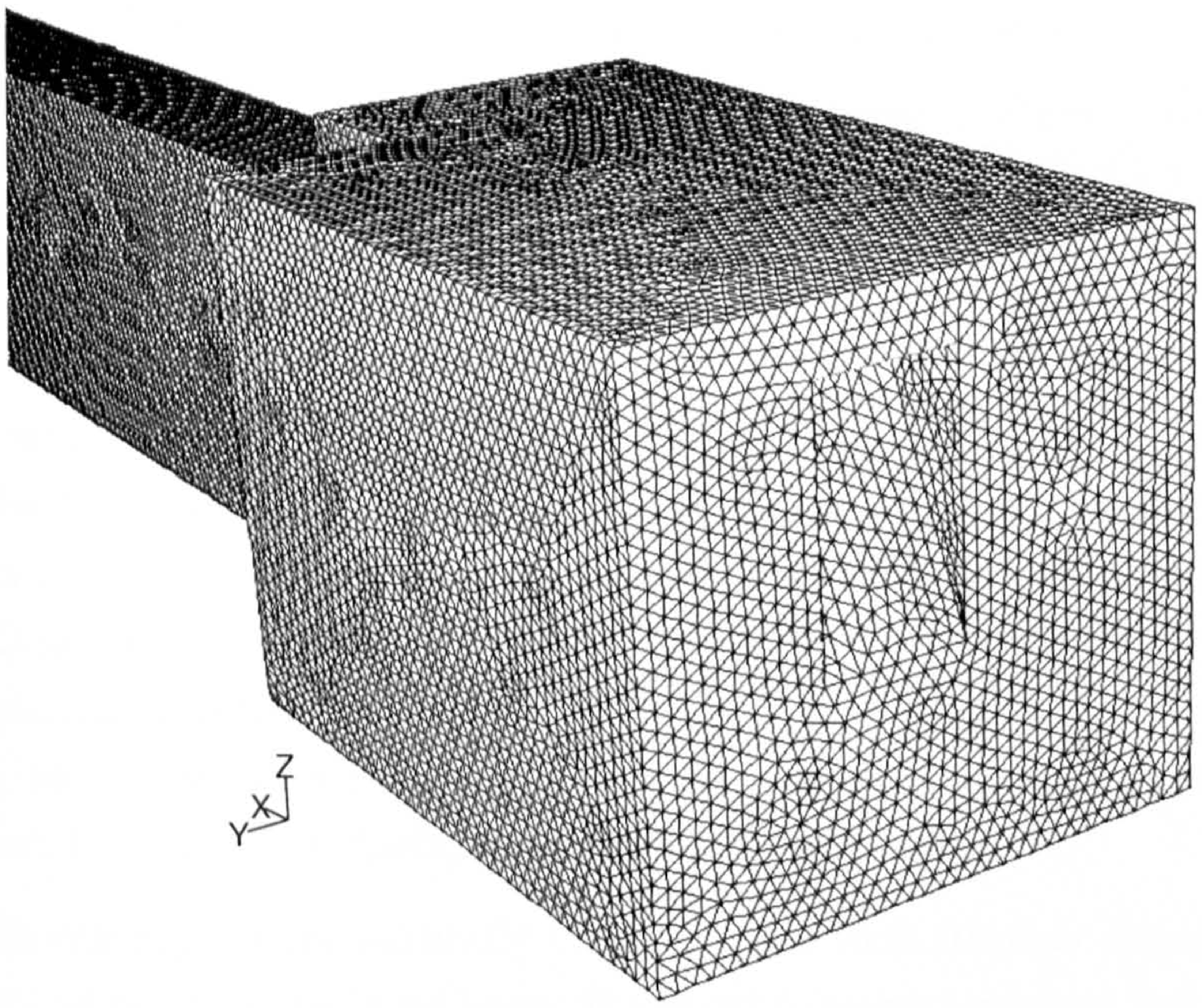

Figure 5.3: The fine grid used for the simulations, 506776 cells.

5.2.2 Boundary conditions

The inflow boundary, highlighted in Figure 5.1, was set at the top of the hopper where there was air speed data collected throughout the experiment that could be used as the setting for a constant velocity boundary. The outflow boundary was set at a distance of 10 m from the door. This extra geometry not present in the experimental room was included to improve the converged solution. When the outflow boundary was set at the door it was impossible to get the mass flow through the outflow boundary to within 10 % of that through the inflow boundary on the two grids of the same mesh densities as those shown in Figures 5.2 and 5.3. When the outflow was set away from the door opening it was possible to get the inflow and outflow mass balances to within 0.5 % of each other.

Two periods during the night were chosen for the basis of a CFD simulation:

1. A period of high wind velocity from 02:51 to 02:59 (referred to as the 3 a.m. period);
2. A period of low wind velocity from 23:58 to 00:10 (referred to as the 12 a.m. period).

The air speed from the hopper opening, and surface temperatures were averaged over these periods to use as the boundary conditions for the CFD simulations, see Table 5.1. Air speed readings from the other anemometers were also averaged over these times to compare the CFD results to the experiment.

The CFD model was a three-dimensional problem in which turbulence was solved using the standard high-Reynolds number k-ε turbulence model. Although the air flow and

Table 5.1: Boundary conditions used in the CFD simulations.

Period	Inlet Velocity ms^{-1}	Inlet Temp. K (°C)	Ceiling Temp. K (°C)	Floor Temp. K (°C)	Wall Temp. K (°C)
3 a.m.	0.8292	283.65 (10.5)	295.15 (22.0)	294.15 (21.0)	294.15 (21.0)
12 a.m.	0.1030	286.0 (12.85)	297.65 (24.5)	294.65 (21.6)	296.15 (23.0)

thermal environment is one that is transient in nature a steady state solution was sought due to the fact that the temperature of the ceiling, floor and walls can be assumed to be constant over the short (~10min) periods chosen for the comparison with the experimental data. Also it was time averaged air velocities that were used for the comparison. N.B. Although a steady state solution was calculated it was necessary to use a fully transient solver (using a time step of 1 s) to converge the solution towards the steady state when buoyancy was included in the CFD calculation.

Air flow inside night-time naturally ventilated spaces is strongly dependent on buoyancy forces caused by the outside air being at a lower temperature than the room air and room surfaces. As the inlet air velocity increases then momentum forces become more dominant while the importance of buoyancy forces decreases. Thus, an isothermal numerical solution should compare better with the experimental data at the 3 a.m. period rather than the low wind velocity period at 12 a.m. To check this hypothesis an isothermal simulation, along with a simulation where thermal energy and buoyancy were included, were calculated for both periods and used for comparison.

5.3 Results

5.3.1 Grid Dependence

Grid dependence was examined on the three grids produced using the isothermal simulation of the higher wind velocity period. The pressure difference between the inflow and outflow boundaries was used for the comparison. The pressure drop across the room will depend on the frictional energy losses which in turn depends on the velocity field. The pressure drops on the 63347, 203445 and 506776 cell meshes were 0.3135 Pa, 0.3055 Pa and 0.3049 Pa respectively. The difference in the pressure drop between the coarse and fine mesh was 2.8%, while the difference between the intermediate and fine mesh was 0.2%. Therefore, a grid independent solution was considered attained on the 203445 and 506776 cell meshes for the isothermal case. The 203445 cell mesh was assumed to be sufficient for the non-isothermal cases.

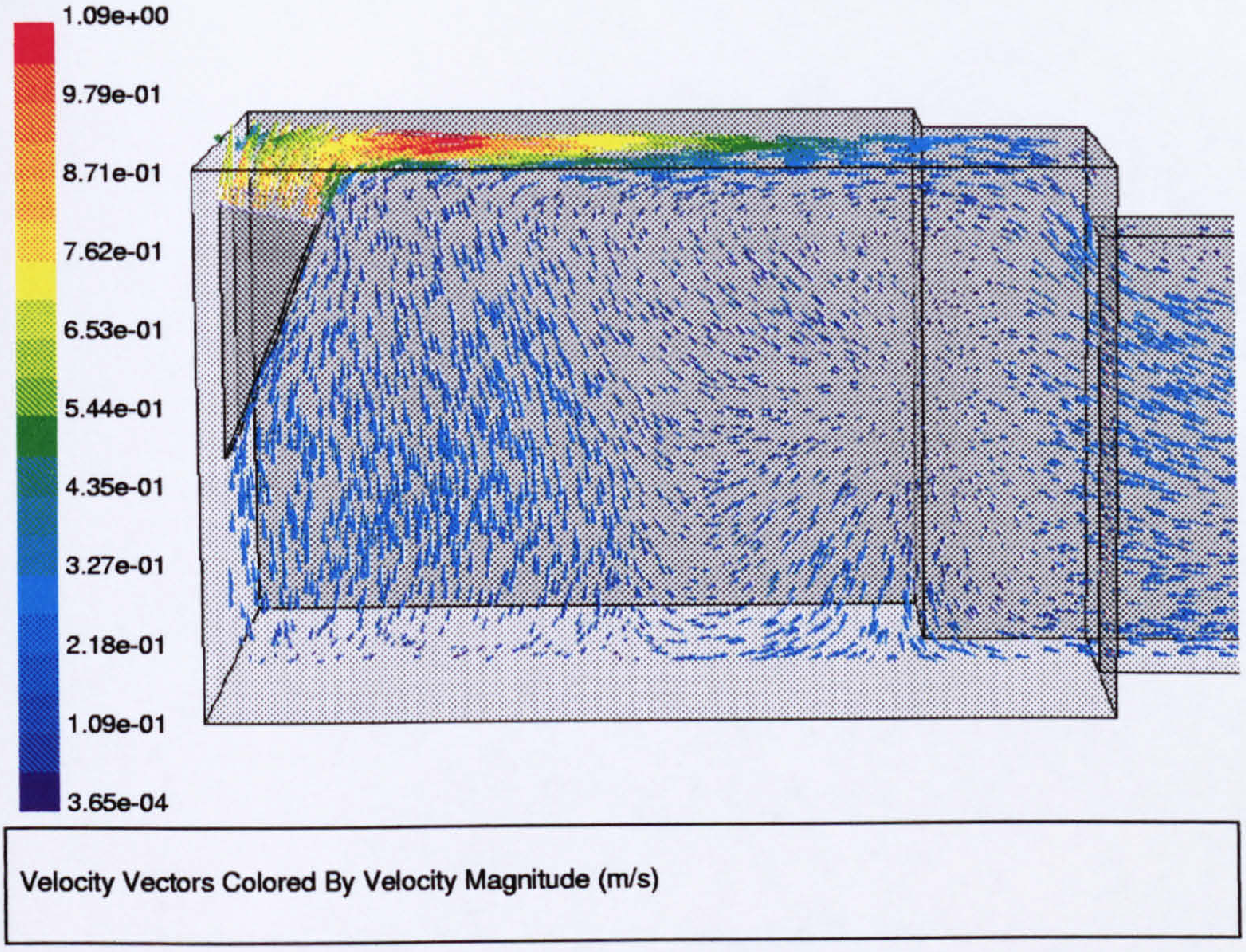

Figure 5.4: Vector plot along y plane near the middle of the room from an isothermal simulation of the 3 a.m. period.

5.3.2 Flow Field

3 a.m. Isothermal Simulation

Figure 5.4 shows a slice through the room where the main flow stream can be seen across the length of the ceiling. In the first half of the room the vectors clearly show the entrainment of air near the floor into the main flow stream.

Figure 5.5 shows the secondary flow that exists in the room. Air flows down the north and south walls and is entrained upwards into the main flow stream in the middle of the room.

Figure 5.6 is a z-plane vector plot that shows the complex flow regime present in the room when the flow is attached to the ceiling. The secondary flow regime in the first half of the room causes the air near the floor to flow from the walls to the centre of the room where it is entrained upwards into the main flow stream. The flow near the floor in the second half of the room is very different, affected by the asymmetry in the room and the presence of the hardboard section. Near the hardboard section the air flows back towards the window to feed the entrainment into the main flow stream.

Stream lines taken from the inflow boundary of the 3 a.m. isothermal simulation show how the main flow stream travels along the ceiling before dropping steeply to exit through the door, see Figure 5.7. The main flow stream also flows down the side walls before being

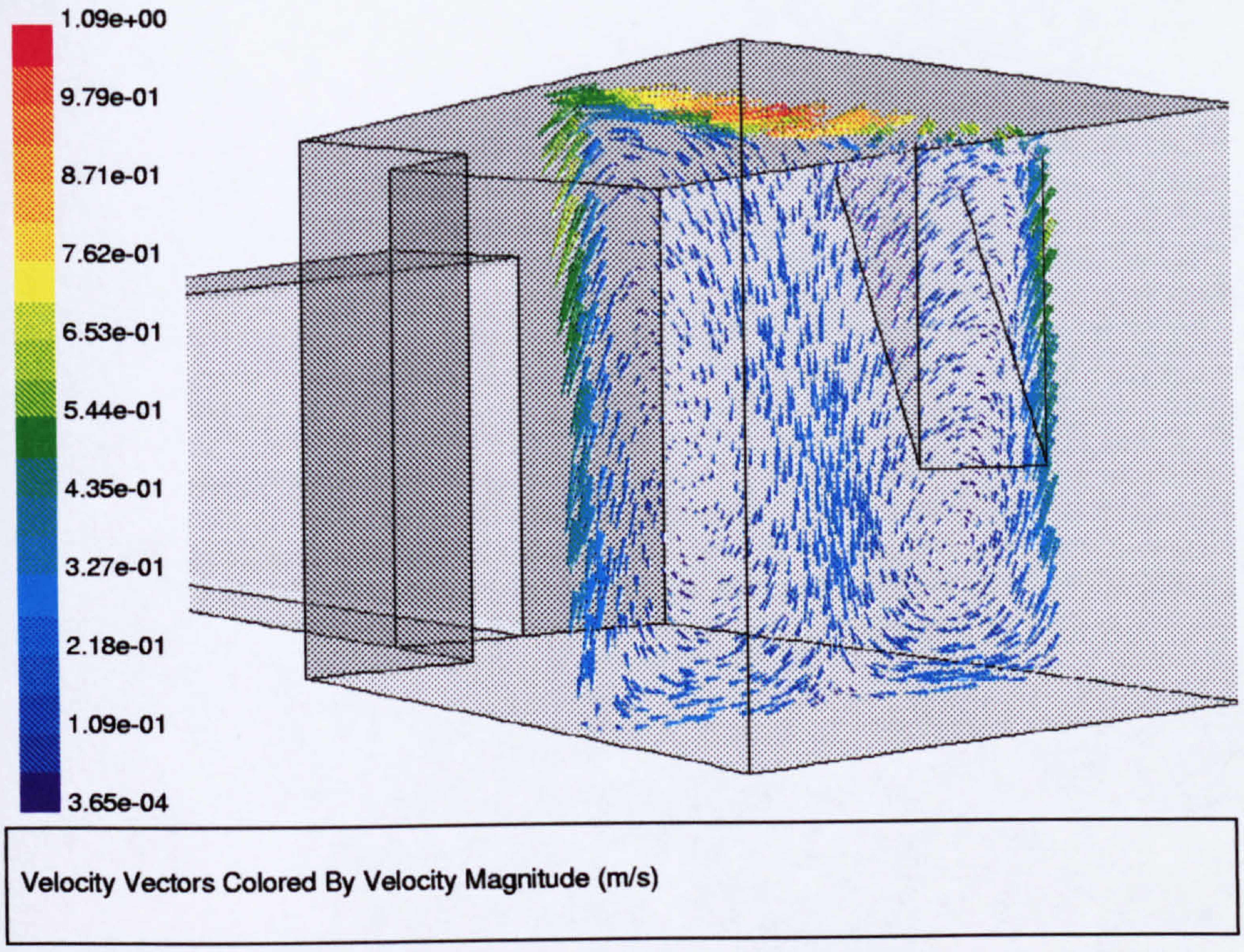

Figure 5.5: Vector plot along x plane from an isothermal simulation of the 3 a.m. period.

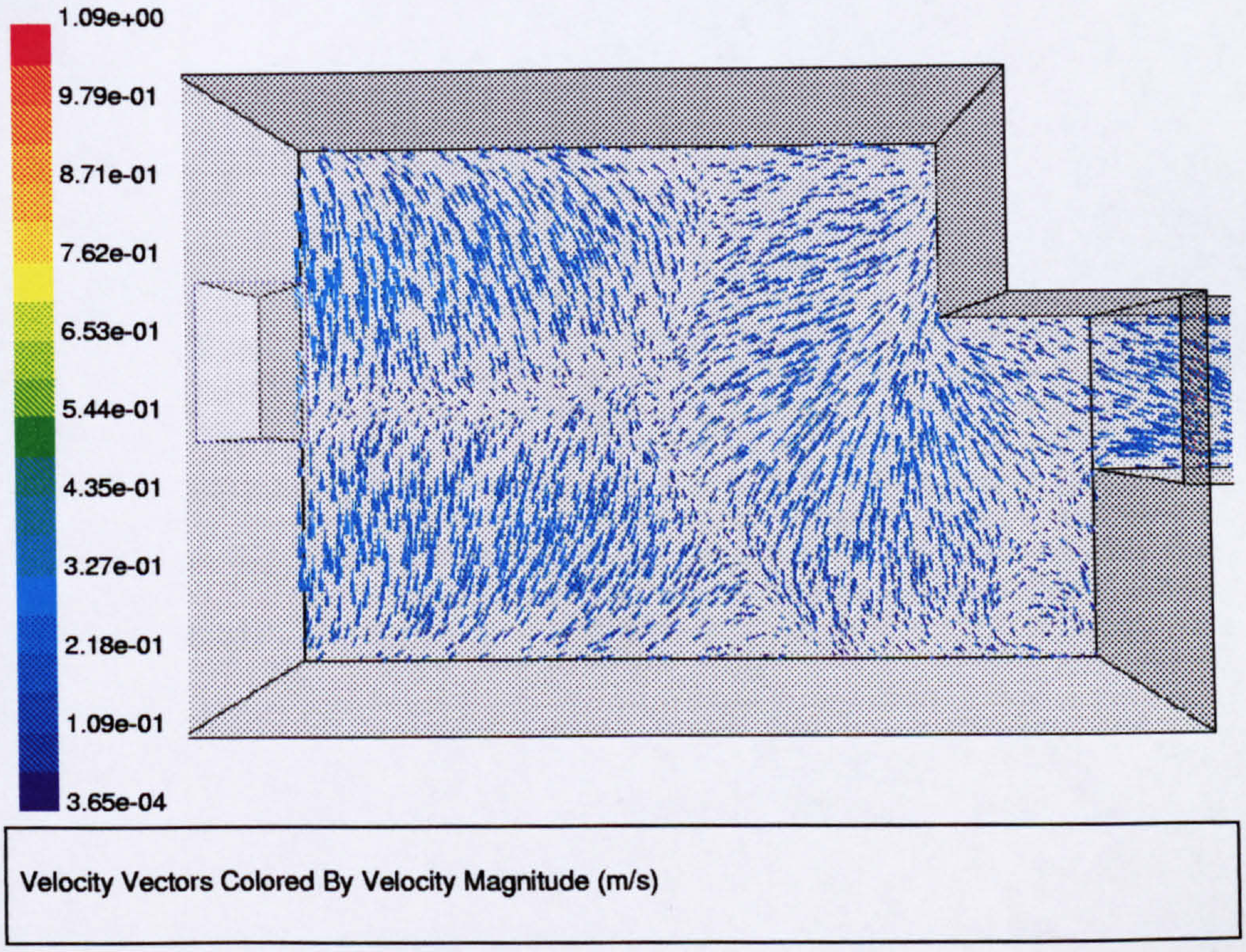

Figure 5.6: Vector plot along z plane 0.1 m above the floor from an isothermal simulation of the 3 a.m. period.

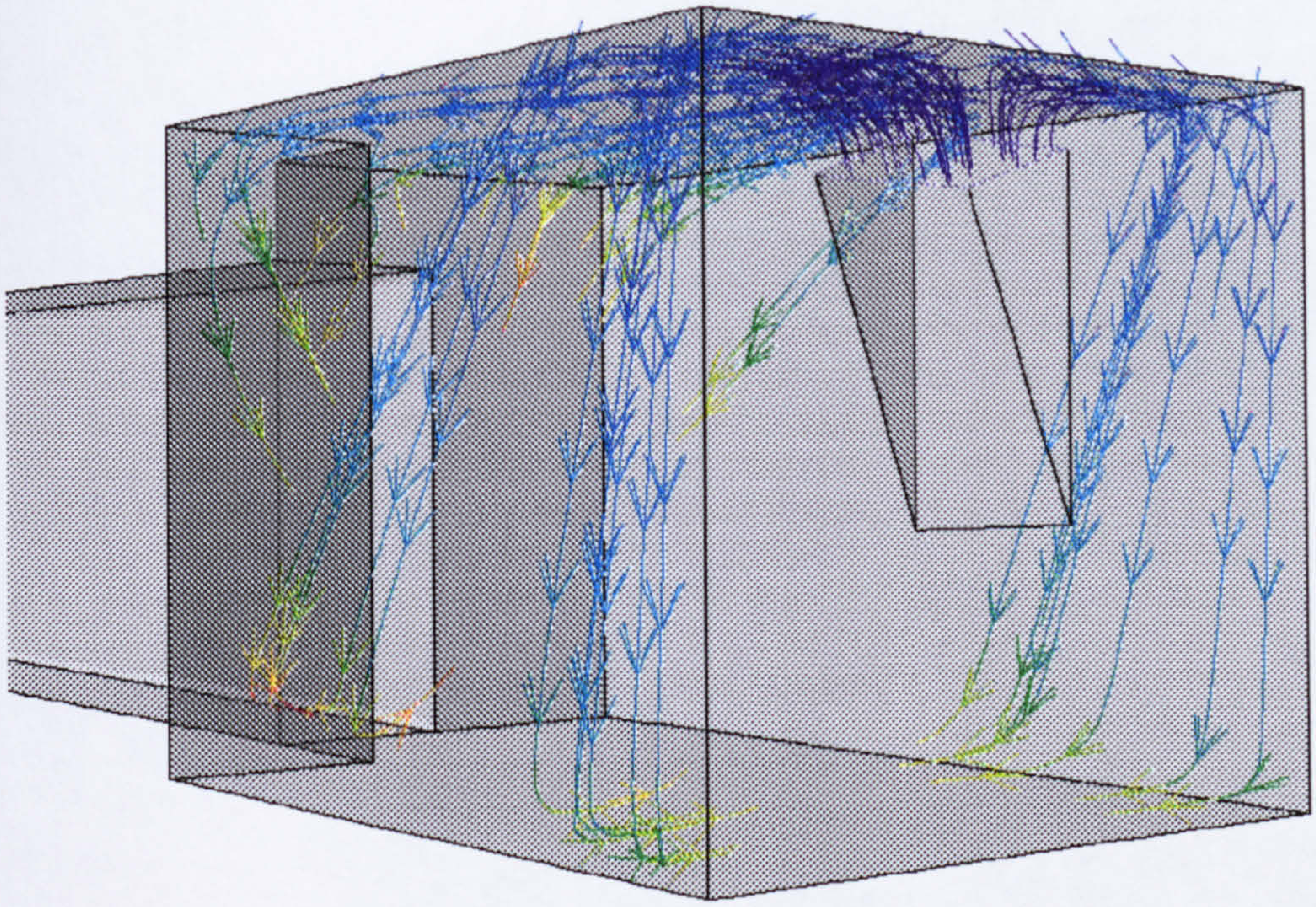

Figure 5.7: Stream lines from the inflow boundary from an isothermal simulation of the 3 a.m. period.

entrained back into the main flow stream in the middle of the room. Figure 5.8 shows stream lines along the north wall boundary. Some of the flow rounds the hardboard obstruction to exit at the bottom of the door. Figures 5.9 and 5.10 show stream lines from the top and the bottom of the south wall boundary respectively. The inlet air flows down the south wall along the floor to be entrained into the main flow stream in the middle of the room. Air at the rear of the room is entrained into the air flow exiting through the middle of the door opening. Figure 5.11 shows that flow in the middle of the room is entrained upwards into the main flow stream, except near the door where it flows along the floor out of the room.

3 a.m. Thermal Simulation

Figures 5.12 and 5.13 show y-plane and x-plane vector plots respectively. Although the main flow stream is across the ceiling, the flow regime is different to that predicted by the isothermal simulation. When buoyancy is simulated there is higher flow at the bottom of the door. In the isothermal simulation there is more flow through the top of the door. The flow bias towards the north wall is increased when buoyancy is simulated. The secondary flow is also altered, the vortex near the north wall increasing in size while the vortex near the south wall decreases.

Stream lines taken from the inflow boundary of the 3 a.m. thermal simulation shows how

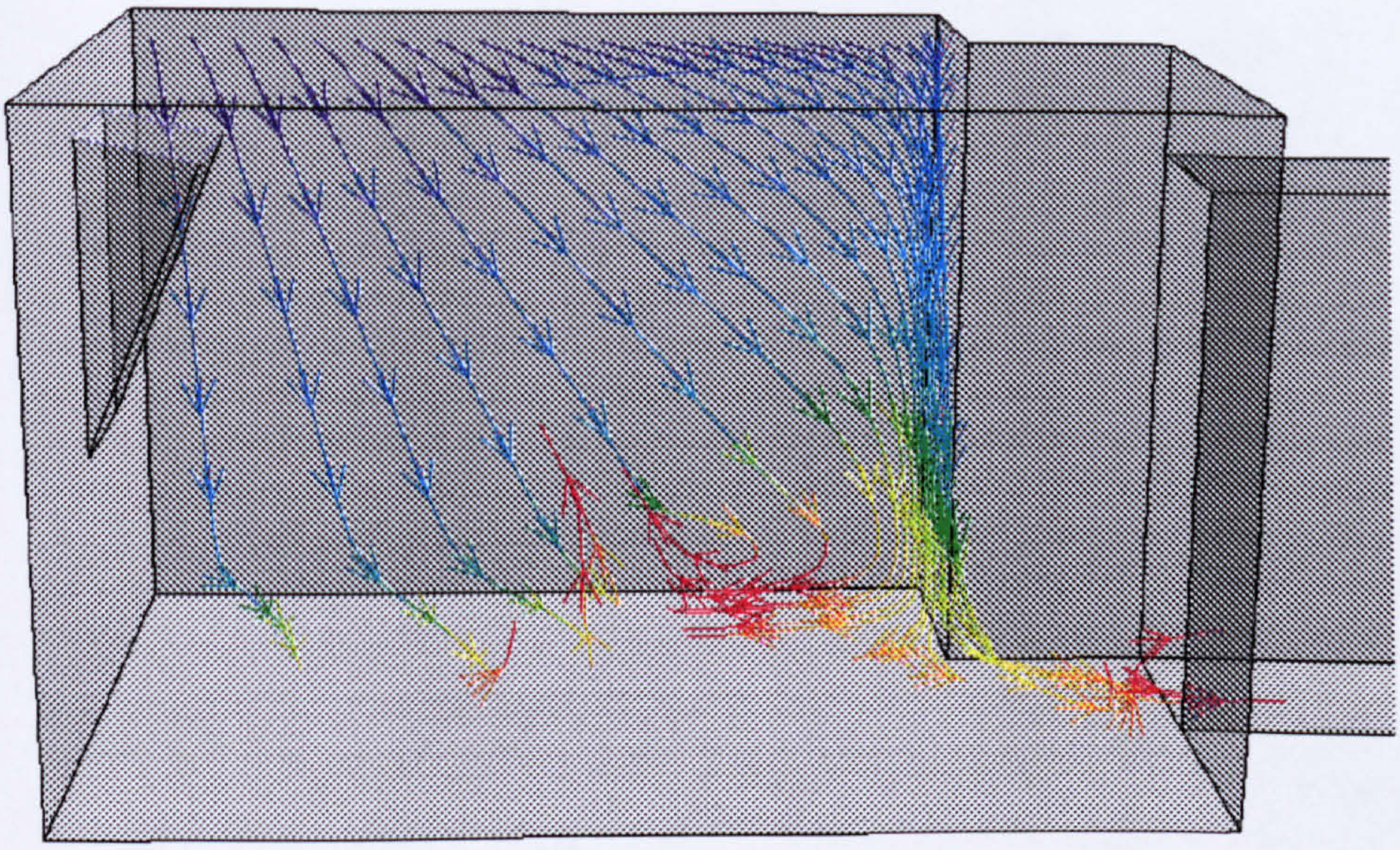

Figure 5.8: Stream lines along the north wall boundary from an isothermal simulation of the 3 a.m. period.

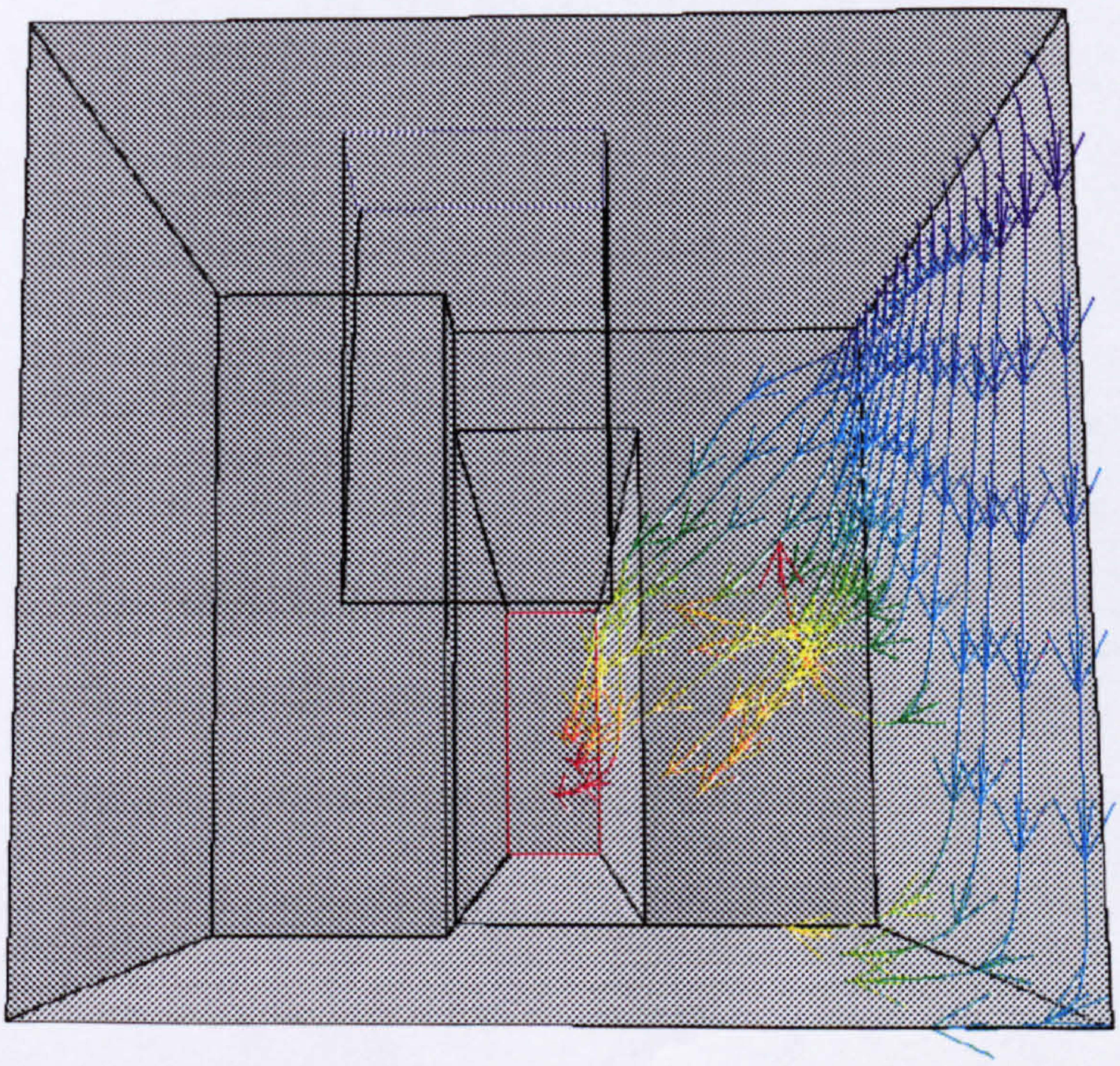

Figure 5.9: Stream lines from the top of the south wall boundary from an isothermal simulation of the 3 a.m. period.

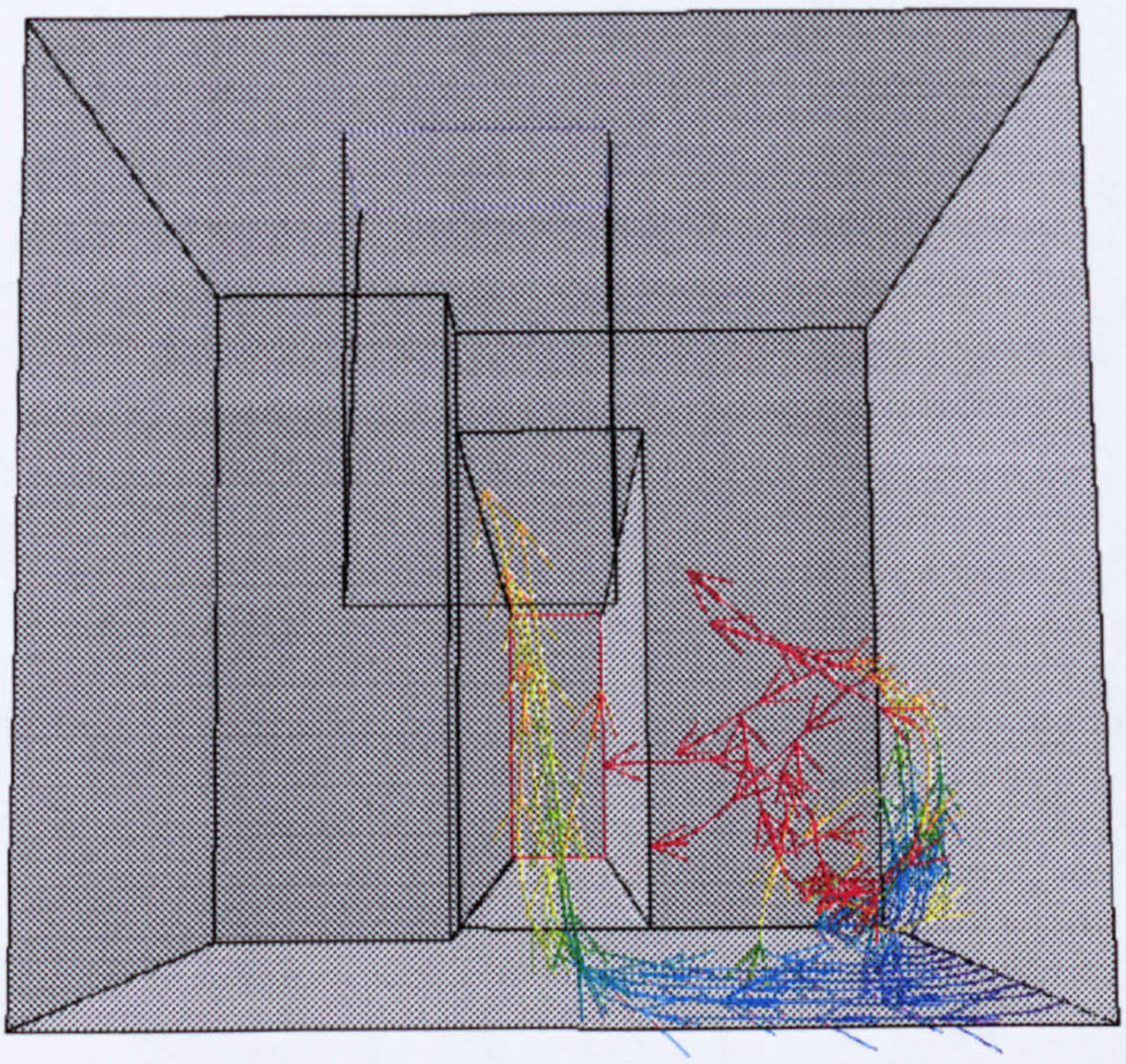

Figure 5.10: Stream lines from the bottom of the south wall boundary from an isothermal simulation of the 3 a.m. period.

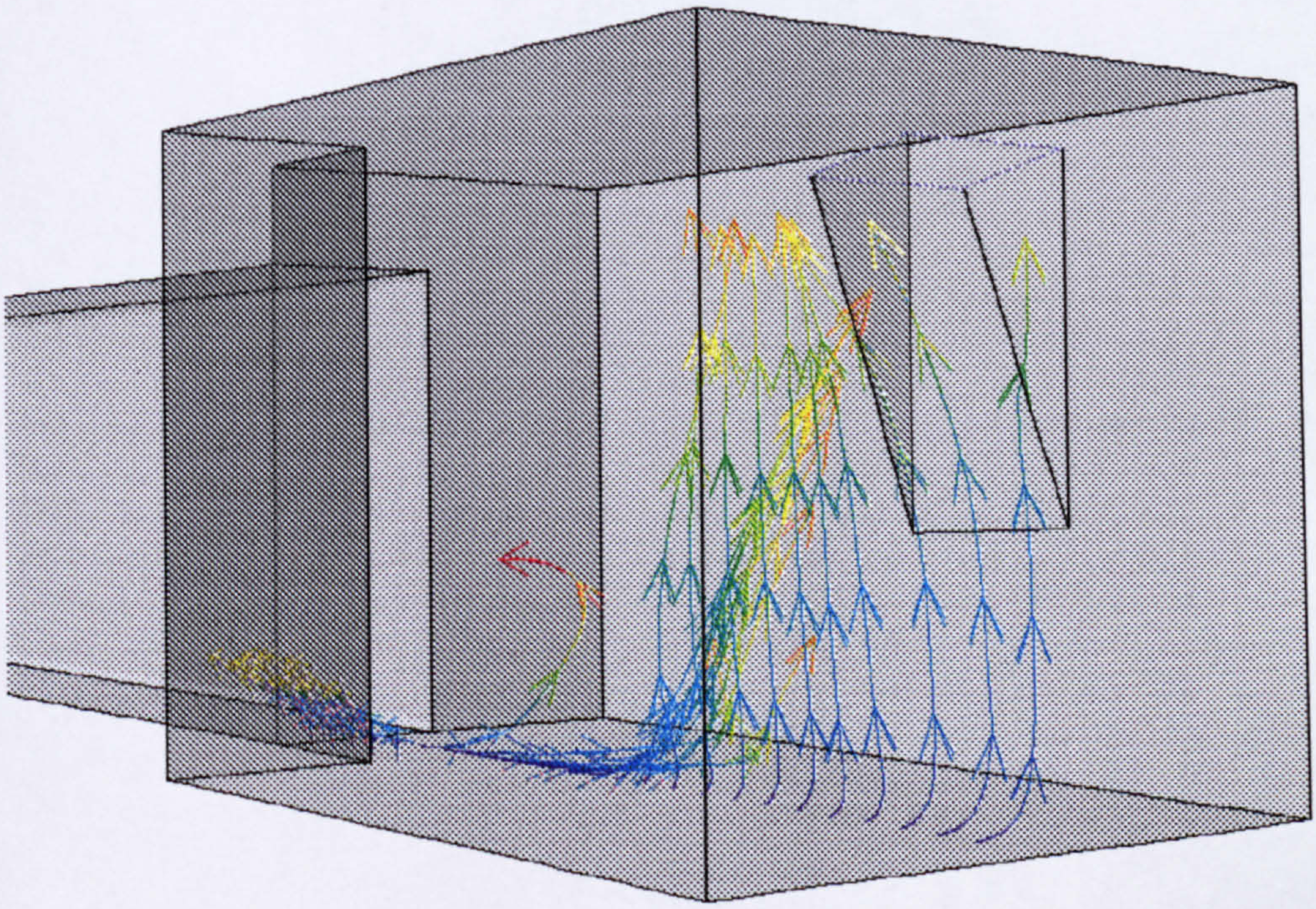

Figure 5.11: Stream lines released near the floor boundary from an isothermal simulation of the 3 a.m. period.

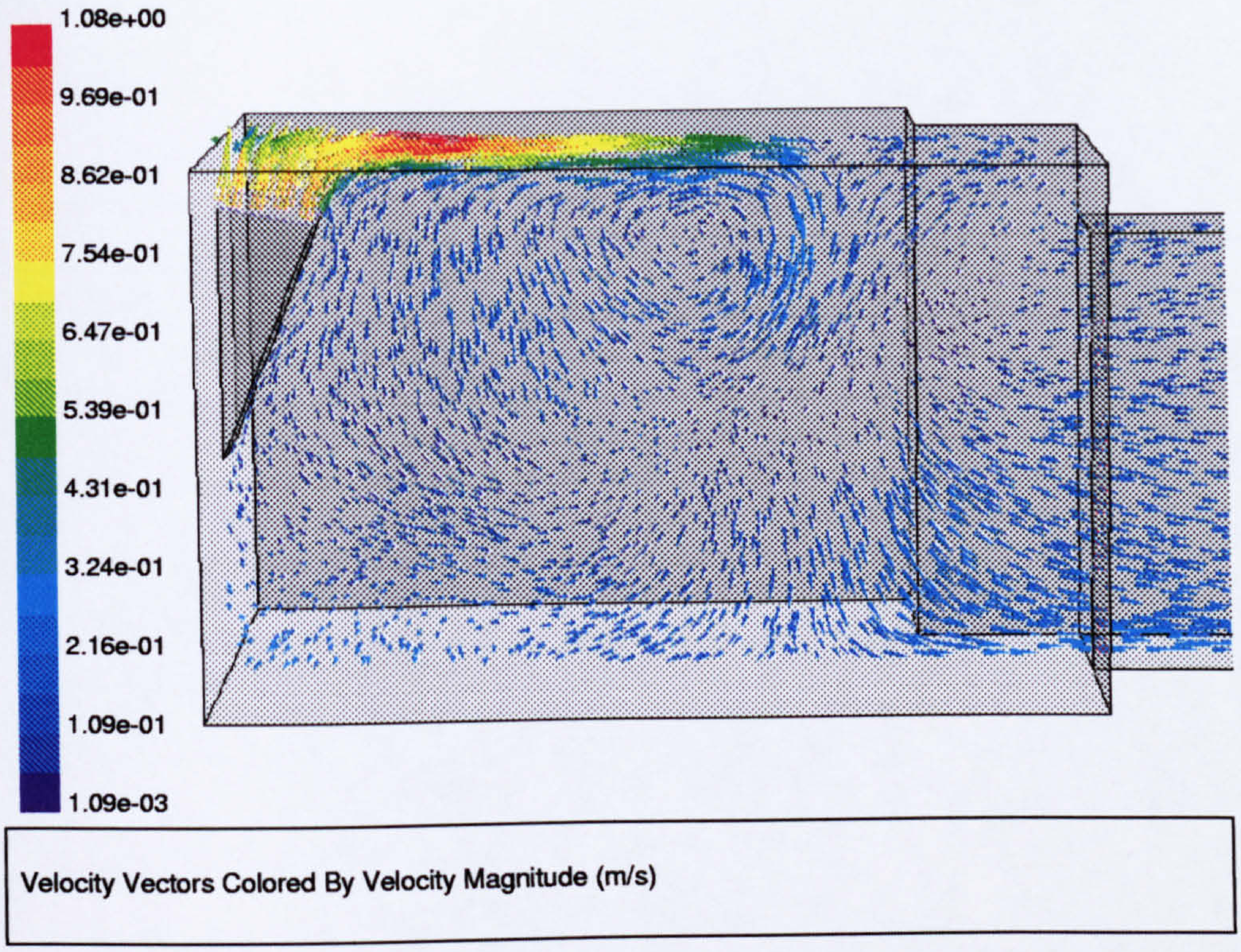

Figure 5.12: Vector plot along y plane near the middle of the room from a thermal and buoyancy simulation of the 3 a.m. period.

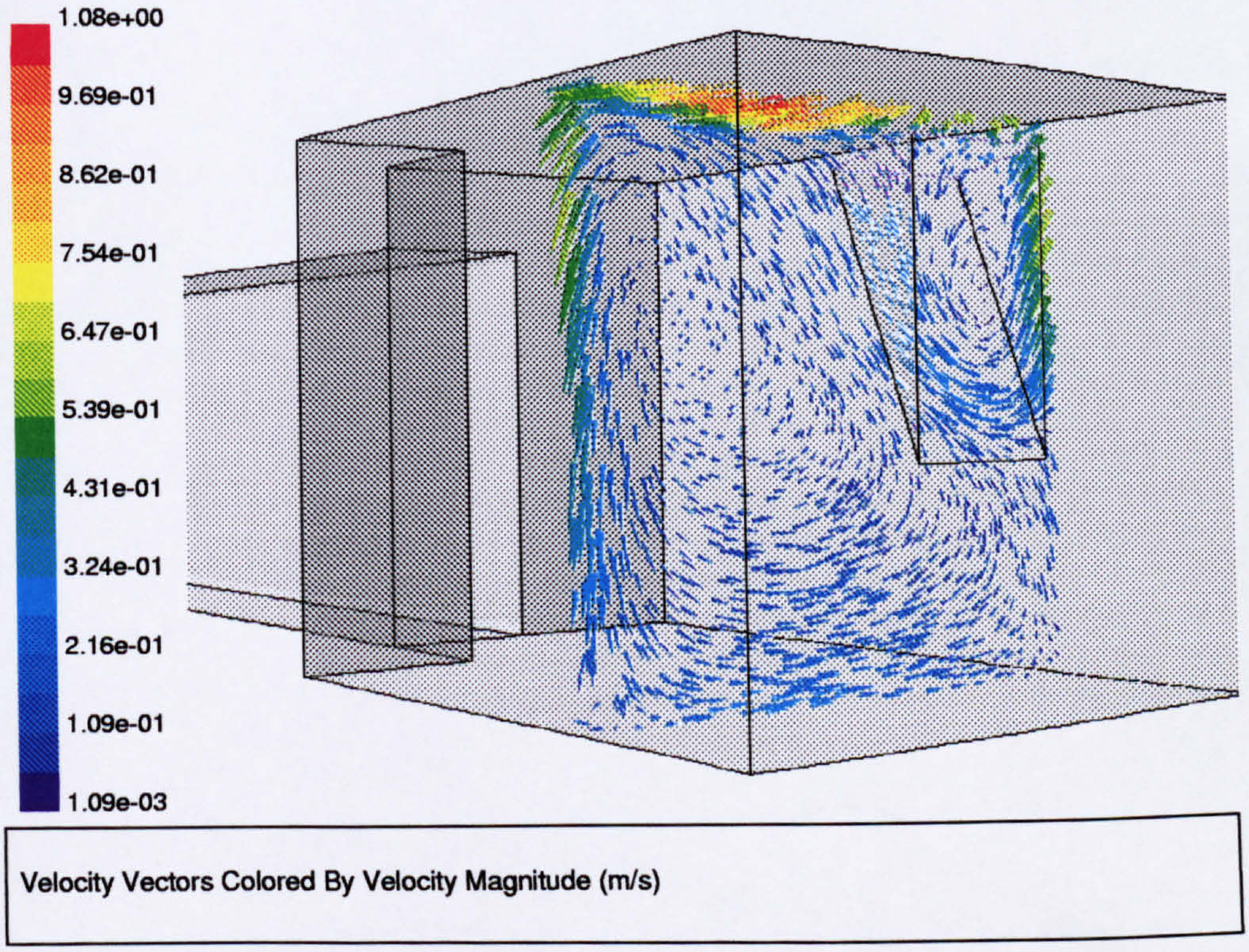

Figure 5.13: Vector plot along x plane from a thermal and buoyancy simulation of the 3 a.m. period.

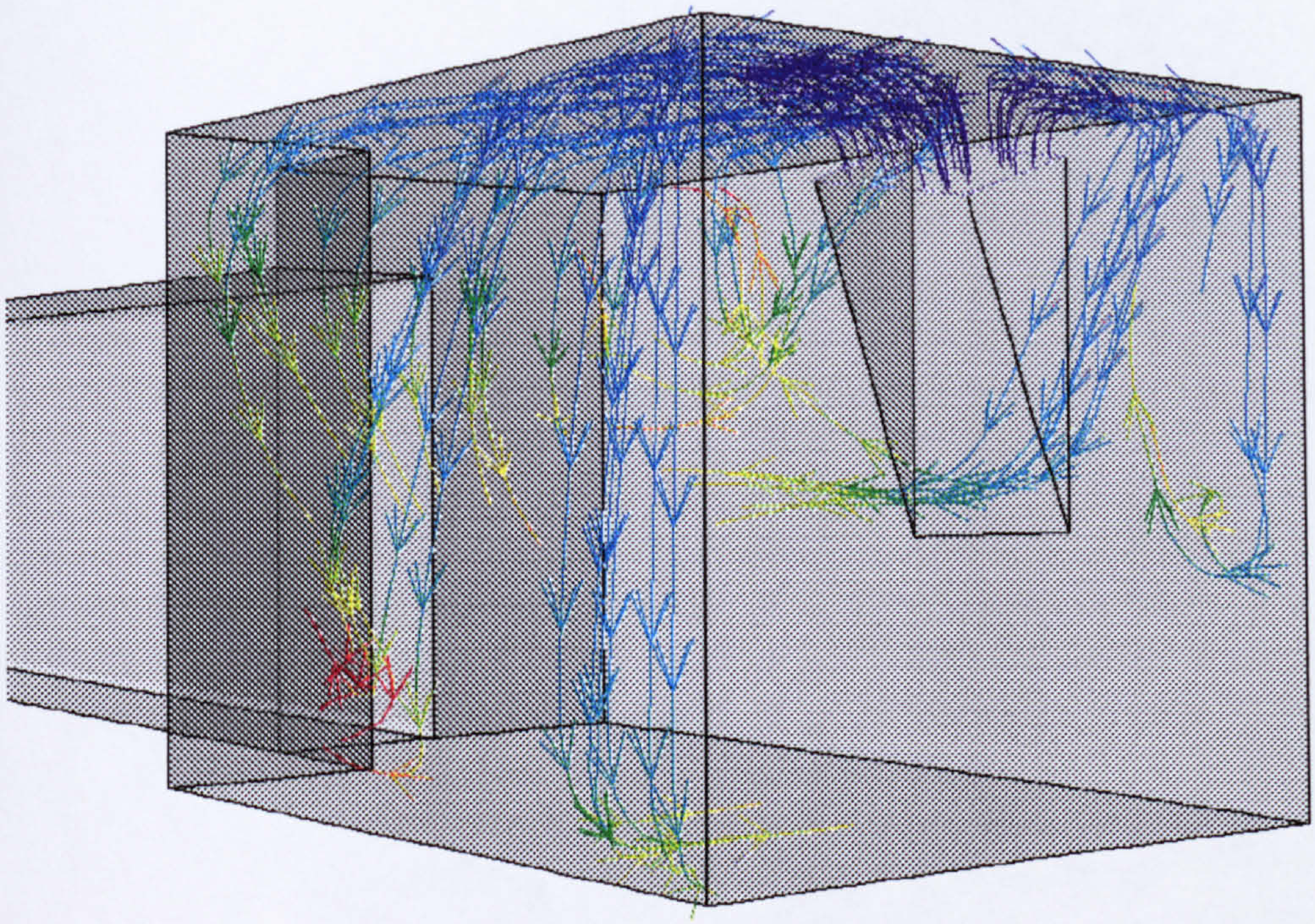

Figure 5.14: Stream lines from the inflow boundary from a thermal and buoyancy simulation of the 3 a.m. period.

the main flow stream still travels along the ceiling, but it detaches before reaching the rear wall, see Figures 5.14 and 5.12.

Figures 5.15 and 5.16 shows stream lines from the top and the bottom of the south wall boundary respectively. When compared with Figures 5.9 and 5.10 it can be seen that the flow field is significantly different if buoyancy is simulated. When buoyancy is included in the simulation, air flows down the south wall from the top, and up from the bottom, before flowing into the middle of the room. Figure 5.17 shows a z-plane vector plot 1 m above the floor. It can be seen that air does not flow into the middle of the room to be entrained upwards into the main flow stream as in the isothermal case. Instead air flows across the floor from the north to the south wall. The exit flow is biased towards the bottom of the door when buoyancy is included in the simulation.

12 a.m. Thermal Simulation

Stream lines taken from the inflow boundary of the 12 a.m. thermal simulation shows how the main flow stream does not attach to the ceiling but falls to the floor on entering the room, see Figure 5.18. Stream lines along the north and south walls show that air flows up the walls, rather than down as in the 3 a.m. isothermal and buoyancy cases, see Figures 5.19 and 5.20. The vectors in Figure 5.21 show the main flow stream as it flows across the floor. Velocities near the door are smaller than close to the window. Dissi-

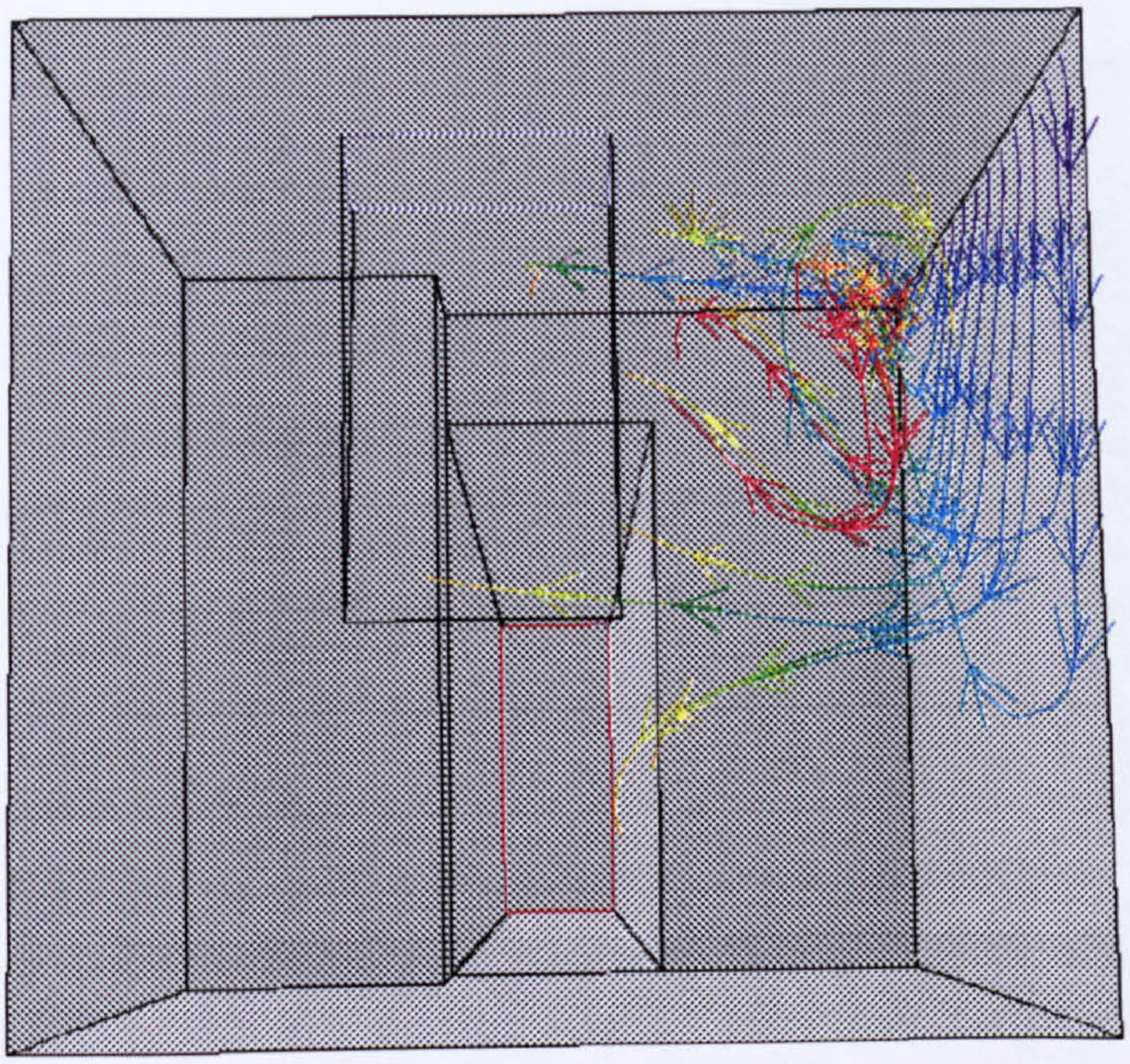

Figure 5.15: Stream lines from the top of the south wall boundary from a thermal and buoyancy simulation of the 3 a.m. period.

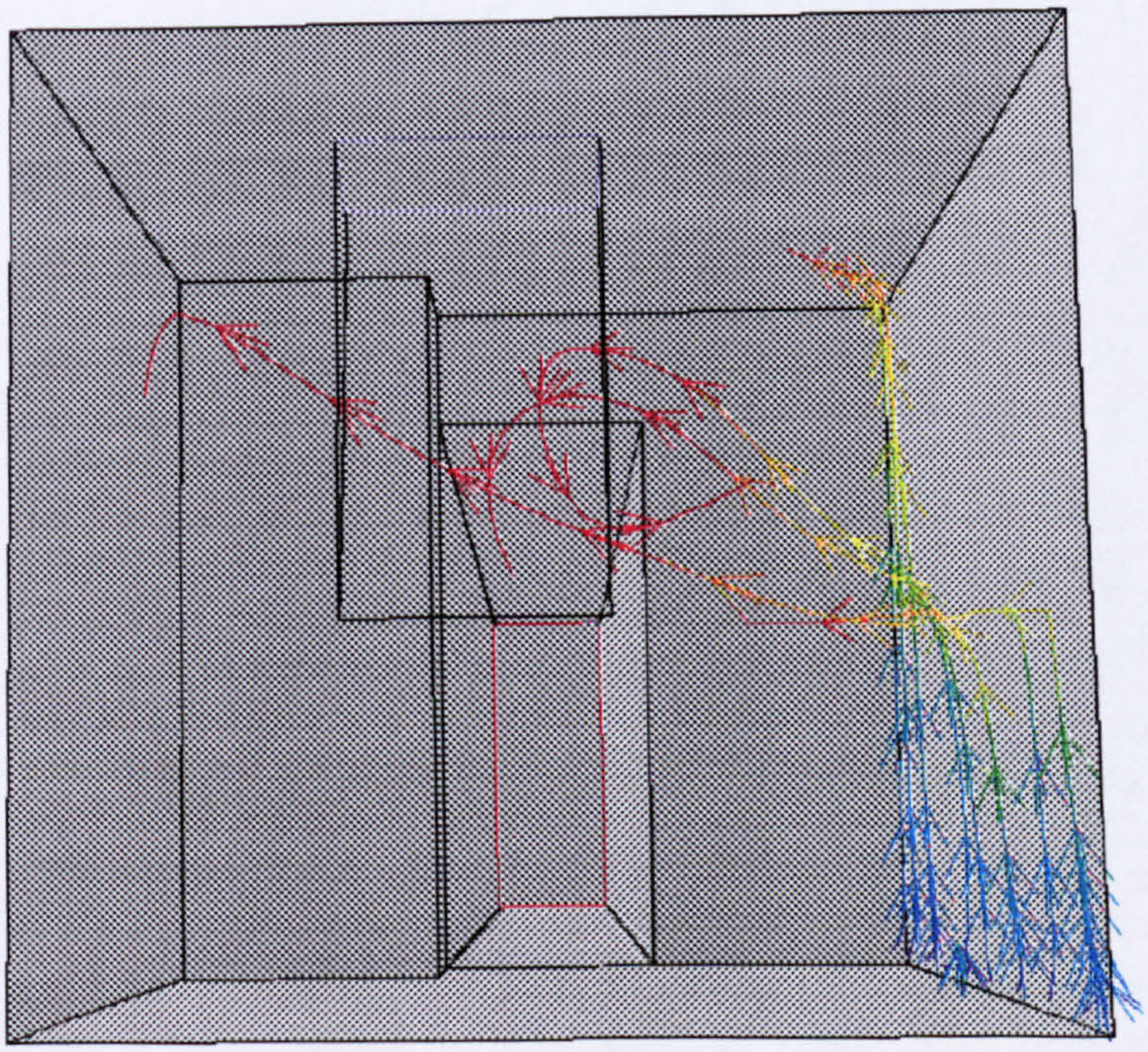

Figure 5.16: Stream lines from the bottom of the south wall boundary from a thermal and buoyancy simulation of the 3 a.m. period.

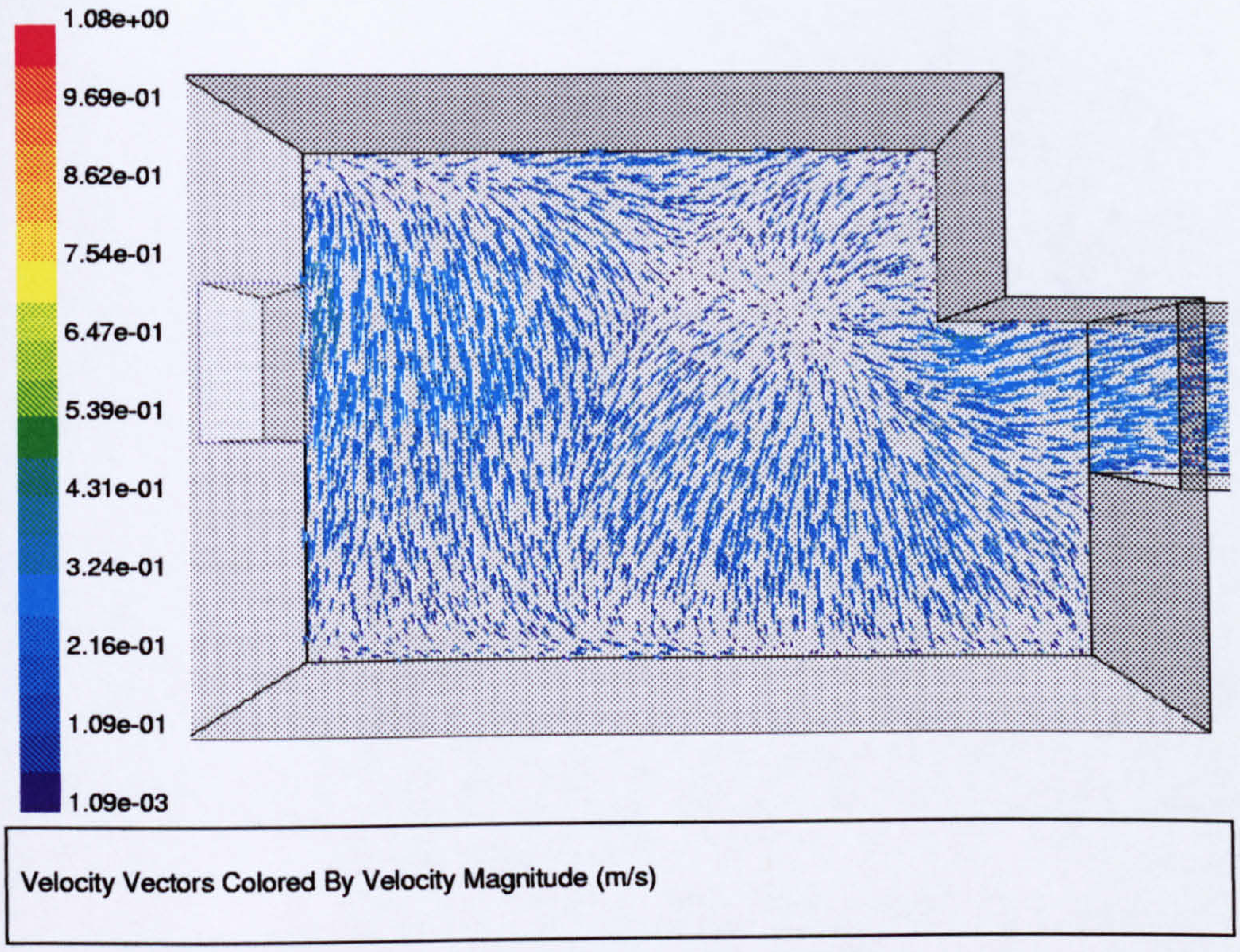

Figure 5.17: Vector plot close to the floor from a thermal and buoyancy simulation of the 3 a.m. period.

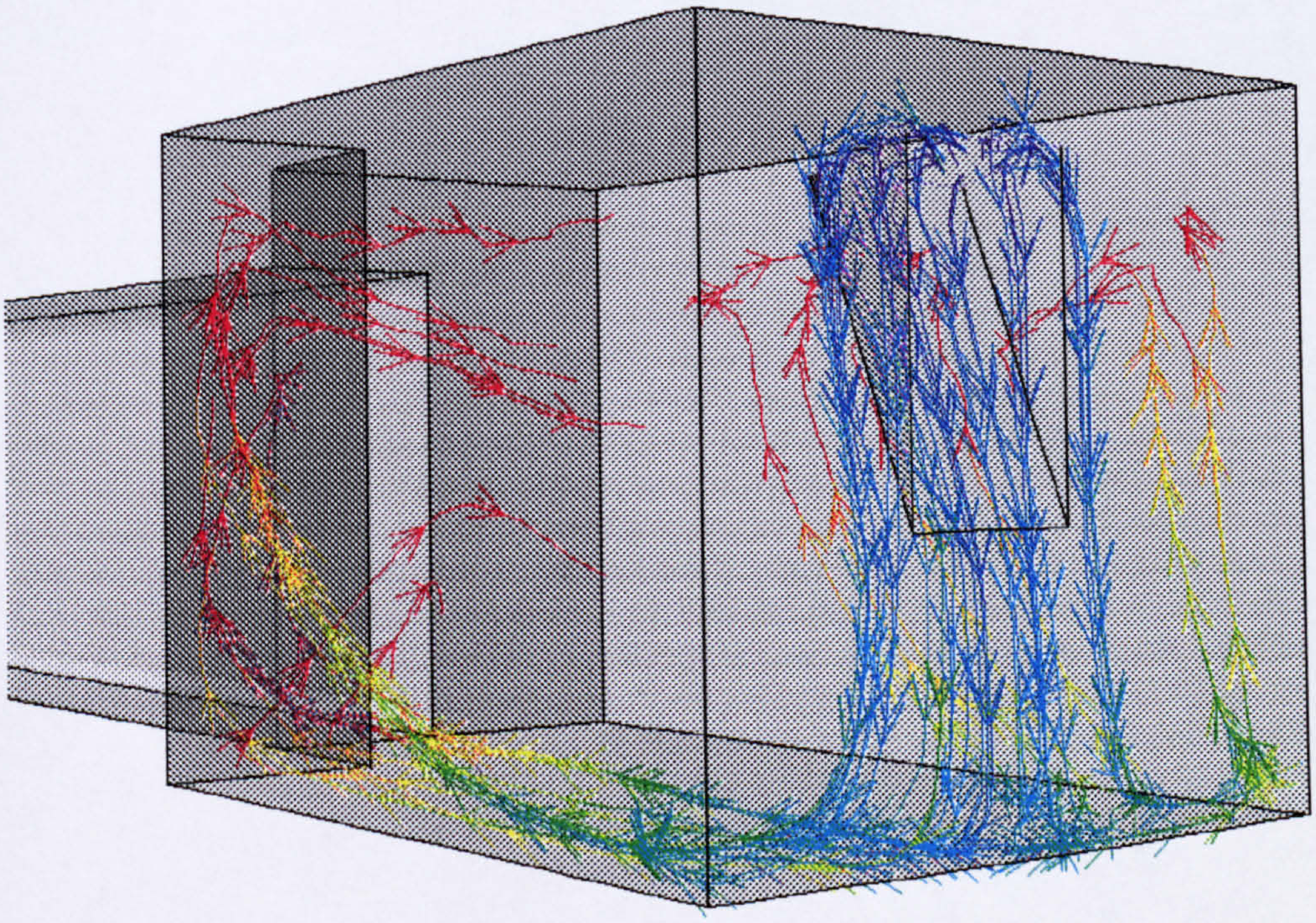

Figure 5.18: Stream lines from the inflow boundary from a thermal and buoyancy simulation of the 12 a.m. period.

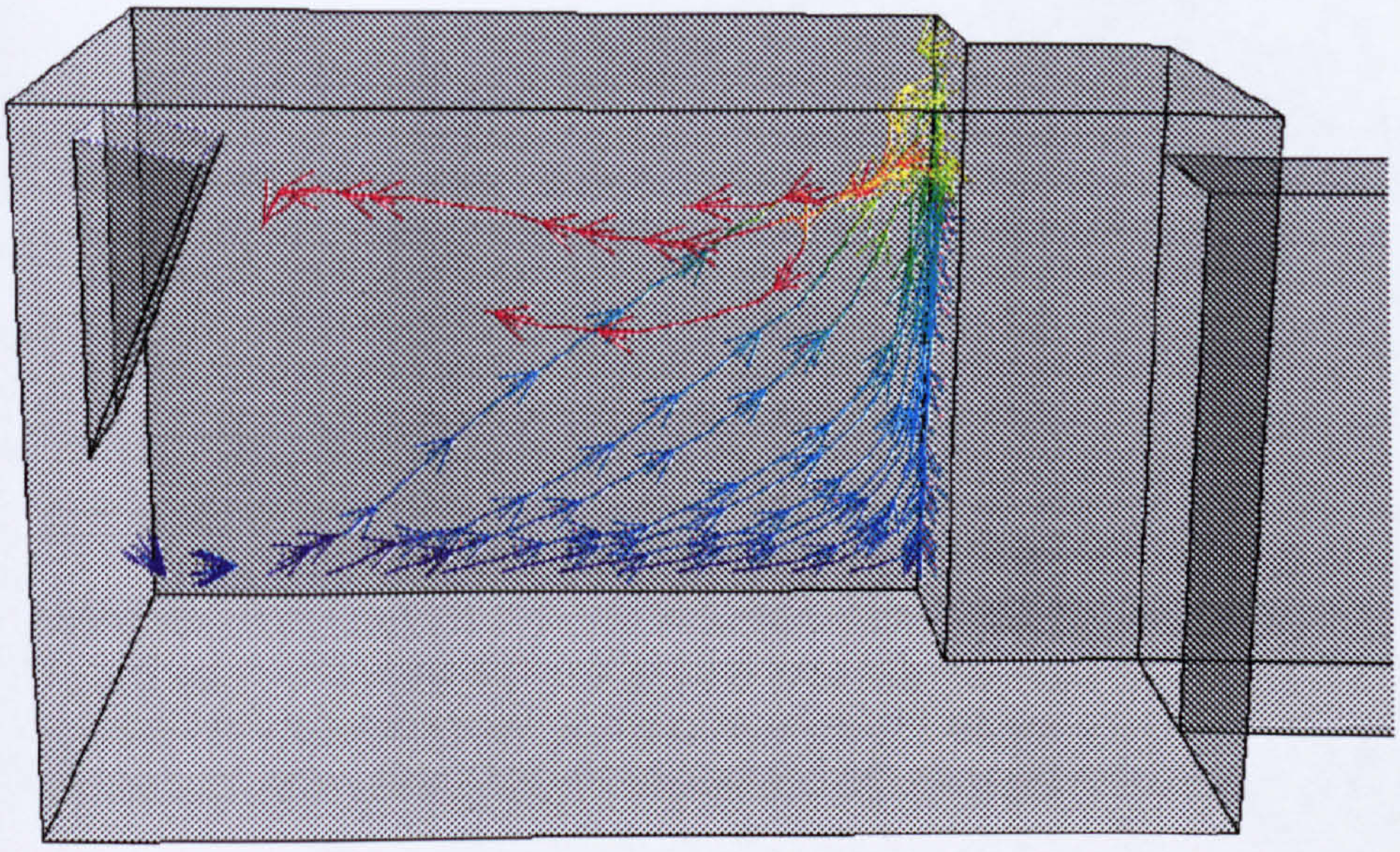

Figure 5.19: Stream lines along the north wall boundary from a thermal and buoyancy simulation of the 12 a.m. period.

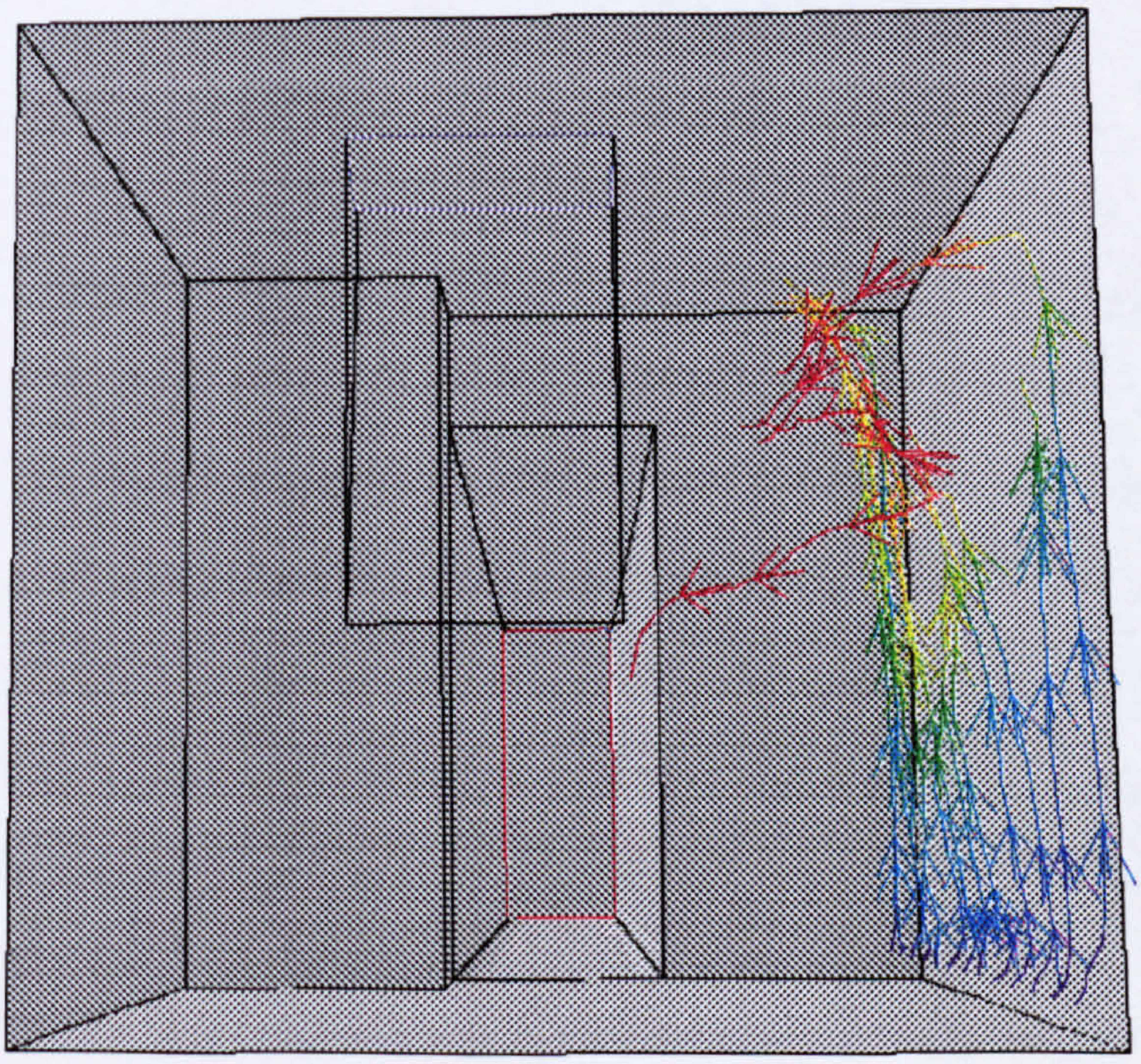

Figure 5.20: Stream lines from the bottom of the south wall boundary from a thermal and buoyancy simulation of the 12 a.m. period.

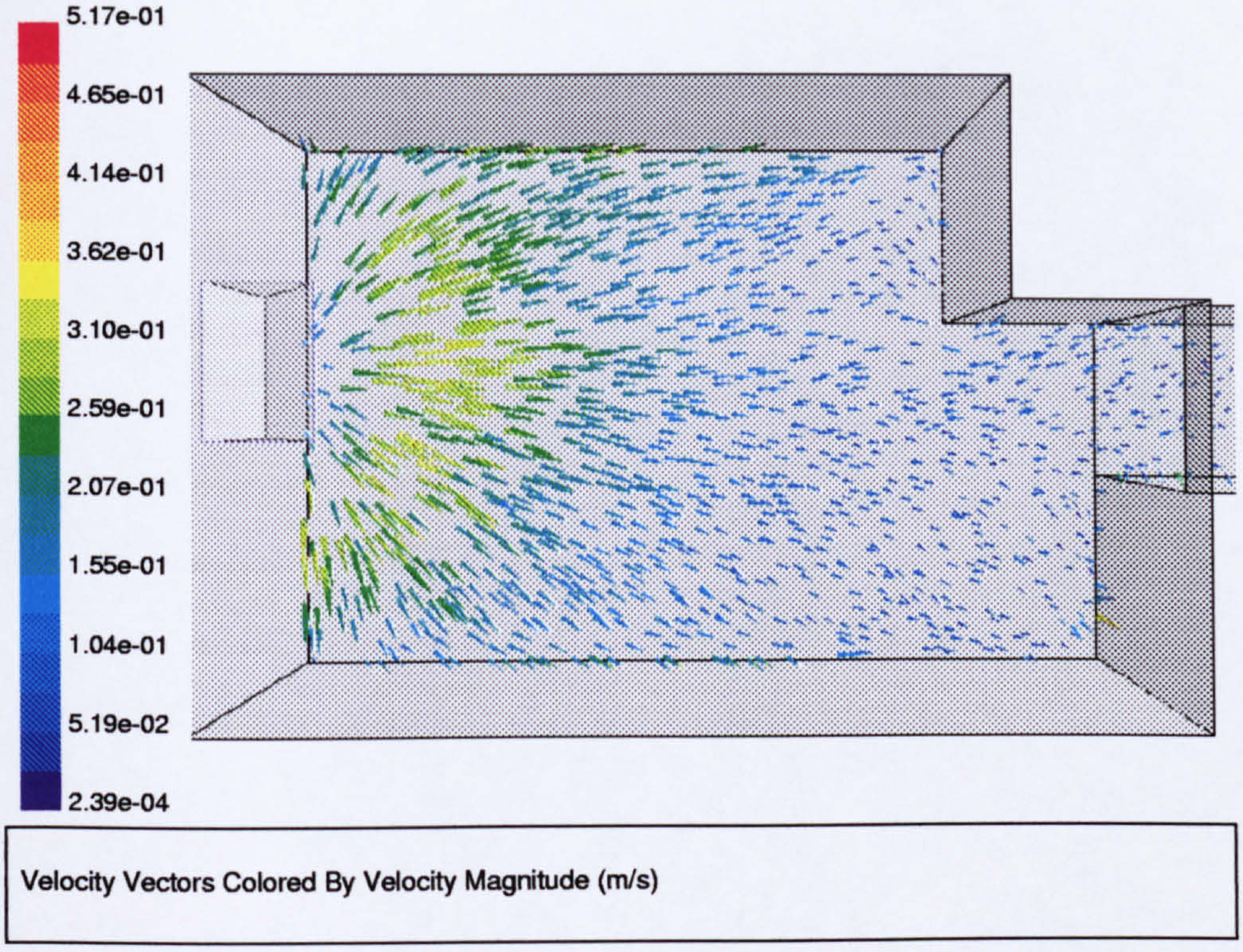

Figure 5.21: Vectors on a z-plane 0.1 m above the floor from a thermal and buoyancy simulation of the 12 a.m. period.

pation of kinetic energy is much higher in the 3D simulations than the 2D simulations from Chapter 3. Figure 5.22 shows the flow up the east wall near the door that forms the recirculating region above the main flow stream across the floor.

5.3.3 Detachment Point

We are able to see if the relationship between Archimedes number (Ar) and detachment point derived from the two-dimensional CFD parametric study is supported by the results from the three-dimensional simulation presented in this chapter. If we examine the 3 a.m. period first, using Equation 3.81 derived in Chapter 3 and repeated below,

$$\begin{aligned} Ar &= \frac{1}{T_{in}} \frac{g \Delta T_{ci}}{v_{in}^2} \frac{A_{in}}{l} \\ &= 0.0034 * \frac{9.81 * 11.5}{0.83^2} * 0.113 \\ &= 0.063, \end{aligned}$$

where:

g is the gravitational acceleration;

T_{in} is the temperature of the inlet;

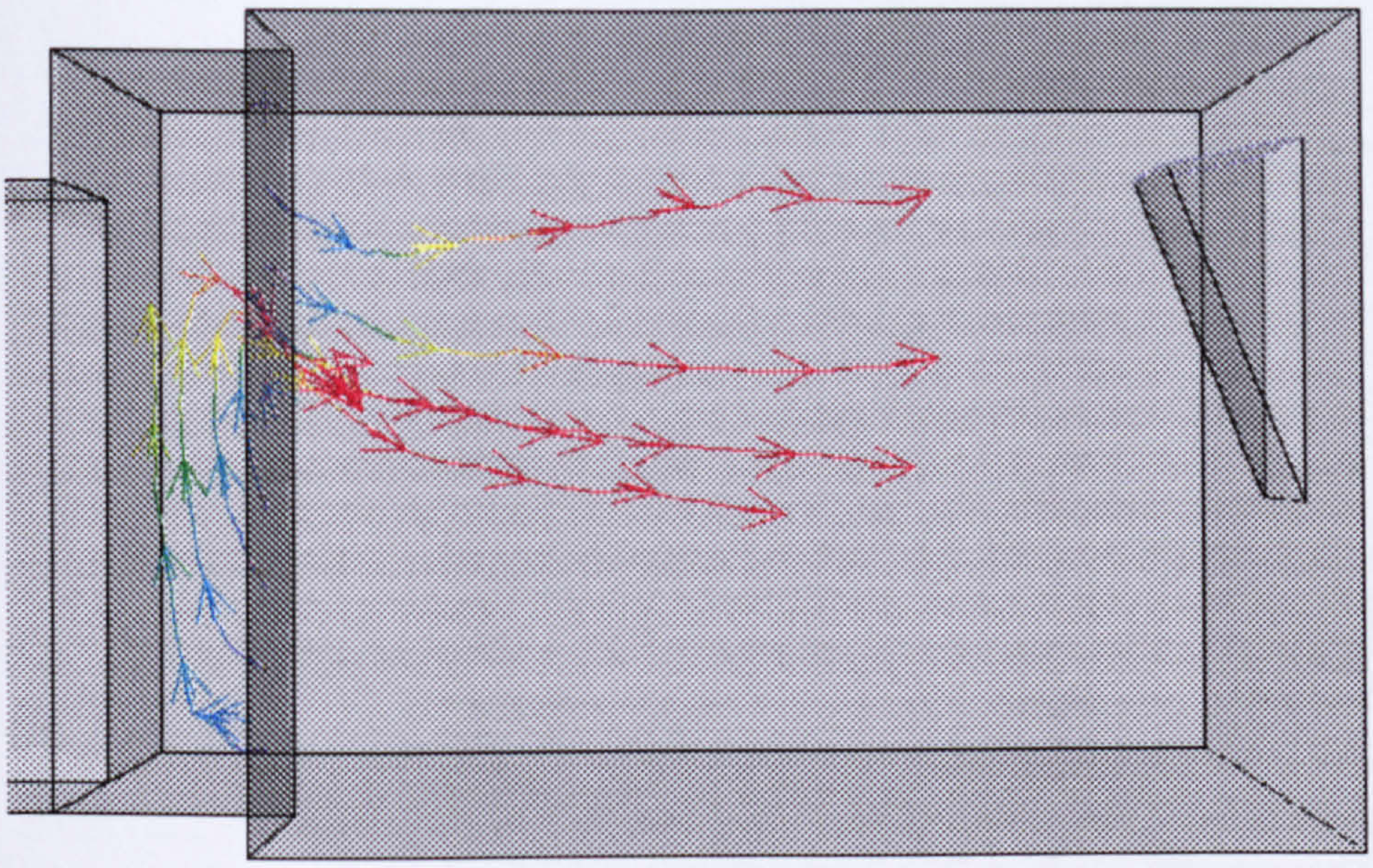

Figure 5.22: Stream lines along the south and east wall boundaries from a thermal and buoyancy simulation of the 12 a.m. period.

ΔT_{ci}	is the temperature difference between the inflow air and the ceiling;
$\frac{A_{in}}{l}$	is the area of the window per unit length of facade;
v_{in}	is the inlet velocity.

From the two-dimensional parametric study an Archimedes number of 0.063 is in the region where flow detaches from the ceiling in zone 4. Figure 5.12 shows that the flow detaches from the ceiling after the half way point.

Secondly, we can look at the 12 a.m. period,

$$\begin{aligned} Ar &= \frac{1}{T_{in}}\frac{g\Delta T_{ci}}{v_{in}^2}\frac{A_{in}}{l} \\ &= 0.0034 * \frac{9.81 * 11.65}{0.1^2} * 0.113 \\ &= 4.4. \end{aligned}$$

From the two-dimensional parametric study an Archimedes number of 4.4 is in the region where flow detaches from the ceiling upon entry to the room. Figure 5.18 shows that the flow does indeed detach from the ceiling upon entry to the room.

Here, the 3D CFD simulations agree well with the correlation between detachment position and Archimedes number derived from the 2D CFD parametric study.

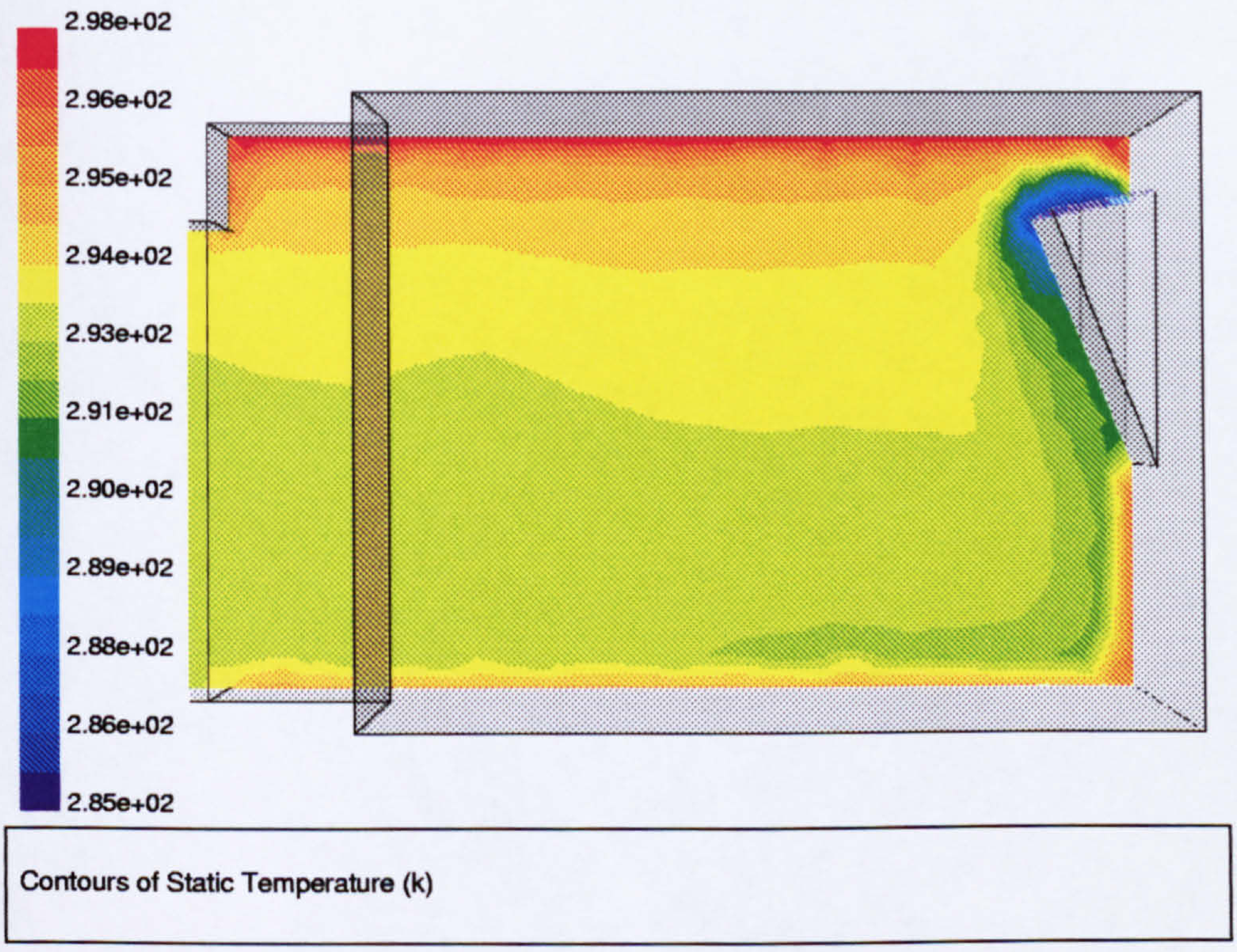

Figure 5.23: Temperature contour plot, 12 a.m. period.

5.3.4 Temperature Field

Figures 5.23 and 5.24 show a temperature contour plot from the 12 a.m. period and the 3 a.m. period respectively. At 12 a.m. there is significant thermal stratification, with high temperatures close to the ceiling. This is due to the cooler air falling to the floor on entry to the room and is in sharp contrast to the 3 a.m. when the room air flow is reasonably well mixed.

The CFD prediction and the experimental measurements of temperature at each of the anemometer stands at 12 a.m. and 3 a.m. are shown in Figures 5.25 and 5.26. At 12 a.m. and 3 a.m. the temperature in the experimental room is higher than the CFD predictions, this could be for a number of reasons:

- The thermal boundary conditions are not adequately treated;
- The mass flow through the inlet is too high in the CFD model;
- Convective heat transfer at the wall boundaries is under-predicted in the CFD model.

At 12 a.m. both the CFD prediction and the experimental measurements show thermal stratification, at all the anemometer stand positions, although, the temperature gradient is higher in the experimental room. The experimental temperature gradient at Stand B

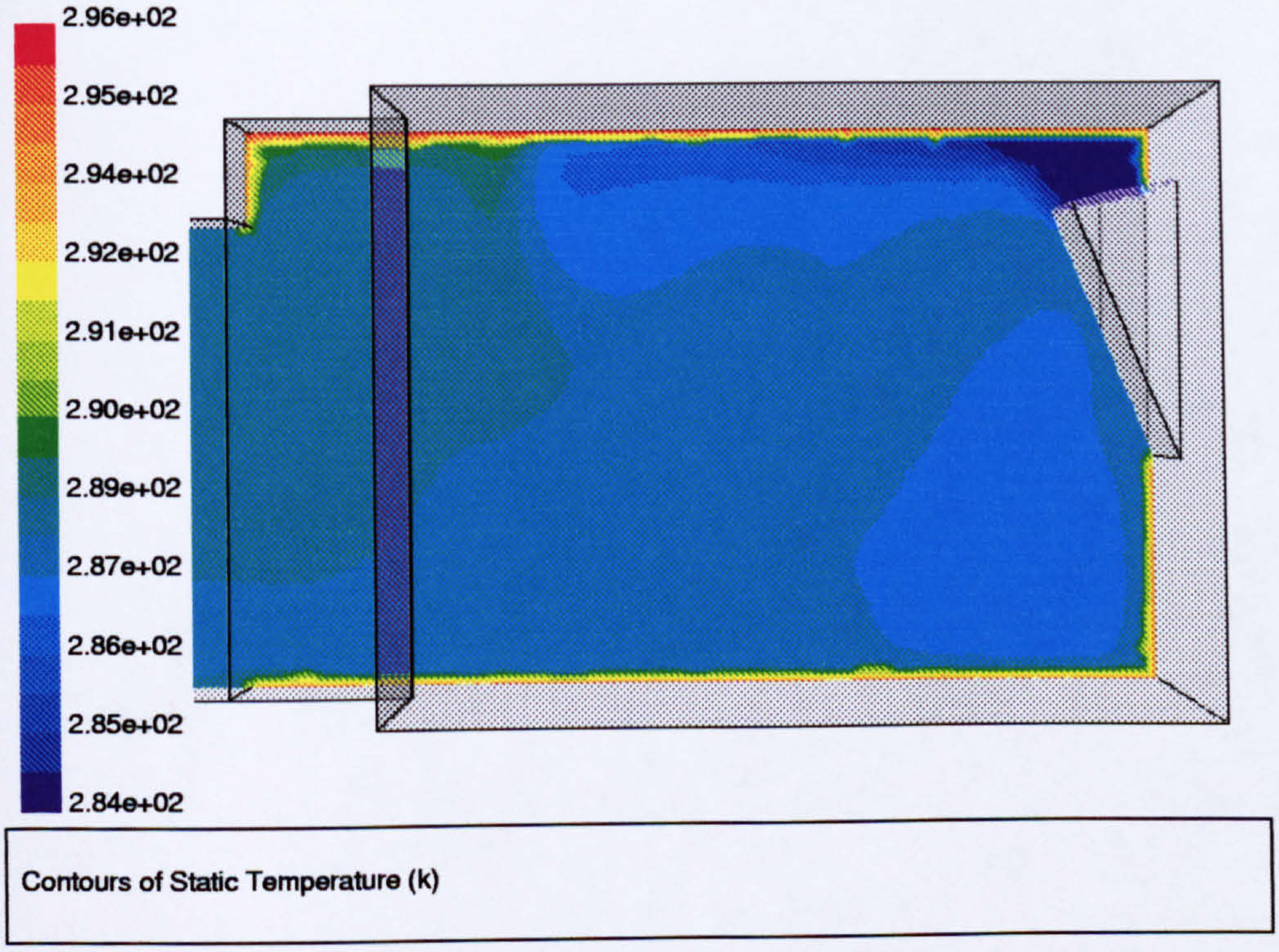

Figure 5.24: Temperature contour plot, 3 a.m. period.

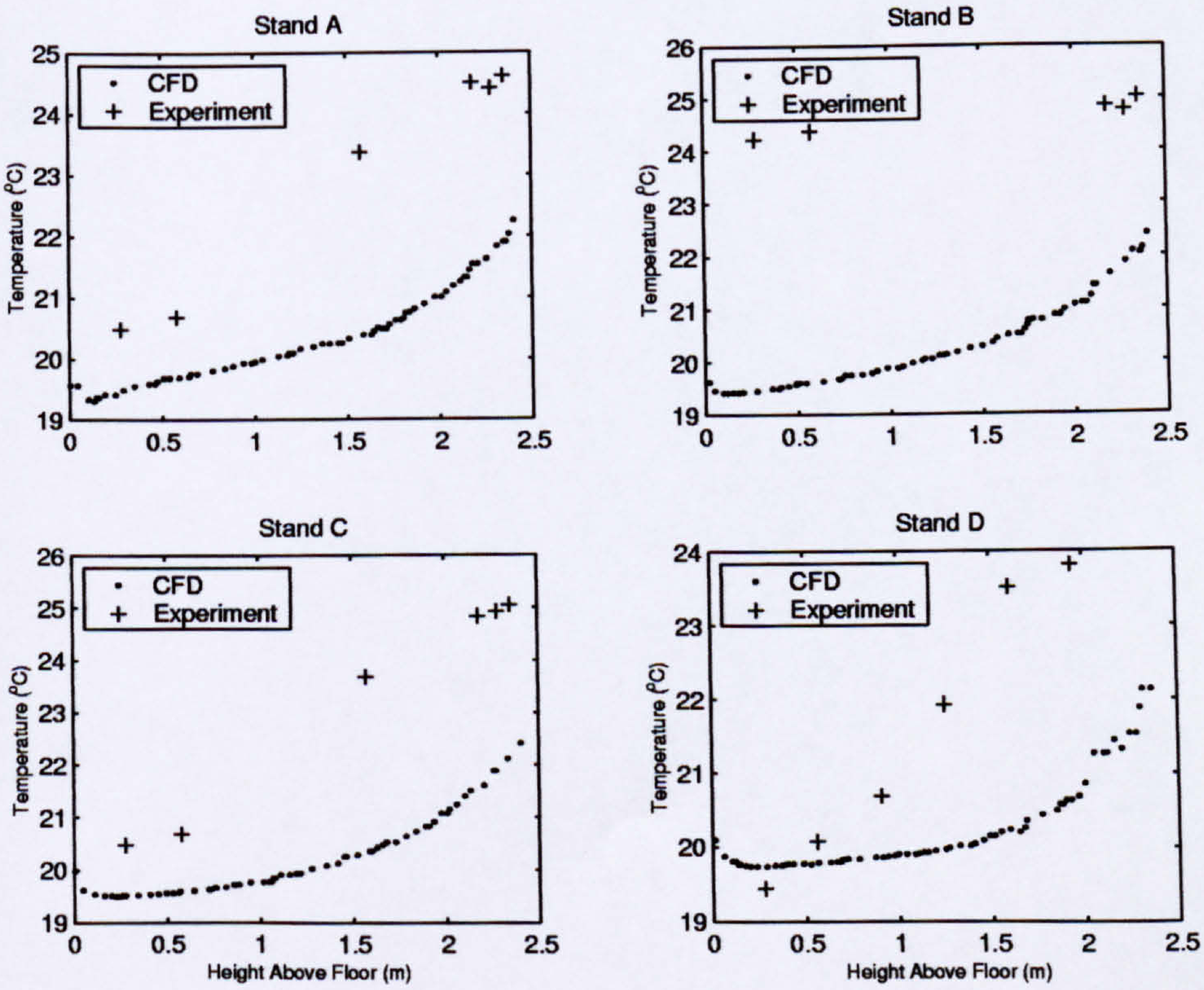

Figure 5.25: Comparison between CFD and experimental temperatures at 12 a.m.

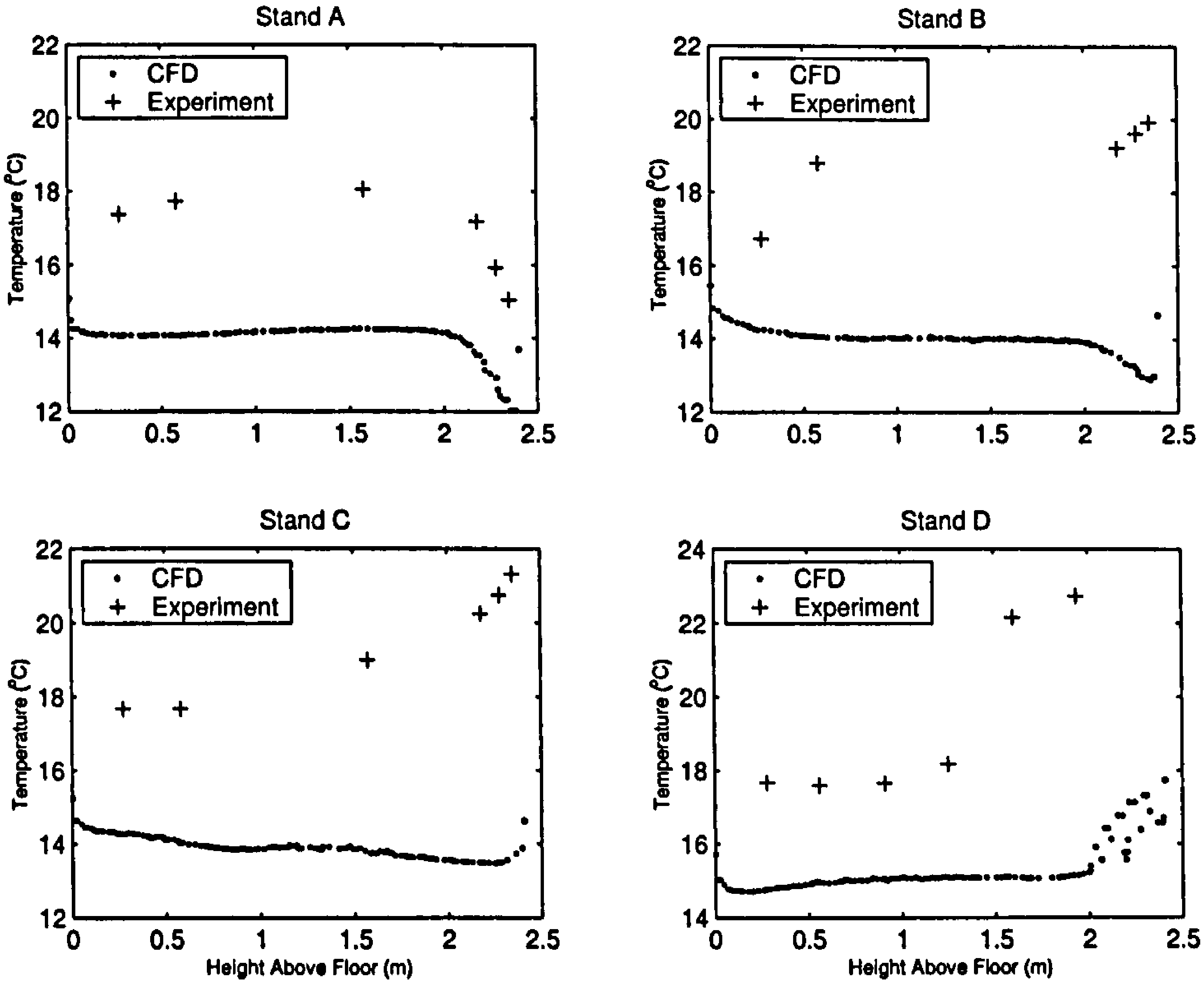

Figure 5.26: Comparison between CFD and experimental temperatures at 3 a.m.

is much smaller than at A, C and D, see Figure 5.27 for stand positions. This is most likely due to experimental error.

At 3 a.m. the picture is more complex. The experimental measurements suggest there is cooler air at the ceiling at A, and warmer air at B and C. At Stand A the CFD prediction and the experimental measurements correlate well with reasonably constant temperature below 2 m and lower temperature above 2 m, decreasing towards the ceiling. This indicates that the cooler incoming air is flowing across the ceiling. At Stands B and C the experimental measurements point to thermal stratification while the CFD prediction at Stand B shows cooler air at the ceiling. The 3 a.m. temperature profiles show that the CFD prediction at Stand D agrees partly with the experimental results, with a fairly constant temperature below the top of the door. In the CFD results there is an increase in temperature above the top of the door. There were no experimental readings taken above the top of the door but there is a jump in measured temperatures above 1.5 m. This may be due to warmer air from the corridor flowing into the room, which is not predicted by the CFD simulation.

5.3.5 Air Speed

During the experiment air speed measurements were taken at four locations using stands with six omni-directional anemometers attached, see Figure 5.27. These experimental

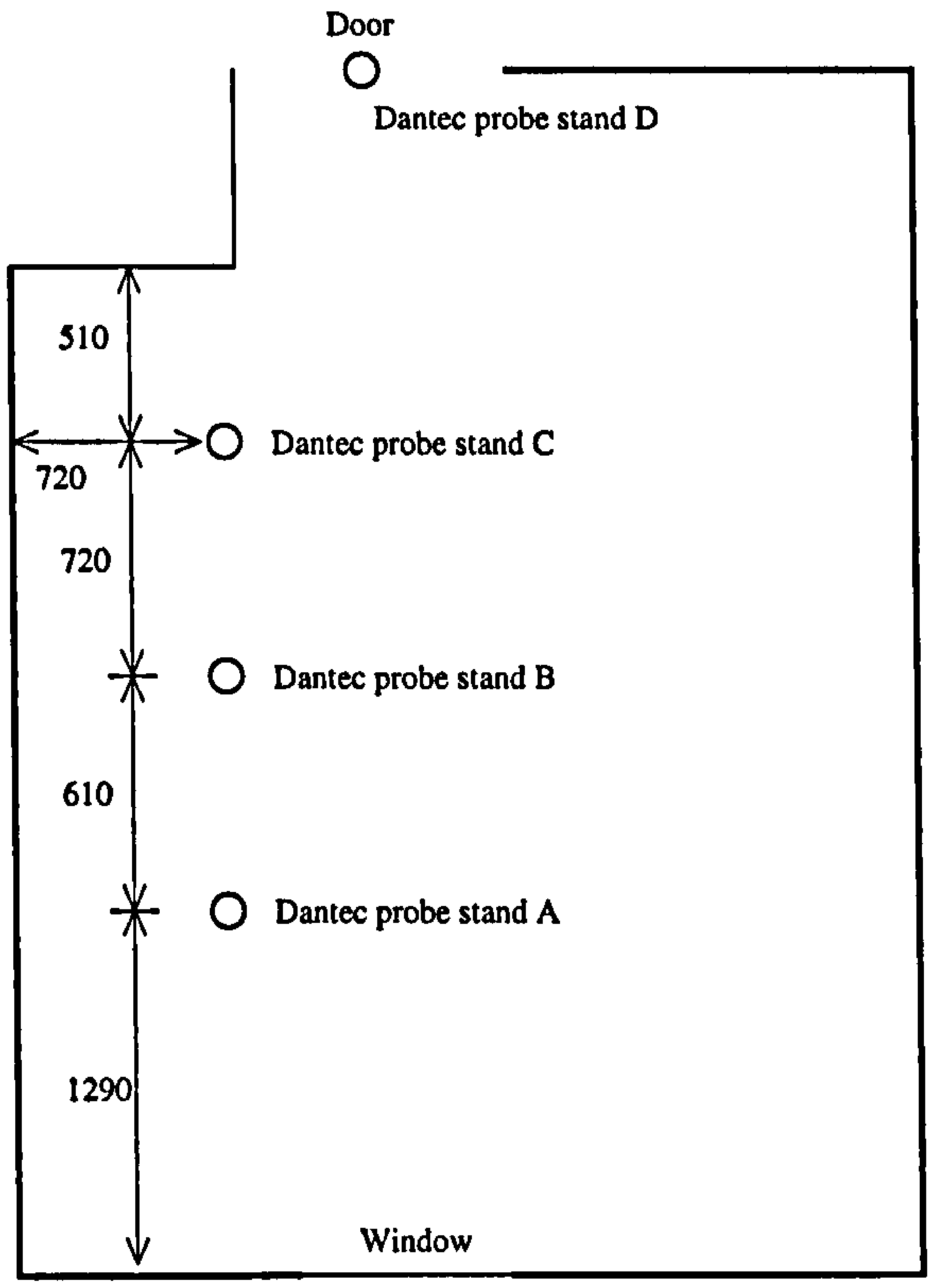

Figure 5.27: Dantec stand locations.

readings were compared with numerical results presented here.

Figure 5.28 shows that an isothermal simulation of the 3 a.m. period produces a velocity profile that correlates well with the experimental results at all stand locations. The correlation is best at Stand A nearest the window. At Stands B and C the numerical result over-predicts the air speed close to the ceiling and under-predicts it near to the floor. This is probably due to the fact that with buoyancy forces ignored, entrainment into the main flow stream across the ceiling is under-predicted, and therefore so is the decrease in velocity of the flow stream. Figure 5.29 shows that including thermal energy and buoyancy into the CFD calculation of the 3 a.m. period worsens the CFD predictions, particularly at Stand C.

Figure 5.30 shows that an isothermal simulation of the 12 a.m. period under-predicts the air speed in the middle and bottom part of the room at all stand locations. The isothermal simulation predicts the main flow stream is across the ceiling while the experimental data indicates that air speed is similar over the whole of the room height with only small increases near the floor and ceiling. Figure 5.31 shows that a thermal simulation with buoyancy improves the correlation between the numerical and the experimental results for the 12 a.m. period.

There are many possible sources of error in this procedure:

- Setting the inflow boundary velocity using one anemometer velocity reading means

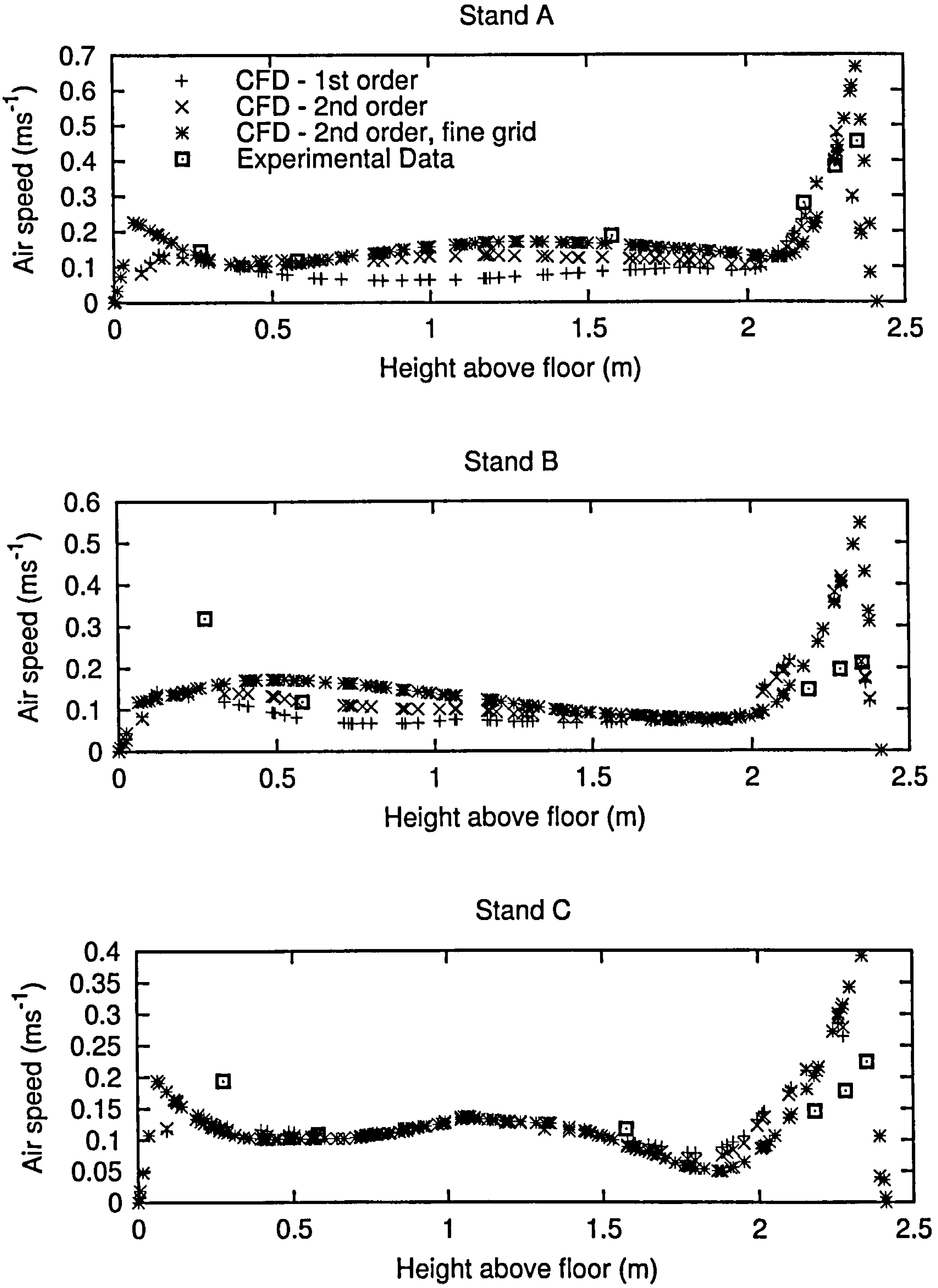

Figure 5.28: Average air speed at three vertical locations during the 3 a.m. period. Comparison between the experimental data and the numerical results from the isothermal simulations. Stand A nearest the window (top), Stand B (middle), and Stand C furthest from window (bottom).

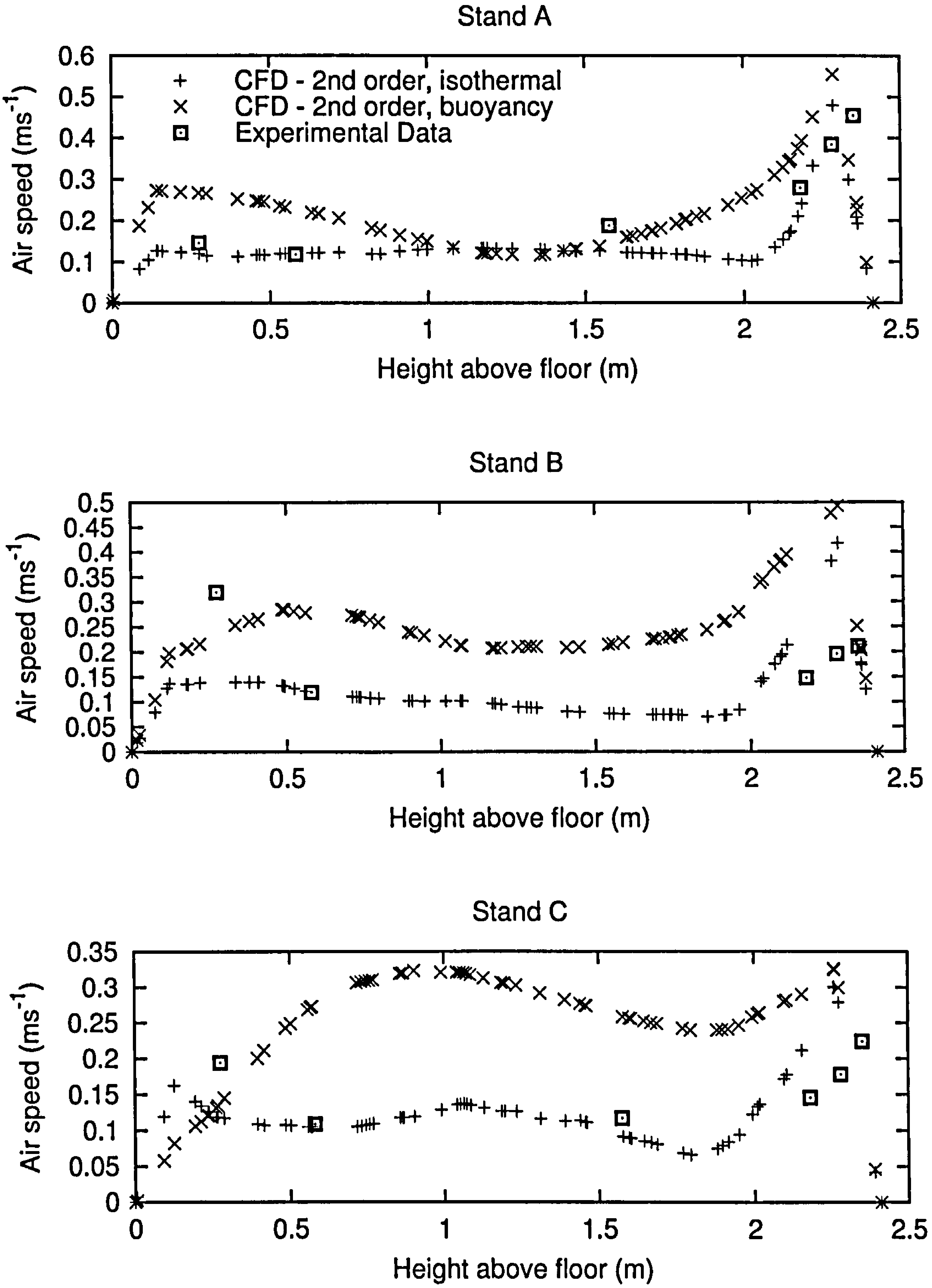

Figure 5.29: Average air speed at three vertical locations during the 3 a.m. period. Comparison between the experimental data and the numerical results from the isothermal, and the thermal simulations.

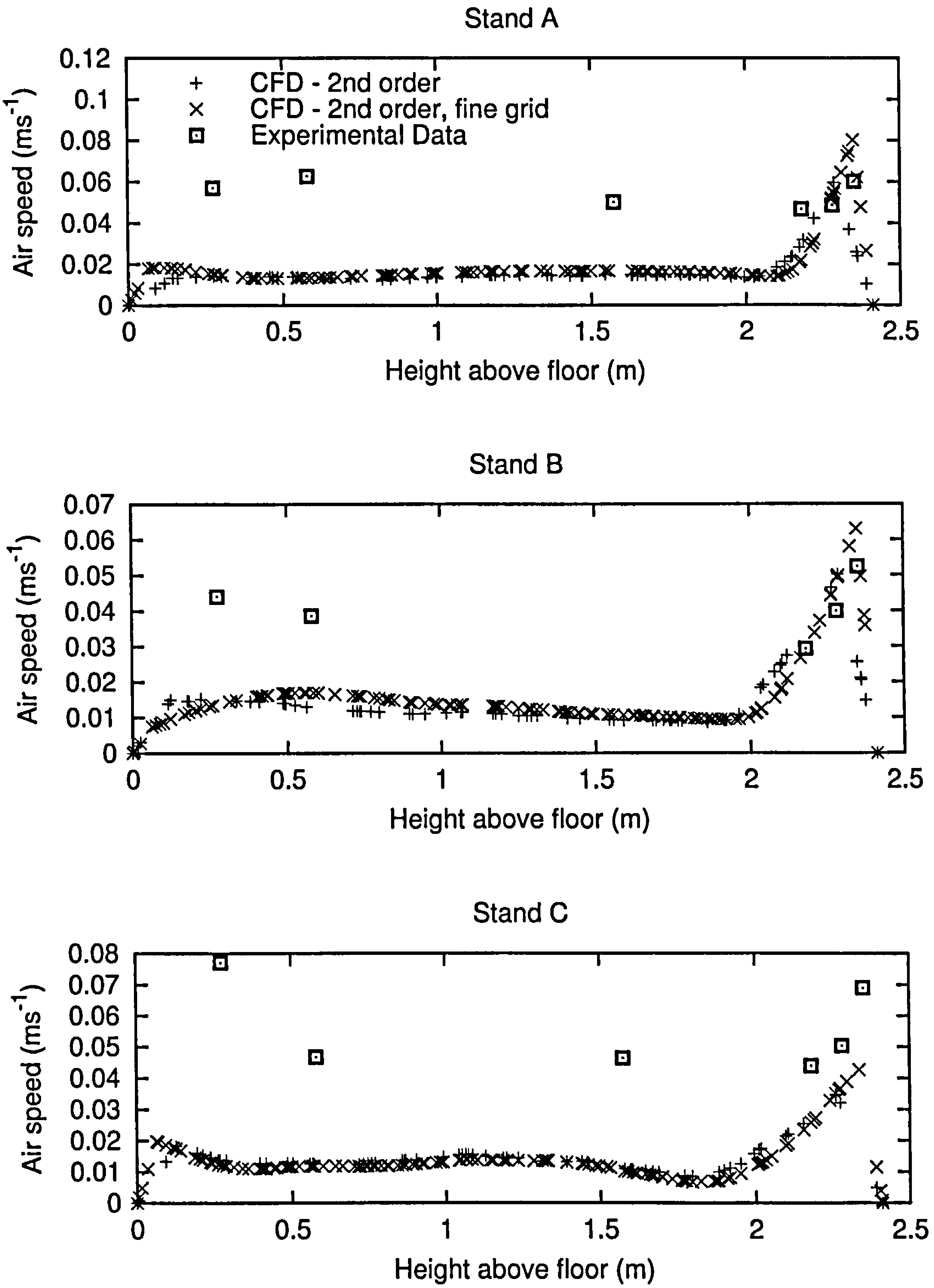

Figure 5.30: Average air speed at three vertical locations during the 12 a.m. period. Comparison between the experimental data and the numerical results from the isothermal simulations.

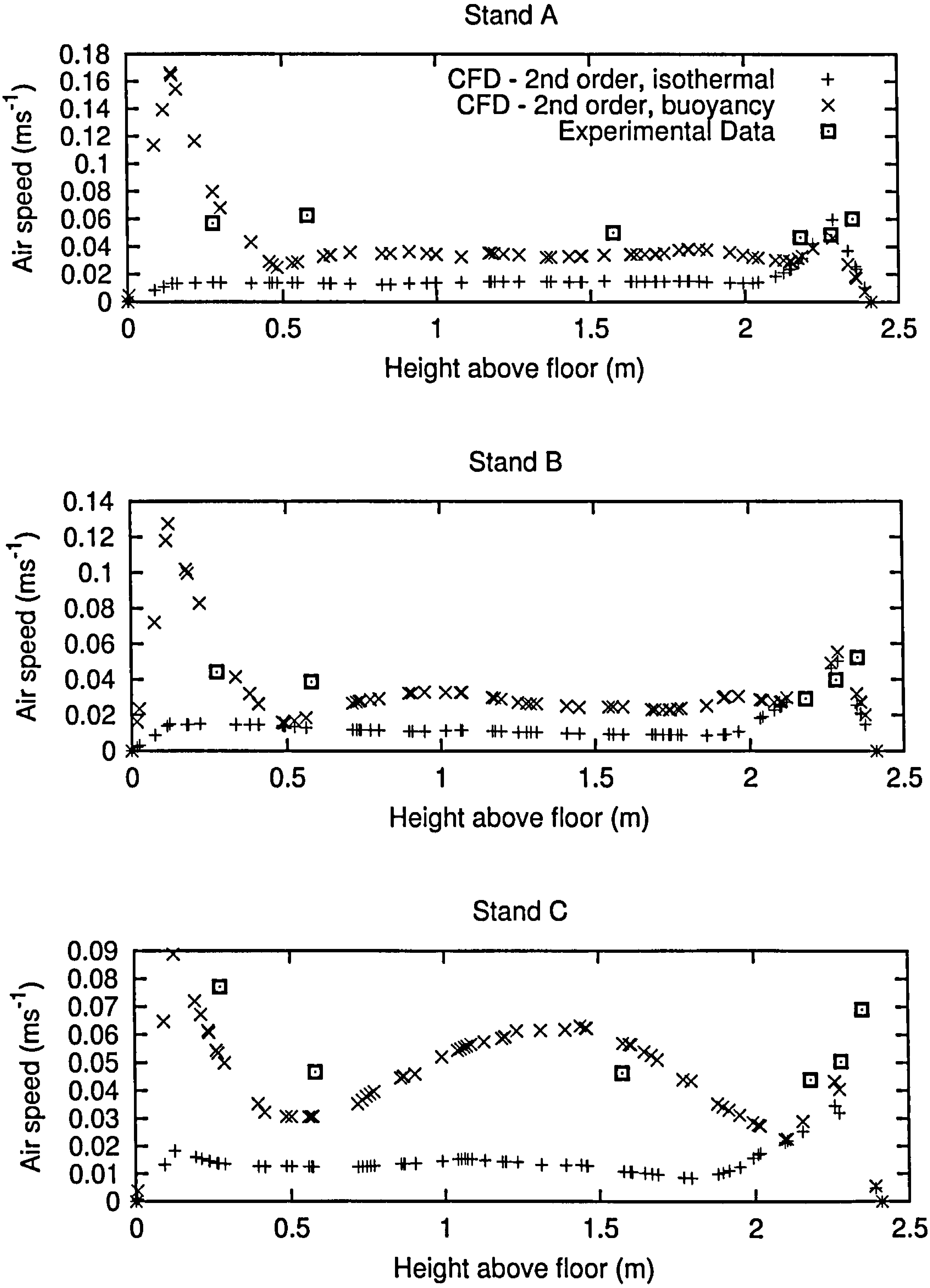

Figure 5.31: Average air speed at three vertical locations during the 12 a.m. period. Comparison between the experimental data and the numerical results from the isothermal, and the thermal simulations.

that the average mass flow through the experimental room may differ significantly to that in the CFD simulations. The hopper velocity profile may also differ significantly from the constant velocity boundary condition applied in the simulations.

- The surface temperatures in the CFD simulations were an average of four thermocouple readings on that surface. This does not represent the true complexity of the thermal environment. There was a large thermal gradient on the vertical walls in the experimental room.
- Error in experimental readings as well as the numerical calculations.

5.4 Conclusions

5.4.1 Findings

1. The main flow features seen in the experiment were captured in the results from the CFD simulations described in this chapter. The CFD results predicted that the flow can: remain attached to the ceiling throughout its passage through the room; detach on entry to the room; or detach part way through the room. The CFD also predicted the flow bias towards the north wall as well as the air flow down this wall whether the flow detached from the ceiling or not.
2. The fact that flow is seen to detach from the ceiling in different places provides further support for the decision to structure the zonal model with multiple flow detachment positions.
3. The 3D numerical results support the relationship between Archimedes number and detachment point derived from the 2D parametric study.
4. The CFD simulation with thermal energy and buoyancy included showed good agreement with experimental measurements when modelling the low room air speed period. An isothermal simulation is not sufficient here as the flow is dominated by buoyancy forces.
5. The isothermal and buoyancy simulations of the 3 a.m. period have significant differences. The flow through the door is biased towards the floor in the buoyancy case, and the top of the door in the isothermal case. The secondary flow is also different, with the main flow stream entraining air from the middle of the floor in the isothermal case, and the air flowing across the floor towards the south wall in the buoyancy case.
6. The main flow stream kinetic energy dissipates more quickly in the 3D model presented in this chapter when compared to the results of the 2D model in Chapter 3.

7. Thermal stratification is seen in both the experimental measurements and the numerical prediction at 12 a.m. At 3 a.m. the experimental and numerical temperature profiles agree well at Stand A, but there are significant differences at stand locations B and C, indicating possible differences in the experimental flow regime when compared to the CFD prediction.

8. The temperature in the experimental room is higher than the CFD predictions, this could be for a number of reasons.

   (a) The thermal boundary conditions are not adequately treated, for example, the temperature gradient over the vertical wall surfaces was not modelled.
   (b) The mass flow through the inlet is too high in the CFD model. This is very likely as the CFD inlet velocity is set from one air speed measurement near the front of the hopper. The inlet velocity profile was not modelled or determined by the experimental measurements.
   (c) Convective heat transfer at the wall boundaries is under-predicted in the CFD model.

   Determining how much the differences between the experimental measurements and CFD results is due to numerical inaccuracies and how much to the boundary conditions of the CFD simulation being set incorrectly is impossible to determine.

9. Although the experimental procedure was not undertaken for the purpose of CFD validation conclusions can be made about the difficulty in using such measurements for this purpose. For a full validation a more controlled environment, where inlet mass flow and the thermal environment was better known, would allow CFD boundary conditions to be set closer to reality. Experimental studies of convective heat transfer coefficient have sought to limit the error in the radiative heat flux calculation by keeping all the surfaces at the same temperature (Spitler, Perdersen, and Fisher 1991; Chandra and Kerestecioglu 1984). A similar technique could be employed in an experiment designed directly for CFD validation, to make the setting of the thermal boundary conditions easier and more accurate. It would have the added benefit that any heat flux measured at a surface must be due to convection rather than radiation. Improved air velocity and temperatures field measurements, as well as surface heat flux measurements would allow CFD to be compared with experimental data with more confidence. Having a constant and known inlet velocity/mass flow, although not natural ventilation per se, would allow equipment measuring air velocity magnitude and direction to traverse the experimental space. From these detail air velocity measurements a more detail picture of flow regime could be built.

5.4.2 Further Work

1. Extra 3D simulations would enable a check on whether the relationship between Archimedes number and detachment point derived from the 2D parametric study stayed true for more boundary conditions.
2. Although the difference between the coarse and the fine mesh was small in the 3 a.m. isothermal case a full grid dependence study was not undertaken. A grid dependence study could determine whether a grid independent solution was possible for the geometry and boundary conditions described in this chapter.
3. Simulations could be repeated with different turbulence models and wall boundary treatments.

CHAPTER 6

Using the Zonal Model

6.1 Objectives

Chapter 2 described the zonal model as implemented within the thermal analysis program LIGHTS (Sowell 1989), Figure 6.1 is the network diagram of the zonal model. Chapters 3–5 reports how CFD data and experimental results have been collected to enable the parameters of the zonal model to be set. This chapter presents the parametric information for use in a number of simulations. The aim of these simulations was:

- To compare the predictions from the zonal model with those from a 'fully mixed' model that would, typically, be employed within an existing thermal simulation program;
- To find the sensitivity of the zonal model to its parameters.

6.2 Method

6.2.1 Comparison between the zonal model and a 'fully mixed' model

The zonal model and a 'fully mixed' model were implemented within LIGHTS. The predictions of the zonal model were compared to those of a fully mixed model using the heat extracted from the ceiling, floor and walls during a 12 hour night-time period.

The zonal model proposed has very different parametric values when the air flows along the ceiling compared with when it falls on entry to the room, flowing along the floor. Therefore, simulations were run that would allow comparisons between the zonal model and a fully mixed model under both of these cases, see Table 6.1. The flow in cases with inlet velocities of $0.1\,\mathrm{ms}^{-1}$ falls to the floor on entry to the room, while the flow in cases with inlet velocities greater than or equal to $0.75\,\mathrm{ms}^{-1}$ remains attached to the ceiling.

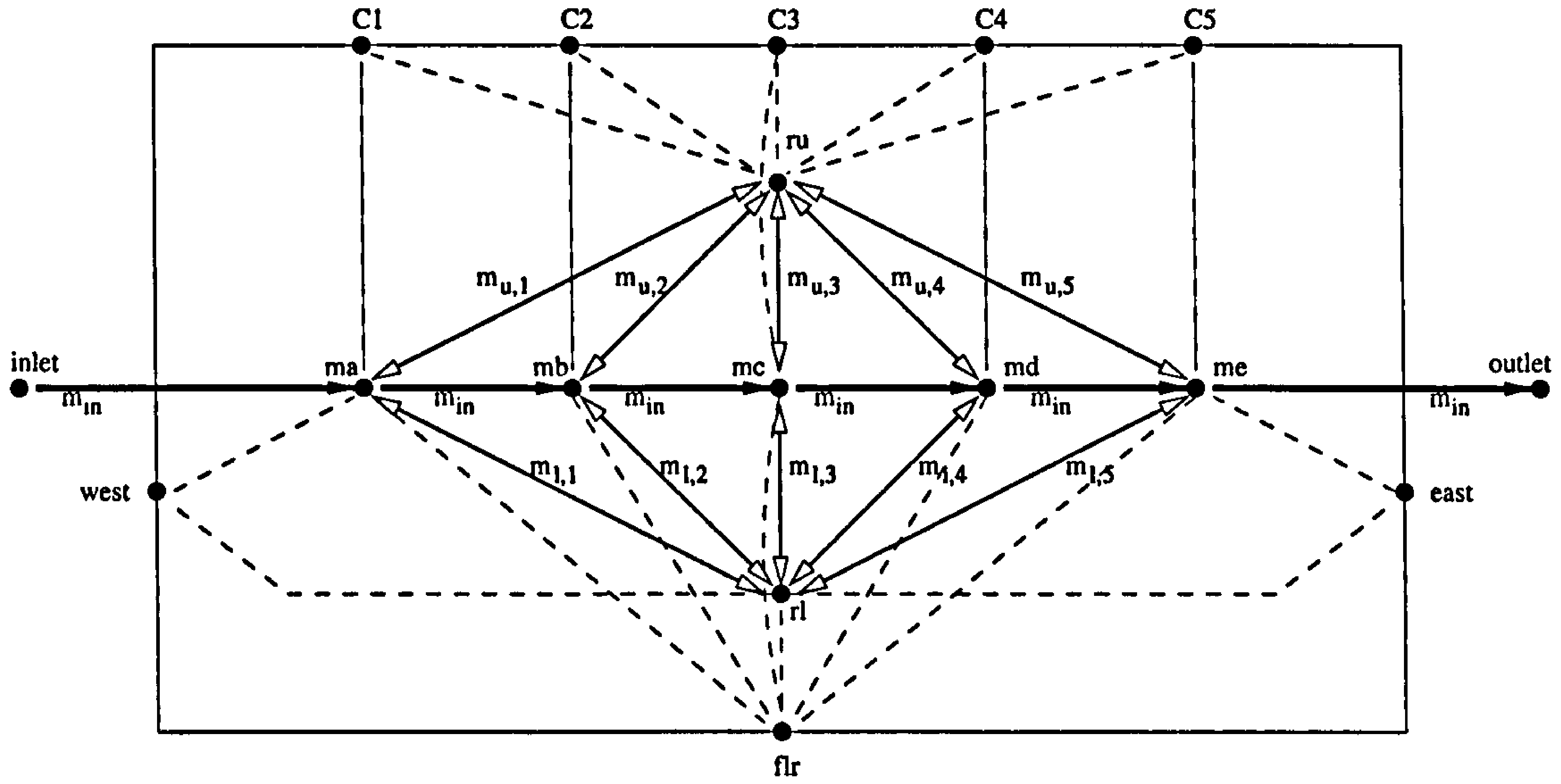

Figure 6.1: The zonal model network diagram.

Table 6.1: Zonal model simulation cases.

Case	Inlet Velocity (m/s)	Initial ΔT (K)	Thermal mass ratio wall/ceiling	Model
1	0.1	10	0	fully mixed
2	0.1	10	0	zonal
3	0.1	10	0.2	fully mixed
4	0.1	10	0.2	zonal
5	0.1	10	0.5	fully mixed
6	0.1	10	0.5	zonal
7	0.1	10	1	fully mixed
8	0.1	10	1	zonal
9	0.75	10	0	fully mixed
10	0.75	10	0	zonal
11	0.75	10	0.2	fully mixed
12	0.75	10	0.2	zonal
13	0.75	10	0.5	fully mixed
14	0.75	10	0.5	zonal
15	0.75	10	1	fully mixed
16	0.75	10	1	zonal
17	1.5	10	0	fully mixed
18	1.5	10	0	zonal
19	1.5	10	0.2	fully mixed
20	1.5	10	0.2	zonal
21	1.5	10	0.5	fully mixed
22	1.5	10	0.5	zonal
23	1.5	10	1	fully mixed
24	1.5	10	1	zonal

A room geometry was needed to set the parameters of the model and to calculate the view factors for the radiation calculation. The room geometry chosen was similar to the two-dimensional CFD model geometry used to derive the zonal model parameters—3 m high by 12 m wide (distance between inflow and outflow boundaries) by 12 m long. The inflow boundary was chosen to be 0.3 m deep and to extend the whole length of the building facade.

- The areas of the wall surfaces are used in setting the surface convection parameters ($h_c A_s$).
- The area of the inlet is used to define the capacity rate parameter through it ($\dot{m}_{in} c_p = \rho v_{in} A_{in} c_p$).
- The lengths of the individual walls are used in calculating the view factors of the surface using well known formulas (Modest 1993).

The thermal mass of the ceiling, $m_{ceil} c_{p_{ceil}}$, was set to a value equivalent to a concrete slab approximately 0.275 m deep. The thermal mass per unit area of the wall and floor nodes were set relative to the ceiling mass. Three values of wall to ceiling thermal mass ratio (TMR) were used: 0, 0.2, 0.5 and 1,

$$TMR = \frac{\frac{m_{surf} c_{p_{surf}}}{A_{surf}}}{\frac{m_{ceil} c_{p_{ceil}}}{A_{ceil}}} \tag{6.1}$$

where $\frac{m_{surf}}{A_{surf}}$ is the mass per unit area of the wall and floor surfaces.

6.2.2 Zonal Model Parameters

There are a number of possible approaches to determining the values of the model parameters. These can be summerised as follows:

- Using the results of numerical simulations of cross-flow ventilation;
- Using published correlations for the convection coefficients;
- Using experimental data from measurements taken in a cross-flow ventilated room.

In Chapter 3 a two-dimensional CFD model was run parametrically to derive the model parameters over a wide range of boundary conditions: inlet velocities of 0.1–5.0 m/s; and temperature difference between the ceiling surface and the incoming air of 0–15 K. Section 3.5 gives empirical relationships that can be used to set the zonal model parameters.

In Chapter 4 a cross-flow experiment determined ceiling convective heat transfer coefficients. The experimental data as well as other studies (Chandra and Kerestecioglu

1984; Spitler, Perdersen, and Fisher 1991), agreed sufficiently well with the correlation indicated by the CFD work reported in Chapter 3 to give confidence in the use of CFD models as input to the zonal model.

A procedure for setting the zonal model parameters from the CFD simulations presented in Chapter 3 has been defined as follows:

a. The pressure difference between the inlet and outlet is found from empirical correlations from studies on wind-generated surface pressure distributions such as that of Ernest (1991);

b. The average temperature of the ceiling nodes is calculated;

c. The temperature difference between the inflow air and the ceiling is calculated;

d. Pressure and temperature difference are used in Equation 3.77 to calculate the inlet velocity;

e. Temperature difference and inlet velocity are used in Equation 3.81 to calculate Archimedes number;

f. Table 3.5 can be used to find at which ceiling node the flow detaches using the Archimedes number;

g. Inlet velocity and flow detachment position are used with Table 3.6 to find the convective heat transfer parameters;

h. Inlet velocity and flow detachment position are used with Table 3.8 to calculate the capacity rate parameters.

Appendix B gives the calculation procedure in a general more form that may be used to implement the zonal model in another thermal modelling program.

The zonal model network, as described in Chapter 2 and shown in Figure 6.1, has four parameters not found in the 2D CFD parametric analysis (Chapter 3), $h_{c_{ln}}A_n$, $h_{c_{un}}A_n$, $h_{c_{ls}}A_s$ and $h_{c_{us}}A_s$. These parameters are the convective heat transfer between the north and south wall and the two recirculating regions, where:

$h_{c_{ln}}$	is the convective heat transfer coefficient between the north wall and the lower recirculating region;
$h_{c_{un}}$	is the convective heat transfer coefficient between the north wall and the upper recirculating region;
$h_{c_{ls}}$	is the convective heat transfer coefficient between the south wall and the lower recirculating region;

$h_{c_{us}}$	is the convective heat transfer coefficient between the south wall and the upper recirculating region;
A_n	is the area of the north wall;
A_s	is the area of the north wall.

These parameters have not been extracted from the CFD simulations because the north and south walls are not present in the simulations, and therefore a velocity dependent convective heat transfer coefficient cannot be found, as was done for the other room surfaces. To set the convective heat transfer of the north and south walls, the average of the corresponding coefficient for the east and west walls was taken, i.e.,

$$h_{c_{ln}} = h_{c_{ls}} = \frac{h_{c_{le}} + h_{c_{lw}}}{2},$$

and,

$$h_{c_{un}} = h_{c_{us}} = \frac{h_{c_{ue}} + h_{c_{uw}}}{2},$$

where:

$h_{c_{le}}$	is the convective heat transfer coefficient between the east wall and the lower recirculating region;
$h_{c_{uw}}$	is the convective heat transfer coefficient between the west wall and the upper recirculating region;
$h_{c_{le}}$	is the convective heat transfer coefficient between the east wall and the lower recirculating region;
$h_{c_{uw}}$	is the convective heat transfer coefficient between the west wall and the upper recirculating region.

6.2.3 The Fully Mixed Model

The fully mixed model was implemented within LIGHTS using a similar method to that of the zonal model. Figure 6.2 shows a schematic diagram of the model. There are two capacity rate parameters (solid arrow) equal to $\dot{m}_{in}c_p$, and four convective heat transfer parameters (dashed line) equal to h_cA_s, where h_c was set to $3\,\mathrm{Wm^{-2}K^{-1}}$, and A_s is the area of the surface in question.

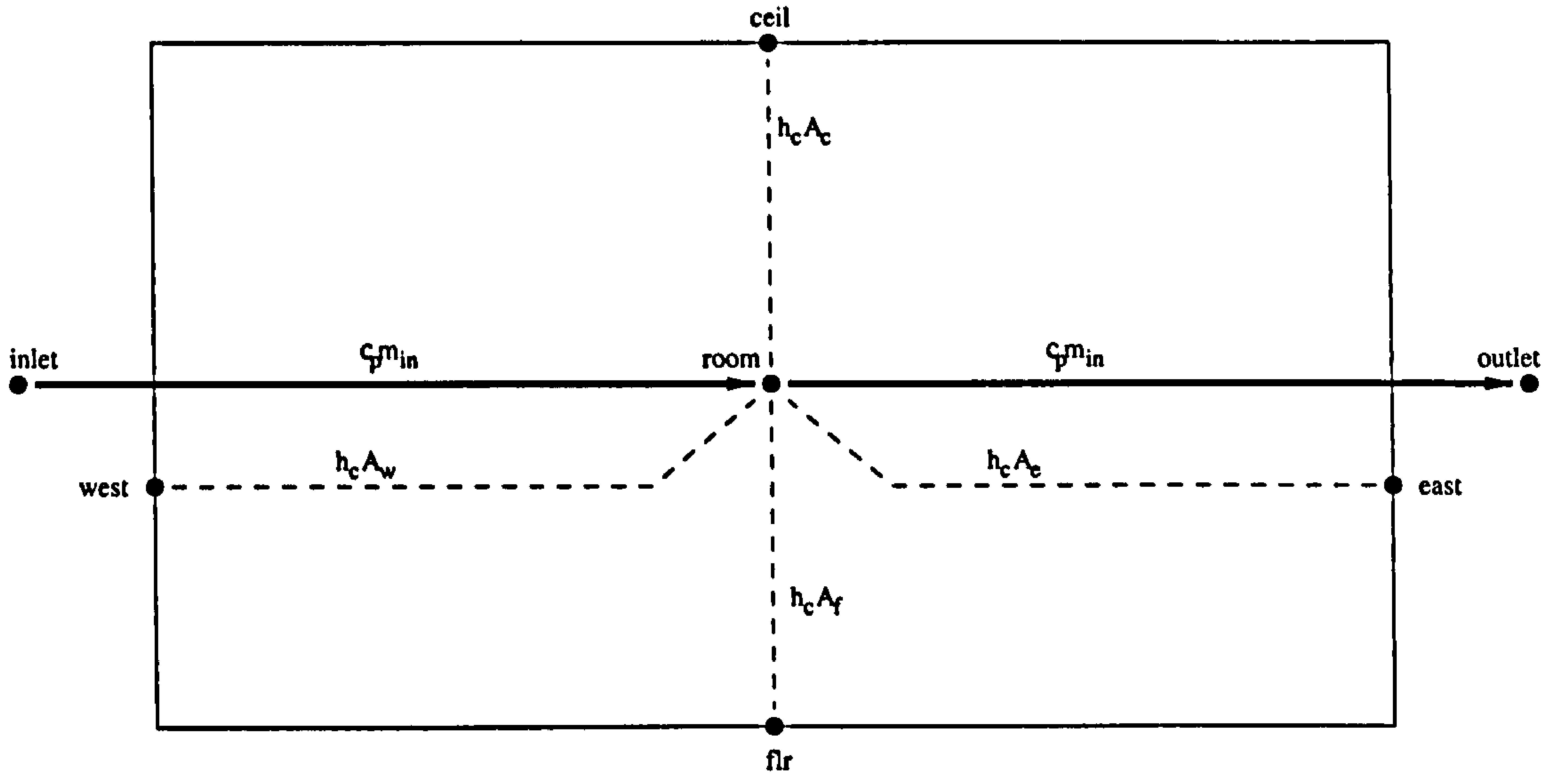

Figure 6.2: Fully mixed model.

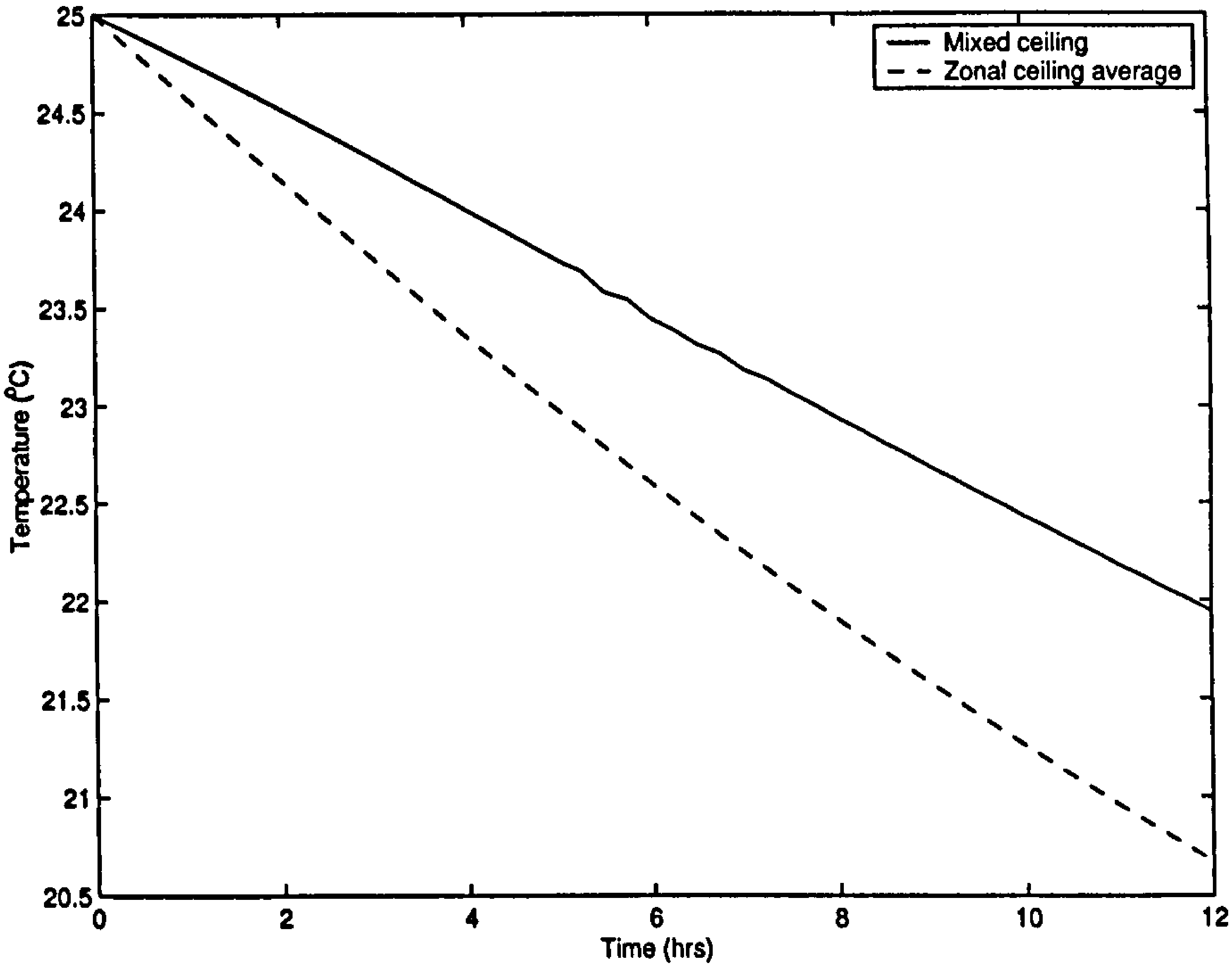

Figure 6.3: Comparison of ceiling temperature prediction using the zonal model and the fully mixed model with an inlet velocity of 1.5 m/s and wall/ceiling thermal mass ratio of 0.2.

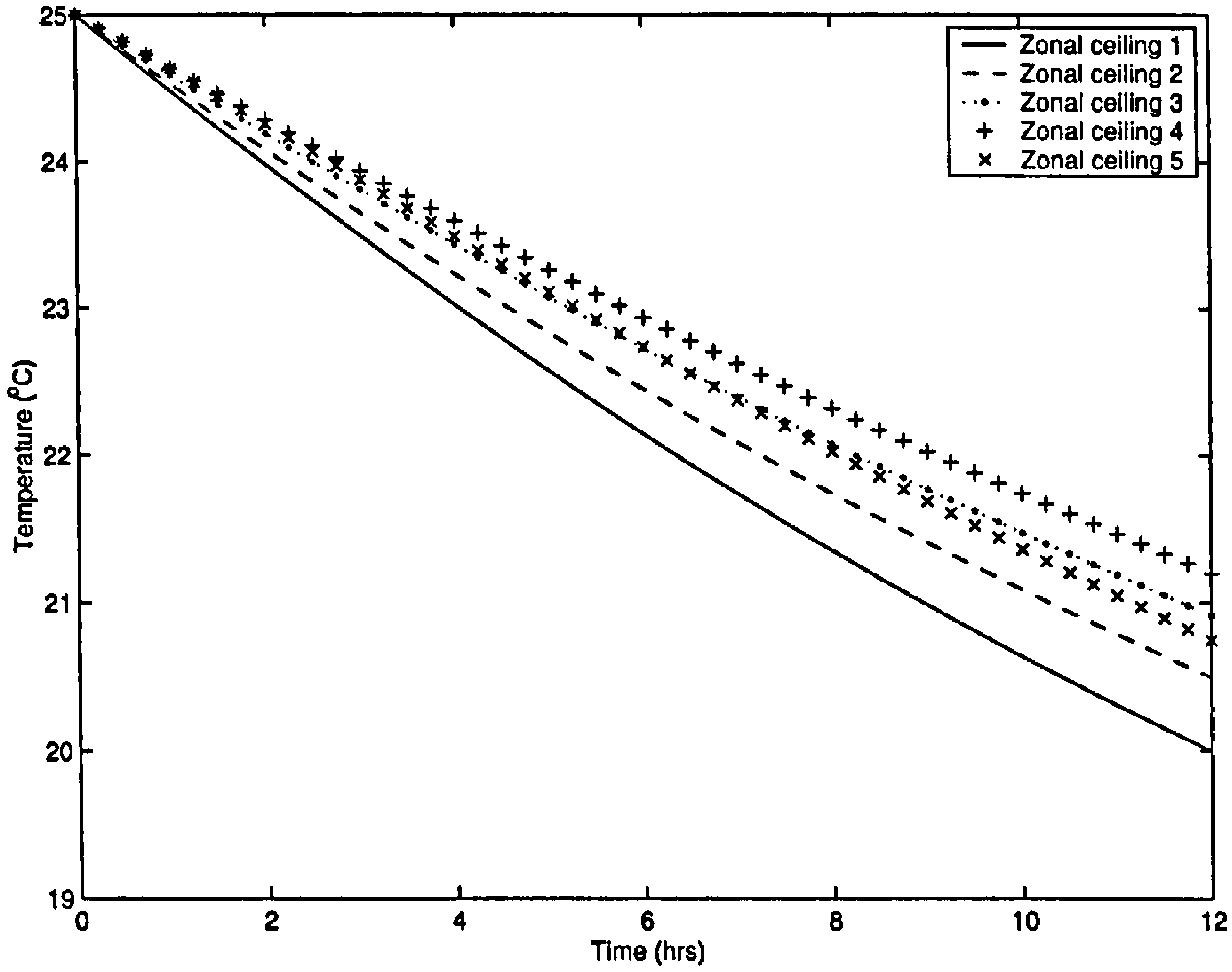

Figure 6.4: Temperature at the 5 ceiling nodes in the zonal model with an inlet velocity of 1.5 m/s and wall/ceiling thermal mass ratio of 0.2.

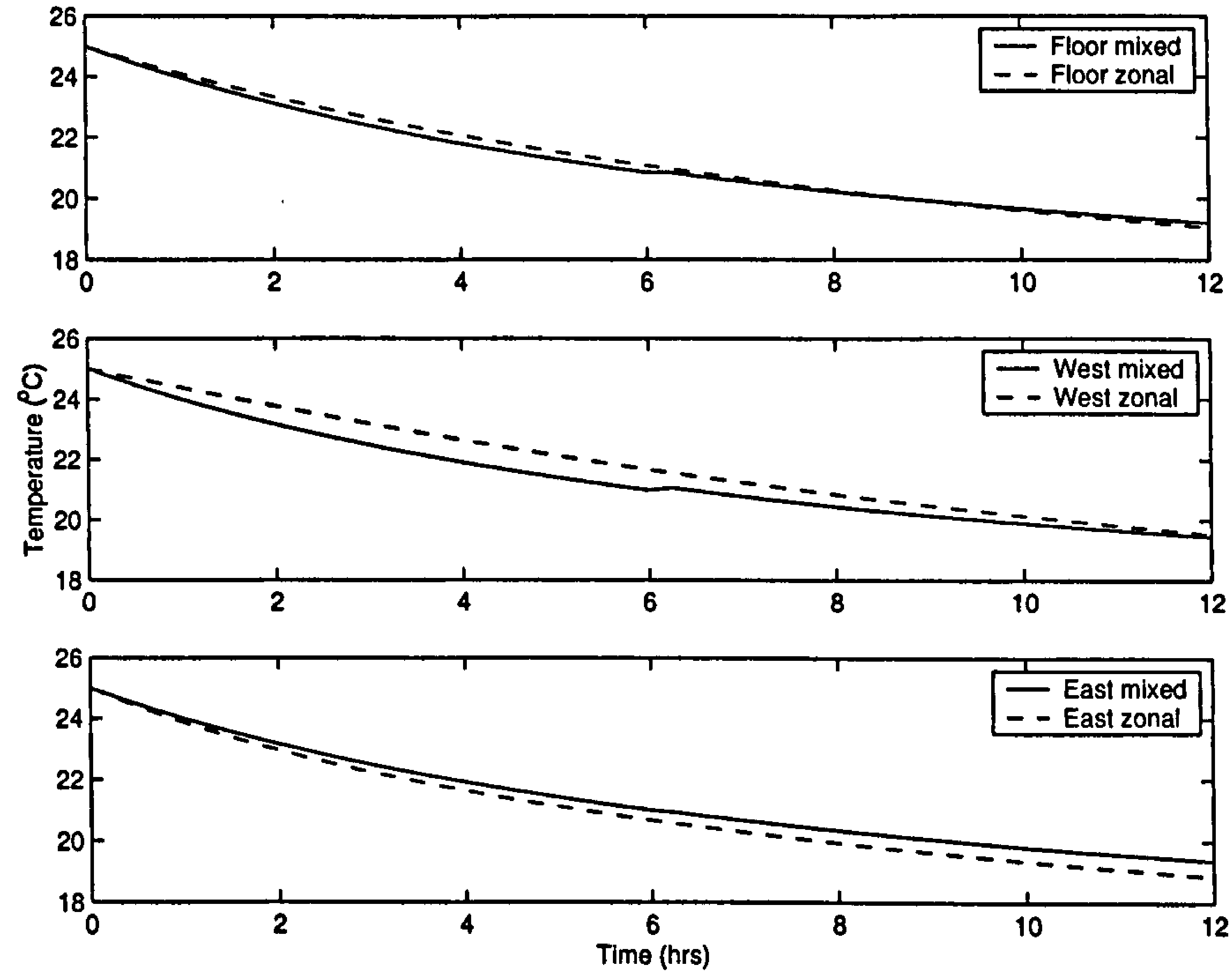

Figure 6.5: Comparison of wall and floor temperature prediction using the zonal model and the fully mixed model with an inlet velocity of 1.5 m/s and wall/ceiling thermal mass ratio of 0.2.

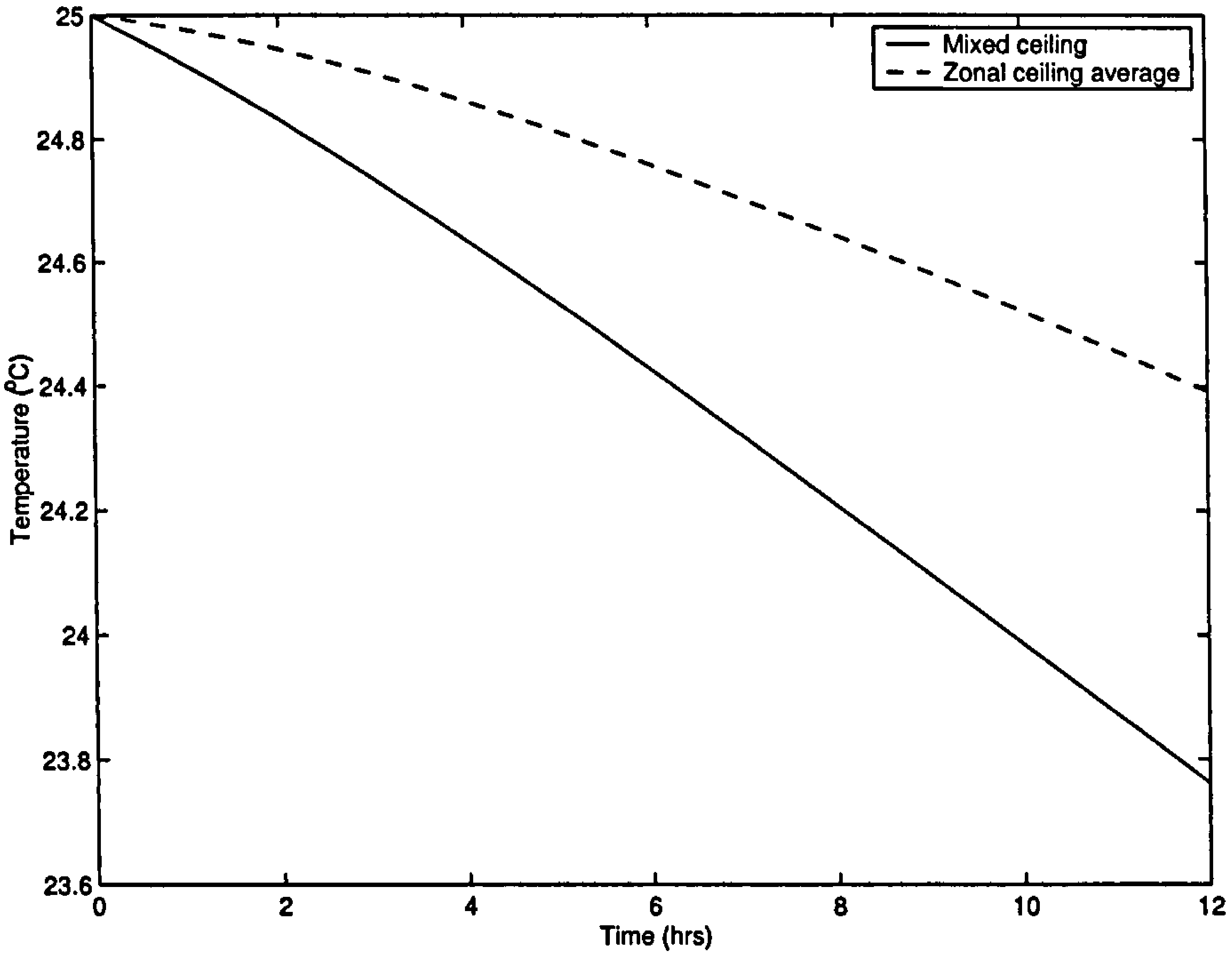

Figure 6.6: Comparison of ceiling temperature prediction using the zonal model and the fully mixed model with an inlet velocity of 0.1 m/s and wall/ceiling thermal mass ratio of 0.2.

6.3 Results

6.3.1 Comparison between the zonal model and a 'fully mixed' model

Figures 6.3, 6.4 and 6.5 compare the predictions of the ceiling, floor and wall temperatures with a wall/ceiling thermal mass ratio of 0.2, and an inlet velocity of 1.5 ms^{-1}. Figure 6.3 shows the temperature of the five ceiling nodes in the zonal model over the 12 hour simulation period. The temperature of ceiling node one drops quickest due to the fact that the convective heat transfer coefficient is largest here, as well as the fact that the bulk convection into the lower recirculating region is higher than for the other main flow stream zones. Figure 6.4 shows the average zonal model ceiling temperature plotted alongside the mixed model ceiling temperature. The zonal model ceiling temperature drops significantly faster than the mixed model prediction, this is due to the fact that the zonal model takes into account the high speed air next to the ceiling. Figure 6.5 shows the temperature prediction for the floor, and the east and west wall nodes. Here the zonal model and the mixed model predictions are closer as their convective heat transfer coefficients are similar. The zonal model convective heat transfer coefficients are lower than those of the mixed model, but a reduction in heat loss due to convection is offset by the larger radiative heat loss to the cooler ceiling.

Figures 6.6, 6.7 and 6.8 compare the predictions of the ceiling, floor and wall temperatures with a wall/ceiling thermal mass ratio of 0.2, and an inlet velocity of 0.1 ms^{-1}. Figure 6.6

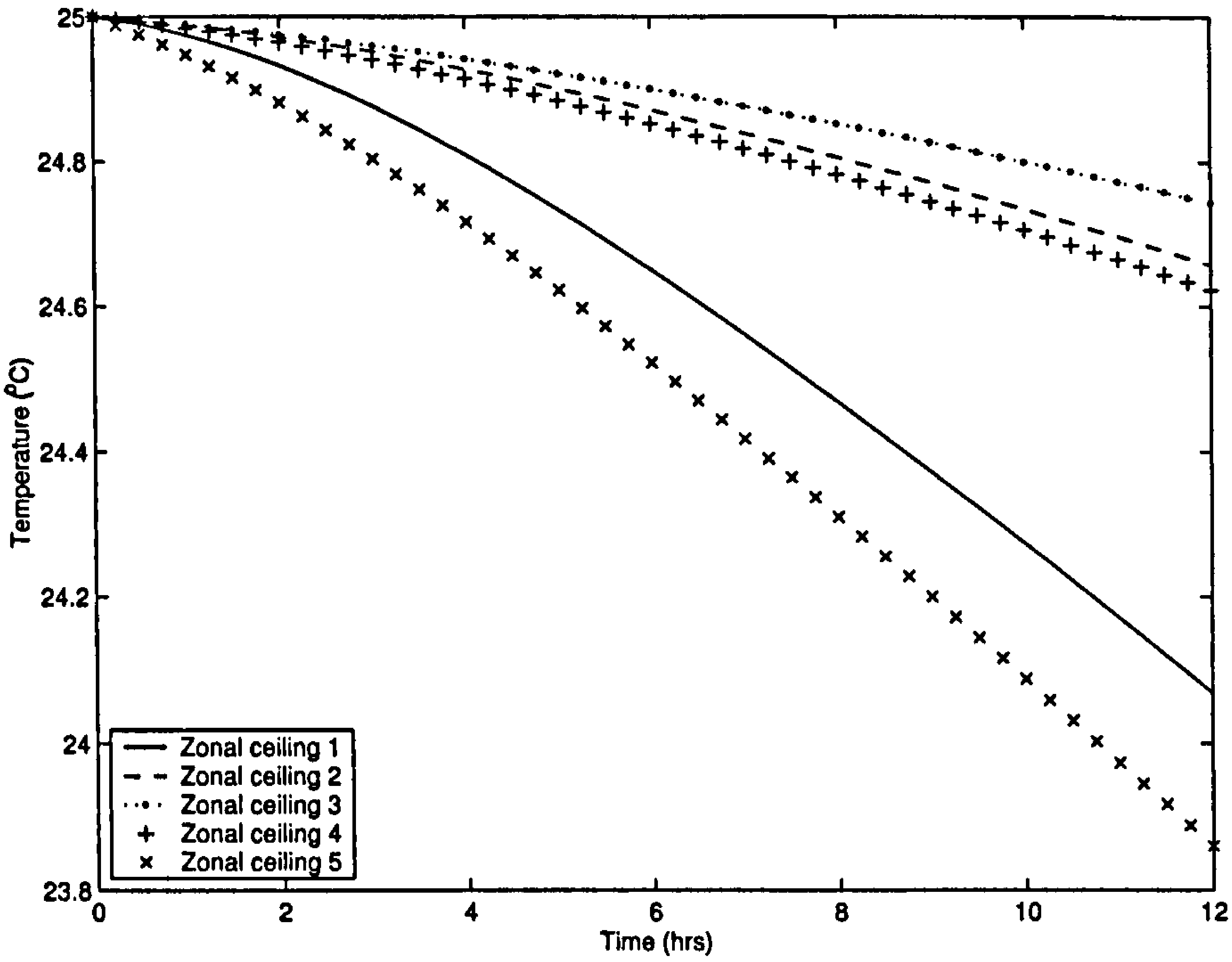

Figure 6.7: Temperature at the 5 ceiling nodes in the zonal model with an inlet velocity of 0.1 m/s and wall/ceiling thermal mass ratio of 0.2.

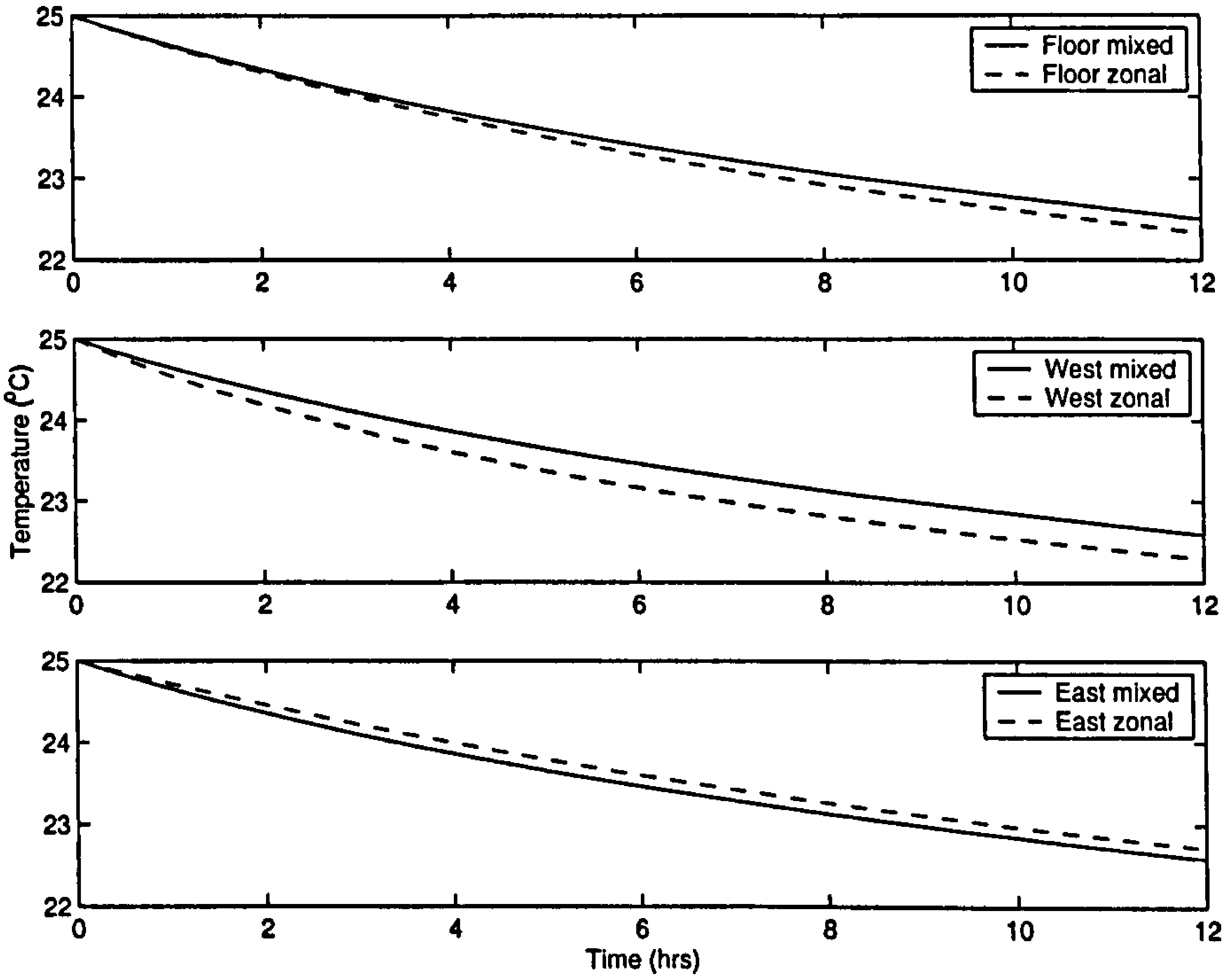

Figure 6.8: Comparison of wall and floor temperature prediction using the zonal model and the fully mixed model with an inlet velocity of 0.1 m/s and wall/ceiling thermal mass ratio of 0.2.

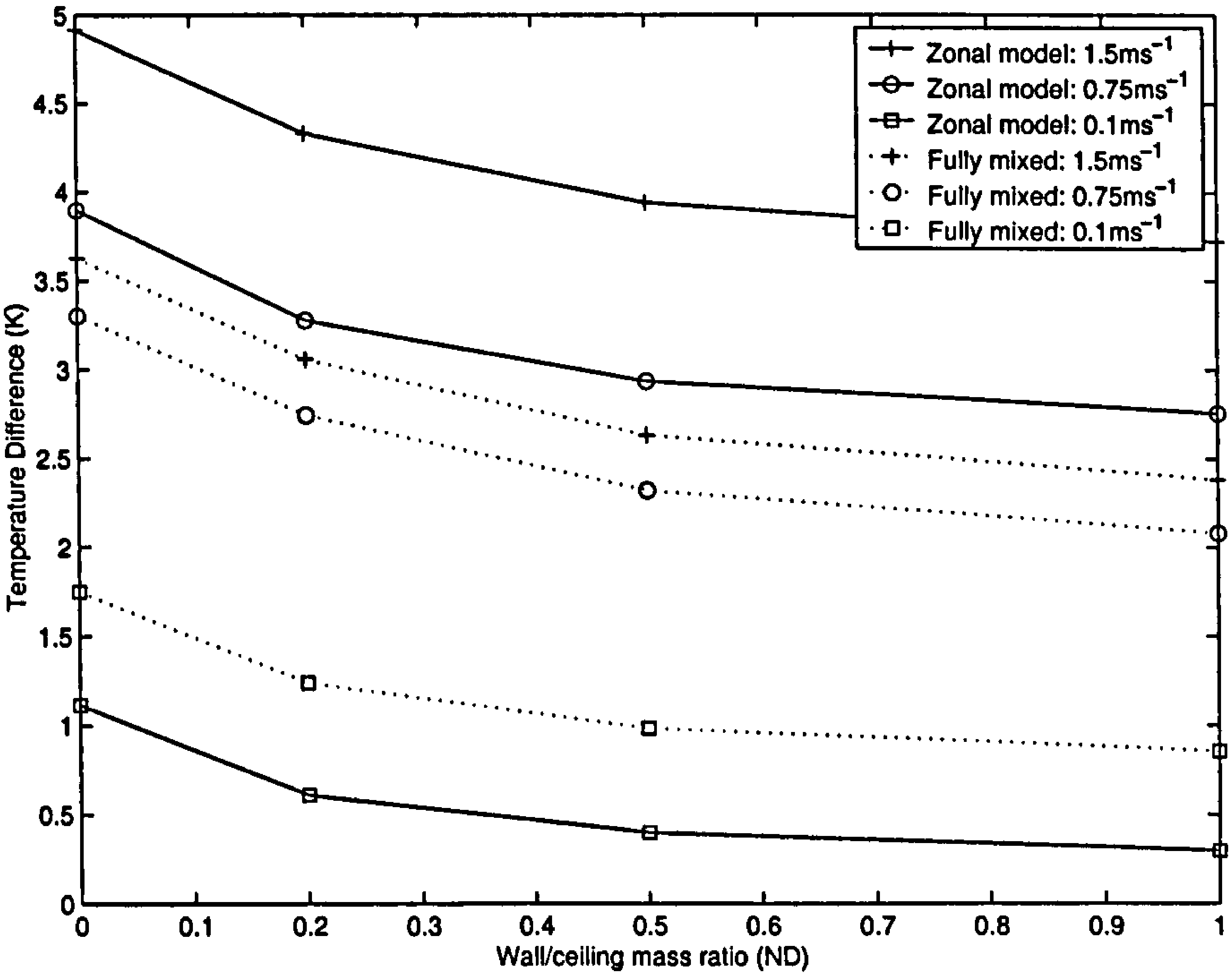

Figure 6.9: Comparison of temperature drop of the ceiling between the beginning and end of the 12 hour simulation using the zonal model and the fully mixed model for a range of wall/ceiling thermal mass ratios.

shows the temperature of the five ceiling nodes in the zonal model over the 12 hour simulation period. The temperature of ceiling node 5 is lower than the other ceiling nodes due to the air speed being higher close to the outlet than the rest of the ceiling, and thus the convective heat transfer coefficient is larger.

The ceiling temperature drops faster at the end of the night than at the beginning because the radiative heat transfer increases throughout the night as the main flow stream cools the floor and walls. Figure 6.7 shows the average zonal model ceiling temperature plotted along side the mixed model ceiling temperature. The mixed model ceiling temperature drops significantly faster than the zonal model prediction, this is due to the fact that the zonal model takes into account the main flow stream flowing along the floor and the resulting thermal stratification. Figure 6.8 shows the temperature prediction for the floor, and the east and west wall nodes. Again, the zonal model and the mixed model predictions are closer than the ceiling temperature prediction.

Figure 6.9 shows a comparison of temperature drop of the ceiling between the beginning and end of the 12 hour simulation using the zonal model and the fully mixed model for the range of wall/ceiling thermal mass ratios. It plots the total temperature drop over the 12 hour simulation period against the wall/ceiling thermal mass ratio. Unsurprisingly, heat extracted from the ceiling increases with the mass flow of air through the inlet. The heat extracted from the ceiling decreases with increasing wall and floor thermal mass due to the fact that the inflow air has to extract heat from more thermal mass.

Table 6.2: Heat extracted from the ceiling over a twelve hour simulation period.

Case	Heat extracted from ceiling (% of zonal model)
Zonal model (fully attached)	100%
Convective heat transfer coeffients doubled	146%
Mass flow rate (MFS to lower recirc. region) doubled	99.8%
Main flow stream mass flow doubled	105%
Flow detaches on entry	21%

6.3.2 Zonal model sensitivity study

The accuracy of the data used for the model parameters is limited for two reasons:

- They are based on numerical calculations;
- The experimental studies outlined in Chapter 4 give different correlations of convective heat transfer coefficient with air velocity.

A sensitivity study was carried out to examine how the zonal model output was effected by the varying its parameters:

- The convective heat transfer coefficients;
- The mass flow rate between the main flow stream and the lower recirculating region;
- The main flow stream mass flow;
- The flow detachment position.

To do this sensitivity study each parameter was doubled from its value in the zonal model (with an inlet velocity of $1.5\,\mathrm{ms}^{-1}$) as determined from the procedure outlined in Section 6.2.2. To determine the sensitivity to flow detachment position the case with flow attached to the ceiling was compared to the case where the flow detached on entry to the room, keeping the air flow rate through the inlet the same. Also two experimentally derived convective heat transfer coefficient parameters were used in the zonal model for comparison. Table 6.2 shows the results of the sensitivity study, giving the heat extracted from the ceiling over a twelve hour simulation period.

The results show the zonal model is not sensitive to mass flow rate through the main flow stream or to the mass flow rate from the main flow stream to the lower recirculating region. The flow detachment position has a large effect on the heat extracted from the ceiling for the same flow rate. Thus, models that cannot include the thermal consequence of a flow regime switch are not likely to make very accurate modelling tools. Nearly 5 times as much heat is extracted when the main flow stream flows along the ceiling

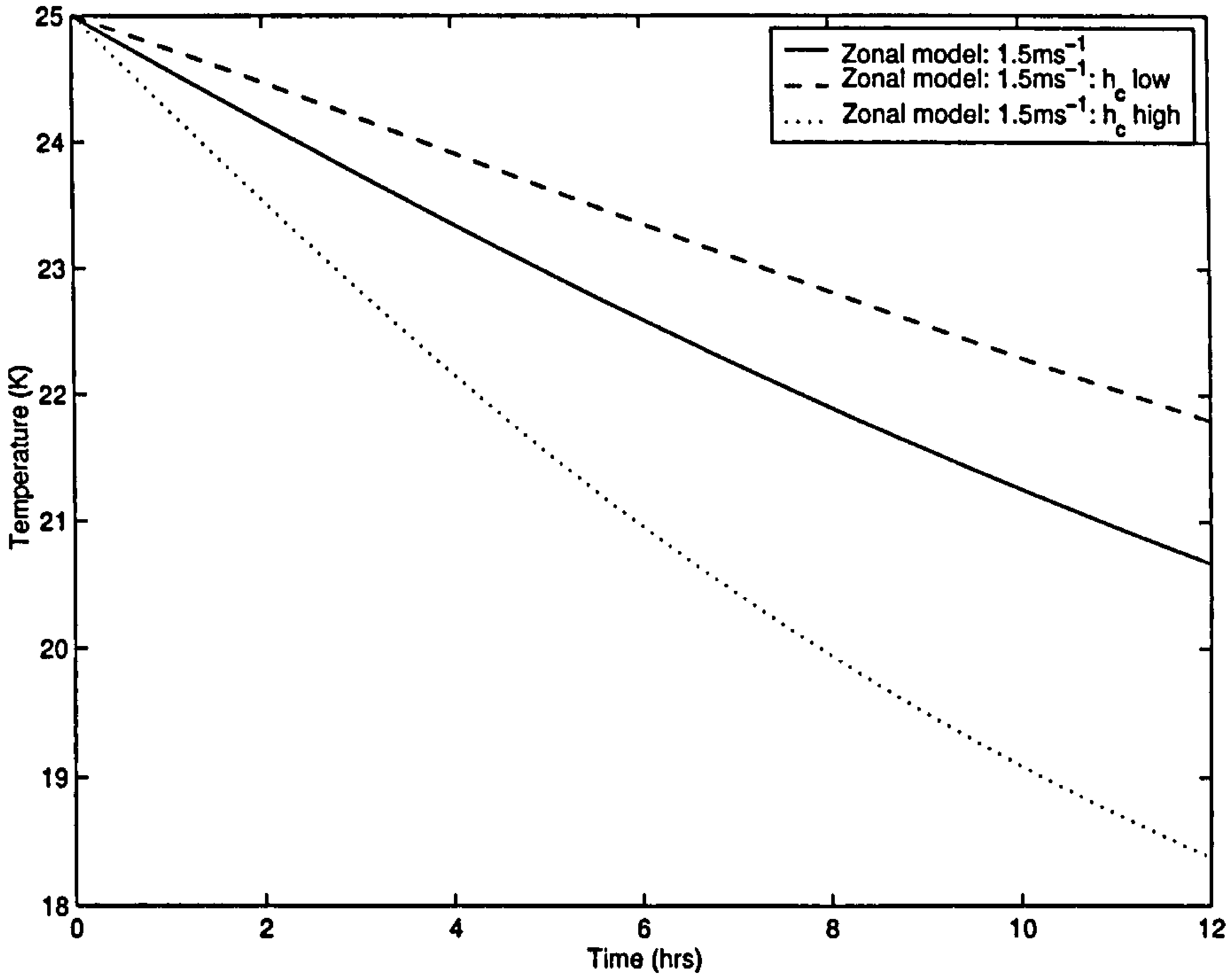

Figure 6.10: Comparison of ceiling temperature prediction using the zonal model with an inlet velocity of 1.5 m/s and different convective heat transfer coefficients.

compared to when it flows along the floor. This is due to the fact that the heat transfer coefficients, found using Table 3.6, change significantly with flow regime. This means the relationship between Archimedes number and detachment position is an important one if the zonal model is to be accurate. Although, the relationship between Archimedes number and detachment position was found using the 2D CFD study in Chapter 3 both the experimental work and the 3D CFD simulations agreed well with the correlation postulated.

After flow detachment position it is the convective heat transfer coefficient parameters that have the largest effect on the zonal model predictions. When the convective heat transfer coefficient parameters are doubled 46% more heat is extracted from the ceiling. Figure 6.10 shows the effect of using experimentally derived convective heat transfer coefficient parameters on the zonal model ceiling temperature prediction. The cases compared are:

- The zonal model using the parameters as determined in Section 6.2.2;
- The low h_c case is the zonal model using the CIBSE still air convective heat transfer coefficient correlation (3.22 Wm^{-2}K^{-1});
- The high h_c case is the zonal model using the correlation of Chandra and Kerestecioglu (1984) (11.81 Wm^{-2}K^{-1} for an air velocity of 1.5 ms^{-1}).

Over the 12 hour simulation period the different convective heat transfer coefficients have a large effect on the amount of heat extracted from the ceiling. The final average ceiling temperature of the zonal model was 20.67°C, 21.80°C for the zonal model using the low convective heat transfer coefficient, and 18.38°C for the zonal model using the high convective heat transfer coefficient. The heat extracted from the ceiling using the high convective heat transfer coefficient is 2.07 times as much as the low coefficient case.

6.4 Conclusions

A zonal model has been developed to represent room heat transfer in night-time cross-flow ventilated rooms. The following conclusions concerning the structure, parameters and performance of the model can be made.

1. The zonal model provides a number of improvements over single air node or fully mixed models:
    (a) By modelling 5 different flow regimes the zonal model is able to represent the thermal consequence of whether the cool inflow air remains in thermal contact with the ceiling slab or detaches and flows along the floor;
    (b) The thermal gradient possible across the width of the ceiling is represented by the use of 5 ceiling nodes.
    (c) The surface convection coefficient parameters change with flow regime and inflow air velocity.
    (d) The bulk airflow capacity rate parameters change with flow regime and inflow air velocity.
2. Zonal model flow regime is derived from the ceiling/inflow air temperature difference and the pressure difference between the inflow and outflow openings. The pressure difference between the inlet and outlet can be found from empirical correlations from studies on wind-generated surface pressure distributions such as that of Ernest (1991).
3. It is possible to define the convection coefficient parameters for the model using the results of CFD simulations. The advantage of using the CFD parametric study to set the air-surface node connections is that the correlations derived from the numerical study are able to use the temperatures averaged over the control volumes and surface areas used in the zonal model.
4. The bulk air flow capacity rates of the zonal model have been derived from numerical calculations of the dispersal of an additional scalar, the numerical equivalent of a tracer gas experiment, and crucially include a description of flow detachment.

5. The zonal model has been compared with a single air node, 'fully mixed', model for a number of inlet mass flow rates, as well as for a number of ceiling/wall thermal mass ratios.
    (a) The zonal model predicts higher ceiling heat loss, than the fully mixed model, when the flow remains attached to the ceiling.
    (b) The zonal model predicts lower ceiling heat loss, than the fully mixed model, when the flow falls to the floor on entry to the room.
6. The zonal model output is insensitive to the bulk air flow parameters chosen.
7. The zonal model output is sensitive to the convective heat transfer coefficient parameters chosen, doubling the convective heat transfer coefficients increases the heat extracted from the ceiling by 46% when the main flow stream is attached to the ceiling.
8. The detachment position is the parameter that has the largest effect on zonal model output. When the main flow stream detaches from the ceiling the model network changes and the convective heat transfer coefficients change.
9. The time taken to run a 12 hour simulation of the zonal model is approximately 1 second on a 450 MHz Intel Pentium II processor, making its use in an annual building simulation feasible.

CHAPTER 7

Conclusions

The purpose of this thesis has been to develop a design tool for the evaluation of the performance of night-time cross-flow ventilated buildings. This concluding section starts with an outlook on the importance of natural ventilation. Then, the scope of the investigations conducted and the major findings obtained are summarised. The importance and limitations of these findings are then discussed and finally, directions for future work are proposed.

7.1 Outlook

Since the advent of air conditioning, members of the engineering community have resisted considering natural ventilation as a cooling strategy citing:

- Reliable methods to predict the efficacy of natural ventilation do not exist;
- Compared to air conditioning, wind-induced natural ventilation is intrinsically unreliable.

The purpose of the work presented here has been to address the first of these concerns. To respond to the second argument, one must weight the pros and cons of both air conditioning and natural ventilation. In the short term air conditioning may present a more consistent ventilation scheme than wind driven ventilation but political will has increased the importance of other factors. By reducing energy consumption of buildings less CO_2 is released into the atmosphere to exacerbate global warming, and the life of our depleting fossil fuel reserves is extended. Other factors such as pollution due to the burning of fossil fuels, and the continued instability in the Middle East, add to the political will backing a more sustainable way of living. Furthermore, from a purely economic standpoint, natural ventilation might offset the cost of unnecessary mechanical cooling equipment, which can represent up to 10 % of the cost of a building. There is also the possibility of health related problems with the use of air conditioning, such as sick building syndrome.

Existing building energy analysis programs generally have the common feature that the thermal conditions within each room are modelled on the basis of the air being fully mixed. It is this drawback principally, that needs to be overcome to enable systems like natural ventilation to be modelled realistically, for example, the 'fully mixed' model cannot hope to accurately model the situation when cool night-time air flows into a room and along the floor—where thermal stratification is an important process.

The overall objective of the work described here has been to develop a suitable thermal model that incorporates the relevant features of natural ventilation. In developing the model the aim has been to achieve sufficient detail to enable heat transfer and comfort conditions to be predicted with reasonable accuracy, whilst retaining sufficient computational speed to enable the zonal model to be incorporated into an annual energy simulation program. The model presented here is, accordingly, of intermediate complexity between that of a single air node model, and that of a CFD model. The model is of the type that has been called a 'zonal model'. In this type of model the room heat transfer paths are described by a network of nodes, at which heat balances are calculated, that are interconnected by conductances representing bulk air movement or convective heat transfer paths.

7.2 Scope

The study was divided into four phases. In the first, a zonal model of night-time cross-flow ventilation was proposed that modelled whether the cool incoming air flowed along the ceiling, or the floor, or a combination of the two. The parameters of this zonal model were identified so that they could be determined in the other three phases of the study.

In the second phase, a two-dimensional steady-state CFD parametric study was employed to derive the surface convection parameters of the zonal model over a wide range of flow driving forces, inlet/outlet pressure difference, and room/inlet air temperature difference. The parametric study was then run transiently to find the bulk air flow capacity rate parameters between zonal model air nodes. For this, an extra scalar variable was introduced at the inlet boundary and its dispersal through the room was used to calculate the mass flow across zonal model control volume boundaries due to turbulence—the numerical equivalent of a tracer gas experiment.

There is a question about the accuracy of the surface convective heat transfer predictions of the standard high-Reynolds k-ε model with wall functions (Chen and Jiang 1992; Yuan, Moser, and Suter 1993). Therefore, experimental data to support the findings of the numerical work was needed. Research on convective heat transfer coefficients (Spitler, Perdersen, Fisher, Menne, and Cantillo 1991; Spitler, Perdersen, and Fisher

1991; Chandra and Keresteciogiu 1984) was used for a comparison with the numerical predictions but the different techniques of calculating the coefficients made a direct comparison difficult. Furthermore, of particular interest in this study was the convective heat transfer coefficients at the ceiling when a high level opening is used for the inlet. Thus, in the third phase, an experimental procedure was employed to derive ceiling convective heat transfer coefficients in a room ventilated by night-time cross-flow means. Air speed and temperature measurements, as well as surface temperature and flux measurements were taken and correlations with local site weather station data were sought. Surface temperatures were used to calculate radiative heat flux at two ceiling positions. Correlations between ceiling convective flux and air speed were determined (using a local air speed, as well as an inflow opening air speed measurement).

In the fourth phase, the experimental measurements were used to set boundary conditions of three-dimensional numerical simulations of the experimental room. The experimental measurements were also used as a check whether the CFD models were giving reasonable results, although, the data collected was not sufficient for full validation. Two periods were chosen as a basis for the numerical simulations, the first with low inlet air speed, and the second with higher air speed and more gusty conditions.

During this study, a general process for the development of the zonal model of night-time cross-flow ventilation was conducted along the following lines:

1. Devise a network of nodes to represent the bulk air movement within a naturally ventilated space as seen in experimental and numerical results;
2. Specify how those air nodes are connected to the room surfaces via convective heat transfer paths;
3. Use CFD to determine values for the parameters of the zonal model, convective heat transfer coefficients and capacity rates associated with bulk air movement;
4. Derive empirical relationships between the parameters and boundary conditions of the zonal model.

7.3 Major Findings

A zonal model has been proposed that models three heat transfer processes important in naturally ventilated systems:

1. The radiation between room surfaces nodes;
2. Convective heat transfer between surface and air nodes;
3. Bulk convection between air nodes.

From early CFD simulations and engineering knowledge it was decided that the zonal model must incorporate the thermal consequences of whether or not the main flow stream remained in contact with the ceiling. A zonal model was implemented within a general thermal analysis program, LIGHTS, that divided the room air into three distinct regions: the main flow stream (MFS) that flows between the inlet and the outlet openings; the lower recirculating region under the MFS (while the MFS flows along the ceiling); and the upper recirculating region over the MFS (while the MFS flows along the floor).

The MFS was divided into 5 control volumes or zones, while a single zone was used for both the upper recirculating region and lower recirculating regions. Each zone represents a fixed volume of room air which depends on the path of the main flow stream which in turn depends on the driving forces of the flow (the pressure difference between the room openings and the buoyancy forces generated by room air at differing temperatures).

There are ten surface nodes which comprise of five ceiling nodes, four wall nodes, and a node for the floor. The surface nodes are connected together via view factors supplied to LIGHTS to form radiative heat transfer paths.

There are three types of zonal model parameters:

1. 24 convective heat transfer parameters;
2. 26 bulk air convection capacity rates;
3. 10 surface emissivity values used in the radiation calculation.

The zonal model provides a number of improvements over single air node or fully mixed models:

1. By modelling 5 different flow regimes the zonal model is able to represent the thermal consequence of whether the cool inflow air remains in thermal contact with the ceiling slab or detaches and flows along the floor;
2. The thermal gradient possible across the width of the ceiling is represented by the use of 5 ceiling nodes;
3. The surface convection coefficient parameters change with flow regime and inflow air velocity;
4. The bulk airflow capacity rate parameters change with flow regime and inflow air velocity.

The time taken to run a 12 hour simulation of the zonal model is approximately 1 second on a 450 MHz Intel Pentium II processor, making its use in an annual building simulation feasible.

Numerical calculations have been made using CFD to help derive the structure of the zonal model and determine the model parameter values. The principle conclusions of these numerical calculations can be summarised as follows.

1. A steady-state two-dimensional CFD model was used parametrically to derive the 24 zonal model convective heat transfer parameters for a wide range of driving forces. The control volumes for each case were determined by integrating the horizontal mass flow at each vertical cross section corresponding with the cell centres of the CFD mesh. This integration allowed the upper and lower boundaries of the MFS to be determined which in turn defines the extent of each of the zonal model control volumes. Once the control volumes were known, a convective heat transfer coefficient between each surface and the adjacent control volume could be determined. The coefficient calculation used the average air temperature in the control volumes, the average temperature over the zonal model surface, and the average convective flux over the zonal model surface.

2. A transient CFD model was designed to calculate mass transfer between zones of the zonal model which relies on the fact that contaminant dispersal in the room will depend on the entrainment from the recirculating region or regions into the main flow stream. This numerical technique is similar to how a tracer gas experiment could be used to determine mass transfer around the room, although the level of detail obtained numerically would not be practical to obtain experimentally. Contaminant dispersal was modelled using the scalar transport equations of the CFD software (CFX 1997b). An extra scalar was included in the simulation with a diffusivity set to a value equal to that of nitrogen in air (this value was chosen so that the properties of the contaminant were as close to those of air).

3. An empirical relationship between inlet/outlet pressure difference and inlet velocity was derived that allows the zonal model to be linked with the many studies on wind-generated surface pressure distributions (Equation 3.77).

4. A relationship between Archimedes number and the MFS detachment position was found. Once Archimedes number is calculated Table 3.5 can be used to find at which ceiling node the flow detaches. Five flow regimes are identified:

   (i) Flow falls to floor on entry to room;
   (ii) Flow detaches in MFS zone 2;
   (iii) Flow detaches in MFS zone 3;
   (iv) Flow detaches in MFS zone 4;
   (v) Flow remains attached to the ceiling through its path through the room.

5. A convective heat transfer coefficient is then derived for each of the 24 air-surface connections for each of the five flow regimes listed above. Table 3.6 can be used to look up each of the convective heat transfer coefficients for a particular flow regime. The coefficients are correlated with inlet velocity and these correlations have been compared with experimental studies in the literature. Although a direct comparison is difficult, due to the different methods of calculating the coefficient, the numerically derived correlations compare well with the those of Spitler, Perdersen, and Fisher (1991) who use a non-dimensional form of the inlet velocity as their reference velocity. They compare less favourably with those of Chandra and Kerestecioglu (1984), who used a local air speed measurement as their reference velocity, and the vertical wall forced convection coefficient in ASHRAE fundamentals (1997) for air speeds below 5 m/s.

6. The zonal model capacity rates parameters are then derived for flow regimes 1–5 and are given in Table 3.8 as dimensionless mass flow rates. The dimensionless mass flow rates can be converted into zonal model capacity rates by multiplying them with the mass flow rate through the inflow boundary ($\dot{m}_{in} = \rho_{air} v_{in} A_{in}$):

7. A procedure for setting the zonal model parameters has been defined.
    (a) The pressure difference between the inlet and outlet is found from empirical correlations from studies on wind-generated surface pressure distributions such as that of Ernest (1991);
    (b) The average temperature of the ceiling nodes is calculated;
    (c) The temperature difference between in inflow air and the ceiling is calculated;
    (d) Pressure and temperature difference are used in Equation 3.77 to calculate the inlet velocity;
    (e) Temperature difference and inlet velocity are used in Equation 3.81 to calculate Archimedes number;
    (f) Table 3.5 can be used to find at which ceiling node the flow detaches using the Archimedes number;
    (g) Inlet velocity and flow detachment position are used with Table 3.6 to find the convective heat transfer parameters;
    (h) Inlet velocity and flow detachment position are used with Table 3.8 to calculate the capacity rate parameters.

8. The procedure for calculating the model parameters, outlined in Point 7, could easily be implemented within the code of thermal analysis software (along with the zonal model). Appendix B gives the calculation procedure in a more general form that may be used to implement the zonal model in another thermal modelling program.

Experiments were conducted of night-time cross-flow ventilation in a room altered to promote airflow next to the ceiling. The experimental measurements were taken to gain understanding of the physical processes involved in natural ventilation as well as to provide data that can be used to determine the structure and parameters of the zonal model. Due to the tentative nature of the CFD results it was felt important enough to seek experimental evidence for the flow regimes postulated in the zonal model. The significant findings of the experimental work can be summarised as follows.

1. The flow visualisation experiment using a laser and smoke supported by hand-held anemometer readings described in Section 4.3.2 showed that it was possible to get at least two flow regimes in the experimental room.

    (a) In the first flow regime the main flow path is across the ceiling. Near to the door the flow detaches from the ceiling due to wall obstruction above the door. The flow then leaves the room mostly at the top of the door opening.

    (b) In the second flow regime the flow went along the ceiling for only part of the room depth before rapidly dropping to the floor. Then the flow travels along the floor and exits at the bottom of the door opening.

    This finding provides support for the decision to include a method to model the impact of whether the flow remains attached to the ceiling or not within the zonal model.

    In both cases flow was biased towards the northern wall. As the window is off-centre the flow is more likely to attach to the nearer north wall surface due to the Coanda effect. Along this wall there was a strong downward flow whether the flow through the middle of the room remained attached to the ceiling or not. This was due to the hardboard section, shown in Figure 4.3, forcing the flow downwards and around the corner made by the north wall and the hardboard section.

2. Ratios were taken of the air speed next to the ceiling and near to the floor to see if a flow regime could be inferred. It was possible to determine where the main flow stream path was from the omnidirectional anemometer data collected using the air speed ratio—the ratio between the air speed near the ceiling and at midheight.

3. The correlation between Archimedes number and detachment position postulated in Chapter 3 from CFD simulation results was found to agree well with the experimental measurements.

4. The convective heat transfer coefficients calculated in this study were of the same order of magnitude as both the correlation of Chandra and Kerestecioglu (1984) and the ASHRAE forced convection correlation for air speeds below $5\,\mathrm{ms}^{-1}$ (ASHRAE

1997; McAdams 1954). The measured convective heat transfer coefficients are sufficiently close to the correlation indicated by the CFD work reported in Chapter 3 to give confidence in the use of CFD models as input to the zonal model.

The experimental measurements provided boundary conditions for a series of CFD simulations of cross-flow ventilation in a geometry that represented the experimental room. Although not being detailed enough to allow full validation, the experimental measurements taken allowed the CFD modelling approach taken in Chapter 3 to be verified against observed and computed flow patterns. The major findings of the experimental room CFD modelling exercise can be summarised as follows.

1. CFD analysis of the experimental room agreed qualitatively with the experimental results. At low inlet air speeds the flow fell to the floor on entry to the room, while at higher inlet air speeds the air flowed along the ceiling before exiting through the door. Flow was biased towards the north wall of the experimental room where air flowed downwards whether the flow remained attached to the ceiling or not.
2. The fact that flow is seen to detach from the ceiling in different places provide further support for the decision to structure the zonal model with multiple flow detachment positions.
3. The 3D numerical results support the relationship between Archimedes number and detachment point derived from the 2D parametric study.

7.4 Importance and Limitations of this Study

To design naturally ventilated buildings, architects need methods to predict their effectiveness before they are built. To compete with air conditioning as a cooling strategy, natural ventilation must be shown to be effective. Thus, the importance of being able to predict the impact of natural ventilation on cooling load and occupant comfort cannot be over-estimated. Prediction tools must therefore be accessible to designers to support decision making during the design process. The prediction method presented here fulfills the requirements of accuracy and accessibility with a number of important qualifying statements (the appropriateness of any prediction method must always be carefully considered).

The zonal model is semi-empirical in that it relies on a combination of physical law relationships and empirically derived correlations in its formulation. As with any prediction method based on empirical correlations, an important factor to be considered is its accuracy outside the range of parameters used to generate it. Although a wide range of boundary conditions were used in the CFD study used to generate the model parameters there is no guaranty of the model's accuracy beyond these.

The CFD geometry used to derive the zonal model parameters was 12 m between the inflow and outflow openings which ran the length of the room facade. The experimental investigation and the 3D CFD study based on the experimental room showed that zonal model could be applied to rooms of 4 m depth and with a window approximately 1/4 of the room facade. The zonal model could be applied to spaces from single person size offices to large open plan offices where the depth of the room does not exceed the recommendation for cross flow ventilation or 5 times the ceiling height, typically 18 m (BRE 1994).

It was not possible to account for the infinite design variables possible in a naturally ventilated building. CFD could have been used to model the flow around as well as through the building though, allowing issues such as window design and building floor plan to be investigated, but by decoupling the external environment from the room air flow it has enabled the study to concentrate on the internal environment. The zonal model produced can then be interfaced with other studies that derive inlet/outlet pressure coefficients for a large number of building configurations, wind incident angles, and obstructions etc. The goal of this investigation was to add the effect of the thermal environment on the flow regime inside the building ignored by wind tunnel experiments that precede this work.

The zonal model parameters were generated from a numerical study of flow inside a room with high-level openings, where the incoming air may flow along the ceiling even if it is more dense than the rest of the room air. If the inlet is a mid or low-level opening, then the flow will descend to the floor due to buoyancy forces. In this case, it would be possible to apply the zonal model using the parameter values for flow regime 1 (flow descends to the floor on entry to the room). The model is likely to be less accurate for mid or low-level inlets, though, as the upper recirculating region is modelled with one control volume which means thermal stratification may not be accurately predicted.

The model has more nodes in the ceiling than the floor and wall surfaces, if there is significant thermal mass in the floor and/or walls then it would be possible to add more nodes and to use the correlations in Chapter 3 to set the values of the associated heat transfer paths.

The model was developed with night-time cooling performance rather than daytime occupant comfort performance in mind. This, along with the fact that internal loads were not considered, means that the model is less well suited for daytime ventilation performance prediction. It would be a simple task to use the existing parametric study results to look at local air velocity and turbulence that could be used for occupant comfort performance under low internal load situations. In high internal load situations, the internal load may alter the flow regime causing thermal stratification. The method used to calculate Archimedes number (Equation 3.81), is not suited to determine whether the flow detaches from the ceiling in this situation as the room air temperature, and therefore the likelihood of the flow detaching, is coupled to the internal load as well as the ceiling and other surface temperatures.

Internal geometry can also alter the main flow stream flow path, but it is not considered by the model. Furniture and partitions will have significant effect on the local air velocities, and turbulence levels in the region of occupation. Beams may act to deflect the flow away from the ceiling.

The program LIGHTS used to develop the zonal model allows the development of networks that describe the convective and radiative heat flow paths that exist in a space but it was not designed as a tool for use within the building industry for yearly energy simulations of whole building structures. For this reason, it is fair to say that the zonal model presented here has not yet been developed to a stage that it can be used in the design process without significant effort. For this situation to change the model needs to be implemented with an existing thermal analysis program that might be used within the engineering community. LIGHTS has already been adapted for use with HVACSIM+ (Sowell 1991) and could also be easily implemented within other modular thermal simulation environments more typically used with the building engineering community.

7.5 Directions for Further Work

The field of wind-induced indoor air motion and its effect on building thermal and occupant comfort performance offers numerous possible research directions for the future. Firstly, CFD could be used to investigate the effect of many building design parameters on internal air flows including:

1. Window, and purpose built ventilation opening design;
2. Internal geometry, furniture and office partition type;
3. The effect of internal load due to solar, occupant and equipment gain;
4. External building geometry;
5. External obstructions;
6. Wind incident angle.

The zonal model can be improved in many ways including:

1. The model should be extended to include the effects of solar, equipment, and occupant heat gains. It could then be used with more confidence for daytime ventilation.

2. The zonal model should be implemented within an existing thermal analysis program that might be used within the engineering community. The thermal analysis program must supply accurate pressure values for the inlet and outlet openings so that the zonal model parameters can be set. If accurate pressure values cannot be supplied to the zonal model then it would be possible to include the work of wind tunnel experimentalists.

The CFD modelling used for zonal model development should in future:

1. Use a more robust procedure with more emphasis on checking the accuracy of the numerical results through the use of a grid independence study, different discretisation schemes, and different turbulence models and wall boundary treatments.
2. Faster computers, and possibly the use of a coupled solver that would negate the need to use time-stepping to achieve a converged solution, would allow the parametric study to be based on a three-dimensional geometry. A number of typical office geometries could be used to improve or generalise the parameter values used in the model.
3. CFD model validation may be based on experimental results from a more controlled environment than the one used in this study. The net radiative heat transfer between surfaces should be kept near zero by having the individual room surfaces at one temperature. A known air flow rate should be supplied to the room to keep flow regime inside the room fairly constant. Room air velocity rather than air speeds should be measured for flow validation.

APPENDIX A

LIGHTS Zone definition example

```
/*
   detach zone = 2
   vel = 0.75
*/
/* Program Control Parameters */
/* Newton-Raphson controls */
/*eps   max tries */
 0.000001      100
/* Predictor-corrector controls */
/* min_te    max_te   init_step min_step max_step   final time(hrs)*/
1.e-6     1.e-5      .005       0.0001      2.0                   12.0
 /* Min recognized mass      equilibrium start flag*/
/*       5001.0                          0 */
              1                          0
/*  shortwave limits (microns)*/
/* ms    1st    last */
   1     0.3     0.8
/* longwave limits (microns)*/
/* ml    1st    last */
   1     1.0    200.0
/*node     mass      area      r-sw  r-lw  t-sw  t-lw   q  iconq   t    icont*/
/*=====    ====      ====      ====  ====  ====  ====  ===  ===   ===  =====*/
19
ceil1     500000  25833.386  0.50  0.05  0.0   0.0   0.0   1    77.00   0
ceil2     500000  25833.386  0.50  0.05  0.0   0.0   0.0   1    77.00   0
ceil3     500000  25833.386  0.50  0.05  0.0   0.0   0.0   1    77.00   0
ceil4     500000  25833.386  0.50  0.05  0.0   0.0   0.0   1    77.00   0
ceil5     500000  25833.386  0.50  0.05  0.0   0.0   0.0   1    77.00   0
floor     500000  129166.93  0.50  0.05  0.0   0.0   0.0   1    77.00   0
north     1500.0     387.50  0.50  0.05  0.0   0.0   0.0   1    77.00   0
```

```
south    1500.0      387.50  0.50  0.05  0.0   0.0   0.0   1    77.00   0
eastw    125001    32291.73  0.50  0.05  0.0   0.0   0.0   1    77.00   0
westw    125001    32291.73  0.50  0.05  0.0   0.0   0.0   1    77.00   0
inlet      0.00        0.00  1.00  1.00  0.0   0.0   0.0   0    59.00   1
acei1      0.00        0.00  1.00  1.00  0.0   0.0   0.0   1    73.40   0
acei2      0.00        0.00  1.00  1.00  0.0   0.0   0.0   1    73.40   0
acei3      0.00        0.00  1.00  1.00  0.0   0.0   0.0   1    73.40   0
acei4      0.00        0.00  1.00  1.00  0.0   0.0   0.0   1    73.40   0
acei5      0.00        0.00  1.00  1.00  0.0   0.0   0.0   1    73.40   0
outlt      0.00        0.00  1.00  1.00  0.0   0.0   0.0   1    59.00   0
aroom      0.00        0.00  1.00  1.00  0.0   0.0   0.0   1    73.40   0
aroob      0.00        0.00  1.00  1.00  0.0   0.0   0.0   1    73.40   0

/* view factors between surface nodes */
45
ceil2 ceil1 0
ceil3 ceil1 0
ceil3 ceil2 0
ceil4 ceil1 0
ceil4 ceil2 0
ceil4 ceil3 0
ceil5 ceil1 0
ceil5 ceil2 0
ceil5 ceil3 0
ceil5 ceil4 0
floor ceil1 .13107
floor ceil2 .01919
floor ceil3 .00921
floor ceil4 .01919
floor ceil5 .13107
north ceil1 .06816
north ceil2 .08205
north ceil3 .08452
north ceil4 .08205
north ceil5 .06816
north floor .38500
south ceil1 .06816
south ceil2 .08205
south ceil3 .08452
south ceil4 .08205
south ceil5 .06816
south floor .38500
south north .00001
```

```
eastw ceil1 .01465
eastw ceil2 .02356
eastw ceil3 .04323
eastw ceil4 .09667
eastw ceil5 .25943
eastw floor .43754
eastw north .00138
eastw south .00138
westw ceil1 .25943
westw ceil2 .09667
westw ceil3 .04323
westw ceil4 .02356
westw ceil5 .01465
westw floor .43754
westw north .00138
westw south .00138
westw eastw .12216

/*   row  col det. by conservation   */
ceil1 ceil1
ceil2 ceil2
ceil3 ceil3
ceil4 ceil4
ceil5 ceil5
floor floor
north north
south south
eastw eastw
westw westw
inlet inlet
aceil aceil
acei2 acei2
acei3 acei3
acei4 acei4
acei5 acei5
outlt outlt
aroom aroom
aroob aroob

/* Radiant transmission coupling vector */
ceil1 0
```

```
ceil2 0
ceil3 0
ceil4 0
ceil5 0
floor 0
north 0
south 0
eastw 0
westw 0
inlet 0
aceil 0
acei2 0
acei3 0
acei4 0
acei5 0
outlt 0
aroom 0
aroob 0

/*                 Conduction/convection data            */
/* Num. of Conductors  */
32
aceil -inlet 170640    0.0        0.0      1.0 /* detach at 2 */
acei2 -aceil 170640    0.0        0.0      1.0
acei3 -acei2 170640    0.0        0.0      1.0
acei4 -acei3 170640    0.0        0.0      1.0
acei5 -acei4 170640    0.0        0.0      1.0
outlt -acei5 170640    0.0        0.0      1.0
inlet -outlt 170640    0.0        0.0      1.0
aceil  ceil1 22752     0.0        0.0      1.0
acei2  ceil2 22752     0.0        0.0      1.0
acei2  floor 11376     0.0        0.0      1.0
acei3  floor 11376     0.0        0.0      1.0
acei4  floor 11376     0.0        0.0      1.0
acei5  floor 11376     0.0        0.0      1.0
acei5  eastw 11376     0.0        0.0      1.0
aroom  floor 22752     0.0        0.0      1.0
aroom  westw 22752     0.0        0.0      1.0
aroob  ceil2 11376     0.0        0.0      1.0
aroob  ceil3 11376     0.0        0.0      1.0
aroob  ceil4 11376     0.0        0.0      1.0
```

```
aroob  ceil5 11376    0.0        0.0      1.0
acei1 -aroom 11376    0.0        0.0      1.0
aroom -acei1 11376    0.0        0.0      1.0
acei2 -aroom 11376    0.0        0.0      1.0
aroom -acei2 11376    0.0        0.0      1.0
acei2 -aroob 11376    0.0        0.0      1.0
aroob -acei2 11376    0.0        0.0      1.0
acei3 -aroob 11376    0.0        0.0      1.0
aroob -acei3 11376    0.0        0.0      1.0
acei4 -aroob 11376    0.0        0.0      1.0
aroob -acei4 11376    0.0        0.0      1.0
acei5 -aroob 11376    0.0        0.0      1.0
aroob -acei5 11376    0.0        0.0      1.0
/*
other parameters are 0 and can be left out
acei3  ceil3 0    0.0        0.0      1.0
acei4  ceil4 0    0.0        0.0      1.0
acei5  ceil5 0    0.0        0.0      1.0
aroom  eastw 0    0.0        0.0      1.0
acei3 -aroom 0    0.0        0.0      1.0
aroom -acei3 0    0.0        0.0      1.0
acei4 -aroom 0    0.0        0.0      1.0
aroom -acei4 0    0.0        0.0      1.0
acei5 -aroom 0    0.0        0.0      1.0
aroom -acei5 0    0.0        0.0      1.0
acei1  westw 0    0.0        0.0      1.0
acei1  floor 0    0.0        0.0      1.0
aroob  ceil1 0    0.0        0.0      1.0
acei1 -aroob 0    0.0        0.0      1.0
aroob -acei1 0    0.0        0.0      1.0
*/

/*  Luminous input */
1
ceil1 0
ceil2 0
ceil3 0
ceil4 0
ceil5 0
floor 0
north 0
```

```
south 0
eastw 0
westw 0
inlet 0
acei1 0
acei2 0
acei3 0
acei4 0
acei5 0
outlt 0
aroom 0
aroob 0

/*  Vector indicating which is ballast surface */
ceil1 0
ceil2 0
ceil3 0
ceil4 0
ceil5 0
floor 0
north 0
south 0
eastw 0
westw 0
inlet 0
acei1 0
acei2 0
acei3 0
acei4 0
acei5 0
outlt 0
aroom 0
aroob 0

/* Lamp luminous distribution vs. wave length */
/* No. of points on the curve */
   39
/* wavelength,output pairs */
         0       0       .3080     0       .3081     15e-4
         .3179   15e-4   .3180     0       .3290     0
         .3291   5e-4    .3389     5e-4    .3390     0
```

```
                .3610   10e-4   .3611       40e-4     .3709         40e-4
                .3710   15e-4   .4000       30e-4     .4001         90e-4
                .4099   90e-4   .4100       40e-4     .4310         50e-4
                .4311   195e-4  .4409       195e-4    .4410         65e-4
                .4750   85e-4   .5200       80e-4     .5410         108e-4
                .5411   190e-4  .5509       190e-4    .5510         135e-4
                .5730   175e-4  .5731       225e-4    .5829         225e-4
                .5830   190e-4  .6000       185e-4    .6150         150e-4
                .6250   110e-4  .6500       55e-4     .6750         30e-4
                .7000   20e-4   .7500       0         0.9999        0
/*NMRT*/
 1
ceil1 1
ceil2 0
ceil3 0
ceil4 0
ceil5 0
floor 0
north 0
south 0
eastw 0
westw 0
inlet 0
aceil 0
acei2 0
acei3 0
acei4 0
acei5 0
outlt 0
aroom 0
aroob 0

1
0.93
0.98
3
-50000    1.0     1.0
10000   1.0     1.0
60000   1.0     1.0

/*        Q- LOAD PROFILE        */
```

```
ceil1 0
ceil2 0
ceil3 0
ceil4 0
ceil5 0
floor 0
north 0
south 0
eastw 0
westw 0
inlet 0
acei1 0
acei2 0
acei3 0
acei4 0
acei5 0
outlt 0
aroom 0
aroob 0

/*        T- LOAD PROFILE         */
ceil1 0
ceil2 0
ceil3 0
ceil4 0
ceil5 0
floor 0
north 0
south 0
eastw 0
westw 0
inlet 0
acei1 0
acei2 0
acei3 0
acei4 0
acei5 0
outlt 0
aroom 0
aroob 0
```

```
/* Report file writers */
1
/*     File name         Writing interval(Hrs)   Nodes reported */
       de2-temp.out              0.25                  19
inlet    1        -1
aceil    1        -1
acei2    1        -1
acei3    1        -1
acei4    1        -1
acei5    1        -1
aroom    1        -1
outlt    1        -1            /* EQUALS INLET */
ceil1    1        -1
ceil2    1        -1
ceil3    1        -1
ceil4    1        -1
ceil5    1        -1
eastw    1        -1
floor    1        -1
westw    1        -1
north    1        -1            /* EQUALS SOUTH */
south    1        -1
aroob    1        -1
```

APPENDIX B

Zonal Model Equations

Figure B.1 shows the zonal model proposed to represent night-time cross-flow ventilation. There are ten surface nodes which comprise of five ceiling nodes, (*C1, C2, C3, C4, C5*), four wall nodes, (*west, east, north,* and *south*), and a node for the floor, (*flr*). The network diagram in Figure B.1 does not show the *north* and *south* wall nodes for clarity. There are nine air nodes, two of these are outside of the room modelled, (*inlet* and *outlet*), five specify the main flow stream from the inlet opening to the outlet opening, (*ma, mb, mc, md* and *me*), while the remaining two specify the two possible recirculating regions, (*rl* and *ru*).

B.1 Calculating the Zonal Model Parameters

The solution procedure is as follows:

1. The pressure difference between the inlet and outlet is found from empirical correlations from studies on wind-generated surface pressure distributions such as that of Ernest (1991).
2. The average temperature of the ceiling nodes is calculated:

$$T_c = \frac{T_{C1} + T_{C2} + T_{C3} + T_{C4} + T_{C5}}{5}. \tag{B.1}$$

3. The temperature difference between in inflow air and the ceiling is calculated:

$$\Delta T_{ci} = T_c - T_{in}. \tag{B.2}$$

4. Pressure and temperature difference are used to calculate the inlet velocity:

$$v_{in} = \sqrt{\frac{\Delta P_{io}}{0.5(0.0001\Delta T_{ci}^3 - 0.0016\Delta T_{ci}^2 + 0.0169\Delta T_{ci} + 1.3504)\rho_{air}}}. \tag{B.3}$$

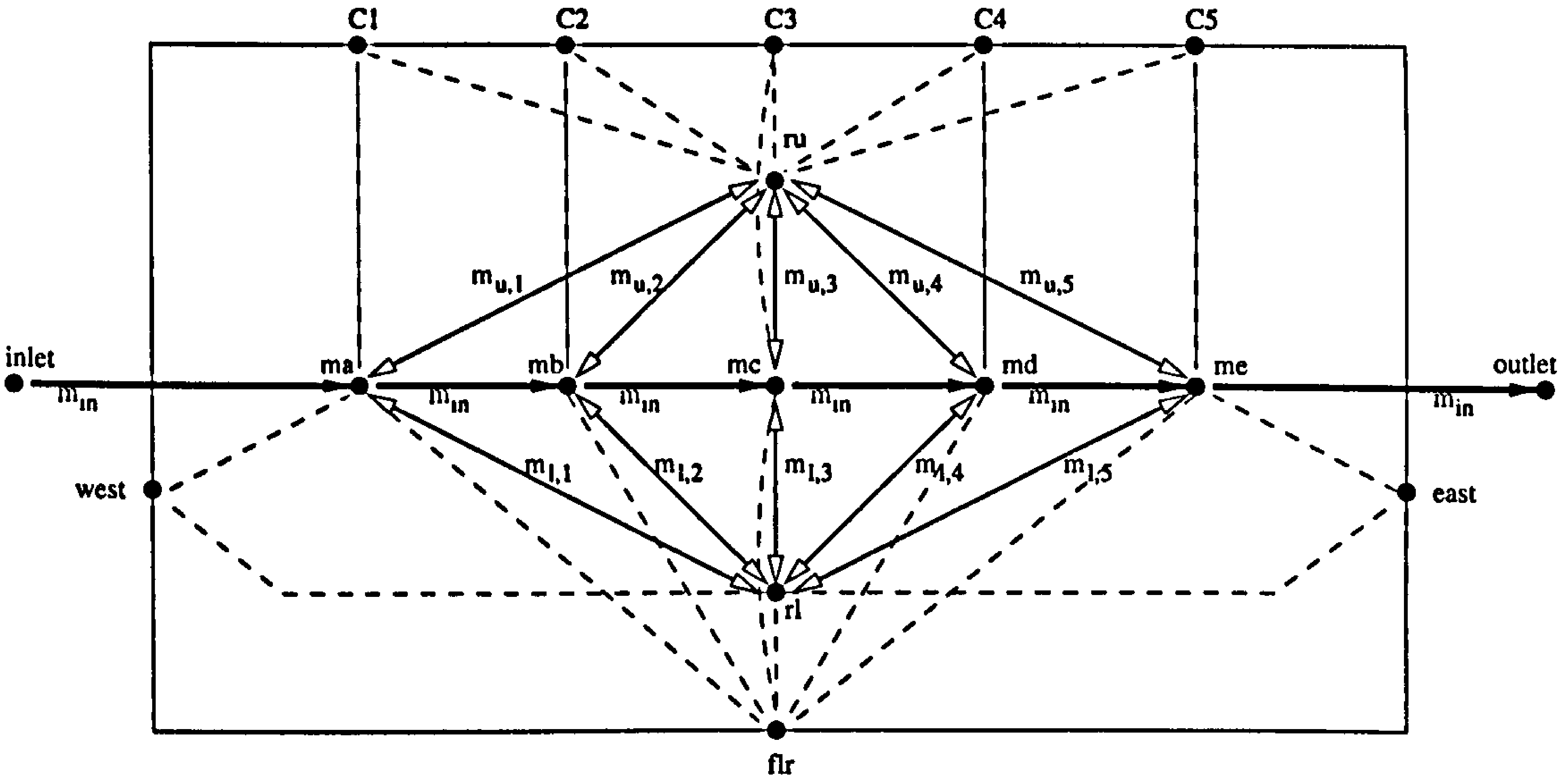

Figure B.1: Zonal model for nighttime cross-flow ventilation.

5. Temperature difference and inlet velocity are used to calculate Archimedes number:

$$Ar = \frac{1}{T_{in}} \frac{g\Delta T_{ci}}{v_{in}^2} \frac{A_{in}}{l}. \tag{B.4}$$

6. The ceiling node at which the flow detaches can be found using the Archimedes number and the following table:

Flow Regime	Description	Relationship
1	flow falls to floor on entry to the room	$Ar > 1.14$
2	flow detaches in zone 2	$0.89 < Ar < 1.14$
3	flow detaches in zone 3	$0.64 < Ar < 0.89$
4	flow detaches in zone 4	$0.39 < Ar < 0.64$
5	flow remains attached to ceiling	$Ar < 0.39$

1. Inlet velocity and flow detachment position are used to find the convective heat transfer parameters using the equation:

$$h_c = av_{in} + b, \tag{B.5}$$

where the coefficients a and b are given in the table below. The table also gives a minimum value for the flr, east and west nodes which should be used if the value calculated using Equation B.5 is below this minimum value.

	Flow Regime 1	Flow Regime 2	Flow Regime 3	Flow Regime 4	Flow Regime 5
C1	a=0.0, b=0.3	a=3.4, b=1.45	a=3.4, b=1.45	a=3.4, b=1.45	a=3.4, b=1.45
C2	a=0.0, b=0.2	a=3.2, b=1.3	a=3.2, b=1.3	a=3.2, b=1.3	a=3.2, b=1.3
C3	a=0.0, b=0.2	a=0.0, b=0.2	a=3.0, b=1.0	a=3.0, b=1.0	a=3.0, b=1.0
C4	a=0.0, b=0.3	a=0.0, b=0.3	a=0.0, b=0.3	a=2.8, b=0.65	a=2.8, b=0.65
C5	a=0.0, b=1.0	a=0.0, b=1.0	a=0.0, b=1.0	a=0.0, b=1.0	a=2.8, b=0.65
flr	a=1.08, b=1.25, min=1.5	a=1.08, b=1.25, min=1.5	a=1.08, b=1.25, min=1.5	a=1.08, b=1.25, min=1.5	a=1.08, b=1.25, min=1.5
east	a=2.4, b=0.2, min=1.5	a=2.4, b=0.2, min=1.5	a=2.4, b=0.2, min=1.5	a=2.4, b=0.2, min=1.5	a=2.4, b=0.2, min=1.5
west	a=0.26, b=1.48, min=1.5	a=0.26, b=1.48, min=1.5	a=0.26, b=1.48, min=1.5	a=0.26, b=1.48, min=1.5	a=0.26, b=1.48, min=1.5

1. Inlet velocity and flow detachment position are used to find dimensionless mass flow rates in the table below. The dimensionless mass flow rate is multiplied by the mass flow through the inlet, $\dot{m}_{in}$, to give the mass flow rate.

	Flow Regime				
Dimensionless mass flow	1	2	3	4	5
$m_{l,1}$	0.0	1.0	1.0	1.0	0.36
$m_{l,2}$	0.0	4.6	0.27	0.27	0.21
$m_{l,3}$	0.0	0.0	4.6	0.27	0.20
$m_{l,4}$	0.0	0.0	0.0	4.6	0.16
$m_{l,5}$	0.0	0.0	0.0	0.0	0.05
$m_{u,1}$	0.16	0.0	0.0	0.0	0.0
$m_{u,2}$	0.18	0.30	0.0	0.0	0.0
$m_{u,3}$	0.28	0.27	0.30	0.0	0.0
$m_{u,4}$	0.32	0.27	0.27	0.30	0.0
$m_{u,5}$	1.5	1.5	0.5	0.5	0.0
$m_{in,ma}$	1.0	1.0	1.0	1.0	1.0
$m_{ma,mb}$	1.0	1.0	1.0	1.0	1.0
$m_{mb,mc}$	1.0	1.0	1.0	1.0	1.0
$m_{mc,md}$	1.0	1.0	1.0	1.0	1.0
$m_{md,me}$	1.0	1.0	1.0	1.0	1.0
$m_{me,out}$	1.0	1.0	1.0	1.0	1.0

B.2 Heat Balance Equations

The heat balance equations for each node of the zonal model can be written as follows:

1. At node *ma*:

$$\begin{aligned} 0 &= c_p(\dot{m}_{in}T_{in} + \dot{m}_{l,1}T_{rl} + \dot{m}_{u,1}T_{ru} - \dot{m}_{in}T_{ma} - \dot{m}_{l,1}T_{ma} - \dot{m}_{u,1}T_{ma}) \\ &\quad + h_{C1}A_{C1}(T_{C1} - T_{ma}) + h_{west}A_{west}(T_{west} - T_{ma}) \\ &\quad + h_{flr}A_{flr}(T_{flr} - T_{ma}) \end{aligned} \tag{B.6}$$

2. At node *mb*:

$$\begin{aligned} 0 &= c_p(\dot{m}_{in}T_{ma} + \dot{m}_{l,2}T_{rl} + \dot{m}_{u,2}T_{ru} - \dot{m}_{in}T_{mb} - \dot{m}_{l,2}T_{mb} - \dot{m}_{u,2}T_{mb}) \\ &\quad + h_{C2}A_{C2}(T_{C2} - T_{mb}) + h_{flr}A_{flr}(T_{flr} - T_{mb}) \end{aligned} \tag{B.7}$$

3. At node *mc*:

$$\begin{aligned} 0 &= c_p(\dot{m}_{in}T_{mb} + \dot{m}_{l,3}T_{rl} + \dot{m}_{u,3}T_{ru} - \dot{m}_{in}T_{mc} - \dot{m}_{l,3}T_{mc} - \dot{m}_{u,3}T_{mc}) \\ &\quad + h_{C3}A_{C3}(T_{C3} - T_{mc}) + h_{flr}A_{flr}(T_{flr} - T_{mc}) \end{aligned} \tag{B.8}$$

4. At node *md*:

$$\begin{aligned} 0 &= c_p(\dot{m}_{in}T_{mc} + \dot{m}_{l,4}T_{rl} + \dot{m}_{u,4}T_{ru} - \dot{m}_{in}T_{md} - \dot{m}_{l,4}T_{md} - \dot{m}_{u,4}T_{md}) \\ &\quad + h_{C4}A_{C4}(T_{C4} - T_{md}) + h_{flr}A_{flr}(T_{flr} - T_{md}) \qquad \text{(B.9)} \end{aligned}$$

5. At node *me*:

$$\begin{aligned} 0 &= c_p(\dot{m}_{in}T_{md} + \dot{m}_{l,5}T_{rl} + \dot{m}_{u,5}T_{ru} - \dot{m}_{in}T_{me} - \dot{m}_{l,5}T_{me} - \dot{m}_{u,5}T_{me}) \\ &\quad + h_{C5}A_{C5}(T_{C5} - T_{me}) + h_{east}A_{east}(T_{east} - T_{me}) \\ &\quad + h_{flr}A_{flr}(T_{flr} - T_{me}) \qquad \text{(B.10)} \end{aligned}$$

6. At node *rl*:

$$\begin{aligned} 0 &= c_p(\dot{m}_{l,1}T_{rl} + \dot{m}_{l,2}T_{rl} + \dot{m}_{l,3}T_{rl} + \dot{m}_{l,4}T_{rl} + \dot{m}_{l,5}T_{rl}) \\ &\quad - c_p(\dot{m}_{l,1}T_{ma} + \dot{m}_{l,2}T_{mb} + \dot{m}_{l,3}T_{mc} + \dot{m}_{l,4}T_{md} + \dot{m}_{l,5}T_{me}) \\ &\quad + h_{west}A_{west}(T_{west} - T_{rl}) + h_{east}A_{east}(T_{east} - T_{rl}) \\ &\quad + h_{flr}A_{flr}(T_{flr} - T_{rl}) \qquad \text{(B.11)} \end{aligned}$$

7. At node *ru*:

$$\begin{aligned} 0 &= c_p(\dot{m}_{u,1}T_{ru} + \dot{m}_{u,2}T_{ru} + \dot{m}_{u,3}T_{ru} + \dot{m}_{u,4}T_{ru} + \dot{m}_{u,5}T_{ru}) \\ &\quad - c_p(\dot{m}_{u,1}T_{ma} + \dot{m}_{u,2}T_{mb} + \dot{m}_{u,3}T_{mc} + \dot{m}_{u,4}T_{md} + \dot{m}_{u,5}T_{me}) \\ &\quad + h_{west}A_{west}(T_{west} - T_{ru}) + h_{east}A_{east}(T_{east} - T_{ru}) \\ &\quad + h_{flr}A_{flr}(T_{flr} - T_{ru}) \qquad \text{(B.12)} \end{aligned}$$

B.3 Mass Balance Equations

The LIGHTS program does not calculate mass balances, the user must ensure the capacity rate parameters that describe the mass flows present are included in the input file correctly. The mass balance equations for each node of the zonal model are included here for completeness:

1. At node *ma*:

$$\dot{m}_{in} + \dot{m}_{l,1} + \dot{m}_{u,1} - \dot{m}_{in} - \dot{m}_{l,1} - \dot{m}_{u,1} = 0 \qquad \text{(B.13)}$$

2. At node *mb*:

$$\dot{m}_{in} + \dot{m}_{l,2} + \dot{m}_{u,2} - \dot{m}_{in} - \dot{m}_{l,2} - \dot{m}_{u,2} = 0 \qquad \text{(B.14)}$$

3. At node *mc*:

$$\dot{m}_{in} + \dot{m}_{l,3} + \dot{m}_{u,3} - \dot{m}_{in} - \dot{m}_{l,3} - \dot{m}_{u,3} = 0 \qquad \text{(B.15)}$$

4. At node *md*:

$$\dot{m}_{in} + \dot{m}_{l,4} + \dot{m}_{u,4} - \dot{m}_{in} - \dot{m}_{l,4} - \dot{m}_{u,4} = 0 \tag{B.16}$$

5. At node *me*:

$$\dot{m}_{in} + \dot{m}_{l,5} + \dot{m}_{u,5} - \dot{m}_{in} - \dot{m}_{l,5} - \dot{m}_{u,5} = 0 \tag{B.17}$$

6. At node *rl*:

$$\dot{m}_{l,1} + \dot{m}_{l,2} + \dot{m}_{l,3} + \dot{m}_{l,4} + \dot{m}_{l,5} - \dot{m}_{l,1} - \dot{m}_{l,2} - \dot{m}_{l,3} - \dot{m}_{l,4} - \dot{m}_{l,5} = 0 \tag{B.18}$$

7. At node *ru*:

$$\dot{m}_{u,1} + \dot{m}_{u,2} + \dot{m}_{u,3} + \dot{m}_{u,4} + \dot{m}_{u,5} - \dot{m}_{u,1} - \dot{m}_{u,2} - \dot{m}_{u,3} - \dot{m}_{u,4} - \dot{m}_{u,5} = 0 \tag{B.19}$$

APPENDIX C

Instrument Calibration

C.1 Anenometer Calibration

Each sensor of the Dantec 54N10 system had been calibrated by the manufacturer in a low velocity wind tunnel. The calibration data is provided in the form of a velocity reading error at a high and low calibration velocity. This data was used to post-correct the air speed measurements using a linear calibration correction for each sensor. The general accuracy of the air speed sensors is quoted as ±5% in the 0.05–1.0 ms^{-1} range typical during the experiment with a minimum error of ±0.01 ms^{-1}. The temperature sensors of the system have a quoted accuracy of ±0.5 K at moderate air velocities and above ($\geq$0.1 ms^{-1}). At lower velocities often seen during this experiment the accuracy of the system decreases but the error here is unquantified.

C.2 Thermocouple Calibration

C.2.1 Water Bath Calibration

Calibration corrections to the raw thermocouple data have been applied using a linear correlation between the raw data and temperature for each thermocouple/input channel combination. The temperature-voltage characteristic of the type T thermocouple is known to be non-linear over its full working range of -300–800°C however, the temperature range used here of ~15–28°C is small enough that a linear approximation should give acceptably accurate results. The method initially used to derive the coefficients of the linear equations used for the correlation was to take readings from the thermocouples immersed in a water bath at two known temperatures.

The thermocouples (both surface and air) were calibrated inside watertight balloons by submerging them in a water bath, with an electric stirrer, at a known temperature. The water bath was then operated at ~20°C and then at ~30°C after being left for the temperature to stabilise. Measurements of the water bath temperature were made with a mercury in glass thermometer with a 0.2°C scale. Thermocouple readings were logged and a set of readings at each temperature used to calculate the constants in the line equation $T = aT_{in} + c$, where T_{in} is the raw thermocouple reading.

It was observed that the 'a' coefficients (i.e.,the gains) varied only slightly between input channels ($a = 1.0 \pm 0.02$). The 'C' coefficient (i.e., the offset) varied more widely, between -0.83 and 0.33. To test whether this variability was due to differences in the thermocouples or differences in the the data logging channels thermocouples were swapped to other channels and temperature readings taken from the constant temperature water bath. This investigation indicated that the variations is offset were due to differences between input channels.

C.2.2 In-situ Calibration of the Surface Thermocouples

The surface temperature thermocouples calibration was further checked by making independent measurements of surface temperature at each thermocouple site. These measurements were taken with a hand held digital thermometer using a type 'K' thermocouple surface probe and a second thermocouple in an ice bath as a reference. (This combination of thermocouples and digital thermometer was previously calibrated against the mercury/glass thermometer used in the water bath.) The handheld thermocouple reading was taken on top of each surface mounted thermocouple and was compared to the corresponding one recorded by the data acquisition equipment. This process was repeated twice and the data is recorded in Table C.1. Column 1 of Table C.1 is of the thermocouple sensor name. Columns 2 and 3 show the difference between the hand held thermocouple and the sensor readings from the in-situ calibration procedure performed on two different days (dates shown in Table C.1). Columns 4 and 5 are the mean and the standard deviation of the two differences for each sensor. The last two rows show the mean and standard deviation of each column—allowing any day related inconsistencies to be detected. The second date of the in-situ calibration procedure corresponds to the morning after the main night-time cross-flow experiment described in the document.

The differences between the hand held thermocouple and the sensor readings do not show any systematic error as they vary randomly about zero. If the calibration error was larger than this random error the differences would always be positive or negative for a particular sensor.

The random error seen is a combination of the error in the hand held thermocouple measurement and the error in the surface thermocouple sensor readings. As the error in the hand held thermocouple measurement is not know it must be assumed that the error seen is completely due to the error in the surface thermocouple measurement. Thus, the error in the experimental surface temperature measurements equals the standard

Table C.1: Difference between the hand held thermocouple and the logged surface mounted thermocouples readings.

Sensor Name	Difference(28/08/96)	Difference (22/08/96)	Mean	Std. dev.
c1	0.129	0.199	0.135	0.049
c2	0.139	0.169	0.125	0.0212
c3	-0.251	0.209	-0.050	0.325
c4	-0.131	0.099	-0.045	0.163
n5	0.119	-0.041	0.010	0.113
n6	-0.011	-0.221	-0.145	0.148
n7	0.209	-0.101	0.025	0.219
n8	-0.051	0.099	-0.005	0.106
s9	0.169	0.039	0.075	0.092
s10	-0.051	0.119	0.005	0.120
s11	-0.281	-0.111	-0.225	0.120
s12	-0.051	0.359	0.125	0.290
w13	-0.031	0.469	0.190	0.354
w14	0.259	0.399	0.300	0.099
w15	0.009	0.199	0.075	0.134
w16	0.209	0.269	0.210	0.042
e17	-0.291	0.059	-0.145	0.247
e18	-0.011	0.099	0.015	0.078
e19	0.049	0.089	0.040	0.028
e20	-0.151	-0.141	-0.175	0.007
f21	-0.181	-0.031	-0.135	0.106
f22	-0.031	-0.051	-0.070	0.014
f23	-0.251	-0.201	-0.270	0.057
f24	-0.201	0.119	-0.070	0.226
Mean	-0.059	0.059	0.000	
Std. dev.	0.167	0.181	0.142	

deviation of the difference between the hand held thermocouple measurements and the surface thermocouple measurements, i.e., ±0.181 K.

C.3 Heat Flux Meter Calibration

The heat flux meters had been calibrated previously by the manufacturer and have an output of $49.0\mu V.W^{-1}.m^{2}$. This meant that only the input channels of the data acquisition system used for the heat flux meters needed a linear calibration correction applied. The channels of the signal processing/multiplexing channels have a full scale of ±6.25 mV which gives a resolution of $0.15W.m^{-2}$ per bit. A precision DC voltage source was used to apply five known voltages between +5 mv and -5 mv to each input channel. The gain and offset corrections were then calculated, and along with the data supplied by the manufacturer, used to derive a heat flux measurement from a voltage recorded from both heat flux meters by the data acquisition equipment.

C.4 Uncertainty in convective heat flux coefficient, h_c

The convective heat transfer coefficient, h_c, is found from

$$h_c = \frac{q_c}{Tc - Ta} \tag{C.1}$$

$$= \frac{q_t - \varepsilon\sigma\Sigma(f_i\,(T_c^4 - T_i^4))}{T_c - T_a}, \tag{C.2}$$

where q_c is the convective heat flux calculation, q_t is the total heat flux measurement, ε is the surface emissivity, T_c is the temperature of the ceiling, T_a is the air temperature measurement from the nearby anemometer, T_i is the temperature of the surface i, σ is the Stefan Boltzmann constant and f_i is the view factor from the heat flux meter to surface i.

The error in convective heat flux coefficient, σ_{hc}, is given by

$$\sigma_{hc} = \frac{\partial h_c}{\partial q_t}\sigma_{qt} + \frac{\partial h_c}{\partial T_c}\sigma_{tc} + \frac{\partial h_c}{\partial T_a}\sigma_{ta} + \Sigma\frac{\partial h_c}{\partial T_i}\sigma_{ti}, \tag{C.3}$$

where σ_{qt}, σ_{tc}, σ_{ta} and σ_{ti} are the errors in the total heat flux, ceiling temperature, air temperature and surface temperature measurements respectively, the values of which are given in Table C.2. The partial derivatives in Equation C.3 are as follows.

$$\frac{\partial h_c}{\partial q_t} = \frac{1}{T_c - T_a}, \tag{C.4}$$

$$\frac{\partial h_c}{\partial T_c} = -\frac{qt}{(T_c - T_a)^2} - \varepsilon\sigma\Sigma(f_i(\frac{4T_c^3}{T_c - T_a} - \frac{T_c^4 - T_i^4}{(T_c - T_a)^2})), \tag{C.5}$$

$$\frac{\partial h_c}{\partial T_a} = \frac{qt}{(T_c - T_a)^2} - \frac{\varepsilon\sigma}{(T_c - T_a)^2}\Sigma f_i(T_c^4 - T_i^4), \tag{C.6}$$

Table C.2: The errors for the different experimental measurements.

Measurement	Error
Heat flux	$\pm 0.15 \mathrm{W.m^{-2}}$
Air temperature	$\pm 0.5\,\mathrm{K}$
Air speed	$\pm 5\%$ (min $\pm 0.01\,\mathrm{ms^{-1}}$)
Surface temperature	$\pm 0.181\,\mathrm{K}$

$$\frac{\partial h_c}{\partial T_i} = \frac{4\varepsilon\sigma}{T_c - T_a}\Sigma(f_i T_i^3). \tag{C.7}$$

C.5 Summary of Measurement Errors

The experimental measurement errors assumed are given in Table C.2.

References

Alamdari, F. (1991, November). Thermo-fluid analysis in the built environment: expectations and limitations. In *Computational Fluid Dynamics—Tool or Toy?*, London. Institution of Mechanical Engineers.

Alamdari, F., S. Edwards, and S. Hammond (1991, November). Microclimate performance of an open atrium office building: a case study in thermo-fluid modeling. In *Computational Fluid Dynamics—Tool or Toy?*, London, pp. 81–92. Institution of Mechanical Engineers.

Allard, F. and C. Inard (1992, July). Natural and mixed convection in rooms: Prediction of thermal stratification and heat transfer by zonal models. In *1992 International Symposium on Room Air Convection and Ventilation Effectiveness*, Tokyo, Japan, pp. 335–342. American Society of Heating, Refrigerating and Air-Conditioning Engineers, Inc.

Arai, Y., S. Togari, and K. Miura (1994). Unsteady-state thermal analysis of a large space with vertical temperature distribution. *Transactions of the American Society of Heating Refrigeration and Air Conditioning Engineers 100*(2), 396–411.

ASHRAE (1997). *Handbook of Fundamentals.* Atlanta, GA: American Society of Heating, Refrigerating and Air-Conditioning Engineers.

Awbi, H. (1998). Calculation of convective heat transfer coefficients of room surfaces for natural convection. *Energy and Buildings 28*, 219–227.

Awbi, H. and G. Gan (1991, November). Computational fluid dynamics in ventilation. In *Computational Fluid Dynamics—Tool or Toy?*, London, pp. 67–79. Institution of Mechanical Engineers.

Awbi, H. and A. Hatton (1999). Natural convection from heated room surfaces. *Energy and Buildings 30*, 233–244.

Awbi, H. and A. Hatton (2000). Mixed convection from heated room surfaces. *Energy and Buildings 32*, 153–166.

Aynsley, R. (1982). Natural ventilation model studies. In *International Workshop on Wind Tunnel Modeling Criteria and Techniques for Civil Engineering Applications*, pp. 465–485. Cambridge University Press.

Aynsley, R. (1988). A resistance approach to estimate air flow through buildings with large openings due to wind. *Transactions of the American Society of Heating Refrigeration and Air Conditioning Engineers 94*, 1661–1669.

Baker, A. (1983). *Finite Element Computational Fluid Dynamics.* Hemisphere.

Bakhmeteff, B. (1936). *The Mechanics of Turbulent Flow.* Princeton University Press.

BESG (1982). *DOE-2 Engineers Manual, part 1-2, version 2.1A.* Berkeley, CA: Building Energy Simulation Group, Lawrence Berkeley Laboratory.

BLAST (1986). *BLAST (Building Loads and System Thermodynamics).* University of Illinois at Urbana-Champaign.: BLAST Support Office.

BRE (1992). *Breeze User Manual.* Building Research Establishment.

BRE (1994). *Natural ventilation in non-domestic buildings, BRE Digest 399.* Building Research Establishment, UK.

Caudill, W. and B. Reed (1952). Geomtery of classrooms as related to natural lighting ans natural ventilation. Technical Report 36, Texas Engineering Experiment Station.

CFX (1997a). *CFX-4.2 Radiation.* Harwell, Didcot, Oxfordshire: AEA Technology, CFX International.

CFX (1997b). *CFX-4.2 Solver.* Harwell, Didcot, Oxfordshire: AEA Technology, CFX International.

Chand, I. and N. Krishak (1969). Effect of window size, location and orientation on indoor air motion. *Journal of the Institution of Engineers (India) 49*, 375–378.

Chand, I. and N. Krishak (1971). Laboratory studies of the effects of louvers on room air motion. *Building Science 6*, 247–252.

Chand, I., N. Krishak, and V. Sharma (1975). Studies of air motion is shielded buildings. *The Indian Architect 19*(9), 23–29.

Chand, I., V. Sharma, and P. Bhargava (1977). Influence of plan dimension ratio of enclosures on indoor air motion. *Indian Journal of Technology 15*, 358–359.

Chand, I., V. Sharma, and P. Bhargava (1978). Effect of height and type of roof on air motion in industrial buildings. *The Indian Architect*, 115–119.

Chand, I., V. Sharma, and N. Krishak (1989). Ventilation survey of typical airy buildings — a few case studies in hot dry and hot humid zones in india. *Building and Enivronment 24*(3), 229–238.

Chandra, S. (1983). A handbook for designing ventilated buildings. Technical report, Florida Solar Energy Center.

Chandra, S. and A. Keresteciogiu (1984). Heat transfer in naturally ventilated rooms: Data from full-scale measurements. *Transactions of the American Society of Heating Refrigeration and Air Conditioning Engineers 90*(1B), 211–225.

Chandra, S., A. Keresteciogiu, P. Fairey, and W. Cromer (1982). Comparison of model and full-scale natural ventilation studies. In *International Workshop on Wind Tunnel Modeling Criteria and techniques for Civil Engineering Applications*, pp. 669–684. Cambridge University Press.

Chen, Q. and Z. Jiang (1992). Significant questions in predicting room air motion. *Transactions of the American Society of Heating Refrigeration and Air Conditioning Engineers 98*(1), 929–939.

Chikamoto, T., S. Murakami, and S. Kato (1992, July). Numerical simulation of velocity and temperature fields within atrium based on modified k-ε model incorporating damping effect due to thermal stratification. In *1992 International Symposium on Room Air Convection and Ventilation Effectiveness*, Tokyo, Japan, pp. 501–510. American Society of Heating, Refrigerating and Air-Conditioning Engineers, Inc.

Clark, D. (1985). *HVAC+ Building Systems and exquipment simulation program — Reference manual.* National Institute of Standards and Technology.

Cook, M. and K. Lomas (1998). Buoyancy-driven displacement ventilation flows: evaluation of two eddy viscosity turbulence models for prediction. *Building Services Engineering Research & Technology 19*(1), 15–21.

Dalicieux, P. and H. Bouia (1993). *Présentation d'une meélisation simplifiée des mouvements d'air à l'intérieur d'une pièce d'habitation.* Electricite de France report HE 12 W 3269, 29 p.

Dantec (1993a). *54G301 Multichannel Flow Analyser - Software Manual.* Dantec Document Department, Scientific Research Equipment Division.

Dantec (1993b). *54N10 Multichannel Flow Analyser - Instruction Manual.* Dantec Document Department, Scientific Research Equipment Division.

De Moor, M. and D. Berckmans (1994, December). Building a grey box model to model the energy and mass transfer in an imperfectly mixed fluid by using experimental data. In *System Simulation in Buildings '94*, Liege, Belgium.

EDS (1992). *Tas Users Manual.* Stoney Stratford, Bucks, UK: Environmental Design Solutions Limited.

Ernest, D. (1991). *Predicting wind-induced indoor air motion, occupant comfort, and cooling loads in naturally vetilated buildings.* Ph. D. thesis, University of California.

FACET (1991). *APACHE User manual.* St Albans, UK: FACET Ltd.

Feustel, H. and A. Rayner-Hooson (1992). *COMIS 1.0 — User Guide.* AIVC.

FLUENT (1999a). *FLUENT 5.0 User Manual 1-4.* FLUENT Incorporated.

FLUENT (1999b). *Gambit User Manual.* FLUENT Incorporated.

Gan, G. and H. Awbi (1994). Numerical simulation of the indoor environment. *Building and Environment 24*(4), 449–459.

Gandamer, J. and G. Barnaud (1989). Ventilation naturelle en climat tropical humide: Prise en compe du vent dans l'habite. In *11th Triennial Congress of the Information Council for Building Research, Studies and Documentation (CIB)*, pp. 227–236.

Gautier, B. and F. Rongere (1991). Clim 2000: The building energy simulation tool and the modelling method. In *Building Simulation '91.*

Gill (1991). *Gill Instruments 3 Axis Logging Ultrasonic Anemometer Product Specification.* Solent House, Cannon Street, Lymington, Hampshire: Gill Instruments Limited. Issue 3.0.

Givoni, B. (1962). Basic studies of ventilation problems in housing in hot countries. Technical report, Building Research Station, Technion, Israel.

Givoni, B. (1965). Laboratory study of the effect of window size and location on indoor air motion. *Architectural Science review 8*(2), 42–45.

Givoni, B. (1969). *Man, Climate and Arcitecture.* Applied Science Publishers Limited.

Gough, M. (1999). A review of new techniques in building energy and environmental modelling. Technical Report BREA-42, Building Research Establishment.

Hensen, J. and M. Hamelinck (1995). Energy simulation of displacement ventilation in offices. *BSERT 16*(1), 77–81.

Howarth, A. (1983). *Temperature Distribution and Air movements in Rooms with Convective Heat Source.* Ph. D. thesis, University of Manchester Institute of Science and Technology.

IES (1999a). *The ESP System — General Introduction.* Integrated Environmental Systems Limited.

IES (1999b). *The MicroFlo System.* Integrated Environmental Systems Limited.

Inard, C. and D. Buty (1991). Simulation of thermal coupling between a radiator and a room with zonal models. In *Building Simulation '91*, pp. 113–117.

Iwamoto, S., A. Ishii, T. Katayama, and J. Tsutsumi (1992, July). Numerical prediction of indoor airflow by cross-ventilation. In *1992 International Symposium on Room Air Convection and Ventilation Effectiveness*, Tokyo, Japan, pp. 453–456. American Society of Heating, Refrigerating and Air-Conditioning Engineers, Inc.

Jayatilleke (1969). The influence of Prandtl number and surface roughness on the resistance of the laminar sublayer to momentum and heat transfer. *Progress in Heat and Mass Transfer 1*, 269–289.

Jones, I. (1995). The convergence of a simple iterative strategy for strongly stratified flows. Technical report, Computer Science and Systems Division, AERE Harwell, Oxon.

Jones, P. and G. Whittle (1992). Computational fluid dynamics for building air flow prediction - current status and capabilities. *Building and Environment 27*(3), 321–338.

Kato, S., S. Murakami, S. Shoya, F. Hanyu, and J. Zeng (1995). Cfd analysis of flow and temperature fields in atrium with ceiling height of 130m. *Transactions of the American Society of Heating Refrigeration and Air Conditioning Engineers 101*(2), 1144–1157.

Khalifa, A. and R. Marshall (1990). Validation of heat transfer coefficients on interior building surfaces using a real-sized indoor test cell. *Int. J. Heat Mass Transfer 33*, 2219–2236.

Klein, S., W. Beckmann, and J. Duffie (1976). Trnsys — a transient simulation program. *Transactions of the American Society of Heating Refrigeration and Air Conditioning Engineers 82*(1), 623–633.

Launder, B. and D. Spalding (1974). The numerical computation of turbulent flow. *Computer Methods in Applied Mechanics and Engineering 3*, 269–289.

Lebrun, J. (1970). *Exigences physiologiques et modalitês physiques de la climatisation par source satique concentrêe.* Ph. D. thesis, University of Liêge.

Lebrun, J. and P. Ngendakumana (1987). Air circulation induced by heating emitters and corresponding heat exchanges along the walls: Test-room results and modelling. In *ROOMVENT-87*, Stockholm, Sweden, pp. 15.

Linden, P., G. Lane-Serff, and D. Smeed (1990). Emptying filling boxes: the fluid mechanics of natural ventilation. *Journal of Fluid Mechanics 212*, 309–335.

Lockwood, F. and N. Shah (1980). A new radiation solution method for incorporation in general combustion prediction procedures. In *Eighteenth Symposium (International) on Combustion*, pp. 1405–1412. The Combustion Institute.

Malalasekera, W. and E. James (1993). Thermal radiation in a room: Numerical evaluation. *Building Services Engineering Research and Technology 4*(14), 159–168.

McAdams, W. (1954). *Heat Transmission* (3rd ed.). New York: McGraw-Hill.

McGuirk, J. and G. Whittle (1991, November). Calculation of buoyant air movement in buildings—proposals for a numerical benchmark test case. In *Computational Fluid Dynamics—Tool or Toy?*, London, pp. 13–32. Institution of Mechanical Engineers.

Modest, M. (1993). *Radiative Heat Transfer.* New York: McGraw-Hill.

Ozeki, Y., S. Higuchi, T. Salto, S. Ohgaki, and Y. Sonda (1992, July). Simulation of temperature and flow field in an atrium part2: Comparison of results from experiments and numerical analysis, and applications. In *1992 International Symposium on Room Air Convection and Ventilation Effectiveness*, Tokyo, Japan, pp. 491–500. American Society of Heating, Refrigerating and Air-Conditioning Engineers, Inc.

Patankar, S. (1980). *Numerical Heat Transfer and Fluid Flow.* New York: Hemisphere.

Patankar, S. and D. Spalding (1972). A calculation procedure for heat, mass and momentum transfer in three-dimensional parabolic flows. *International Journal of Heat and Mass Transfer 15*, 1787–1806.

Pelletret, R. and W. Keilholz (1997). Comis 3.0 a new simulation environment for multizone air flow and pollutant transport modelling. In *Building Simulation '97.* IBPSA.

Poreh, M., J. Cermak, and J. Peterka (1982). Wind tunnel research of flowfields within naturally ventilated rooms of simple geometry. Technical Report CER82-83MP-JEC-JAP17, Fluid Dynamics and Diffusion Laboratory, Colorado State University, Fort Collins, CO.

Rees, S. (1998). *Modelling of Displacement Ventilation and Chilled Ceiling Systems Using Nodal Models.* Ph. D. thesis, Loughborough University.

Sahlin, P. (1996). Nmf handbook. an introduction to the neutral model format. Technical Report RP-839, ASHRAE.

Sahlin, P. and A. Bring (1991). Ida solver - a tool for building and energy systems simulation. In *Building Simulation '91.* IBPSA.

Schild, P., P. Tjelflaat, and D. Aiulfi (1995). Guidelines for cfd-modelling of atria. *Transactions of the American Society of Heating Refrigeration and Air Conditioning Engineers 101*(2), 1311–1332.

Shah, N. (1979). *New Method of Computation of Radiant Heat Transfer in Combustion Chambers.* Ph. D. thesis, Dept. of Mechanical Engineering, Imperial College, London.

Smith, E. (1951). The feasibility of using models for predetermining natural ventilation. Technical Report 26, Texas Engineering Experiment Station.

Snyckers, W. (1970). Wind tunnel studies of the flow of air through rectangular openings with application to natural ventilation of buildings. Master's thesis, University of Pretoria, South Africa.

Sobin, H. (1981). Window design for passive ventilative cooling: An experimental model-scale study. In *1981 International Passive/Hybrid Cooling Conference*, pp. 191–195.

Sobin, H. (1983). *Analysis of wind tunnel data on naturally ventilated models.* Tucson: Harris Sobin Assoc.

Sowell, E. (1989). *LIGHTS User's Guide.* California State University. CA, USA.: Department of Computer Science.

Sowell, E. (1991). A general zone model for HVACSIM+: Users manual. Technical Report OUEL 1889/91, University of Oxford.

Sowell, E. and P. O'Brien (1972). Efficient computation of radiant-interchange configuration factors within the enclosure. *A.S.M.E. transactions C*(95), 326–328.

Spalding, D. (1972). A novel finite difference formulation for differential expressions involving both first and second derivatives. *International Journal of Numerical Methods in Engineering 4*, 551–559.

Spitler, J., C. Perdersen, and D. Fisher (1991). Interior convective heat transfer in buildings with large ventilative flow rates. *Transactions of the American Society of Heating Refrigeration and Air Conditioning Engineers ?*(1), 505–515.

Spitler, J., C. Perdersen, D. Fisher, P. Menne, and J. Cantillo (1991). An experimental facility for investigation of interior convective heat transfer. *Transactions of the American Society of Heating Refrigeration and Air Conditioning Engineers ?*(1), 497–504.

SRG (1997). *Simulation Problem Analysis Research Kernel (SPARK) - Users Manual.* Simulation Research Group, Lawrence Berkeley Laboratory.

Togari, S., Y. Arai, and K. Miura (1993). A simplified model for predicting vertical temperature distribution in a large space. *Transactions of the American Society of Heating Refrigeration and Air Conditioning Engineers 99*(1), 84–99.

Tsutsumi, J., T. Katayama, T. Hayashi, and P. He (1992, July). Numerical simulation of cross-ventilation in a single-unit house. In *1992 International Symposium on Room Air Convection and Ventilation Effectiveness*, Tokyo, Japan, pp. 447–452. American Society of Heating, Refrigerating and Air-Conditioning Engineers, Inc.

Tsutsumi, J., T. Katayama, T. Hayashi, and P. He (1995, September). Numerical simulation for air flow of single-unit houses by cross-ventilation. In *TSINGHUA-HVAC-95, 2nd International Symposium on HVAC*, Beijing, China.

Van Doormaal, J. and G. Raithby (1984). Enhancements of the simple method for predicting incompressible fluid flows. *Numerical Heat Transfer 7*, 147–163.

Versteeg, H. and W. Malalasekera (1995). *An introduction to computational fluid dynamics. The finite volume method.* Longman Scientific & Technical.

Vickery, B. and C. Karakatsanis (1987). External wind pressure distributions and induced internal ventilation flow in low-rise industrial and domestic structures. *Transactions of the American Society of Heating Refrigeration and Air Conditioning Engineers 93*(2), 2198–2213.

Walton, G. (1997). *CONTAM96 — User Manual NISTIR 6056.* National Technical Information Service.

Walton, G. and S. Emmerich (1994). Contam93: A multizone airflow and contaminant dispersal model with graphical user interface. *Air Infiltration Review 16*(1), 6–8.

Warsi, Z. and I. Chand (1967). Wind tunnel study of the effect of building orientation and ceiling height on indoor air motion. *Indian Journal of Technology 5*, 362–363.

Wurtz, E., J.-M. Nataf, and F. Winkelmann (1999). Two and three-dimensional natural and mixed convection simulation using modular zonal models in buildings. *International Journal of Heat and Mass Transfer 42*, 923–940.

Yuan, X. (1995). *Wall Functions for Numerical Simulation of Natural Convection along vertical surfaces.* Ph. D. thesis, Laboratorium für Engergiesysteme, ETH Zürich.

Yuan, X., A. Moser, and P. Suter (1993). Wall functions for numerical simulation of turbulent natural convection along vertical plates. *International Journal of Heat and Mass Transfer 36*(18), 4477–4485.